Neutron Scattering, Muon Spin Rotation/Relaxation, and Charge Transport Study of the Electron-Doped Cuprate Superconductors

A DISSERTATION
SUBMITTED TO THE FACULTY OF THE GRADUATE SCHOOL
OF THE UNIVERSITY OF MINNESOTA
BY

YANGMU LI

IN PARTIAL FULFILLMENT OF THE REQUIREMENTS
FOR THE DEGREE OF
DOCTOR OF PHILOSOPHY

MARTIN GREVEN, ADVISER

MAY, 2017

Acknowledgements

During my Ph.D. study, I have benefited a lot from collaborations and discussions with many people. Without their contributions, it would have been impossible for me to complete this Thesis work. Here I would like to thank them for helping me along the way.

I learned a lot from my Thesis advisor Martin Greven. He guided me into the field of cuprates and offered me many opportunities to collaborate with people on various experimental techniques. I was very fortunate to have this freedom, because understanding the cuprates requires knowledge from various perspectives. It was a wonderful experience, and I am still excited about the coherent story we built based on neutron scattering, μSR, and transport data. Martin is always optimistic, persistent, encouraging and open-minded. These attributes are essential for performing research in such a challenging field. Thank you, Martin.

I also benefited a lot from discussions with Neven Barišić, who was a mentor on our charge transport studies. Neven has great knowledge of transport techniques. He taught me how to prepare samples and to perform the measurements. In addition, it was because of him that I realized the significance of providing a coherent answer to complex questions. Thank you, Neven.

Many of my collaborators and colleagues educated me on various experimental techniques, and they deserve my gratitude. These people include all present and many former group members of the Greven group. In particular, I highly appreciate the help from Guichuan Yu, from whom I learned the floating-zone crystal growth and neutron scattering techniques. I would also like to thank Philippe Bourges at LLB, Masa Matsuda at ORNL, and Yuan Li at PKU for their collaboration on neutron scattering experiments. Through these collaborations, I was able to hone my neutron scattering

skills. Thanks to Professor Yasutomo Uemura at Columbia University and Professor Graeme Luke at McMaster University, and their group members, who taught me the μSR technique. I also learned how to use high-field dc magnets from Jan Jaroszynski at NHMFL, the MPMS from Mun Chan, and the PPMS from Timothy Peterson. Thank you all very much.

Numerous other people helped me to run experiments and to understand theoretical analysis. In particular, Ryan Frink, Rajendra Beekie, Curtis Peterson and Biqiong Yu helped me with materials syntheses. Instrument scientists Songxue Chi, Wei Tian and Doug Abernathy at ORNL helped me with neutron scattering experiments. Jeremy Carlo, Travis Williams, Soo Kyung Kim, and Tatsuo Goko helped me with μSR measurements. Changjiang Liu helped with PPMS measurements. Zach Anderson and Yang Tang helped with MPMS measurements. Bill Voje helped with the liquid helium recycling system. Jiashen Cai helped with magnetoresistivity calculations. For most of the neutron scattering, μSR, and charge transport experiments, I used samples that were synthesized by Eugene Motoyama and Patrick Mang. They all contributed a lot to this Thesis work.

I would like to further thank Eugene Motoyama. Much of my Thesis directly builds on his prior work on the electron-doped cuprates. He deserves my deep gratitude for having laid the groundwork for my Thesis.

I enjoyed and benefited from discussions with many professors and fellow students. Professors Allen Goldman, Dan Dahlberg, Paul Crowell, Rafael Fernandes, Andrey Chubukov, Chris Leighton, and their group members taught me a lot of science and presentation skills. I would like to thank three young theorists in particular: Chun Chen, Xiaoyu Wang, and Jian Kang. I had a lot of fun talking about crazy ideas with them.

I thank all my friends at the University of Minnesota who made my Ph.D. life cheerful and all fellow graduate students in the department who contributed to an inspiring environment. I highly appreciate the support that I received from our administrative staff Julie Murphy, Shelley Frankel, and the department head Ronald Poling.

A very special thanks to the late Allen Knutson, who was a staff member in the electronics shop of the department. I only had the chance to talk to Mr. Knutson for about 15 minutes, on the way from Tate to PAN. He was helping me to measure the

electrical voltage in the new PAN lab rooms. On the scholar's walk, Mr. Knutson told me about his memory of the university in the late 1960s and early 1970s. Only long after his bike accident, I realized that it was him. I was so fortunate to have talked to him and subsequently shared his memory with my friends in the department.

Finally, I extend my deepest gratitude to my family. I thank Biqiong for her companionship and unbounded love, and I am very grateful to my mother for her unending love and support. It is all because of them that I am able to pursue a scientific career.

Abstract

Exploring and understanding the exotic properties, phases, phase transitions exhibited by quantum materials are central research thrusts in contemporary condensed matter physics and materials science. One class of quantum materials that has attracted much attention during the past three decades is the family of copper-oxide (cuprate) high-transition-temperature superconductors. This family not only manifests superconductivity, a technologically useful macroscopic quantum state, but offers great opportunities for us to understand and control quantum phase transitions in the presence of strong electron-electron correlations. Investigating the competing, coexisting, and intertwined orders exhibited by the cuprate materials challenges us to consider new theoretical descriptions.

This Thesis focuses on a specific type of cuprate superconductor, namely the electron-doped cuprate materials. The phases exhibited by these materials (antiferromagnetism, superconductivity, and charge order) depend on the degree of chemical substitution and oxygen reduction. Because these chemical manipulations induce simultaneous modifications to multiple parameters (e.g., chemical potential, band structure, local disorder, etc.), the electron-doped cuprate materials exhibit a rich and complex phase diagram that remains to be fully understood. The results presented in this Thesis provide crucial links between the normal and superconducting states and between the electron- and hole-doped parts of the phase diagram.

High-quality single crystals of the archetypal electron-doped cuprate superconductor $Nd_{2-x}Ce_xCuO_{4+\delta}$ (NCCO) are synthesized using the state-of-the-art traveling-solvent floating-zone technique, and characterized by various in-house techniques, including Laue X-ray diffraction, magnetization (using a superconducting quantum interference device), scanning electron microscopy, and energy dispersive X-ray spectroscopy. The magnetic properties (Néel temperature, staggered magnetization, instantaneous spin-spin correlation length, magnetic volume fraction, and spin fluctuation timescales) and the electronic properties (Fermi surface topology, electrical resistivity, Hall constant, magnetoresistivity, upper critical field, superconducting volume fraction, and superfluid density) are studied with neutron scattering, muon spin rotation/relaxation (μSR),

and high-magnetic-field transport measurements at national laboratories in the United States and Canada. Published data for NCCO and other electron-doped cuprates are reanalyzed and compared with the new results obtained for NCCO. Simulations are performed for the instantaneous spin-spin correlation length and magnetoresistivity.

A revised phase diagram of the electron-doped cuprates is constructed in the multi-dimensional parameter space of temperature, chemical substitution, and oxygen reduction. Three distinct phases are observed as a function of chemical substitution and oxygen reduction: (1) a long-range antiferromagnetic phase, where the Fermi surface consists of small electron pockets; (2) a bulk superconducting phase, where the Fermi surface consists of small electron and hole pockets; (3) a phase at high doping levels with a large hole Fermi surface. A disorder-smeared, first-order phase transition with microscopic phase separation is identified between the long-range antiferromagnetic and bulk superconducting phases. Specifically, this phase transition is observed to be volume-wise, and distinct spin fluctuation timescales are found for each phase.

The magnetoresistivity measurements presented in this Thesis together with previous charge transport studies show two-band (electron and hole) contributions to the normal-state transport properties in electron-doped cuprate samples with bulk superconductivity. In addition, the two-band features are observed in the characteristic properties of the superconductor, including the upper critical field and the superfluid density. Universal scaling is demonstrated between the superconducting transition temperature and the hole superfluid density for both electron- and hole-doped cuprates, which clearly points to hole-related superconductivity in the nominally electron-doped cuprates. This scaling extends the famous Uemura scaling established for the hole-doped cuprates. The analysis of the superfluid density of the electron-doped cuprates follows that of prior theoretical work.

Furthermore, new and published data for the ab-plane resistivity, Hall coefficient, cotangent of the Hall angle, and c-axis resistivity for the electron- and hole-doped cuprates are analyzed. The ab-plane resistivity of the electron- and hole-doped cuprates and the c-axis resistivity of the electron-doped cuprates features an upturn at low temperature/doping and a quadratic temperature-dependent contribution. Universal scaling between coefficients that characterize the low-temperature upturn is obtained for both electron- and hole-doped cuprates, indicative of a single underlying origin of the

resistivity upturns, regardless of the nominal dopant type. The *ab*-plane transport scattering rate exhibits a quadratic (Fermi-liquid) temperature dependence, and is nearly independent of doping, compound and carrier type (electrons versus holes).

Contents

List of Tables

List of Figures

Chapter 1

Introduction

This Chapter briefly describes the scientific history that led to the current stage of research in the field of strongly-correlated materials, in particular the cuprates. I introduce the structural, electronic and magnetic properties of the cuprates and give an outline of this Thesis.

1.1 A roadway to quantum materials

Exploring, understanding, and describing the behavior and interactions of matter from the atomic scale to the macroscopic scale is the central focus of condensed matter physics and materials science. The quantum theory of solids developed in the 20^{th} century can explain many structural, electronic, and magnetic properties of materials. Materials that defy this conventional description are often referred to as quantum materials. Such materials exhibit a variety of unusual emergent phenomena (i.e., cooperative, collective behavior) [1]. These emergent phenomena typically result from strong many-body interactions among electrons and give rise to various fascinating states of matter (e.g., superconductivity, magnetism, and fractional quantum Hall states). Understanding how to determine ground states, excitations, and the relationships among different states of matter is at the heart of the quantum materials research.

Quantum theory can be traced back to the early 19^{th} century, following the development of the wave theory for light. John Dalton [2], intrigued by the observation of different absorption rates of gases in liquids, introduced the first evidence-based concept

of atoms (the idea of atoms was proposed by the ancient Greeks). Transitions between different states of matter (e.g., solid, liquid, and gas) at macroscopic scale were investigated at the phenomenological level [3]. At the end of 19^{th} century, light radiation from matter was intensively studied. Based on a peculiar (at the time) relation between the temperature of matter and its dominant radiation frequency, Max Planck proposed that the energy of radiated light, instead of being continuous, is quantized [4]. Albert Einstein later extended this proposal while solving the puzzle of the photoelectric effect. He suggested that light can only be emitted or absorbed by matter in discrete quanta, and thus that light can be characterized as a particle [5]. The elementary particle of light is the photon, and a photon with a given frequency carries a certain quantum of energy. Niels Bohr then studied light emitted from atoms (atomic line spectra) and postulated that in order to emit light with discrete energies, electrons can only occupy a discrete set of orbits [6]. After the establishment of the dual characteristics (particle and wave) of light, Louis de Broglie hypothesized a momentum-energy-frequency relation between the particle and wave descriptions [7]. Subsequently, this relation was found to be true for particles other than the photon.

The development of the single-particle quantum theory included Werner Heisenberg's matrix mechanics [8] and Erwin Schrödinger's wave mechanics [9]. The renowned Schrödinger equation was built by replacing the term of kinetic momentum in the energy conservation equation with an operator obtained using a plane wave as the wave function. Subsequently, angular quantum numbers were obtained upon introducing the Coulomb potential. The spin degree of freedom (an additional quantum number) was later proposed by Wolfgang Pauli (non-relativistic) [10] and Paul Dirac (relativistic electron with four-component spinor) [11, 12], which explained the Stern-Gerlach [13, 14] and Zeeman experiments [15]. The concept of electron spin was used to explain Wolfgang Pauli's exclusion principle [10].

A real difficulty appeared when physicists began to study multi-particle systems well beyond the reach of the single-particle quantum theory. The Schrödinger equation can no longer be exactly solved when including complex interactions among particles. In order to simplify the Schrödinger equation, approximations such as Hartree-Fock [16], random phase [17], and configuration interaction [18] methods were applied to estimate wave functions. In addition, computational methods, such as density functional theory

[19] and quantum Monte Carlo [20], were developed. These methods, which occasionally describe experimental results with good accuracy, are typically inadequate when dealing with the complex phenomena exhibited by quantum materials.

In parallel with the development of theoretical descriptions, new states of matter were observed experimentally. In 1911, Heike Kamerlingh Onnes discovered that the electrical resistivity of mercury becomes zero below about 4 K [21]. In the 1930s, Walther Meissner and Robert Ochsenfeld [22] observed that materials in their zero-resistant states also actively expel magnetic fields from their interior. Materials with these two defining properties were named superconductors in order to distinguish them from (hypothetical) perfect conductors that do not exhibit the Meissner-Ochsenfeld effect. A natural subsequent question was how far a magnetic field can penetrate into superconductors. The London brothers applied electromagnetic theory and found that an external magnetic field is exponentially suppressed on a certain length scale (the London penetration depth) [23]. Measurements of the thermal conductivity of superconductors showed the existence of an electronic gap in the superconducting state. The superconducting transition temperature (T_c) was observed to depend on the choice of isotope, an indication that the vibrations of lattice atoms (phonons) are relevant to superconductivity. In 1957, John Bardeen, Leon Cooper, and John Robert Schrieffer (BCS) proposed a superconducting wave function by assuming an attractive interaction between electrons due to phonons [24]: two electrons with opposite kinetic momentum and spin form a boson called a Cooper pair. The Cooper pairs condense and constitute a new ground state. The BCS theory successfully described superconductors with an isotropic energy gap (later named s-wave, type-I superconductors [25]).

There exist two basic categories of superconductors. In contrast to type-I superconductors, which are perfect diamagnets, type-II superconductors form magnetic vortices above a threshold magnetic field (the lower critical field H_{c1}), and thus do not exhibit a complete Meissner-Ochsenfeld effect. The magnetic field that suppresses superconductivity completely is named the upper critical field (H_{c2}). The type-II superconductors were described by Ginzburg-Landau theory [26], which argues that the formation of magnetic vortices is the result of a superconducting coherence length htat is shorter than the London penetration depth.

The wave functions that describe the superconducting states have both spin and

orbital components. S-wave superconductors constitute the simplest realization (Cooper pairs have total spin $S = 0$ and angular momentum $l = 0$). Superconductors with higher-order wave functions, such as p-wave ($S = 1$, $l = 1$), d-wave ($S = 0$, $l = 2$), and f-wave ($S = 1$, $l = 3$) were proposed [25, 27, 28]. The cuprates exhibit d-wave superconductivity, and the possible observation of p-wave superconductivity [28] is still under debate.

Following the discovery of superconductivity, numerous technological applications were proposed. Based on the electrical properties of superconductors, electrical cables were built to enhance energy densities and to minimize energy-loss during electricity transfer [29]. Because of the Meissner-Ochsenfeld effect, electromagnets made from superconductors began to be used in many aspects of human activity, such as in public transportation (maglev train [30]), health care (magnetic resonance imaging [31]), and scientific research (high-field magnets [32]). Applications were also achieved by utilizing other delicate characteristics of superconductors (such as Josephson junctions based on the current-phase relation [33]). In order to utilize their fascinating electrical and magnetic properties, superconductors have to be cooled below their respective T_c. The highest T_c achieved in 70 years following Kamerlingh Onnes' discovery of the superconductors was only at 23.2 K (Nb_3Ge [34]), rendering difficulties in applications.

In 1986, Georg Bednorz and Alex Müller [35] reported the discovery that a layered cuprate material, $La_{2-x}Ba_xCuO_4$, exhibits superconductivity at about 30 K. Superconducting transition temperatures as high as 134 K at ambient pressure (163 K under high pressure) were soon found in other cuprate materials [36]. The discovery of this family of high-transition-temperature (high-T_c) superconductors was big news at the time, not only due to the unprecedented high values of T_c and the associated technological potential (liquid nitrogen used to cool high-T_c superconductors, with a boiling point at about 77 K, is much cheaper than liquid helium used to cool superconductors with a lower T_c), but also because the observed T_c values exceeded the theoretical upper limit of about 30 K thought to exist at the time. Interestingly, the parent state of the cuprate superconductors, instead of being a good metal, was soon found to be an antiferromagnetic Mott insulator. Such insulating behavior, which can not be understood by the conventional band picture, was proposed by Mott to be caused by large onsite Coulomb repulsions which can cause localization of electrons and result in magnetism [37, 38].

The emergence of superconductivity at high temperatures is generally thought to be related to the strong electron correlations, but the pairing mechanism has remained elusive. In addition, many exotic electronic and magnetic properties were observed in the non-superconducting "normal" state at temperature above T_c. How to best understand their properties and how the superconductivity emerges upon doping and cooling are central questions posed by these fascinating materials.

1.2 Cuprate superconductors

1.2.1 Crystal structures and phase diagram

A defining characteristic of the cuprate superconductors is their quintessential square-planar, copper-oxygen (CuO_2) layer (Fig. 1.1). The crystal structures of the cuprates are similar to the three-dimensional perovskite structure (ABO_3) of, e.g., strontium titanate ($SrTiO_3$). The CuO_2 layers are stacked with charge-reservoir layers in between. Those charge reservoir layers supply electrons or holes to the CuO_2 layers [42], a process referred to as doping. For isolated copper and oxygen atoms, the atomic orbital configurations of the electrons are $[Ar]3d^{10}4s^1$ and $[He]2s^22p^4$, respectively. For the "ions" in the undoped parent compounds, experiments suggested that copper can be approximately thought of as Cu^{2+} with $[Ar]3d^9$ configuration and oxygen approximately as O^{2-} with $[He]2s^22p^6$ configuration [42]. The actual situation is more complex than this simple ionic picture. For example, a partial covalent nature of the copper-oxygen bonds was observed in nuclear magnetic resonance (NMR) work [43]. The copper-oxygen structures can be classified into three categories: tetragonal (T, copper-oxygen octahedron), tetragonal prime (T′, copper-oxygen planar structure), and tetragonal star (T*, with only one apical oxygen site occupied). The degree of orbital hybridization differs for these different structures. Because the CuO_2 layer is universal and the charge-reservoir layers are not, the CuO_2 layer is thought to be responsible for existence of unusual behavior exhibited by the cuprates, including the emergence of unconventional superconductivity [42].

As shown in Fig. 1.1, two primary oxygen sites exist in typical cuprate structures: (1) a site in the CuO_2 layer; (2) a site in the charge reservoir layer or, alternatively, the apical site directly above or below copper atoms. In addition, interstitial oxygen atoms

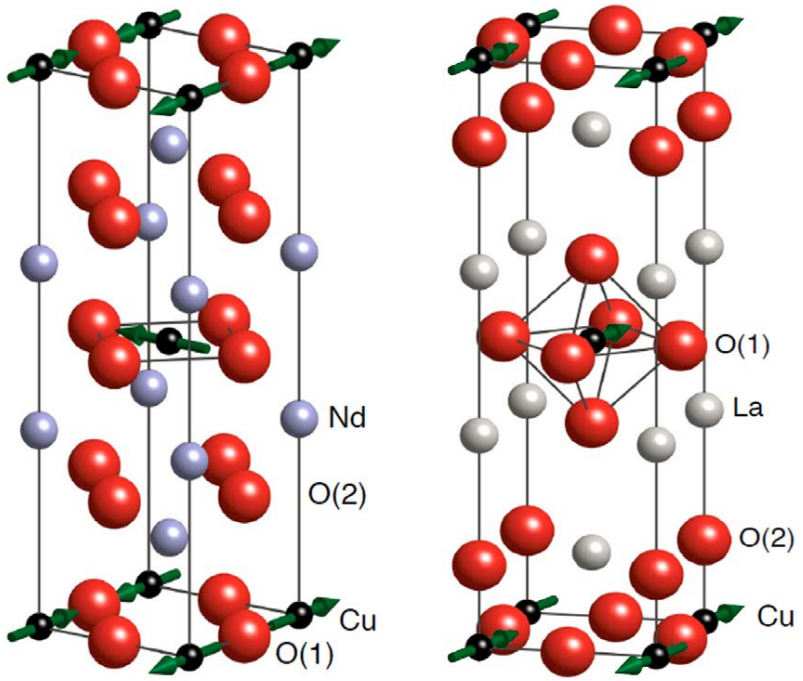

Figure 1.1: Crystal structures of two single-CuO_2-layer cuprate superconductors. The electron-doped compound $Nd_{2-x}Ce_xCuO_{4+\delta}$ (NCCO) has the T′ structure and the hole-doped compound $La_{2-x}Sr_xCuO_4$ (LSCO) has the T structure. Red and black spheres indicate the oxygen and copper atoms, respectively. The gray spheres show Neodymium and Lanthanum atoms for NCCO and LSCO, respectively. Spin orientations on copper sites in the antiferromagnetically ordered state are shown as green arrows. While NCCO remains tetragonal to low temperatures, LSCO undergoes a structural transition to an orthorhombic phase below a doping (x)-dependent temperature [39]. Figure adapted and modified from [40].

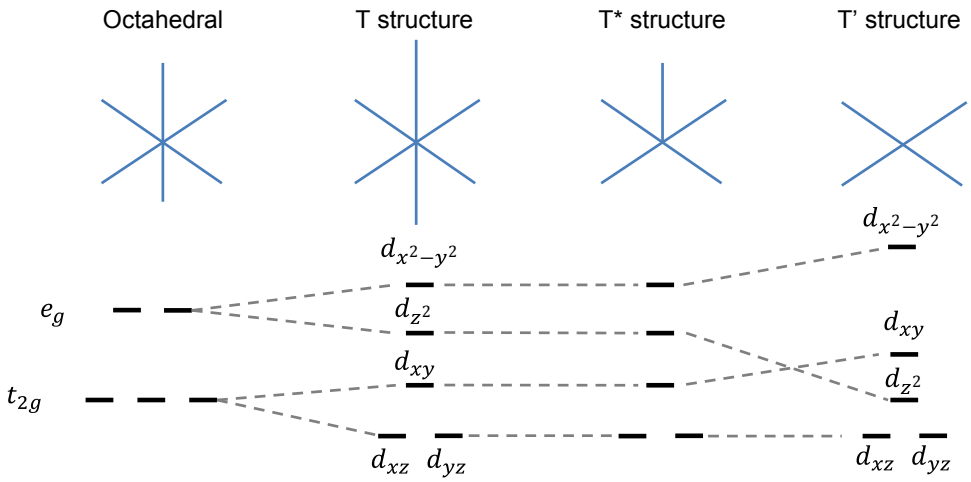

Figure 1.2: Crystal-field diagram for the T, T′ and T* structures. Figure constructed based on quantum chemistry calculations (see e.g., [41]).

(not shown in Fig. 1.1) can typically be introduced to (or removed from) the charge-reservoir layers. The electron-doped cuprates, e.g., $Nd_{2-x}Ce_xCuO_{4+\delta}$ (NCCO), has the T′ structure. Single-CuO_2 layer hole-doped cuprates $La_{2-x}Sr_xCuO_4$ (LSCO) have the T structure, with fully occupied apical oxygen sites and elongated Cu - apical O bonds. The T* structure labels a material in which only one of the two apical oxygen sites is occupied (not shown). These structural differences affect the crystal field splitting of the Cu-3d/ O-2p orbitals. For the T and T* structures, electrons can be shared between copper and apical oxygen atoms, thus the electronic hybridization has a z component. The crystal field splitting of the 3d Cu orbitals for these structures is shown in Fig. 1.2. The relevant highest energy level for all structures is the $3d_{x^2-y^2}$ orbital. Note that the orbitals with the second highest energy differ for the T and T′ structures. Because of the nominal [Ar]$3d^9$ electronic configuration of copper, the orbital configuration of the second highest energy is often neglected in theoretical descriptions. An illustration of the planar copper-oxygen orbital hybridization is shown in Fig. 1.3.

In the antiferromagnetically order state of the insulating parent compounds, the spin structure have been determined using neutron scattering techniques. A collinear antiferromagnetic structure with spins oriented along the diagonal direction ([1 1 0], in

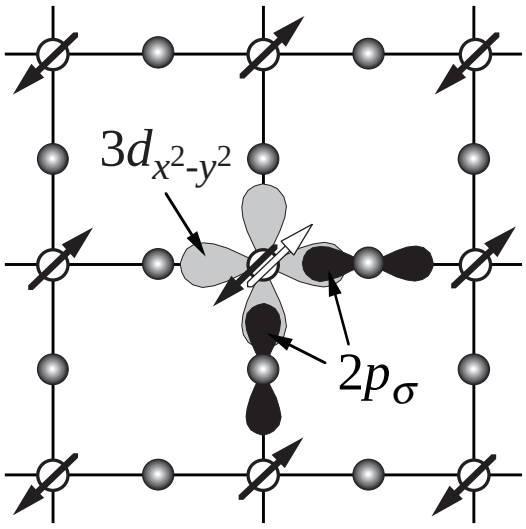

Figure 1.3: Illustration of the copper-oxygen orbital hybridization in the CuO_2 plane. White spheres, gray spheres, and arrows indicate copper atoms, oxygen atoms, and the copper spin-1/2 magnetic moments, respectively. The white arrow indicates the spin of an additional electron doped into the CuO_2 plane of a T′ material via chemical substitution (Ce^{4+} doping in NCCO). Doped electrons prefer to stay in the Cu $3d_{x^2-y^2}$ orbital. Figure adapted from [44].

the CuO_2 layers) was observed for the T structure, and a non-collinear, layer-alternating antiferromagnetic structure with spins oriented along the copper-oxygen bond ([1 0 0] and [0 1 0], in the CuO_2 layers) was observed for the T′ structure [56, 57]. Because the spin structure strongly depends on a material's atomic structure and magnetic superexchange energy [58], it can change as a function of temperature, pressure, etc. For example, the Cu moments of Nd_2CuO_4 (Fig. 1.1), which order antiferromagnetically below a Néel temperature of about $T_N = 270$ K [57], reorient at $T = 75$ K and 30 K.

For many cuprates, chemical substitution is used to introduce electrons or holes into the CuO_2 layers. For example, Nd^{3+} ions can be replaced by Ce^{4+} ions to dope electrons in NCCO, and La^{3+} ions can be replaced by Sr^{2+} ions to dope holes in LSCO. In addition, the doping level (chemical potential) also depends on deviations from stoichiometric chemical composition. Figure 1.4 shows a schematic band digram for NCCO and LSCO.

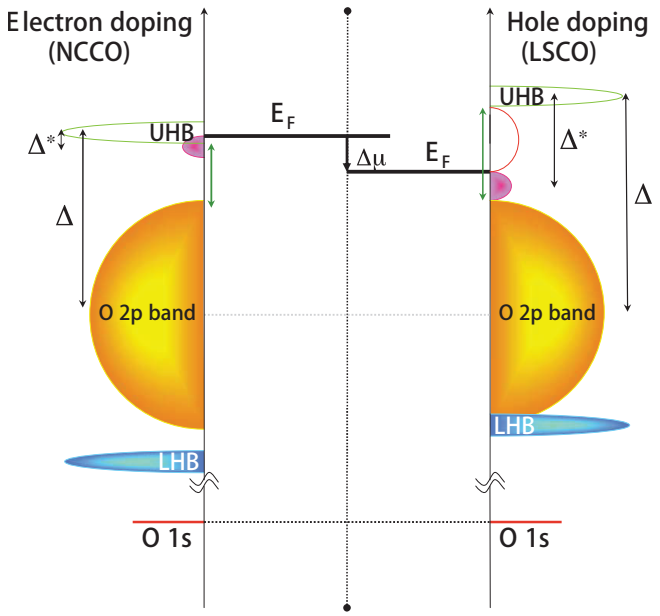

Figure 1.4: Schematic band diagram for NCCO and LSCO. UHB (LHB) denotes the upper (lower) Hubbard band, and E_F denotes the Fermi energy. Doped electrons or holes introduce states shown in magenta. Figure adapted from [45].

Because of the large onsite Coulomb repulsion (the [Ar]$3d^{10}$ configuration has a much higher potential energy than [Ar]$3d^9$ configuration for copper), the $3d_{x^2-y^2}$ orbital is split into upper (UHB) and lower (LHB) Hubbard bands, with a gap on the order of 10 eV. The oxygen $2p$ bands lie between the UHB and LHB, and thus the Mott-insulating parent compounds are technically charge-transfer insulators. Doped electrons stay near the bottom of UHB and doped holes stay near the top of oxygen $2p$ bands. Detailed discussions of the electronic and magnetic structures of the cuprates can be found in review articles such as [42, 59–64].

A schematic temperature-doping phase diagram for cuprates is shown in Fig. 1.5 [42]. Near half-filling (zero doped carriers, one $d_{x^2-y^2}$ electron per copper site), the ground state of the cuprates is an antiferromagnetic insulator. At large electron and hole doping concentrations, the cuprates are non-magnetic and exhibit conventional Fermi-liquid behavior. Superconductivity is observed at intermediate doping concentrations.

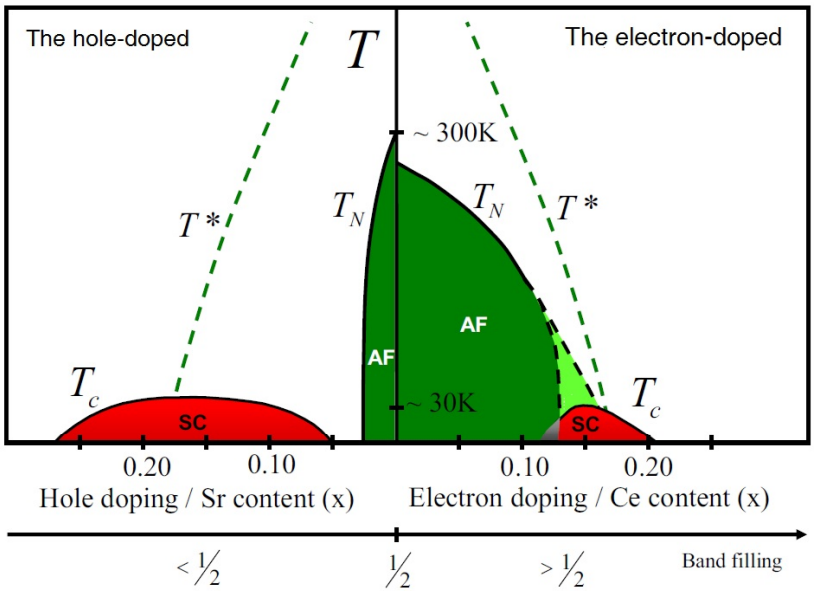

Figure 1.5: Schematic temperature-doping phase diagram of the hole-doped (LSCO) and the electron-doped (NCCO) cuprates. The antiferromagnetic (AF) and superconducting (SC) phases are indicated by dark green and red, respectively. $T_{\rm N}$, T^*, and T_c denote the Néel temperature, pseudogap temperature, and supercomputing transition temperature, respectively. The uncertainty regarding the antiferromagnetic phase boundary on the electron-doped side is shown as a light green area. Figure adapted from [42].

The antiferromagnetic phase does not coexist with the superconducting phase on the hole-doped side, whereas the question of a possible coexistence on the electron-doped side has remained under debate. A partial gap (pseudogap) opens in momentum space at temperatures (T^*) higher than the Néel temperature (T_N).

It is instructive to compare the phase diagram of the cuprates to those of other unconventional superconductors. Phase diagrams for the iron arsenide compounds La(O,F)FeAs, Sm(O,F)FeAs, Ce(O,F)FeAs, and (Ba,K)Fe_2As_2, the organic superconductor κ-(BEDT-TTF)$_2$X, and the heavy-fermion compound $CeRhIn_5$ are shown in Fig. 1.6. The universal existence of a first-order transition in the presence of disorder between the antiferomagnetic and the bulk superconducting order was proposed in [52].

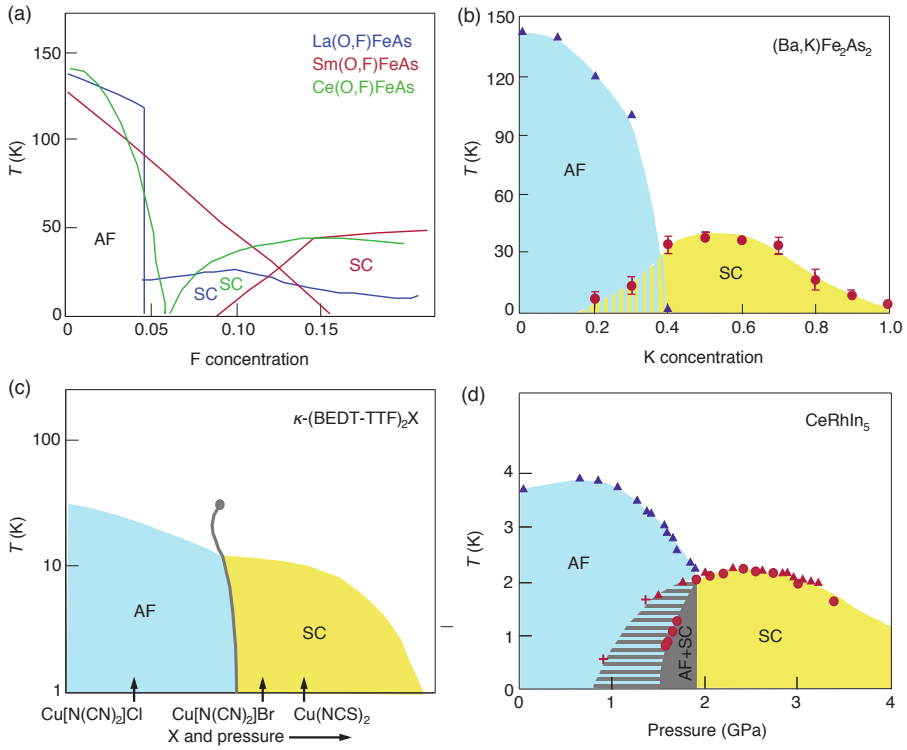

Figure 1.6: Phase diagrams of other unconventional superconductors: (a) the iron arsenide compounds La(O,F)FeAs [46], Sm(O,F)FeAs [47], and Ce(O,F)FeAs [48], (b) the iron arsenide compound (Ba,K)Fe_2As_2 [49], (c) the organic superconductor κ-(BEDT-TTF)$_2$X [50], and (d) the heavy fermion compound $CeRhIn_5$ [51]. Figure reproduced from [52].

The temperature-doping phase diagram for oxygen-reduced NCCO based on neutron-scattering measurements of the instantaneous spin-spin correlation length was previously reported in [55] (Fig. 1.7). The measurements were performed at intermediate Ce concentrations and at temperatures comparable to, or higher than the apparent Néel temperatures. This phase diagram left open the possibility of a quantum critical point around $x = 0.134$. The newer results presented in this Thesis work (Chapter 3), which were obtained for samples with improved chemical homogeneity and extend to temperatures much lower than the apparent Néel temperature, instead reveal a disorder-smeared first-order phase transition between antiferromagnetic and superconducting phases.

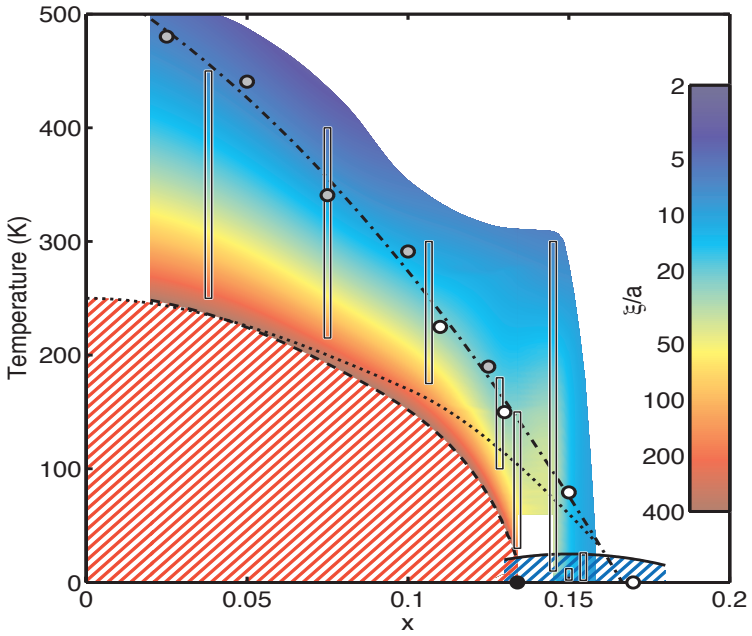

Figure 1.7: Previous temperature-doping phase diagram for oxygen-reduced NCCO based on neutron-scattering measurements of the instantaneous spin-spin correlation length. The red and blue hashed areas indicate long-range antiferromagnetic order and superconductivity, respectively. The instantaneous spin-spin correlation length ξ was measured at the doping levels and over the temperature ranges indicated by the vertical bars. The Néel temperature T_{N} is shown as the dotted line, whereas the dashed line is the extrapolated contour of $\xi/a = 400$ (a is the planar lattice constant). The grey and white circles indicate optical conductivity measurements of of the pseudogap temperature T^* for NCCO crystals[53] and $Pr_{2-x}Ce_xCuO_{4\pm\delta}$ thin films[54], respectively. The dot-dashed curve is a guide to the eye. Figure reproduced from [55].

The origin of the high-T_c superconductivity in the cuprates is highly debated, and this question has been studied with numerous distinct theoretical approaches, ranging from the strong-coupling limit to the weak-coupling limit [27, 61, 65–73]. Among the many proposed pairing mechanisms are antiferromagnetic fluctuations [27], which are best studied via neutron scattering.

1.2.2 Pairing symmetry

The electronic pairing mechanism and pairing symmetry in the cuprates have been intensively studied. Due to the unprecedentedly high T_c, early work questioned the existence of Cooper pairs in cuprates [74], yet experimental work soon revealed a quantization of the magnetic flux that corresponds to two electrons, providing direct evidence of Cooper pairs [75]. Because of the distinct electronic structure of the quintessential CuO_2 plane, the pairing symmetry is limited to a few candidates, including s, $d_{x^2-y^2}$, d_{xy}, and g symmetries [74]: s symmetry corresponds to a constant superconducting gap in the momentum space, whereas $d_{x^2-y^2}$, d_{xy}, and g symmetries correspond to superconducting gaps with nodes and a sign change in the phase of the wave function that describes the superconducting state. The paring symmetry of the cuprates was studied by non-phase-sensitive techniques (such as penetration depth, specific heat, thermal conductivity, angle-resolved photoemission, raman scattering, and nuclear magnetic resonance) and phase-sensitive techniques (such as superconducting quantum interference device (SQIUD) and Josephson-junction).

For the hole-doped cuprates, evidence for predominantly d-wave pairing symmetry was revealed by phase-sensitive techniques in both orthorhombic and tetragonal materials [74]. Calculation based on the t-J model (see the following Sections) also suggested that the d-wave pairing symmetry prevails near half-filling (see references in [74]). In the case of the electron-doped cuprates, interpretations of experimental results (s-wave versus d-wave) were debated for years before a consensus on the pairing symmetry was finally reached (d-wave gap with nonmonotonic gap amplitude) [42, 74].

Raman scattering measures photons absorbed and emitted by materials. With a choice of specific polarization geometries of the initial and emitted photons, Raman scattering can probe specific regions of the k space, and thus detect an anisotropy of

the superconducting gap. In particular, Raman scattering results point to a nonmonotonic $d_{x^2-y^2}$ superconducting gap, with a node along the Brillouin zone diagonal and a maximum gap at antiferromagnetic hot spots ($2\Delta_{\rm SC,max} \approx 4.4 k_B T_c$ for NCCO), i.e., at the intersection of the antiferromagnetic Brillouin zone and the Fermi surface [76]. The doping dependence of superconducting gap amplitude was extracted using Raman scattering [77], and it was concluded that the superconducting gap node exists in a wide doping range.

The existence of a node in the superconducting gap ($\Delta_{\rm SC}$) manifests itself in the temperature dependence of the superfluid density, which measures the phase stiffness ($\rho_s(T)$) of the condensate, such that $\rho_s(T) \sim e^{-\Delta_{\rm SC}/T}$ for an isotropic (s-wave) $\Delta_{\rm SC}$ and $\rho_s(T) \sim 1 - T^2/T_c^2$ for a d-wave superconductor with impurity scattering [78]. The superfluid density can be obtained by probing the London penetration depth or the magnetic field distribution of vortices (see transverse-field μSR in Chapter 2). Because of the strong magnetic response of Nd^{3+} ions, data for NCCO can be contaminated at low temperature [79]. Penetration depth experiments on $Pr_{2-x}Ce_xCuO_{4+\delta}$, which essentially avoided this low-temperature contamination (ordered moment: $Nd^{3+} \approx 1.23\mu_B$, $Pr^{3+} \approx 0.08\mu_B$), observed that $\rho_s(T) \approx 1 - T^2/T_c^2$ [80, 81]. It was proposed that the superfluid density can be decomposed into $\rho_s(T) \approx e^{-\Delta_{\rm SC}/T}$ and $\rho_s(T) \approx 1 - T^2/T_c^2$ contributions [77, 82].

Photoemission spectroscopy, which measures single-particle electronic excitations in k space, probes the superconducting gap through a shift in the spectrum near the Fermi surface. Photoemission experiments detected an anisotropic gap consistent with the Raman scattering results (large gap near the Brillouin zone boundary, and negligible gap along zone diagonal) [83, 84]. The maximum superconducting gap was estimated to be $\Delta_{\rm SC,max} \sim 4$ meV for NCCO. The non-monotonic angular dependence of the superconducting gap was later determined as $\Delta_{\rm SC} = 1.9[1.43\cos 2\phi - 0.43\cos 6\phi]$ meV [85, 86] for $Pr_{1-x}LaCe_xCuO_4$ (PLCCO).

Electron tunneling experiments between a metal and a superconductor are sensitive to the pairing symmetry by measuring the density-of-states as a function of tunneling bias. A V-shape differential conductance (dI/dV), which signifies the d-wave pairing, was observed for NCCO and PLCCO in [87, 88].

Specific heat and thermal conductivity are sensitive probes of low-energy excitations.

For s-wave superconductors, the existence of a superconducting gap was first revealed by such measurements. The expected temperature and field dependences of the electronic specific heat for a d-wave superconductor are given by $C_{el} \sim T^2/T_c^2$ and $C_{el} \sim \sqrt{H}$, respectively [89]. The temperature dependence of the electronic specific heat is difficult to extract due to the dominant phonon contribution, but the $C_{el} \sim \sqrt{H}$ field dependence was observed for $Pr_{2-x}Ce_xCuO_{4+\delta}$ (PCCO) [90–92].

Another characteristic of d-wave superconductivity is the sign change in the phase of the wave function that describes the superconducting state. Such a sign change was detected by measuring trapped flux quanta, i.e., the Josephson effect, between superconductors with different phase of the wave function. The half-flux quantum was observed using a SQUID for tricrystal junctions for PCCO and NCCO [93] and the supercurrent expected for a d-wave gap was found in a zig-zag Josephson junction for NCCO [94].

1.2.3 Pseudogap

The pseudogap is one of the most enigmatic phenomena in condensed matter physics. For the underdoped hole-doped cuprate materials, below a temperature T^* higher than the superconducting transition temperature T_c, a partial gap is observed to open on portions of the Fermi surface near the Brillouin zone boundary, i.e., near (π, 0) and equivalents, in k space, rendering an arc-like Fermi surface. Here, we use notations in which the lattice constant a is unitary and hence the reciprocal lattice constant (r.l.u.) is 2π rather than $2\pi/a$. According to conventional understanding, arc-like Fermi segments can not exist, as the Fermi surface should be a closed boundary of the Fermi sea. The existence of the pseudogap indicates that Fermi statistics may no longer describe the low-energy excitations near the zone boundary (also named antinodal regions, in contrast to the nodal regions on the Fermi arcs where that the node of the d-wave order parameter is located in the superconducting state).

The manifestation of the pseudogap in the electron-doped cuprate materials is different. No arc-like Fermi segments have been observed. However, features of a gap were indeed revealed in the charge degrees of freedom. Optical conductivity spectra (with electrical field both parallel to the CuO_2 plane and along the crystalline c-axis)

[53, 54, 95] revealed the opening of a gap at temperatures much higher than the antiferromagnetic ordering temperature $T_{\rm N}$, in the approximate energy range $\sim 0.2 - 0.3$ eV. Photoemission measurements [85] also found gap features (a suppression of the spectral weight near Fermi energy) near the antiferromagnetic hot spots (which correspond to the intersections of the antiferromagnetic Brillouin zone with the underlying Fermi surface and are different from the antinodal positions for the hole-doped cuprates). Because the energy scales of the gaps observed by optical conductivity and photoemission are similar, it was argued that they have the same origin. The temperature T^* below which the gap opens monotonically decreases with increasing Ce and hence electron concentration [95], just as for the hole-doped cuprates. The gap magnitude was revealed to be $\Delta_{PG} \approx 10 k_B T^*$ [95]. The pseudogap temperature T^* separates the phase diagram into two regions: the Fermi surface is disconnected below T^* and fully connected above T^* for NCCO. The Ce concentration x^* at which T^* extrapolates to zero marks a zero-temperature transition in the Fermi surface topology [53].

In previous neutron scattering studies [55], the instantaneous spin-spin correlation length at the pseudogap temperature ($\xi^* \equiv \xi(T^*)$) was found to be consistent with a power-law dependence on x, with ξ^* on the order of thermal de Broglie length, $\xi_{\rm th}$. Based on theoretical considerations, it has been argued that T^* is the temperature below which the magnetic correlations exceed $\xi_{\rm th}$ [96]. In Chapter 3, it will be shown that our newer, more precise data indicate the break-down of the power-law doping dependence of ξ^* in the normal-state above bulk superconducting phase, i.e., for $x > 0/145$.

Reports for the hole-doped cuprates suggest that T^* coincides with the onset of a novel magnetic order. Polarized neutron diffraction measurements of $YBa_2Cu_3O_{6+x}$ [97, 98] and $HgBa_2CuO_{4+\delta}$ [99] showed that this magnetic order preserves the translational symmetry of the CuO_2 lattice ($\vec{q}$=0 order) and is thus quite different in nature from the antiferromagnetic order (with the $\vec{q}$=(π, π) propagation vector). It remains an open question whether T^* in the electron-doped cuprates is associated with the $\vec{q}$=0 order as well.

1.2.4 General theoretical descriptions

In order to theoretically describe the motion of electrons and ions in materials, the quantum mechanical total energy operator needs to be constructed. The generic Hamiltonian

for a given system can be expressed as

$$H = H_{\mathrm{e-e}} + H_{\mathrm{i-i}} + H_{\mathrm{i-e}}, \tag{1.1}$$

where $H_{\mathrm{e-e}}$, $H_{\mathrm{i-i}}$ and $H_{\mathrm{e-i}}$ are electron-electron, ion-ion and electron-ion energy operators, respectively. The Schrödinger equation is given as

$$H\Psi = i\hbar\frac{\partial}{\partial t}\Psi, \tag{1.2}$$

where Ψ is the wave function. The Hamiltonian and the Schrödinger equation can be written in either real space or momentum space. Once the operator H is specified, various theoretical approches can be applied to extract useful information from Eq. 1.2.

Weakly interacting electron systems

In some materials, a subset of the electrons can (almost) move freely and form an "electron gas." An useful wave function basis is the plane-wave basis. In this case, $H_{\mathrm{i-i}}$ and $H_{\mathrm{e-i}}$ can be ignored (or approximated as a background potential). Written in momentum space, using the notation of second quantization [100], the Hamiltonian can be expressed as

$$H = \sum_{k,\sigma} \varepsilon_k c^\dagger_{k,\sigma} c_{k,\sigma} + \sum_{k,k',q,\sigma,\sigma'} v_{k,k',q} c^\dagger_{k+q,\sigma} c^\dagger_{k'-q,\sigma'} c_{k,\sigma} c_{k',\sigma'}, \tag{1.3}$$

where $c^\dagger$ and c are fermion creation and annihilation operators, k, k', and q denote the electron momenta and the momentum transfer, and σ and σ' denote the spin states. For the electron-electron Coulomb interaction, $v_{k,k',q} = \frac{1}{4\pi\varepsilon_0}\frac{2\pi e^2}{q^2}$ can be obtained by performing Fourier transform of the interaction in real space.

A particularly useful quantity to consider is the momentum-energy particle propagating function $G(k-k',\omega)$ (i.e., the Green's function), which denotes the probability amplitude of finding a particle in state $|k,\sigma\rangle$, given the that it was initially in state $|k',\sigma'\rangle$. For the Hamiltonian in Eq. 1.3, the momentum-energy particle propagating function can be expressed as [101]

$$G(k-k',\omega) = \frac{1}{\omega - \varepsilon_k - \sum(k,\omega)}, \tag{1.4}$$

where $\sum(k,\omega)$ is the one-particle irreducible self-energy. The important single-particle spectral function $A(k,\omega)$, measured in photoemission experiments, is then deduced from the imaginary part of the momentum-energy particle propagating function [101]

$$A(k,\omega) = -\frac{1}{\pi}\lim_{\delta\to 0}\mathrm{Im}[G_R(k-k',\omega+i\delta)]. \tag{1.5}$$

The BCS superconductors

Upon introducing in Eq. 1.3 an additional phonon-mediated, electron-electron attractive interaction, $V_{e-ph} = \sum_{k,q,\sigma} M_q(a^\dagger_{-q} + a_q)c^\dagger_{k+q,\sigma}c_{k,\sigma}$ (where $a^\dagger$ and a are phonon creation and annihilation operator, respectively), the interaction is modified [25]:

$$v_{k,k',q} \to v^{\mathrm{eff}}_{k,k',q} = \frac{1}{4\pi\varepsilon_0}\frac{2\pi e^2}{q^2+q^2_{\mathrm{TF}}} + \frac{2|M_q|^2\omega_q}{\omega^2-\omega_q^2}, \tag{1.6}$$

where ω_q is the eigenvalue of a phonon in a plane-wave state $|q\rangle$ and q_{TF} is the Thomas-Fermi screening wave vector.

Denoting $b_k = \langle c_{-k,\downarrow}c_{k,\uparrow}\rangle$ and $b^\dagger_k = \langle c^\dagger_{k,\uparrow}c^\dagger_{-k,\downarrow}\rangle$, and introducing superconducting gap parameters ($\Delta^\dagger_k = \sum v^{\mathrm{eff}}b^\dagger$, $\Delta_k = \sum v^{\mathrm{eff}}b$), the Hamiltonian can be approximated as

$$H = \sum_{k,\sigma}\varepsilon_k c^\dagger_{k,\sigma}c_{k,\sigma} - \sum_k(\Delta_k c^\dagger_{k,\uparrow}c^\dagger_{-k,\downarrow} + \Delta^\dagger_k c_{-k,\downarrow}c_{k,\uparrow} - b^\dagger_k\Delta_k). \tag{1.7}$$

Rewriting $\gamma_{k,\uparrow} = u_k c_{k,\uparrow} - v_k c^\dagger_{-k,\downarrow}$ and $\gamma_{k,\downarrow} = u_k c_{k,\downarrow} - v_k c^\dagger_{-k,\uparrow}$ (Bogoliubov transformation [102]), the Hamiltonian can be diagonalized with the energy dispersion:

$$E = \sqrt{\varepsilon_k^2 + \Delta_k^2} \tag{1.8}$$

This is the result of the Bardeen-Cooper-Schrieffer (BCS) theory for s-wave type-I superconductors [24].

Hubbard and the t-J models

if the electrons in the system are confined to the ions (localized) and only occasionally move to other atomic sites, the plane-wave basis in momentum space no longer describes the system. Instead, the Hamiltonian can be expressed in real space. For the cuprates,

the most relevant electron orbitals near half-filling are the copper $3d_{x^2-y^2}$, and oxygen $2p_x$ and $2p_y$ orbitals. The Hamiltonian of the three-band Hubbard model is [61]

$$H = -t_{ij} \sum_{\langle i,j\rangle\sigma} (d^\dagger_{i,\sigma} p_{j,\sigma} + p^\dagger_{j,\sigma} d_{i,\sigma}) - t_{jj'} \sum_{\langle j,j'\rangle\sigma} (p^\dagger_{j,\sigma} p_{j',\sigma} + p^\dagger_{j',\sigma} p_{j,\sigma}) + (\varepsilon_d - \mu) \sum_{i,\sigma} (n^d_{i,\sigma} + n^p_{j,\sigma}) + U_{dd} \sum_i n^d_{i,\uparrow} n^d_{i,\downarrow} + U_{pp} \sum_j n^p_{j,\uparrow} n^p_{j,\downarrow} + U_{pd} \sum_{\sigma\sigma',ij} n^d_{i,\sigma} n^p_{j,\sigma'}, \tag{1.9}$$

where i and j denote copper and oxygen sites, σ denotes the spin state, d and p ($d^\dagger$ and $p^\dagger$) denote (creation) annihilation operators for the copper $3d$ and oxygen $2p$ orbitals, respectively, t, ε_d, and μ denote the hopping parameter, energy of the copper $3d$ orbital and the chemical potential, respectively, U_{dd} (U_{pp}) denotes interactions between electrons occupying the same copper (oxygen) site, U_{pd} denote interactions between electrons occupying nearest copper and oxygen sites, and n^d (n^p) denotes electron occupation on copper (oxygen) sites.

In case the Fermi energy lies inside a single conduction band (copper $3d$ orbital for electron-doping and oxygen $2p$ orbital for hole-doping), assuming that the other bands are far away from the Fermi energy and that the interband interactions are sufficiently weak, the three-band Hubbard model can be "projected" to an effective one-band Hubbard model [61]:

$$H = -t_{ij} \sum_{\langle i,j\rangle\sigma} c^\dagger_{i,\sigma} c_{j,\sigma} + U_{\text{eff}} \sum_i n_{i,\uparrow} n_{i,\downarrow} - \mu \sum_i n_i. \tag{1.10}$$

The hopping term (t_{ij}) is typically limited to the nearest-neighbor hopping. The value of U_{eff}, instead of originating from onsite Coulomb repulsion, is given by charge-transfer gap between the copper $3d$ orbital and the oxygen $2p$ orbital ($\varepsilon_d - \varepsilon_p$). The parameter μ denotes the chemical potential.

At small doping levels ($\langle n_i\rangle \sim 1$), four occupation scenarios are possible for each site: (1) no electron occupation, (2) occupied by a spin-up electron, (3) occupied by a spin-down electron, and (4) occupied by two electrons. Because of the large onsite Coulomb repulsion U ($U \gg t$), Anderson assumed that the double occupation is extremely unlikely and introduced the full Gutzwiller projector P [103]

$$P = \prod_i (1 - n_{i,\uparrow} n_{i,\downarrow}), \tag{1.11}$$

where $n_{i,\uparrow}$ and $n_{i,\downarrow}$ are the occupation numbers of spin-up and spin-down electron on the ith site, respectively.

Projecting out the double occupation with the full Gutzwiller projector P, the one-band Hubbard model can be rewritten into the t-J model [61, 104]

$$H_{t-J} = P[-t_{ij}\sum_{\langle i,j\rangle\sigma} c^{\dagger}_{i,\sigma}c_{j,\sigma} + J\sum_{\langle i,j\rangle}(S_i \cdot S_j - \frac{1}{4}n_i n_j)]P, \tag{1.12}$$

where $J = 4t^2_{ij}/U_{\text{eff}}$. The $c^{\dagger}_{i,\sigma}$ and $c_{i,\sigma}$ are true quasiparticle excitations of the system in the unprojected Hilbert space, while $Pc^{\dagger}_{i,\sigma}$ and $c_{i,\sigma}P$ are physical electrons of the system and excitations in the projected space [104]. For the cuprates, experiments revealed that the spins on the copper sites align antiferromagnetically, implying that $J > 0$ [42].

In the limit that $U_{\text{eff}} \to 0$ (weak coupling), the real-space operators $c_{i,\sigma}$ and $c^{\dagger}_{i,\sigma}$ can be Fourier transformed back to the momentum space operators $c_{k,\sigma}$ and $c^{\dagger}_{k,\sigma}$. The Hamiltonian then becomes

$$H = \sum_{k,\sigma} \varepsilon_k c^{\dagger}_{k,\sigma}c_{k,\sigma}, \tag{1.13}$$

where $\varepsilon_k = -2t(\cos k_x + \cos k_y) - \mu$ for a two-dimensional system. Note that Eq. 1.13 only considers nearest-neighbor hopping.

The Hubbard model at intermediate coupling, $U \sim t$, and away from half-filling $\langle n_i\rangle \neq 1$ is much less well understood, and this is exactly the regime where superconductivity emerges in the cuprate materials. Although solutions in the two limits (strong and weak coupling) are well established, how a system evolves from one limit (i.e., strong coupling, undoped parent compound) to the another (i.e., weak coupling, over-doped regime) is still elusive. The accuracy of describing the cuprate materials with the effective one-band Hubbard model is also questionable. A set of well-established parameters for the electron-doped cuprate materials is $t_{ij} \sim 0.4$ eV, $U_{\text{eff}} \sim 2$ eV, and $1 \leq \langle n_i\rangle \leq 1.2$ [42].

1.3 Scope and outline of this Thesis

This Thesis aims to investigate the magnetic and electronic properties of the electron-doped cuprates and is comprised of experiments, data analysis, and simulations.

In Chapter 2, the various experimental techniques used in this work are discussed. Single crystals of NCCO were grown using traveling-solvent floating-zone (TSFZ) technique. Chemical substitution took place during the growth process and oxygen manipulation was performed as a post-growth annealing process. Samples were characterized by Laue X-ray diffraction, SQUID magnetometery, resistivity measurements, electron microscopy and chemical analysis. Chapter 2 furthermore discusses the instrumentation and theoretical background for the neutron scattering, muon spin rotation/relaxation, and charge-transport measurements. The experiments were performed at national laboratories in the united States and Canada.

Chapters 3 presents neutron scattering, μSR, and SQUID magnetization measurements of the Néel temperature, staggered magnetization, instantaneous spin-spin correlation length, magnetic and superconducting volume fractions, muon relaxation rates, and spin fluctuation timescales of NCCO. Simulations of the instantaneous spin-spin correlation length are compared to the experimental results. A multi-dimensional phase diagram of NCCO as a function of temperature, Ce concentration x, and oxygen content/disorder, in which clear relationships are observed between antiferromagnetic and superconducting phases, is constructed. The underlying Fermi surface topology is shown to be directly connected to normal-state magnetic and electronic properties.

Further study in Chapter 4 reveals a surprising relationship between the existence of a two-band Fermi surface and the emergence of bulk superconductivity. New and prior magnetoresistivity data provide crucial links between the normal and superconducting states of the electron-doped cuprates, and between the electron- and hole-doped parts of the phase diagram. The characteristics of the normal-state (magnetoresistivity, quantum oscillations, and Hall coefficient) and those of the superconducting state (superfluid density and upper critical field) consistently indicate two-band (electron and hole) features and clearly pointed to hole-related superconductivity in the nominally electron-doped materials. Building on the well-known Uemura scaling for the hole-doped curpates, we show the existence of universal scaling between the superconducting transition temperature and the hole superfluid density for both electron- and hole-doped cuprates.

In Chapter 5, the normal-state charge-transport properties (resistivity, Hall coefficient, and cotangent of the Hall angle) parallel and perpendicular to the copper-oxygen

plane are studied. The transport scattering rate is found to exhibit a quadratic temperature (Fermi-liquid) dependence in the Néel state of the electron-doped cuprates, and is nearly independent of doping, compound and carrier type (electrons versus holes). Universal scaling between the coefficients that describes the ubiquitous logarithmic low-temperature resistivity upturn is obtained for various electron- and hole-doped cuprates, which points to a single origin of this upturn regardless of nominal dopant type.

Chapter 2

Experimental methods

This Chapter describes the experimental methods that were used throughout this Thesis work. The laboratory work at the University of Minnesota involved crystals growth, characterization, and transport measurements. Key experiments were performed at various national and international laboratories: neutron scattering, μSR, and charge-transport measurements in high magnetic fields.

2.1 Crystal growth

The discoveries of new materials and the exploration of their properties have been crucial for human scientific and technological development. For example, historic periods such as the Stone Age, Bronze Age, Iron Age, Atomic Age and Information Age are named after materials or new technologies driven by the study of materials. Needless to say, a significant portion of contemporary scientific efforts, including in physics, chemistry, biology and engineering, has focused on the discovery of novel materials and on understanding/improving their fascinating properties.

Materials synthesis, to a certain extend, can be regarded as the re-arrangement of atoms and the transformation of phases. Some important concepts and methods relevant to the traveling-solvent floating-zone (TSFZ) single-crystals growth are listed below. For more detailed discussions of materials synthesis, the reader is encouraged to consult with references such as [105, 106].

Crystallization and nucleation: Crystallization is a process by which solid crystals form from other phases, typically a liquid/melt phase. The first step of crystallization is nucleation, in which a small number of atoms assemble and thereby initialize growth sites for further organization of atoms. In the TSFZ method, crystallization is achieved from either small powder-form crystal seeds or a bulk single-crystal seed.

Supersaturation: Supersaturation refers the state of a solution that contains more dissolved material than what could be dissolved under normal circumstances. Carbonated water is an example of supersaturation. Crystal synthesis, to a certain extent, is the action to reduce solubility and drive crystallization. Supersaturation thus is essential for all solution crystallization processes. In the TSFZ method, the molten zone above the seed crystal is supersaturated with target materials (in this Thesis work, the target material is NCCO, and the solvent is CuO).

Surface energy: Surface energy quantifies the degree of interaction force a material surface applies to other materials. The crystal morphology and growth speed at different crystal faces are determined by surface energy. Different crystal shapes (e.g., cylindrical for NCCO when grown by the TSFZ method) are controlled by surface energy.

Diffusion: Diffusion describes the net movement of particles as a result of the kinetic energy of random motion. Material deposition, which is crucial to crystallization, is strongly affected by diffusion processes. Crystals are difficult to form in the absence of a concentration gradient in the surrounding environment.

Adsorption: Adsorption is defined as the adhesion of atoms or other building blocks from a gas, liquid or melt phase to a crystal surface. Details of adsorption control every aspect of crystallization. Hydrophobic or hydrophilic cell surfaces in biochemistry are analogs of material-phobic and material-philic adsorption layers for single crystals.

Congruent and incongruent melting: (In)congruent melting occurs for a compound when the composition of the melt liquid is (not) the same as the composition of the solid. Crystals of incongruent melting materials can not be synthesized upon cooling a melt liquid with the same chemical composition as the solid material. Instead, the composition of melt liquid will change during the growth process. This is the reason why the chemical composition of the solvent for NCCO, an incongruently melting material, differs from that of the crystal.

Materials are typically synthesized either in the form of bulk crystals or thin-film

crystals. Bulk single crystals are usually synthesized using a liquid-solid process, such as melt growth (e.g., the Bridgman, Kyropoulos, and Czochralski methods), flux growth (e.g., self-flux encapsulation and the TSFZ method), solution and hydrothermal growth. Thin-film materials can be obtained by cleaving bulk materials in clever ways (e.g., the exfoliation "scotch tape" method to obtain graphene, or the knife-cleaving method for cuprates), or by sophisticated methods such as sputtering, chemical vapor deposition (CVD) and molecular beam epitaxy (MBE). Other methods include utilizing a focused ion beam (FIB) or optical/electron beam lithography to reduce dimensionality (e.g., recent work on topological materials [107]) or atomic manipulation to assemble layers from single atoms (e.g., early scanning tunneling microscopy (STM) work or more recent work on assembled materials [108]).

2.1.1 Temperature-composition diagram for NCCO

NCCO was firstly reported in 1989 as an electron-doped cuprate superconductor [110] and the growth procedure has been refined since then. The fact that NCCO melts incongruently only at very high temperature ($T \approx 1315$°C) renders the growth of sizable high-quality crystals difficult. The pseudo-binary temperature-composition diagram for NCCO [109] is shown in Fig. 2.1. This diagram is constructed for an oxygen atmosphere of 1 atm, and the diagram will differ if pressure or a different gas atmosphere is applied. In order to improve the crystal quality, our growth procedure uses a mixture of Ar/O_2 atmosphere at 4 atm, and the resultant melt temperature of NCCO is tens of degrees higher.

In order to obtain single crystals from polycrystalline materials, NCCO have to be heated above 1315°C to form a solid-liquid mixture. However, direct cooling of the flux that has the same chemical composition as the target crystal would result in the decomposition of the material into $Nd_{2-x}Ce_xO_{3+\delta}$ and CuO. Because NCCO is an incongruently melting material, the flux used should contain a much higher ratio of CuO than the target crystal. This excludes the possibility of simple self-flux synthesis. In order to resolve this issue, extra CuO material was added to the flux. During the growth, the flux composition obeys the temperature-chemical relation indicated by a liquidus-line (highlighted in blue in Fig. 2.1), which requires a CuO composition between 80% and 90% and a temperature between 1150°C and 1315°C.

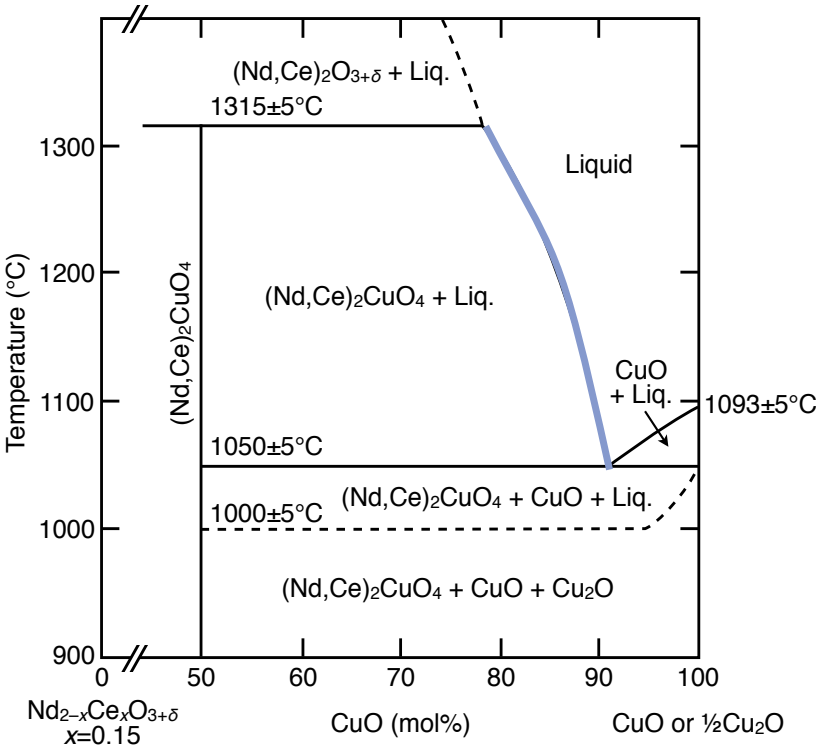

Figure 2.1: Temperature-composition phase diagram for the $Nd_{1.85}Ce_{0.15}O_{3+\delta}$-CuO ($Cu_2O$) mixed system. NCCO with $x = 0.15$, the target material, is shown as a vertical line at 50% CuO composition. Because of its incongruently melting nature, NCCO can not be synthesized by simply cooling down a mixed melt with 50% CuO composition. Instead, NCCO crystallizes at a liquidus-line (highlighted by blue) from a Cu-rich (80% - 90% CuO) melt. Figure adapted and modified from that in [109].

The decomposition temperature of NCCO in air as a function of Ce concentration is shown in Fig. 2.2. NCCO crystals with a high Ce concentration have a tendency to form in regions with higher temperature. In the case of the TSFZ growth, temperature gradients exist both horizontally (along radial direction of the solvent) and vertically (along the co-axis of polycrystalline rod and synthesized single-crystal rod). Thus chemical inhomogeneity is expected, and indeed observed, as a function of the radius of the synthesized crystals.

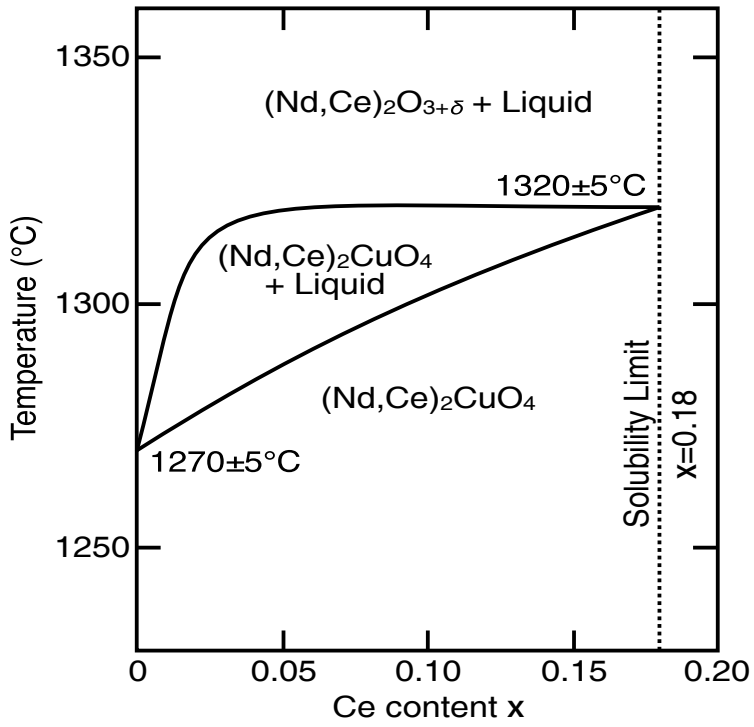

Figure 2.2: Decomposition diagram of NCCO as a function of Ce concentration x in air. This digram depends on the atmosphere (oxygen partial pressure). Figure adapted from [109].

2.1.2 Traveling-solvent floating-zone technique

The origin of the traveling-solvent floating-zone (TSFZ, or image furnace) technique can be traced back to the manufacture of silicon in the 1950s at Bell Laboratories and Siemens (see [105, 106] and reference therein). Optical heating with elliptical mirrors was later developed to enable high-temperature synthesis. This is why the TSFZ technique is also called image furnace technique. More recent TSFZ setups use halogen lamps as a light source. Halogen lamps contain halogen gas and a tungsten filament, producing a halogen cycle that redeposits evaporated tungsten back onto the filament to increase the life-time of the filament and achieve higher temperatures.

The heating system of our TSFZ furnaces includes four ellipsoidal mirrors and four halogen lamps (typically 300 W for NCCO), as shown in Fig. 2.3 and Fig. 2.4. A

Figure 2.3: Picture of three TSFZ furnaces in the Physics and Nanotechnology building at the University of Minnesota (Crystal Systems Corp., models: FZ-T-4000-H-II-P-S, FZ-T-4000-H-III-P-S, and FZ-T-10000-HVP-II-S).

thick-wall (thickness depends on applied pressure, about 5 mm for 4 atm) quartz tube is installed to protect the growth and maintain high pressure. Light emitted from halogen lamps is focused onto the center of the system, with a vertical extent of about 3 mm. The temperature at the molten zone is controlled by the power supplied to the halogen lamps. The molten zone is suspended between a polycrystalline rod and a growing crystal. The polycrystalline rod (connected to the upper shaft) and the growing crystal (connected to the lower shaft) counter-rotate, such that a resonance condition is avoided and convection flow in the molten zone is best adjusted. The halogen lamp stage (mirror stage) moves upward slowly (in the case of NCCO, usually 0.5 mm/h) to support continuous crystallization. The polycrystalline rod is pulled upward at a slower rate (upper shaft pulling rate) that depends on the diameters of the polycrystalline rod and of the target crystal. The upper shaft pulling rate can be calculated based on mass conservation.

A schematic illustration of a typical crystal growth is shown in Fig. 2.5. When the growth is not properly seeded, multiple grains form initially. Because growth speed

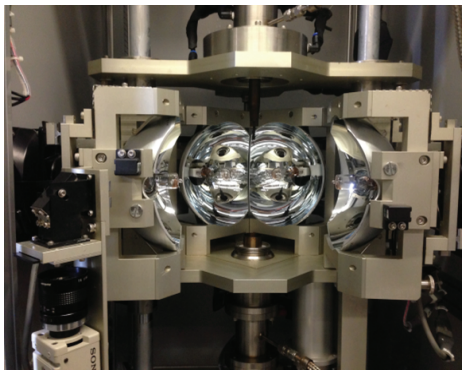

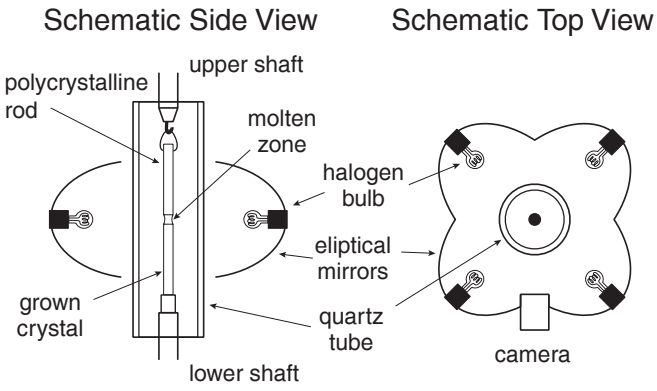

Figure 2.4: Picture (side view) and schematic illustrations of the TSFZ furnace's heating system (mirror stage). Illustration adapted from [111].

varies with grain orientation (the growth speed is fastest in the CuO-plane for NCCO), a single grain will eventually dominate and visible facets will appear.

2.1.3 Synthesis procedure

The NCCO synthesis procedure using the TSFZ technique includes the preparation of a polycrystalline NCCO rod, the preparation of a flux, and the single-crystal growth.

The preparation of the polycrystalline rod includes making a powder mixture and a rod, and sintering at high temperature. Chemical powders of Nd_2O_3 (99.99%, pale blue), CeO_2 (99.99%, pale yellow), and CuO (99.995%, black/dark gray) were dehydrated for

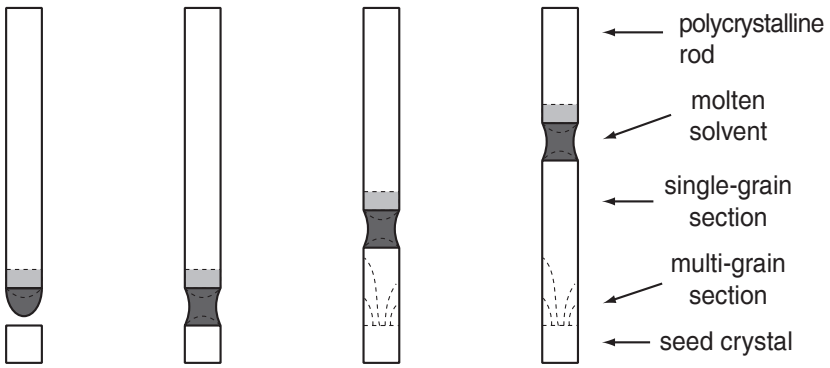

Figure 2.5: Illustration of TSFZ crystal growth stages, adapted and modified from [111].

a sufficient amount of time prior to mixture to ensure accurate chemical composition. The powders were typically left in a furnace for one night for dehydration. The powder was weighted using an analytic balance in stoichiometric amounts, and ground using a mortar and pestle. Ethanol was added to the combined mixture in order to increase homogeneity of the powder and to reduce particle size. Ethanol was used at least for the first round of the mixing process. After having been ground for about 1 hour and sufficiently dried, blue-gray powder was collected into a high-alumina crucible and heated to 900°C for 12 hours. Three subsequent rounds of grinding (approximately 40 minutes each) and baking (at 920°C, 950°C, 980°C for 12 hours, respectively) were performed to obtain single-phase, polycrystalline, black NCCO powder. The chemical reaction can be expressed as

$$(1 - \tfrac{x}{2}) \cdot \mathrm{Nd_2O_3} + x \cdot \mathrm{CeO_2} + \mathrm{CuO} \longrightarrow \mathrm{Nd_{2-x}Ce_xCuO_4} + \tfrac{x}{4} \cdot \mathrm{O_2} \uparrow \qquad (2.1)$$

Once the single-phase NCCO powder was prepared, the next step was to produce a uniform polycrystalline rod of about 15 cm in length. Surgical latex tubes with proper diameter (about 7 mm) and elasticity were used to form NCCO powder into a cylindrical shape. The surgical latex tube was tied at one end and attached to a glass funnel mounted to a stand at another end, as shown in Fig. 2.6. It was found to be crucial to clean both sides of the surgical latex tubes and glass funnel with ethanol. A small amount of NCCO powder was periodically added to the glass funnel and compressed

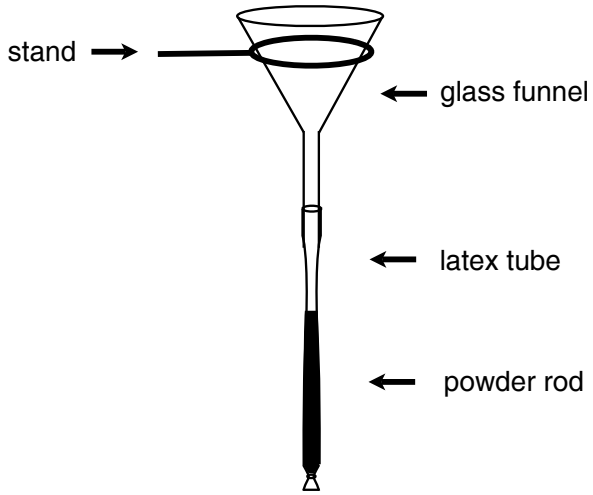

Figure 2.6: Illustration of the powder packing setup, adapted and modified from [40].

with a metal stick. Halves of brass or stainless steel tubes were used to ensure a uniform shape of the powder rod with the chosen diameters. Due to the elasticity of the latex tubes, the diameter of the powder rods can be larger than 7 mm. A larger diameter usually ensures a denser rod because of the surface tension of latex tubes. The powder rods had to be packed tight enough such that no change in shape was observed after a gentle/moderate finger press.

A piece of powder filter (cotton ball) was inserted at the open end of the surgical latex tube (top side of packed NCCO powder), and the surgical latex tube was removed from the glass funnel before it was attached to the nozzle of a vacuum pump. Air in the tube was continuously pumped out for about 30 minutes. The exact duration depended on the diameter of the rod. Next, the open end of the surgical latex tube was twisted and tied so that no air could leak into the tube. The packed powder rod became solid and rigid. The latex tube was then attached to a supporting frame and placed into a hydraulic press with a water-filled chamber (Fig. 2.7), and pressed at 70 MPa. Note that this process requires a high vacuum state inside the latex tube, as otherwise gas bubbles would burst and rupture the latex tubes. The diameter of the packed powder rod was visibly smaller and the rod was much more fragile. The latex tube was then carefully cut away.

Figure 2.7: Hydraulic press with a water-filled chamber.

After removing the latex tube, the powder rod was placed into a zirconia ceramic tube and heated to 980°C for 12 hours to harden the rod. Once hardened, the rod was solid enough to allow hand-drilling of a hole into one of its end. A high-temperature-resistant Ni-Cr wire was then fed through the hole, and the rod was hung vertically over the open mouth of a high-alumina crucible. This was necessary to avoid reaction between the powder rod and crucible during the sintering process. The powder rod-crucible setup was then heated to 1225°C for 12 hours, with temperature ramping rate no faster than 300°C per hour. After having been sintered, the rod became much denser (more than 95% of the ideal crystalline density of about 7.3 g/cm^3) and light reflection could be observed from tiny polycrystals on the surface. The high density of the polycrystalline rod was crucial in enabling successful growths. A photograph of a prepared polycrystalline rod is shown in Fig. 2.8.

CuO flux pellets with masses of about 175 mg, 200 mg, 225 mg, and 250 mg were

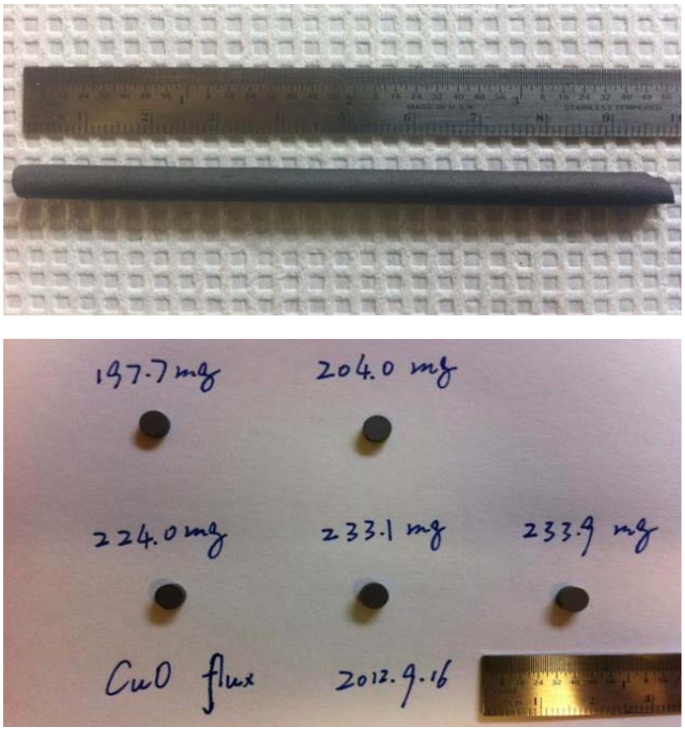

Figure 2.8: Picture of a sintered polycrystalline NCCO rod (about 7 mm in diameter and 10 cm in length) and of CuO flux pellets (about 5 mm in diameter).

produced following similar procedures. CuO powders were ground and compressed with no more than 10 MPa pressure, using a pellet die with a 5 mm bore, before being heated to 980°C for 12 hours. It was found that a small amount of NCCO powder could be added to achieve the ideal chemical composition (80-90% CuO), although this was not required due to the fact that NCCO dissolves into flux during growth.

The polycrystalline rod was mounted up-side down to the lower shaft of a TSFZ furnace, and a CuO flux pellet was placed on top of the polycrystalline rod. The combined system was heated to above the melt temperature of the flux pellet in an oxygen atmosphere to dissolve and attach CuO flux to the polycrystalline rod (oxygen is used in order to suppress gas bubbling during the subsequent growth stage). A seed crystal was cut from a previously grown single crystal. It was found that the seed crystal could be cut from a crystal with multiple grains, and that a short polycrystalline rod

could also serve as a seed.

The next step was to re-mount the polycrystalline rod (with flux attached) to the upper shaft. A shallow groove along the circumference of the polycrystalline rod was carved to allow wrapping with Ni-Cr wire. The position of the polycrystalline rod was adjusted by shaping the Ni-Cr wire loop and a small palladium hook that attached to the upper shaft. The polycrystalline rod and seed crystal were aligned vertically to allow coaxial rotation. Perfect alignment is crucial for the synthesis.

A quartz tube was then put into place, and an Ar/O_2 gas mixture was flowed through the quartz tube, at a pressure of about 4 atm. The ratio of Ar and O_2 gases was optimized. It was found that a 1 to 3 flow rate (50 cc/m of Ar and 150 cc/m of O_2) is most ideal for the crystal growth of NCCO [112]. In certain cases, the elevated pressure could not be achieved at room temperature, and the sealed quartz tube was slightly heated to ensure a tight seal.

The end of the polycrystalline rod (with flux attached) was lowered to the center focal point of the halogen lamps to re-melt the flux while the polycrystalline rod was rotating. The melt temperature of the flux with dissolved NCCO is higher than that of the pure CuO, and corresponds to around 50% of the maximum power level for halogen lamps. The power level increases with the age of the halogen lamps. The flux was left molten for approximately 30 minutes to allow a better mixture before it was attached to the preheated seed crystal. Once carefully attached, the counter-rotating polycrystal-flux-seed system was further heated for about one hour before growth was started by initializing an upward movement of the mirror stage.

For a typical growth, the operating power level was between 50% to 60% of the maximum power level for the 300 W halogen lamps. The mirror stage moving rate was at 0.5 mm/h and the upper shaft moving rate was between 0.2 to 0.3 mm/h. The lower shaft's rotation speed was between 21 rpm to 25 rpm, and that for upper shaft between 17 rpm to 23 rpm.

The success of a crystal growth strongly relies on the stability of the molten zone, which depends on the stability of the power, the translations/rotations of the shafts, the gas flow/pressure, and the uniformity of density and shape of the polycrystalline rod. A picture of a crystal being grown in a TSFZ furnace is shown in Fig. 2.9, and a picture of a grown NCCO crystal is shown in Fig. 2.10. During the growth, the following

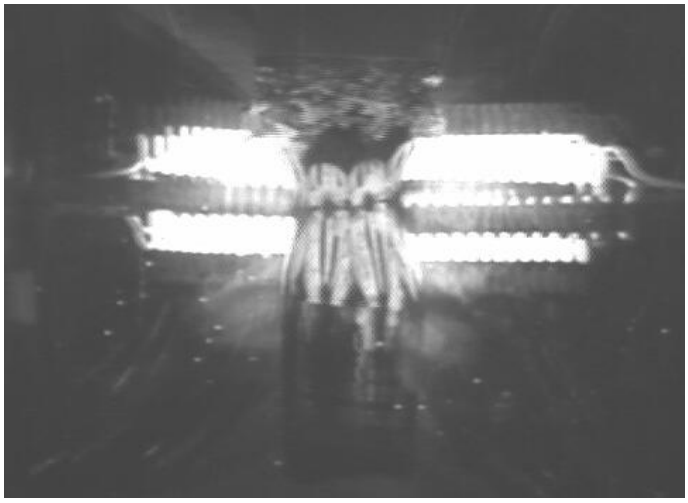

Figure 2.9: Picture of a crystal being grown in a TSFZ furnace. Above the hourglass-shaped molten zone is the polycrystalline feed rod, and below the molten zone is the grown crystal. Reflections of the halogen lamps' filaments are visible behind the molten zone.

situations may arise, which can cause a deviation from the typical hourglass shape of the molten zone and require an adjustment of the growth parameters. A detailed discussion of these situations with illustrations can be found in [106].

"Knocking" between the polycrystalline rod and the grown crystal. This situation arises when the temperature of the molten zone is too low and the growth of the crystal is too fast. The polycrystalline rod and the grown crystal physically touch, "knocking" against each other. The mechanical instability of the crystallization front decreases the quality of the grown crystal and may even lead to a sudden detachment of the flux. In order to resolve this situation, an emergency step is to raise the position of the upper shaft. However, only an increase in temperature can solve the problem in the long term.

Inverse trapezoidal shape of the molten zone. This situation signifies too fast a feeding of the polycrystalline rod while the temperature of the molten zone is not high enough. Although this usually does not result in a sudden detachment of the flux, because the large amount of dissolved material will be eventually deposited onto

Figure 2.10: Picture of a NCCO crystal. The crystal is roughly 12 cm in length and 6 mm in diameter. Most of this crystal is a single grain.

the grown crystal and increases its diameter, it should be avoided so that a crystal of uniform shape and composition is obtained. A faster upper shaft pulling rate can solve the problem.

Big-bottom and thin-neck hourglass molten zone. This shape indicates that the flux is overheated and the feed from the polycrystalline rod is too low. This is a dangerous situation, as the bottom part of molten zone may be suddenly detached from the top at the neck position, once surface tension no longer overcomes the gravitational force. A lower upper shaft pulling rate and a high temperature of the molten zone should resolve the issue.

Termination of the growth involves a long procedure to decrease the temperature of the molten zone. In order to avoid thermal shock to the crystal, the power level of halogen lamps was slowly decreased over the course of several hours (usually less than 2 % per hour) and the polycrystalline rod was slowly pulled away from the grown crystal (the pulling rate is calculated such that no material enters the molten zone when the melt temperature of NCCO is reached). The whole system is left in 4 atm Ar/O_2 atmosphere before the furnace was cooled down.

2.1.4 Oxygen reduction process

The oxygen reduction process after the growth of a crystal has been intensively studied. Without this process, the electron-doped cuprate materials remain non-superconductive even with a change in Ce concentration [42, 110]. After the oxygen reduction process,

antiferromagnetism is weakened and superconductivity emerges at low temperatures for a range of Ce concentrations [113]. The Néel temperature is lowered and the instantaneous spin-spin correlation is shortened. At the same time, the resistivity upturn at low temperature is suppressed, but the temperature dependence of the resistivity at high temperature does not change significantly. The exact effects of the oxygen reduction step in modifying the structure and disorder levels have been heavily debated.

The oxygen reduction process can not be studied via chemical analyses such as inductively coupled plasma (ICP) measurements and energy dispersive X-ray spectroscopy (EDS), as these methods are insensitive to oxygen and have poor spatial resolution. Thermogravimetric analysis only gives information about the overall mass loss. Experimental probes to extract detailed local structure information, such as X-ray and neutron diffraction, are better suited for the task.

NCCO contains three different regular oxygen sites (Fig. 1.1): (1) O(1) oxygen site in the copper-oxygen plane; (2) O(2) oxygen site in the charge reservoir layer; (3) O(3) oxygen site directly above or below the copper atoms that is nominally vacant in the ideal T′ structure. Oxygen atoms can also exist at interstitial positions. Because the oxygen ions are negatively charged (typically O^{2-}), oxygen removal adds electrons to the CuO_2 planes.Recent nuclear quadrapole resonance (NQR) work [43] suggests that the valence of oxygen ions at the O(1) site is less than 2. The effect of increasing the overall electron density and modifying the chemical potential by removing oxygen atoms was observed in [114, 115]: for samples that went through the standard reduction process, the Néel temperature was found to correspond to that of the as-grown samples if an effective shift of the Ce concentration is introduced ($x_{\text{eff}} = x + 0.03$).

Neutron diffraction measurements on as-grown crystals of NCCO revealed that, although the apical O(3) site is nominally unoccupied in the ideal T′ structure, a few percent of oxygen atoms actually exist at this site [116, 117].

The amount of oxygen atoms at the apical O(3) site decreases as a result of the oxygen reduction process, whereas no observable change has been convincingly established regarding the oxygen atoms at the O(1) and O(2) sites [116, 118]. Naively, removal of excess oxygen from O(3) sites restores the ideal T′ structure and eliminates local disorder that potentially disrupts superconductivity and localizes electrons in the copper-oxygen plane (Fig. 2.11). Removal of oxygen from the O(3) site was therefore proposed to be

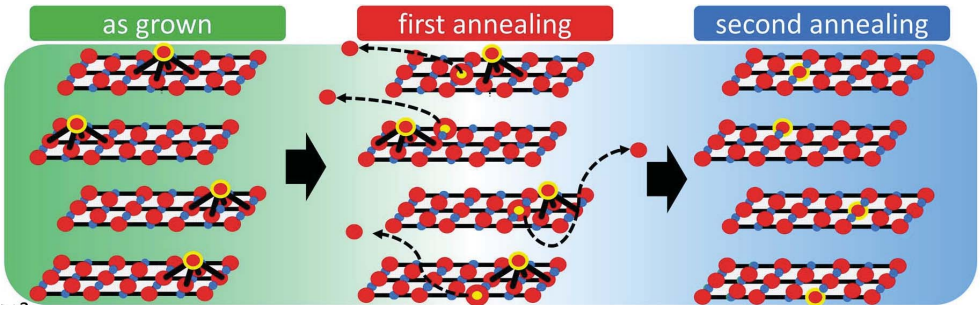

Figure 2.11: Proposed refined two-step reduction protocol. For as-grown materials, a small percentage of O(3) apical oxygen sites is randomly occupied. The rather severe standard reduction protocol may only remove a portion of the unwanted O(3) oxygens and might, in addition, introduce planar O(1) vacancies. A proposed refined two-step reduction process removes oxygens from the O(3) apical site and heals possible planar O(1) deficiency. Figure adapted from [119].

necessary in order to induce superconductivity [42]. This proposal was supported by the fact that the *c*-axis lattice constant is shortened after the reduction process [42].

Neutron scattering, X-ray scattering, and transmission electron microscopy (TEM) studies showed that the reduction process causes the decomposition of a small fraction (1 - 2 % under standard reduction conditions) of the material into the rare-earth oxide $(RE,Ce)_2O_3$ [114, 120], where RE represents the rare earth elements. A TEM image of NCCO after standard oxygen reduction is shown in Fig. 2.12. The $(RE,Ce)_2O_3$ sheet appears parallel to the crystalline *ab*-plane with a typical thickness of less than 10 nm. Because of a somewhat serendipitous lattice match between the lattice constant of $(RE,Ce)_2O_3$ (≈ 11.08 Å) and the diagonal of the CuO_2 layer of NCCO ($2\sqrt{2}a \approx 11.14$ Å), $(RE,Ce)_2O_3$ forms epitaxially. This lattice match results in additional discrete Bragg peaks instead of a powder-sample like scattering ring [44, 114, 121].

Because the $(RE,Ce)_2O_3$ secondary phase contains no copper, it was argued that the copper atoms must migrate to the copper-oxygen planes of the majority NCCO phase. The copper migration may thus heal any presumed pre-existing copper vacancies in the as-grown material (Fig. 2.13). Neutron powder diffraction measurements on $Pr_{1-x}LaCe_xCuO_{4\pm\delta}$ are consistent with the disappearance of about 2% percent copper deficiency after standard reduction [120]. With the decrease of the disorder due to

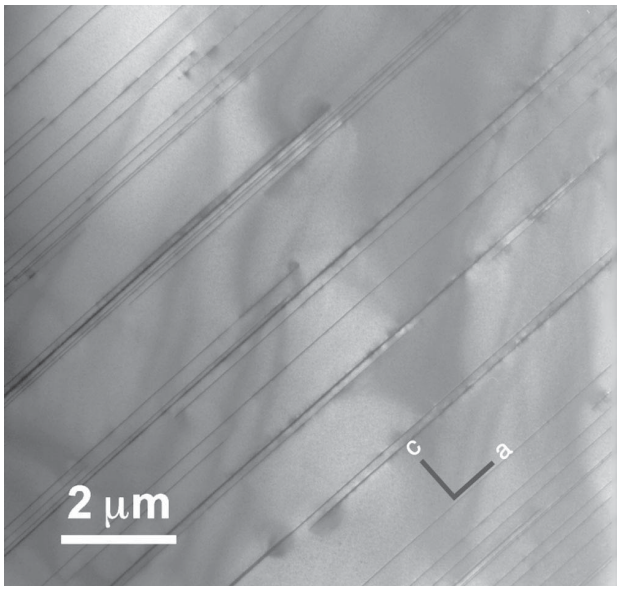

Figure 2.12: TEM image of reduced NCCO. The black thin lines perpendicular to the crystalline c-axis are the $(RE,Ce)_2O_3$ secondary phase. Figure adapted from [114].

healed copper vacancies and the lowered apical oxygen occupation, electrons may be able to form a superconducting coherent state in the copper-oxygen planes.

A third proposal regrading the structural modification due to the oxygen reduction process is related to the first two. Neutron powder diffraction work indicates that the copper-oxygen layer, instead of being a flat plane, may be actually locally distorted and buckled [122]. Distortion and buckling of the copper-oxygen plane can change local potential the orbital hybridization (e.g., induce orbital hybridization in the out-of-plane direction) and thus the electronic properties of the material. Both the removal of apical oxygen and the filling of copper vacancies would affect local distortion, and the emergence of superconductivity may be related to these local structural changes.

Laboratory procedure

The phase stability diagram for NCCO with $x = 0.15$ as a function of oxygen partial pressure and temperature is plotted in Fig. 2.14. Ideally, the oxygen reduction

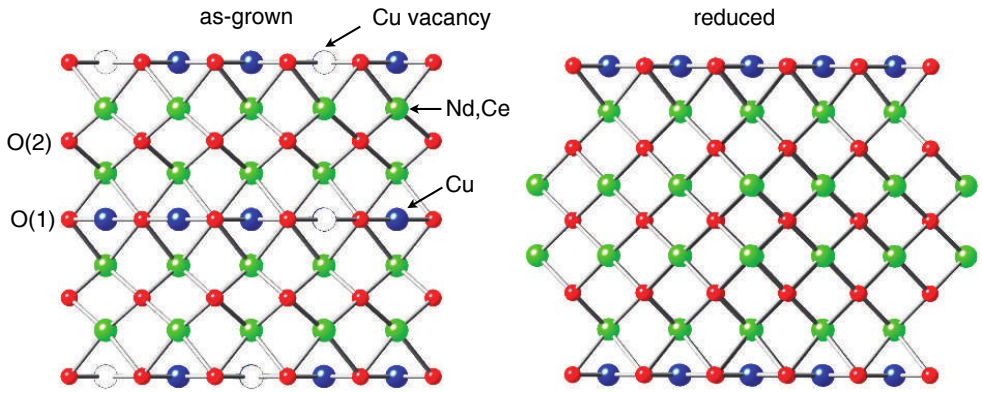

Figure 2.13: Proposed "healing" of copper vacancies during the standard reduction process. Figure reproduced from [120].

condition should lie in the region below the decomposition line in order to avoid the appearance of the secondary phase. However, in the process of optimizing the reduction condition, a two-step temperature protocol was found to be much more efficient [123]. This is the standard reduction protocol used in this Thesis work. Note that this standard reduction protocol differs from the proposed refined two-step protocol described in [119] and Fig. 2.11.

The first step of the standard protocol is to keep the sample for 10 hours at 970° C with an oxygen partial pressure of 10^{-6} atm. Since the furnace temperature read-out may differ from the temperature at the sample position, the furnace temperature needs to be calibrated such that the sample temperature was indeed 970° C. A near vacuum atmosphere created via continuous gas pumping does not allow reliable control of the oxygen partial pressure. Instead, laboratory-grade Ar flow is used. The laboratory-grade Ar gas contains oxygen at roughly 1 ppm which equals to oxygen partial pressure at 10^{-6} atm. The typical Ar flow rate is 100-200 mL/min. Note that the reduction condition of 970° C and oxygen partial pressure at 10^{-6} atm is above the decomposition line in Fig. 2.14. The samples can not stay at in this environment for a long time without complete decomposition.

The second step is to anneal samples for 20 hours at 500° C with an oxygen partial pressure of 1 atm. This step sharpens the superconducting transition and further

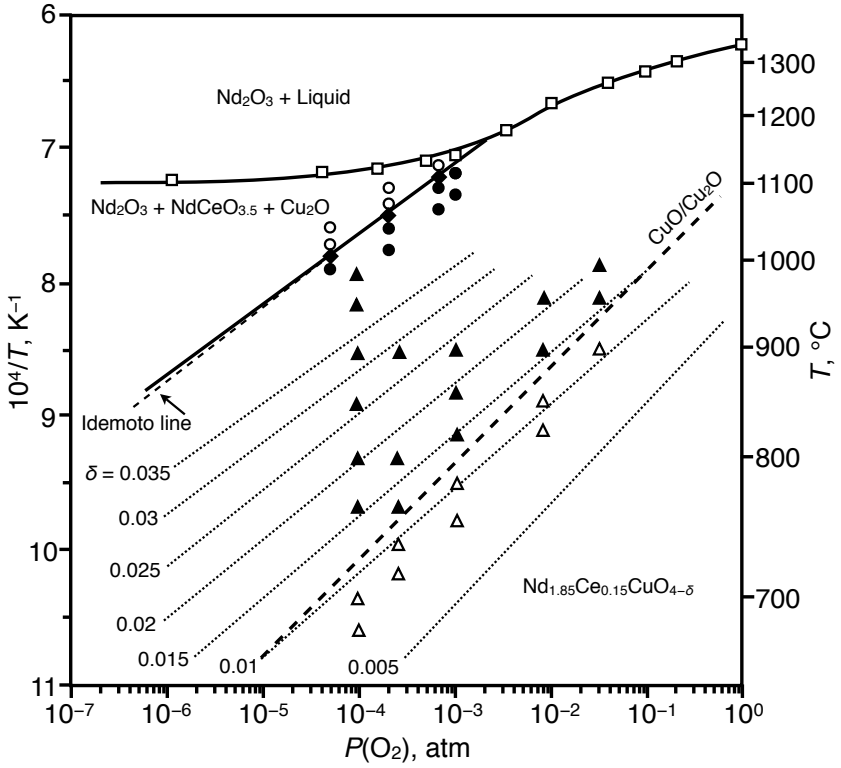

Figure 2.14: Phase stability diagram for NCCO ($x = 0.15$). The diagonal solid curve indicates where NCCO decomposes. (Non)superconductivitive samples are indicated as (open) solid triangles. Figure adapted from [124].

increases the transition temperature by 1-2 K. The second step is believed to release stress induced by the harsh first step and potentially removes part of disorder in the material [44, 123]. Although the phase stability diagram should in principal depend on the Ce concentration, in this Thesis work the same temperature profile was used for the reduction of NCCO samples. The amount of oxygen removed using the same procedure may differ somewhat for samples with different Ce concentration.

2.2 Sample characterization

2.2.1 Laue diffraction

In 1912, Max von Laue was the first to apply a specific type of X-ray diffraction method to study crystal structures [125]. This method, which was subsequently named after Laue, utilizes a white-beam X-ray source (incident X-ray photons with a wide distributions of wave lengths) to study diffraction patterns and elucidate crystal symmetries. The principle of X-ray Laue diffraction is the Bragg scattering condition (which is also used for selecting the energy of neutron beams, as described later in this Chapter),

$$n\lambda = 2d\sin\theta, \tag{2.2}$$

where n is an integer, λ is the wave length of the incident X-ray beam, d is the distance between lattice layers in the material, and θ is the scattering angle. The lattice layers can be characterized using the Miller indices (h, k, l). In order to simultaneously satisfy the Bragg scattering conditions for layers with different Miller indices, a white beam is required.

In this Thesis work, X-ray Laue diffraction was used to determine and characterize the sample quality, namely to determine if a sample is a single crystal, and to orient the sample by comparing the diffraction pattern of the sample to that of a standard single crystal. Although X-ray Laue diffraction is not the only method to achieve this goal (other methods include, e.g., neutron diffraction), in-house Laue diffraction is most convenient and thus routinely performed.

For bulk-crystalline NCCO, the back-reflection method was used, because the X-ray penetration depth is much shorter than the crystal dimensions. The X-ray beam is back-scattered from the sample and then collected by an area detector. To adjust the sample position, two rotators (on a goniometer) and two translational stages (both perpendicular to the incident X-ray beam) were used. For single-crystal NCCO, the Laue diffraction pattern is highly symmetric when the incident beam is parallel to the crystalline c-axis (perpendicular to the CuO_2 plane). Because the c-axis is perpendicular to the fastest growth direction of the material, it is easy to identify prior to the diffraction measurement.

A typical Laue X-ray diffraction pattern for a NCCO single crystal with incident

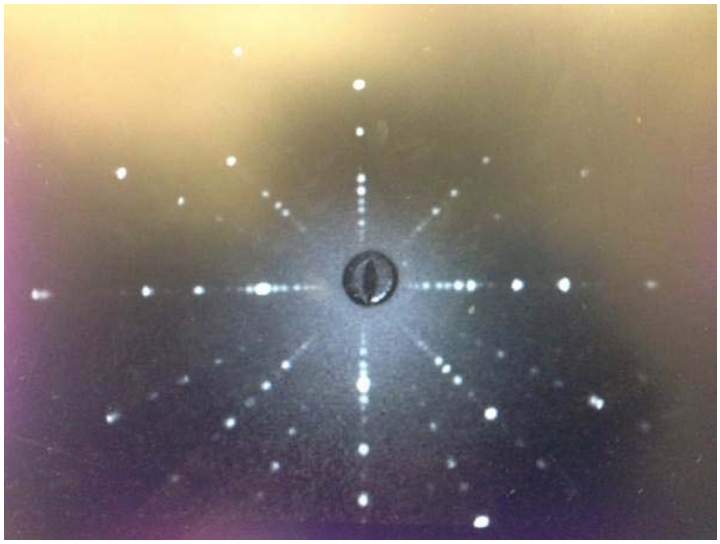

Figure 2.15: Laue X-ray diffraction pattern for a NCCO single crystal with incident X-rays parallel to the crystalline c-axis. The horizontal and vertical patterns correspond to the equivalent crystalline a- and b-axes.

X-ray beam parallel to the crystalline c-axis is shown in Fig. 2.15. The horizontal and vertical patterns correspond to the equivalent crystalline a- and b-axes (i.e., [1 0 0] and [0 1 0]). The diagonal patterns correspond to [1 1 0] and [1 $\bar{1}$ 0]. A useful rule to distinguish [1 0 0] from [1 1 0] is that, the two other patterns with lower scattering intensity than [1 0 0] and [1 1 0] patterns (see Fig. 2.15) lie closer to [1 1 0] patterns.

2.2.2 SQUID and resistivity measurements

The superconducting transitions were characterized via magnetic susceptibility and electrical resistivity as a function of temperature (see Appendix.A). In the superconducting state, a material expels an external magnetic field from its interior (Meissner-Ochsenfeld effect) and the electrical resistivity becomes zero.

A superconducting quantum interference device (SQUID) was used to measure the magnetic susceptibility (induced magnetization divided by the magnetic field strength) [33]. The dc SQUID, a design based on the Josephson Effect, is a very sensitive magnetometer. The Josephson effect can be formulated such that for a single Josephson

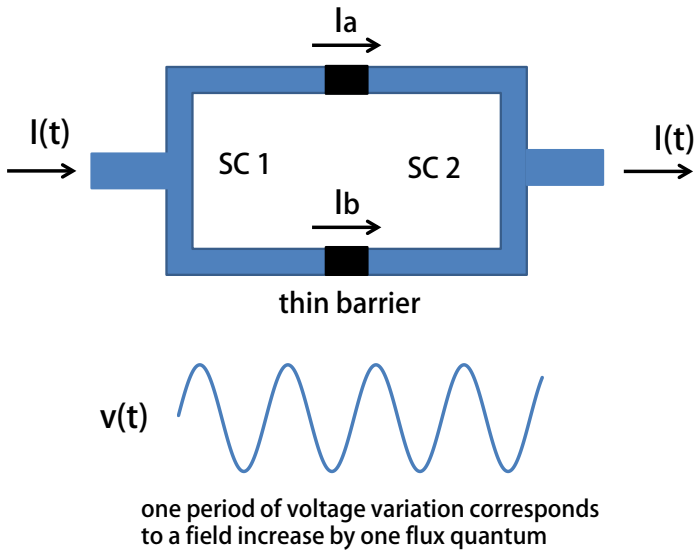

Figure 2.16: Illustration of the scanning loop for a dc SQUID. SC 1 and SC 2 are two superconductors separated by thin barriers [33]. The total current $I(t)$ is split into I_a and I_b. A voltage difference on the two ends is shown as $v(t)$.

junction (two superconductors connected by a weak non-superconducting link):

$$I(t) = I_c \sin[\Delta\phi(t)], \tag{2.3}$$

$$v(t) = \frac{\hbar}{2e}\frac{\partial\phi(t)}{\partial t}, \tag{2.4}$$

where $I(t)$ $[v(t)]$ is the current [voltage] across the single Josephson junction. I_c is the critical current. $\Delta\phi(t)$ is the phase difference between to two superconductors, and $\frac{h}{2e}$ is the magnetic flux quantum.

A dc SQUID consists of two parallel Josephson junctions that form a superconducting loop (Fig. 2.16) [33]. Without an external magnetic field, the current $I(t)$ in the superconducting loop is equally split into $I(t) = I_a + I_b$. With an external magnetic field, a screening current I_s appears in the loop. Assuming that I_s is parallel to I_a (the direction of I_s is determined by direction of the external magnetic field), $I_a = I(t)/2 + I_s$ and $I_b = I(t)/2 - I_s$. In the case that I_a exceeds the critical current ($I_a > I_c$), a voltage

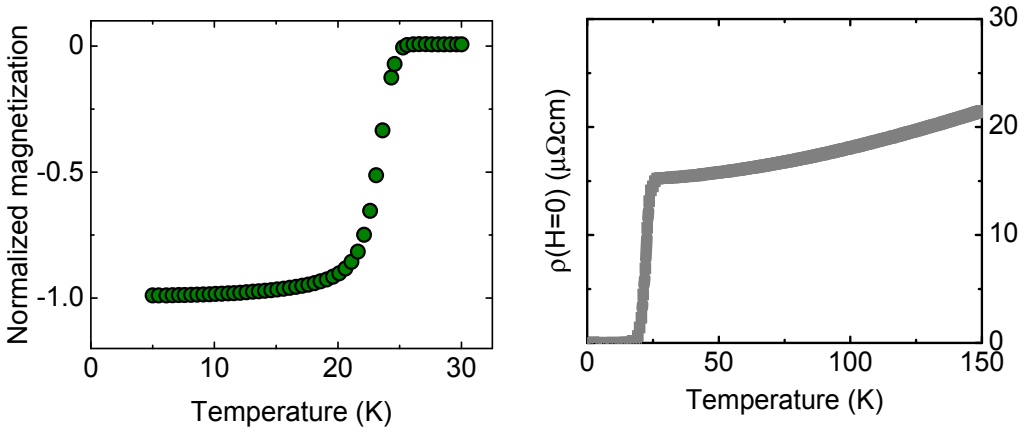

Figure 2.17: Examples of the determination of superconducting transition temperature via magnetization and resistivity measurements for NCCO near optimal doping. Both measurements suggest a transition at $T_c \approx 22$ K.

difference $v(t)$ appears on the two ends of the superconducting loop. When the external magnetic field varies, $v(t)$ varies correspondingly. Each period of voltage variation signifies a field change by one flux quantum through the superconducting loop.

The dc SQUID measurements were preformed with a Quantum Design, Inc., magnetic property measurement system (MPMS XL). Bulk crystal/powder samples were mounted on a transfer rod and inserted into the sample chamber before applying an external magnetic field. Once the field was applied, the magnetization of the material was probed (integrated) by sweeping the sample entirely through the dc SQUID loop. A representative zero-field-cooled magnetization curve as a function of temperature is shown in Fig. 2.17. The magnetization is normalized at low temperature. A superconducting transition occurs at $T_c \approx 22$ K with a transition width of about 2 K. Alternatively, the planar and c-axis electrical resistivity for a sample with the same Ce concentration was measured using a Quantum Design, Inc., physical property measurement system (PPMS). Figure 2.17 shows a representative resistance curve as a function of temperature.

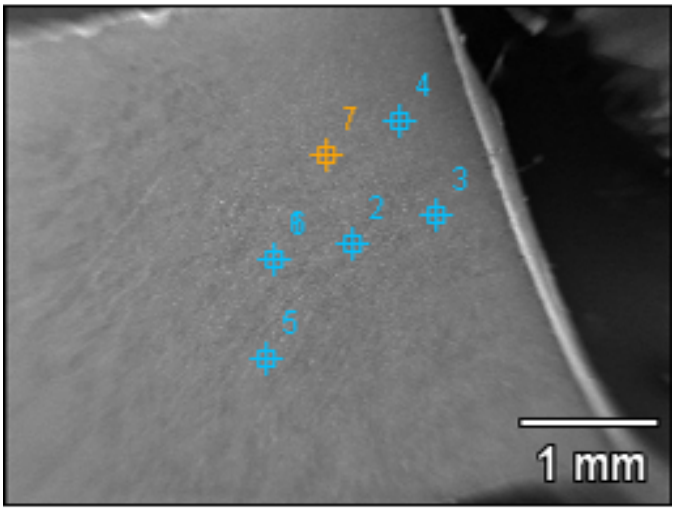

Figure 2.18: Representative SEM image of a NCCO crystal piece. The EDS spectrum at location No. 7 (highlighted in orange) is shown in Fig. 2.19 (image taken with the the JEOL USA, Inc., model JEOL 6500 SEM at the Characterization Facility, University of Minnesota).

2.2.3 SEM and EDS

Scanning electron microscopy (SEM) and energy dispersive X-ray spectroscopy (EDS) were used to characterize sample surfaces and local chemical composition (see Appendix.A).

SEM produces two-dimensional images by scanning the sample with a focused electron beam. The electrons interact with the sample surface (the electron beam has a very short penetration depth, about 10-100 nm, due to the Coulomb interaction) and get back-scattered or produce secondary electrons. Those back-scattered electrons (due to elastic interactions between the incident electrons and the sample) and secondary electrons (due to inelastic interactions between the incident electrons and the sample) contain information about a sample surface's topography and chemical composition [126, 127]. The back-scattered electrons, for which the backscatter coefficient monotonically increases with the target's atomic number, are most efficient for contrasting multiple-phases. The secondary electrons, which provide images with better resolution,

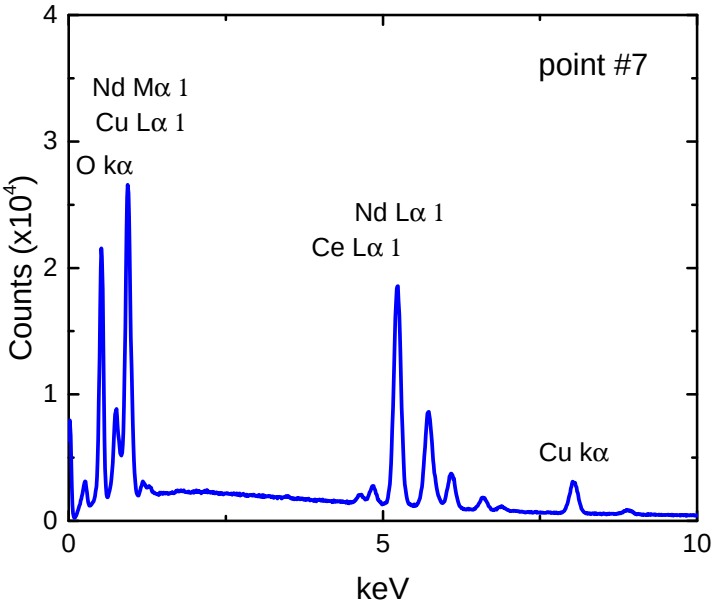

Figure 2.19: Representative EDS spectrum of a NCCO crystal piece (see Fig. 2.18).

are most suitable to measure the surface topography. Spatial resolution of a typical SEM image is about 50 nm. SEM allows analysis of select locations on sample, and thus enables a qualitative determination of chemical composition using EDS. A representative SEM image is shown in Fig. 2.18.

EDS on the SEM system uses a high-energy electron beam to stimulate the emission of characteristic X-rays from the sample. The incident beam excites electrons of the chemical elements in a material from their ground states. When these excited electrons restore to their ground states, X-rays with a characteristic energy/wavelength are emitted from the sample. By collecting information on the intensity and energy of the emitted characteristic X-rays, EDS enables the study of a sample's chemical composition [127]. For the work in this Thesis, EDS results were compared to inductively coupled plasma (ICP) mass spectrometry results taken by previous group members in order to eliminate systematic errors. The EDS spectrum for location No. 7 in Fig. 2.18 is shown in Fig. 2.19. Utilizing the intensity ratio between the observed characteristic X-rays, the sample's chemical composition can be acquired. For example, the Ce concentration

x can be quantified as

$$x \approx (4.83 \text{ KeV Ce peak amplitude})/(3.83 \text{ times } 8 \text{ KeV Cu peak amplitude}). \quad (2.5)$$

In order to obtain an accurate estimate of the peak amplitudes, the 4.83 KeV Ce and 8 KeV Cu peaks were fit simultaneously to a double Gaussian function with zero background slope.

2.3 Neutron scattering

The neutron, a sub-atomic particle and an essential component of all chemical elements except hydrogen, was discovered less than 100 years ago. In 1920, Ernest Rutherford, after the discovery of the proton, speculated that there exists an electrically neutral, massive particle in the nucleus of chemical atoms. in 1932, James Chadwick found that Beryllium atoms when bombarded by alpha particles emit a stream of particles that can approximately be described to have one proton mass and zero charge [128]:

$$^{4}_{2}\alpha + ^{9}_{4}Be \rightarrow ^{1}_{6}2C + ^{1}_{0}n. \quad (2.6)$$

The neutron is a charge-neutral particle with spin $S = 1/2$ and magnetic moment $\mu_n = \gamma e\hbar/2m_p$, where $\gamma = -1.913$ is the neutron gyromagnetic ratio and m_p is the proton rest mass. Outside of a nucleus, neutrons are unstable and decay into a proton, an electron, and an antineutrino with an average life time of about 881.5 seconds [129]. When thermalized, the neutron has a de Broglie wave length on the order of an angstrom (10^{-10} m), comparable to interatomic distances. The energy scale for the thermalized neutron is on the order of tens of meV, similar to many important excitations in materials, such as phonons, magnons, and crystal field excitations. Because of its charge neutral nature, the neutron has the ability to penetrate deeply into matter, and it has been intensively used to probe structural and magnetic properties of materials.

There exist two types of modern neutrons sources - nuclear reactors and spallation sources. Nuclear reactors provide neutrons as a byproduct of fission reactions. The most common fission chain reaction used to obtain neutrons is

$$^{1}_{0}n + ^{235}_{92}U \rightarrow ^{141}_{56}Ba + ^{92}_{36}Kr + 3^{1}_{0}n. \quad (2.7)$$

Research reactors typically use heavy water neutron moderators to control the chain reaction. In thermal equilibrium, the energy of the neutrons can be approximated by a Maxwellian distribution, and thus the average neutron energy is related to the moderator temperature. Averge neutron energies of 5, 26, and 100 meV correspond to moderator temperatures of about 20, 300, and 1400 K, respectively. Accordingly, neutron beams with these approximate energies are classified as cold, thermal, and hot. Following their production, the neutrons are guided to instruments for experiments.

Spallation sources provide intense pulsed rather than continuous neutron beams. Negatively charged hydrogen ions are injected into a linear particle accelerator and accelerated to produce high-energy proton beams. The protons accumulate in "pulsed bunches" in a proton accumulator ring, before striking a target, which in the case of the Oak Ridge National Laboratory Spallation Neutron Source is liquid mercury, to produce neutrons. The neutrons are slowed down in a moderator and guided towards instruments for scattering experiments. The time-of-flight (TOF) spectrometers commonly seen at spallation sources use the overall time-of-flight between the sample and the detector bank, which encompasses a large range of solid angles, to determine neutron energies. Fermi choppers are typically used to select the energy of neutrons incident on a sample.

2.3.1 Scattering theory

The energy (ΔE) and momentum (Δk) transfered to a scattering system by a beam of neutrons with initial momentum $\vec{k}_i$ and energy E_i, final momentum $\vec{k}_f$ and energy E_f, and mass m_n, are

$$\hbar\omega \equiv \Delta E = E_i - E_f = \hbar^2/2m_n(\vec{k}_f^2 - \vec{k}_i^2), \tag{2.8}$$

$$\vec{Q} \equiv \Delta\vec{k} = \vec{k}_f - \vec{k}_i\,. \tag{2.9}$$

Note that, fundamental constants such as $\hbar$, k_B are often set to 1 for simplicity. For elastic scattering, $\omega = 0$, while for inelastic scattering, ω has a non-zero value. The above equations set a kinematic relation between energy and momentum transfers of the scattering process.

The partial differential cross section, defined as the probability of neutrons scattered per unit time into a solid angle $d\Omega = \sin\theta d\theta d\phi$ with final energy between E_f and $E_f + dE_f$, is very useful in describing scattering processes. The partial differential cross

section can be expressed as (Fermi's golden rule [130]) [131, 132]

$$\frac{d\sigma^2}{d\Omega d\omega} = (\frac{m}{2\pi\hbar^2})^2 \frac{k_f}{k_i} \sum_{\lambda_f,\lambda_i} P(\lambda_f)P(\lambda_i)|\langle k_f,\sigma_f,\lambda_f|V|k_i,\sigma_i,\lambda_i\rangle|^2\delta(\hbar\omega + E_i - E_f), \quad (2.10)$$

where $P(\lambda_f)$ ($P(\lambda_i)$) is the statistical weight of the final (initial) states; λ_f (λ_i) is the wave vector of incident (scattered) neutrons; and σ_f (σ_i) is the spin of incident (scattered) neutrons.

The scattering matrix elements $|\langle k_f,\sigma_f,\lambda_f|V|k_i,\sigma_i,\lambda_i\rangle|$ in Eq. 2.10 can be estimated by the Born approximation [131]:

$$|\langle k_f,\sigma_f,\lambda_f|V|k_i,\sigma_i,\lambda_i\rangle| = |\langle\lambda_f|\sum_j e^{i\vec{Q}\cdot\vec{r_j}}|\lambda_i\rangle|V(\vec{Q}), \quad (2.11)$$

$$V(\vec{Q}) \equiv \int d\vec{r}V(\vec{r})e^{i\vec{Q}\cdot\vec{r_j}}, \quad (2.12)$$

where $V(\vec{r})$ is the scattering potential at scattering centers with coordinates $\vec{r_j}$, and $V(\vec{Q})$ is its Fourier transform, i.e., the scattering potential in momentum space.

Nuclear scattering

The nuclear neutron scattering cross section can not be directly calculated. Instead, one can discuss the cross section by introducing a single parameter (the scattering length, with unite of length) for each nuclear isotope. The individual scattering lengths have been measured and documented [131–133]. Because the range of nuclear forces ($\sim$ 1 fm) is much smaller than the wave length of the neutrons, the nuclear scattering potential can be regarded as a delta function in real space, and we can write

$$V(\vec{Q}) \equiv \int d\vec{r}V(\vec{r})e^{i\vec{Q}\cdot\vec{r_j}} = \frac{2\pi\hbar^2}{m}b, \quad (2.13)$$

where b is the nuclear scattering length. The value of the nuclear scattering length, which depends on the spin state of the nucleus, varies greatly among different nuclei (even among isotopes of a single element). The partial differential cross section, when taking into account the motion of scattering potential over time, can be expressed as

[134]

$$\frac{d\sigma^2}{d\Omega d\omega} = N\frac{k_f}{k_i}b^2 S(\vec{Q},\omega), \tag{2.14}$$

$$S(\vec{Q},\omega) = \frac{1}{2\pi\hbar N}\sum_{j,j'}\int dt\langle e^{-i\vec{Q}\cdot\vec{r_{j'}}(t)}e^{i\vec{Q}\cdot\vec{r_j}(t)}\rangle e^{-i\omega t}, \tag{2.15}$$

where N is the number of nuclei and t is the time.

For monatomic materials with b_r and statistical weight c_r, the average nuclear scattering length $\overline{b}$ can be expressed as

$$\overline{b} = \sum_r c_r b_r. \tag{2.16}$$

Due to the presence of isotopes, a random variance of nuclear scattering length may exist from site to site. The coherent scattering cross-section, σ_{coh}, corresponds to collective scattering, while incoherent scattering section, σ_{inc}, corresponds to the variance in spin state and isotopes:

$$\sigma_{\text{total}} = \sigma_{\text{coh}} + \sigma_{\text{inc}} = 4\pi\overline{b^2}, \tag{2.17}$$

$$\sigma_{\text{coh}} = 4\pi\overline{b}^2, \tag{2.18}$$

$$\sigma_{\text{inc}} = 4\pi(\overline{b^2} - \overline{b}^2), \tag{2.19}$$

where σ_{total} is the total scattering section.

The above equations can be understood by considering a scattering process involving a simple incoming plane wave function and an outgoing spherical wave function:

$$\text{Incident plane wave}: \quad \Psi_{\text{in}} = e^{ikx}, \tag{2.20}$$

$$\text{Incident particle number}: \quad I_{\text{in}} = |\Psi_{\text{in}}|^2 = 1, \tag{2.21}$$

$$\text{Scattered spherical wave}: \quad \Psi_{\text{out}} = -\frac{be^{ikr}}{r}, \tag{2.22}$$

$$\text{Scattered particle number}: \quad I_{\text{out}} = |\Psi_{\text{out}}|^2 = b^2/r^2, \tag{2.23}$$

$$\text{Scattering cross section}: \quad \sigma = I_{\text{out}}/I_{\text{in}} \times \text{area} = 4\pi b^2. \tag{2.24}$$

The partial differential cross-section can be expressed as

$$\frac{d\sigma^2}{d\Omega d\omega} = N\frac{k_f}{k_i}\frac{\sigma_{\text{total}}}{4\pi}S(\vec{Q},\omega). \tag{2.25}$$

Nuclear Bragg scattering

In the case of nuclear Bragg scattering for a rigid Bravais lattice (i.e., coherent, elastic nuclear scattering for a periodic solid), Eq. 2.14 and Eq. 2.25 can be rewritten as

$$S(\vec{Q},\omega) = \delta(\hbar\omega)\frac{(2\pi)^3}{V}\sum_G \delta(\vec{Q}-\vec{G}), \tag{2.26}$$

where V is the unit cell volume and G are the reciprocal lattice vectors. Elastic scattering corresponds to $S(\vec{Q},0)$. Due to motion of atoms about their equilibrium positions, Eq. 2.26 needs to be modified by the Debye-Waller factor (DWF). Denoting $\vec{u}$ as the deviation of nuclei from their positions without spatial variance, the DWF can be written as

$$\text{DWF} \equiv e^{-2W} = e^{-\langle(\vec{Q}\cdot\vec{u})^2\rangle}. \tag{2.27}$$

In this case, DWF captures the incoherent scattering. For systems with more than one atomic site per primitive cell: (j^{th} nucleus at position $\vec{d_j}$ with DWF W_j and scattering length $\bar{b}_j$), the partial differential cross section is given by

$$\frac{d\sigma^2}{d\Omega d\omega}|^{\omega=0}_{\text{coh}} = N\frac{(2\pi)^3}{V}\sum_G \delta(\vec{Q}-\vec{G})|F_N(\vec{G})|^2, \tag{2.28}$$

where $F_N(\vec{G}) = \sum_j \bar{b}_j e^{i\vec{G}\cdot\vec{d}_j} e^{-W_j}$ is the nuclear structure factor. If the structure of a system is known, $F_N(\vec{G})$ can be calculated.

Nuclear inelastic scattering

$S(\vec{Q},\omega)$ is called the dynamic structure factor. The dynamic structure factor captures the collective motion (vibration) of the lattice nuclei (i.e., phonons) created or annihilated by neutron-nucleus interactions. Theoretically, the vibration of lattice nuclei is often approximated as simple harmonic oscillations, as obtained by expanding the small-amplitude vibrations in a Taylor series. This approximation gives excitations (phonons) with quantized energy.

Through the fluctuation-dissipation theorem, which states that the fluctuation properties of the system in thermal equilibrium correspond to its linear response to an

external perturbation [135], $S(\vec{Q},\omega)$ is related to the imaginary part of the dynamic susceptibility ($\chi(\vec{Q},\omega)$, which quantifies the linear response of the system to a dynamic perturbation):

$$S(\vec{Q},\omega) = \frac{\chi''(\vec{Q},\omega)}{1-e^{-\hbar\omega/k_BT}}, \tag{2.29}$$

where k_B is the Boltzmann constant. Replacing $\vec{Q}$ by $-\vec{Q}$ and ω by $-\omega$ in Eq. 2.27, a energy-momentum relation (detailed balance condition) for $S(\vec{Q},\omega)$ is obtained:

$$S(-\vec{Q},-\omega) = e^{-\hbar\omega/k_BT}S(\vec{Q},\omega). \tag{2.30}$$

Note that Eq. 2.29 and Eq. 2.30 apply to magnetic scattering as well.

Consider a three-dimensional system with n nuclei in a single unit cell. The system features $3n$ phonon branches, and each phonon branch has an energy-momentum dispersion $\omega_{\vec{q}s}$, where $\vec{q}$ is the wave vector measured from the nearest reciprocal-lattice vector $\vec{G}$, and s denotes different branches with the same wave vector. We can write

$$\chi''(\vec{Q},\omega) = \frac{1}{2}\frac{(2\pi)^3}{V}\sum_{G,q}\delta(\vec{Q}-\vec{q}-\vec{G})\sum_s \frac{1}{\omega_{\vec{q}s}}|F_N(\vec{Q})|^2 \times [\delta(\omega-\omega_{\vec{q}s})-\delta(\omega+\omega_{\vec{q}s})], \tag{2.31}$$

$$F_N(\vec{Q}) = \sum_j \frac{\overline{b}_j}{\sqrt{m_j}}(\vec{Q}\cdot\vec{\xi}_{js})e^{i\vec{Q}\cdot\vec{d}_j}e^{-W_j}, \tag{2.32}$$

where the j$^{\text{th}}$ nucleus is at position d_j, with the DWF W_j, and with mass m_j. ξ_{js} is a polarization vector for a phonon branch with energy $\omega_{\vec{q}s}$. Assuming that the phonons have an infinite life-time (lattice remains at the excited state), the dynamic structure factor can be written as

$$\omega > 0: \quad S(\vec{Q},\omega) = \frac{\chi''(\vec{Q},\omega)}{1-e^{-\hbar\omega/k_BT}}\delta(\omega-\omega_{\vec{q}s}) = \chi''(\vec{Q},\omega)(\frac{1}{e^{\hbar\omega_{\vec{q}s}/k_BT}-1}+1), \tag{2.33}$$

$$\omega < 0: \quad S(\vec{Q},\omega) = \frac{\chi''(\vec{Q},\omega)}{1-e^{-\hbar\omega/k_BT}}\delta(\omega+\omega_{\vec{q}s}) = \chi''(\vec{Q},\omega)\frac{1}{e^{\hbar\omega_{\vec{q}s}/k_BT}-1}. \tag{2.34}$$

The term $1/(e^{\hbar\omega_{\vec{q}s}/k_BT}-1)$ is the Bose factor, which gives the number of phonons at energy E and temperature T.

When the phonons have a finite life-time (lattice restores to its ground state in a finite time), as is the case for real materials, the thermal motion of the nuclei can be

regarded as damped harmonic oscillations, and the delta function in energy needs to be replaced by a Lorentzian function, such that

$$\frac{1}{\omega_{\vec{q}s}}\delta(\omega \pm \omega_{\vec{q}s}) \rightarrow \frac{1}{\omega'_{\vec{q}s}} \frac{\Gamma_{\vec{q}s}}{(\omega \pm \omega'_{\vec{q}s})^2 + \Gamma^2_{\vec{q}s}}, \tag{2.35}$$

where the phonon energy is modified as $\omega'^2_{\vec{q}s} = \omega^2_{\vec{q}s} - \Gamma^2_{\vec{q}s}$, and $\Gamma_{\vec{q}s}$ is the Lorentzian half-width at half-maximum which characterizes the magnitude of the damping effect.

Magnetic scattering

There exist two types of magnetic dipole interactions: (1) between neutron spin and atomic spin and (2) between neutron spin and atomic orbital angular momentum (due to orbital motion of electrons). In case of the cuprates, because of strong crystal fields (4-fold symmetric) and weak spin orbital coupling for $3d$ electrons ($l = 2$, where l is the orbital angular momentum quantum number), the orbital angular momentum is quenched for the d_{xy} orbital ($|m_l = -2\rangle/\sqrt{2} + |m_l = 2\rangle/\sqrt{2}$, where m_l is the magnetic quantum number) and the $d_{x^2-y^2}$ orbital ($|m_l = -2\rangle/\sqrt{2} - |m_l = 2\rangle/\sqrt{2}$) [136]. This is the reason why only dipole interactions between neutron spin and atomic spin need to be considered for the cuprates.

The magnetic dipole moment of the neutron can be expressed as

$$\vec{\mu}_n = \gamma \mu_N \vec{\sigma}, \tag{2.36}$$

where the $\gamma = -1.1913$ and μ_N is the nuclear magneton.

The partial differential cross-section in Eq. 2.10 can be rewritten as

$$\frac{d\sigma^2}{d\Omega d\omega} = (\frac{m}{2\pi\hbar^2})^2 \frac{k_f}{k_i} \sum_{\lambda_f,\lambda_i} P(\lambda_f)P(\lambda_i)|\langle k_f, \sigma_f, \lambda_f|V_M|k_i, \sigma_i, \lambda_i\rangle|^2 \delta(\hbar\omega + E_i - E_f), \tag{2.37}$$

where the V_M is the magnetic scattering matrix. The magnetic scattering matrix can be further expressed as [137]

$$\frac{d\sigma^2}{d\Omega d\omega} = [\frac{\gamma r_0}{2} g f(\vec{Q})]^2 N \frac{k_f}{k_i} e^{-2W} \sum_{\alpha,\beta} (\delta_{\alpha,\beta} - \hat{Q}_\alpha \hat{Q}_\beta) S^{\alpha\beta}(\vec{Q}, \omega), \tag{2.38}$$

where

$$S^{\alpha\beta}(\vec{Q}, \omega) = \frac{1}{2\pi} \int dt e^{-i\omega t} \sum_j e^{i\vec{Q}\cdot\vec{r}_j} \langle S^\alpha_0(0) S^\beta_j(t)\rangle, \tag{2.39}$$

is the magnetic dynamic structure factor and $r_0 = e^2/(m_e c^2)$ is the classical radius of an electron, $f(\vec{Q})$ is the magnetic form factor, g is the Landé factor, and α and β denote the three Cartesian components.

For interactions between neutron spin and a material's atomic spin, the magnetic form factor $f(\vec{Q})$, which is the Fourier transform of magnetic density, $\rho_s(\vec{r})$, in real space, is

$$f(\vec{Q}) = \int \rho_s(\vec{r}) e^{i\vec{Q}\cdot\vec{r}} d\vec{r}. \tag{2.40}$$

If including interactions between neutron spin and a material's atomic orbital angular moment, the magnetic form factor needs to be modified accordingly.

The instantaneous correlation function $S^{\alpha\beta}(\vec{Q}, t=0)$ can be obtained by performing a Fourier transform of the dynamic spin structure factor $S^{\alpha\beta}(\vec{Q}, \omega)$:

$$S^{\alpha\beta}(\vec{Q}, t=0) = \int d\omega S^{\alpha\beta}(\vec{Q}, \omega) \propto \langle S^{\alpha}_{\vec{Q}} S^{\beta}_{-\vec{Q}} \rangle, \tag{2.41}$$

where $S^{\alpha}_{\vec{Q}} = \sum_j e^{-i\vec{Q}\cdot\vec{d}_j} S^{\alpha}_j$ is the spin operator in momentum space (i.e., the Fourier transform of the real-space spin operator). Once integrated over the Brillouin zone, an important sum rule exists:

$$\int d\omega \int_{\mathrm{BZ}} S^{\alpha\beta}(\vec{Q}, \omega) = \frac{(2\pi)^3}{3V} S(S+1)\delta_{\alpha\beta}, \tag{2.42}$$

where S is the spin momentum and $\delta_{\alpha\beta}$ is the delta function.

Magnetic Bragg scattering

Similar to the partial differential cross-section for nuclear Bragg scattering (Eq 2.28), the partial differential cross-section for magnetic Bragg scattering can be written as

$$\frac{d\sigma^2}{d\Omega d\omega}\Big|^{\omega=0}_{\mathrm{coh}} = N_M \frac{(2\pi)^3}{V_M} \sum_{G_M} \delta(\vec{Q} - \vec{G}_M) |F_M \vec{G}_M)|^2, \tag{2.43}$$

where

$$F_M(\vec{G}_M) = \sum_j (\frac{\gamma r_0}{2}) g f(\vec{Q}) \vec{S}^{\perp}_j e^{i\vec{G}_M \cdot \vec{d}_j} e^{-W_j}, \tag{2.44}$$

and $\vec{S}^{\perp}$ is the component of magnetic moment perpendicular to the scattering vector $\vec{Q}$. Note that except for ferromagnetism and the unusual $\vec{Q} = 0$ magnetism exhibited

by the cuprates (e.g., in [99]), the magnetic-lattice vector $\vec{G_M}$ typically differs from the structure-lattice vector $\vec{G}$. The magnetic structure factor $F_M(\vec{G}_M)$ is only sensitive to the component of magnetic moment perpendicular to the scattering vector. In order to obtain the absolute values of the magnetic structure factor, the magnetic Bragg scattering intensity ($I_{\rm mag}$) is usually compared to that of nuclear Bragg scattering ($I_{\rm nuc}$).

Magnetic inelastic scattering

A quantum of the collective excitation of an ordered spin structure is called a magnon or spin wave, which is similar to the phonon (a quantum of collective excitation of the vibration of the crystal lattice). At non-zero temperature, thermal energy results in fluctuations of spin orientations. At zero temperature, quantum fluctuations (e.g., a temporary change of the energy in space, as described by Heisenberg's uncertainty principle) can have a similar effect.

In analogy to the dynamic structure factor (Eq. 2.33), the dynamic magnetic structure factor is

$$\begin{aligned} S_M(\vec{Q},\omega) = S \sum_{G_M,q} [(\frac{1}{e^{\hbar\omega_q/k_BT}-1}+1)\delta(\vec{Q}-\vec{q}-\vec{G_M})\delta(\omega-\omega_q) \\ + \frac{1}{e^{\hbar\omega_q/k_BT}-1}\delta(\vec{Q}+\vec{q}-\vec{G_M})\delta(\omega+\omega_q)]. \end{aligned} \tag{2.45}$$

For a simple Heisenberg ferromagnet with cubic lattice, the spin-wave dispersion at small $\vec{q}$ is [131]

$$\hbar\omega_q = 2JSa^2q^2, \tag{2.46}$$

where J is the exchange energy and a is the lattice parameter, and only nearest-neighbor interactions are considered. Similarly, for a classical Heisenberg antiferromagnet (i.e., neglecting the effect of quantum fluctuation), the spin-wave dispersion at small $\vec{q}$ is [131]

$$\hbar\omega_q = nJSaq^2, \tag{2.47}$$

where n denotes the number of nearest neighbors.

In case that interactions between spin waves are relevant, the effect of damping needs to be considered. Similar to inelastic nuclear scattering, the delta function in energy is

replaced by a Lorentzian function:

$$\frac{1}{\omega_{\vec{q}}}\delta(\omega \pm \omega_{\vec{q}}) \rightarrow \frac{1}{\omega'_{\vec{q}}}\frac{\Gamma_{\vec{q}}}{(\omega \pm \omega'_{\vec{q}})^2 + \Gamma^2_{\vec{q}}}, \tag{2.48}$$

where $\omega'^2_{\vec{q}} = \omega^2_{\vec{q}} - \Gamma^2_{\vec{q}}$.

2.3.2 Triple-axis and two-axis spectrometers

In this Thesis work, two types of research reactor based neutron spectrometers (triple-axis and two-axis spectrometers) were used. A schematic illustration of the triple-axis spectrometer is shown in Fig. 2.20.

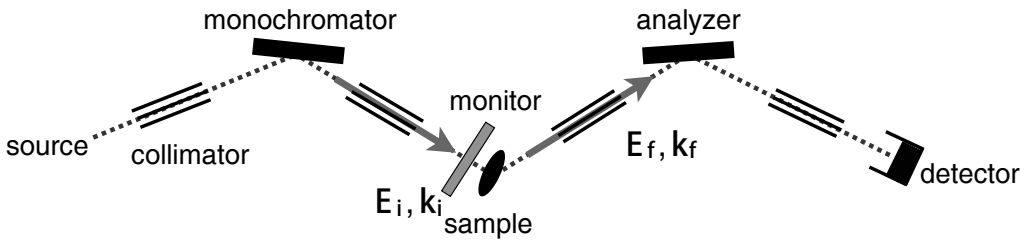

Figure 2.20: Illustration of the triple-axis spectrometer.

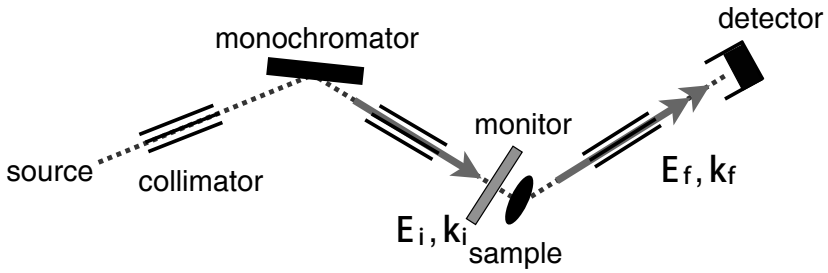

Figure 2.21: Illustration of the two-axis spectrometer.

The term triple-axis refers to the three rotational axes of the instrument: the monochromater, sample, and analyzer axes [138]. The energies of the incident and scattered neutrons are selected by the monochromator and the analyzer, respectively.

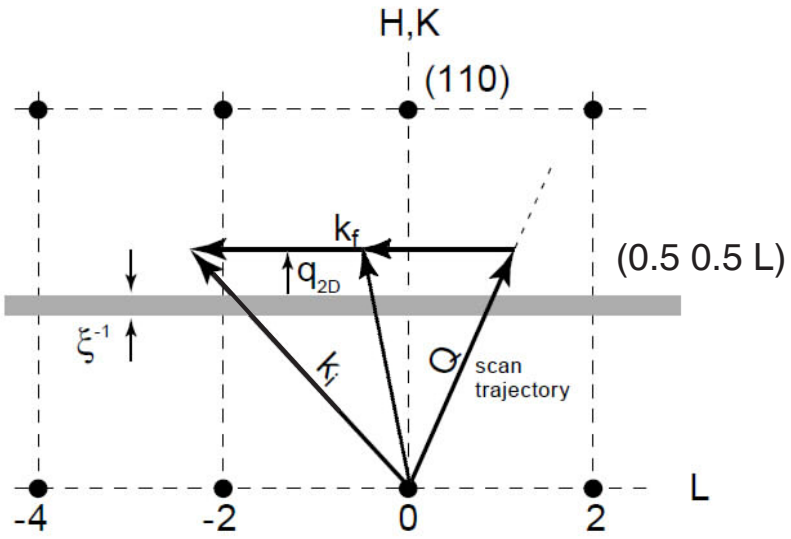

Figure 2.22: Scattering geometry for an energy-integrating two-axis measurement. Such a measurement is feasible for quasi-one-dimensional and quasi-two-dimensional magnetic systems. In the latter case, the cross section is nearly independent of one momentum-transfer direction ([0 0 1] in the case of the lamellar cuprates). The grey horizontal bar shows the one-dimensional magnetic scattering rod above the Néel temperature of the cuprates. Dots and dashed lines indicate the reciprocal lattice of the material. By allowing k_f and hence E_f to vary while fixing the k_i, the momentum-transfer component perpendicular to the scattering rod is kept constant. This special scattering geometry allows the measurement of the energy-integrated (instantaneous) spin structure factor. $\vec{q}_{2D}$ is measured from the center of the scattering rod at (0.5 0.5 L). The inverse half-width of the rod is the instantaneous magnetic correlation length. Figure adapted and modified from [44].

The monochromator and the analyzer are made of special crystals (typically pyrolytic graphite) that select the neutron energies through Bragg scattering. Only neutrons with a chosen energy (or wavelength) satisfy the Bragg scattering condition.

$$n\lambda = 2d\sin\theta \tag{2.49}$$

where n is an integer, d is the distance between lattice planes, and θ is the scattering angle. The initial and final momenta are determined by the initial and final energies and the sample scattering angle.

Neutron filters are commonly used to filter out unwanted neutrons. The neutron filters made of pyrolytic graphite works most efficiently at discrete energies (8, 13.7, 14.7, 30.5, 35 and 42 meV). Before the neutrons reach the sample, they pass through the monitor, which measures the flux of incident neutrons. The neutron intensity measured by the detector is normalized by the incident flux.

Because the incident neutrons have a spatial distribution, collimators were used in the scattering setup to better define the direction and thus momentum of the neutrons. The collimator is made of parallel thin blades of a neutron-absorbing material, such as Cadmium. The separation and length of the blades determine the horizontal angular divergence of the neutrons.

The setup of a two-axis spectrometer is similar to that of the triple-axis spectrometer, as shown in Fig. 2.21. The two-axis spectrometer does not feature an analyzer, and hence measures an energy-integrated cross-section. The energy-integrated cross-section is related to the instantaneous correlation function (see Chapter 3 for data and analysis).

In order to measure the instantaneous spin-spin correlations in a quasi-two-dimensional system, the integration over energy transfer can be performed by allowing the final momentum $\vec{k}_f$ (and hence E_f and ω) to vary while keeping $\vec{k}_i$ fixed. The corresponding scattering geometry is shown in Fig. 2.22. The momentum transfer $\vec{Q} = \vec{k}_f - \vec{k}_i$ is set such that its crucial component $\vec{Q}_{2\mathrm{D}}$ parallel to the CuO_2 plane is constant, while the component along the crystalline c-axis is allowed to vary.

The instantaneous (equal-time) scattering function can be expressed as

$$S(q_{2\mathrm{D}}) = \int S(q_{2\mathrm{D}},\omega)\,d\omega \approx \int_{-k_BT}^{E_i} S(q_{2\mathrm{D}},\omega)\,d\omega. \tag{2.50}$$

Because the integration is over the range from $\omega = -k_BT$ to $\omega = E_i$, E_i has to be large enough to include all the relevant dynamics. In this Thesis work, the initial

energy was chosen as $E_i = 14.7\,\mathrm{meV}$, which was previously established to give good estimation for the magnetic correlation length up to rather high temperature [55, 139]. The energy-integrated neutron intensity is fit to the instrument resolution convolved with a two-dimensional Lorentzian [55, 140]:

$$S(q_{2\mathrm{D}}) = \frac{S(0)}{1 + q_{2\mathrm{D}}^2 \xi^2}, \tag{2.51}$$

where $q_{2\mathrm{D}}$ is the planar distance from center of the two-dimensional antiferromagnetic scattering rod at (0.5 0.5 L).

Instrument resolution

In the previous discussion, the instrument resolution was not considered, i.e., the distributions of the neutrons' momenta and energies were assumed to be delta functions. This assumption does not hold in practice. Denoting Δk_i (Δk_f) as the deviation from the neutrons' initial (final) momentum around their nominal value, respectively, and $p_i(\Delta k_i)$ ($p_f(\Delta k_f)$) as the corresponding distribution function, the neutron intensity $I(\vec{Q}, \omega)$ is given by

$$I(\vec{Q}, \omega) \sim \int p_i(\Delta k_i) S(\vec{Q}, \omega) p_f(\Delta k_f) d\Delta k_i d\Delta k_f. \tag{2.52}$$

When the distribution functions $p_i(\Delta k_i)$ and $p_f(\Delta k_f)$ have the most weight around the nominal momentum values, Eq. 2.52 can be estimated as

$$I(\vec{Q}, \omega) \sim \int R(\Delta\vec{Q}, \Delta\omega) S(\vec{Q}, \omega) d\Delta k_i d\Delta k_f, \tag{2.53}$$

where $R(\Delta\vec{Q}, \Delta\omega)$ is the resolution function.

$R(\Delta\vec{Q}, \Delta\omega)$ is a four-dimensional function (the three-dimensional momentum transfer and the one-dimensional energy transfer). Fortunately, the resolution function perpendicular to the scattering plane (vertical resolution) is decoupled from the remaining dimensions. The collimators in Fig. 2.20 and Fig. 2.21, which are open in the vertical direction and hence give rise to a very coarse vertical distribution, are designed based on this fact.

In this Thesis work, the resolution function of the triple-axis instrument was calculated by a MATLAB program, which was included in [44]. The MATLAB program was

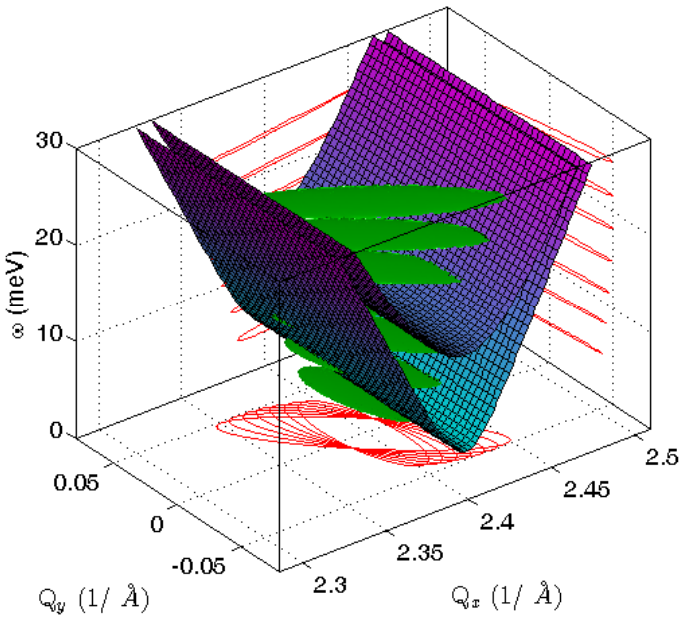

Figure 2.23: Example of calculated triple-axis instrument resolution with collimator configuration 48′-40′-sample-20′-80′ at (H K L)=(1.5 0 0.5) r.l.u.. Q_x and Q_y indicate momentum transfer along [1 0 0] and [0 1 0] parallel to the CuO_2 plane. ω indicates the energy transfer. The resolution function perpendicular to the scattering plane is decoupled from the remaining dimensions of the function and is not shown. The green and red lines shows the resolution function and its projections at a number of energy transfers, respectively. The displayed graph is calculated using the ResLib package [141].

constructed from the ResLib files at Oak Ridge National Laboratory [141]. An example of the resolution function is shown in Fig. 2.23. A detailed discussion of the resolution function for the two-axis case was included in [40].

2.4 Muon spin rotation/relaxation

2.4.1 μSR theory and instrumentation

Muon spin rotation/relaxation (μSR) is a high sensitivity probe of magnetism at the microsecond timescale even in random or dilute spin systems. Detailed discussions of

the μSR technique are included in [142, 143].

Muons with positive charge (μ^+) are produced from the decay of pions (π^+). The pions are obtained by bombarding nuclei of light elements, such as carbon or beryllium, with high energy protons:

$$p + p \rightarrow \pi^+ + p + n, \tag{2.54}$$

$$p + n \rightarrow \pi^+ + n + n. \tag{2.55}$$

The pions are very unstable and subsequently decay into muons and neutrinos:

$$\pi^+ \rightarrow \mu^+ + \upsilon_\mu. \tag{2.56}$$

Because pions carry no spin and the neutrinos' spin is antiparallel to its kinetic momentum (due to parity violation), muons are fully polarized with spin ($S_\mu = 1/2$) antiparallel to their kinetic momentum P_μ. The muons have a typical kinetic energy of 4.12 MeV and an isotropic spatial distribution. When interacting with matter, the muon kinetic energy is affected by the Coulomb interaction and by thermalization, while the muon spin probes the strength and distribution of the local magnetic field.

In a classical picture, the time dependence of muon spin direction ($\vec{S}_\mu$) in a local magnetic field ($\vec{H}_{\text{local}}$) is

$$\frac{d\vec{S}_\mu(t)}{dt} = \gamma_\mu \vec{S}_\mu(t) \times \vec{H}_{\text{local}}(t), \tag{2.57}$$

where γ_μ is the gyromagnetic ratio. The muon is unstable with a mean life-time of about 2.2 μs, and it decays into one positron and two neutrinos:

$$\mu^+ \rightarrow e^+ + \upsilon_e + \overline{\upsilon}_\mu. \tag{2.58}$$

Because of parity violation (a parity transformation is the simultaneous sign flip of all the spatial coordinates), the positrons are preferentially emitted along the muons' spin direction when the decay occurs. The angular distribution of the emitted positrons is

$$W(\phi) = 1 + a(E)\cos(\phi), \tag{2.59}$$

where ϕ is the angle between the positron emission direction and the muon's spin direction. The coefficient $a(E)$ depends on positron energy, and have an average value of $\langle a(E) \rangle = 1/3$.

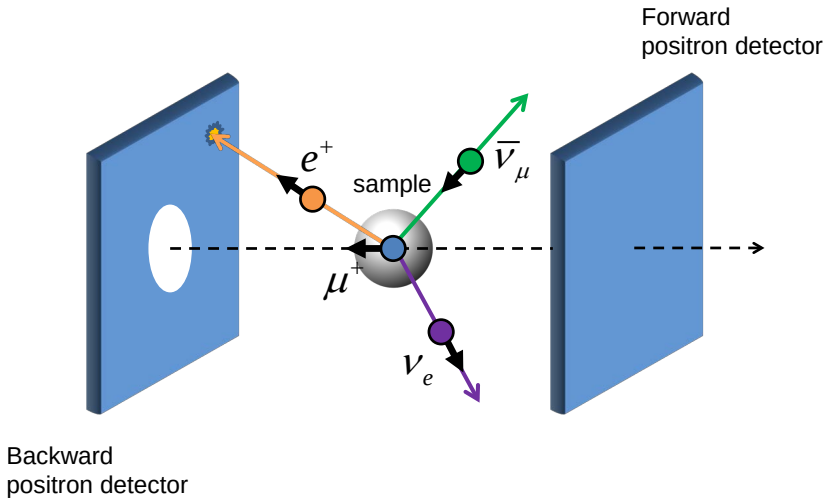

Figure 2.24: Illustration of the detector component of a μSR instrument (zero external magnetic field). The spatial distribution of the emitted positrons is preferentially along the spin direction of the muons when decay occurs (see illustrations for other measurement configurations in [144]).

An illustration of the detector components of μSR instrument is shown in Fig. 2.24. The angular distribution $A(t)$ of the positrons (also named asymmetry function or μSR time spectrum) is obtained with forward (F) and backward (B) positron detectors:

$$A(t) = (B - F)/(B + F). \tag{2.60}$$

This formalism ensures that the asymmetry function $A(t)$ reaches its maximum at $t = 0$.

Typical μSR measurement configurations are: (1) zero external magnetic field, (2) longitudinal external field, and (3) transverse external field. Denoting the angle between the local magnetic field $\vec{H}$ (a combination of the intrinsic and the external magnetic fields) and the muon spin direction ($\vec{S}_\mu$) as θ, the muon precession can be written as

$$\sigma(t) = \cos^2(\theta) + \sin^2(\theta)\cos(\gamma_\mu H t). \tag{2.61}$$

In case that the local magnetic field has a certain spatial distribution, $P(H)$, the correlation function of the muon spin (the relation between muon spin at time t and time

0) can be expressed as

$$\frac{S_\mu(t)}{S_\mu(0)} = \int [\cos^2(\theta) + \sin^2(\theta)\cos(\gamma_\mu H t)] P(H) d^3H. \tag{2.62}$$

The μSR time spectra (asymmetry functions) for several typical spin systems that calculated based on Eq. 2.62:

1. For a paramagnetic system, the time spectrum can be expressed as an exponential decay [142]:

$$A(t) \propto e^{-\lambda t}, \tag{2.63}$$

where λ is the muon spin decay rate.

2. For a two-dimensional material with magnetic moments aligned collinearly (e.g., ferromagnetism or antiferromagnetism), when the initial muon spin direction $\vec{S}_\mu$ is perpendicular to the moment direction [142]:

$$A(t) \propto e^{-\lambda_M t}\cos(\gamma_\mu H t + \phi), \tag{2.64}$$

where $\gamma_\mu H$ (oscillation frequency) is proportional to the local magnetic field strength, and λ_M is the decay rate.

3. For a magnetically ordered polycrystalline sample [142]:

$$A(t) \propto 1/3 e^{-\lambda t} + 2/3 e^{-\lambda_M t}\cos(\gamma_\mu H t + \phi). \tag{2.65}$$

The oscillatory contribution (the prefactor 2/3) comes from the two magnetic moment components perpendicular to the initial muon spin direction. The constant contribution (the prefactor 1/3) comes from the component of the moment parallel to the initial muon spin direction.

4. For a Gaussian-distributed magnetic field parallel to the initial muon spin (the Kubo-Toyabe function) [142]:

$$A(t) \propto 1/3 e^{-\lambda t} + 2/3(1 - \Delta^2 t^2) e^{-\Delta^2 t^2/2}, \tag{2.66}$$

where Δ is the distribution width of the local magnetic field.

5. For an isotropic Lorentzian magnetic field distribution [142]:

$$A(t) \propto (1 - at) e^{-at}, \tag{2.67}$$

where a is the muon spin decay rate.

2.4.2 Analysis of the μSR time spectrum

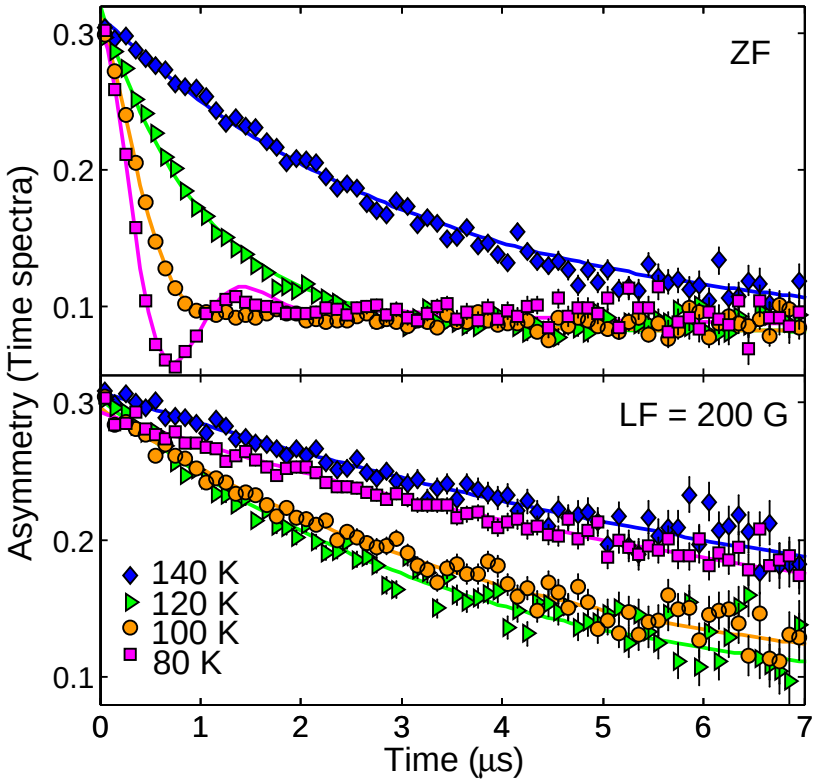

Figure 2.25: Representative ZF and LF μSR time spectra for NCCO with $x = 0.118$ and $T_{\rm N} \approx 115$ K. The solid lines and the full symbols indicate the fits discussed in the text and the raw data, respectively.

Representative μSR time spectra for the zero external field (ZF) and the longitudinal external field (LF) measurement configuration are shown in Fig. 2.25. In case there exist regions with and without magnetic order in a sample (e.g., NCCO at intermediate Ce concentration), the ZF μSR time spectrum can be described by a two-component function:

$$A(t) = A_1 e^{-\lambda_1 t} \cos(\gamma_\mu H t + \phi) + A_2 e^{-\lambda_2 t}, \tag{2.68}$$

where A_1, λ_1, $\gamma_\mu H$ and ϕ are the initial asymmetry, depolarization rate, muon precession frequency, and initial phase for the muon spin in the magnetic regions, respectively, and

A_2, λ_2 are the corresponding parameters for the non-magnetic regions.

Above the magnetic ordering temperature, the internal field strength is small and random, and no oscillatory behavior is observed in the μSR time spectrum. Below the ordering temperature, a local magnetic moment starts to form. Once the spin-spin correlation timescale is longer than the timescale probed by the muons (at about 1 μs, because the muon decay time is about 2.2 μs), oscillatory behavior appears (see Eq. 2.68). The oscillation frequency is proportional to the temperature-dependent local field strength. The muon spin relaxation rate, λ_1, captures the local field distribution.

The LF μSR time spectrum for NCCO can be described as

$$A(t) = A_L e^{-\lambda_L t}. \tag{2.69}$$

Because of the relatively large external magnetic field, the material's intrinsic magnetic field can be treated as a perturbation. When the initial muon spin is parallel to the external field, no oscillatory behavior is observed. At high temperatures, the muon spins, which are initially antiparallel to the external field, repopularize into two principal configurations: (1) muon spins antiparallel to the external field, and (2) muon spins parallel to the external field. This repopulation process causes a relaxation of the muon spins (i.e., the spin-lattice relaxation).

As discussed in Chapter 3, a number of materials properties, including the local magnetic moment (converted from $\gamma_\mu H$), the spin-lattice relation rate (λ_L), the ZF spin relaxation rate (λ_1), and the magnetic volume fraction [calculated as $V_{\rm M} = A_1/(A_1+A_2)$] can be obtained from the ZF and LF μSR time spectra.

A representative transverse-field (TF) μSR time spectrum is shown in Fig. 2.26. The TF μSR time spectrum can be expressed as

$$A(t) = Ae^{-\sigma^2 t^2/2}\cos(\gamma_\mu H t + \phi). \tag{2.70}$$

The decay rate, σ, contains information about the superfluid density. Early μSR experiments for the hole-doped cuprates revealed a phenomenological relation between the extrapolated zero-temperature value of σ and the superconducting transition temperature [145] (see also Chapter 4).

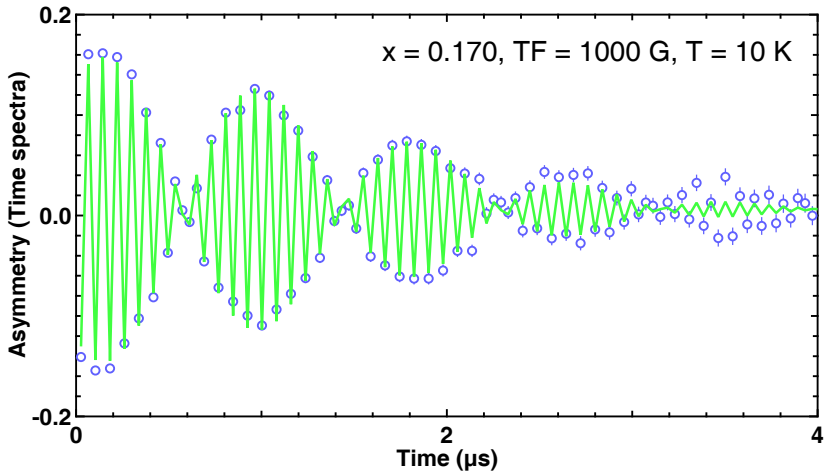

Figure 2.26: Representative TF μSR time spectrum for NCCO with $x = 0.170$. The green solid line and the blue open circles indicate the fit and the raw data, respectively.

2.5 Charge transport measurements

2.5.1 Classical picture of the magnetoresistivity

Magnetoresistivity is an important probe of the Fermi surface of materials. At high magnetic fields ($\omega_c\tau \gg 1$, where ω_c is the cyclotron frequency and τ is the scattering mean free time), quantum oscillations (i.e., Shubnikov-de Haas oscillations in the resistivity) occur as the Fermi energy passes different Landau levels. The oscillation frequency, with respect to the magnetic field strength, contains information about the size of the Fermi surface in the high magnetic field. At low magnetic fields ($\omega_c\tau \ll 1$), where potential Fermi-surface reconstruction induced by the magnetic field is of much less concern, Lifshitz et al. [146–148] studied the magnetoresistivity of open and closed Fermi surfaces and observed that $\Delta\rho/\rho(H = 0) \propto b_2H^2$ for systems with two conduction bands. Here, $\rho(H = 0)$ is the resistivity in zero magnetic field and $\Delta\rho = \rho(H) - \rho(H = 0)$. The magnitude of magnetoresistivity (quantified by b_2) of open Fermi surfaces is usually much less than that of closed Fermi surfaces at low magnetic fields. At intermediate field strength ($\omega_c\tau \approx 1$), the magnetoresistivity of closed Fermi surfaces saturates and

deviates from the quadratic field dependence, but that of an open Fermi surface continues to behave as $\Delta\rho/\rho(H=0) \propto b_2 H^2$ and become much larger. For systems with two (electron and hole) bands, in case the Fermi surface for one type of carriers is much smaller than that for the other, the deviation of magnetoresistivity from the quadratic field dependence reflects a saturation effect of the small Fermi surface. The carrier density can be estimated from the size of the Fermi surface. The formulae for calculating the magnetoresistivity based on the Fermi surface of the electron-doped cuprates are included in Chapter 4.

2.5.2 Measurement geometries and instrumentation

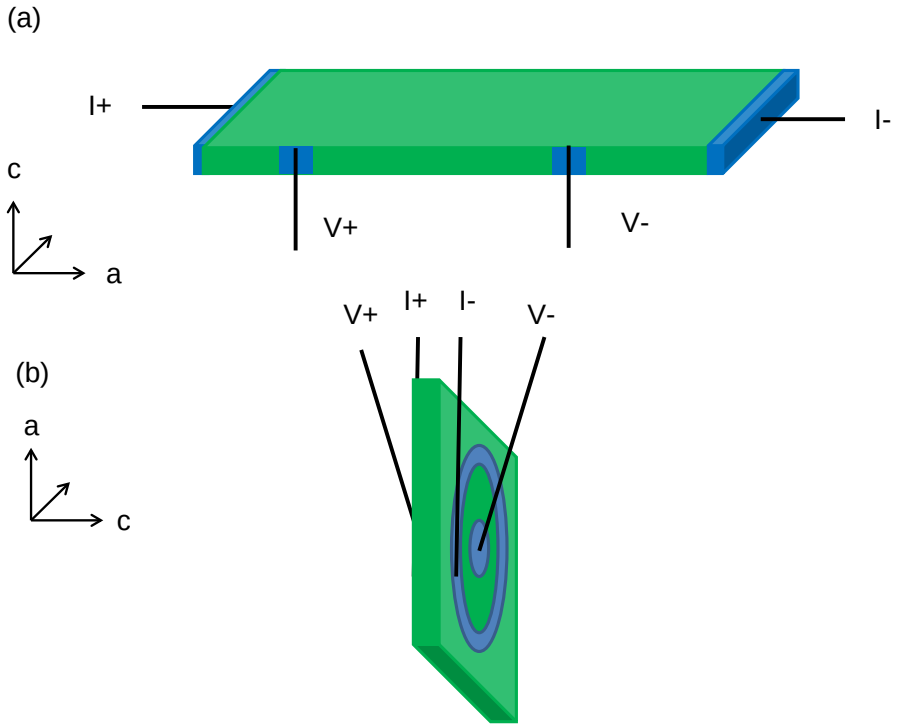

Figure 2.27: Illustrations of the four-point contact geometries for (a) *ab*-plane and (b) *c*-axis resistivity measurements. Blue areas indicate the silver paste deposition on the sample (shown in green). The black lines indicate gold wires embedded in the silver paste.

Well-characterized high-quality single crystals were cut with a wire saw to desirable sizes and shapes. For *ab*-plane resistivity measurements, typical sample dimensions were $4.0 \times 1.0 \times 0.2$ mm^3 (length $\times$ width $\times$ thickness). The crystal pieces were oriented such that the crystalline *a*-axis was parallel to the longest edge and crystalline *c*-axis was parallel to the shortest edge. For *c*-axis resistivity measurements, typical sample dimensions were $3.0 \times 3.0 \times 0.3$ mm^3. The samples were oriented such that the crystalline *c*-axis was parallel to the shortest edge. The cut crystal piece was polished using diamond sand paper with grain size smaller than 1 μm, and subsequently contacted with silver paste (Dupont 6368 silver paste) and gold wires (1 μm in diameter). The accuracy of the sample orientation was estimated to be better than 2°. In order to cure the silver paste, a mild heat treatment (20 mins at 500°C) was applied. In case in which the direct deposition of the silver paste on the crystal surface was difficult, gold deposition was used.

Measurement geometries include the four-point contact, Hall bar, and Van der Pauw configurations. Illustrations of the four-point contact geometry for *ab*-plane and *c*-axis resistivity measurements are shown in Fig. 2.27. For measurements with current flow along the *ab*-plane, the current contacts need to cover the entire side area of the crystal slab in order to enable homogeneous current flow, and the voltage contacts should cross the entire width. If the current contact was deposited on the *ab*-plane, current would flow through a shortcut path instead of the whole sample. For measurements along the *c*-axis, the current and voltage contacts form coaxial circles. The current flow through the larger circle to ensure a homogeneous current flow along *c*-axis. A simple ohmic relation exists between the measured voltage and the current source in the non-superconducting state:

$$R = (V_+ - V_-)/(I_+ - I_-). \tag{2.71}$$

Illustration of the Hall bar geometry for *ab*-plane measurements is shown in Fig. 2.28. The resistance and the Hall constant (with an external magnetic field H) can be calculated as:

$$R = (V_1 - V_2)/(I_+ - I_-) = (V_3 - V_4)/(I_+ - I_-), \tag{2.72}$$

$$R_H = (V_1 - V_3)/(I_+ - I_-) = (V_2 - V_4)/(I_+ - I_-). \tag{2.73}$$

In practice, contacts on the sides (i.e., V_1, V_3, V_2, and V_4) can hardly be aligned such

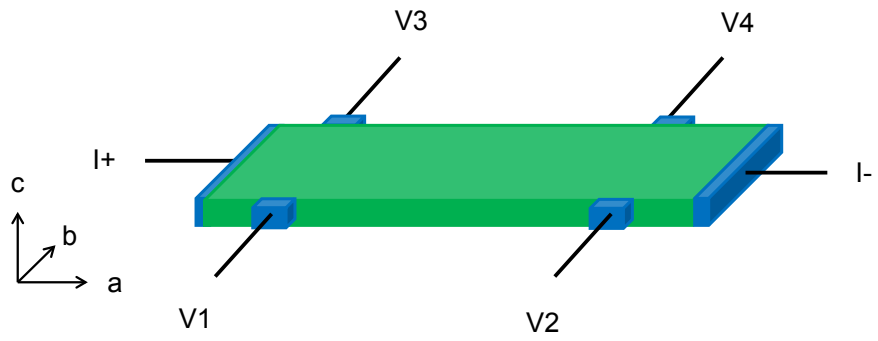

Figure 2.28: Illustrations of the Hall bar geometry. Blue areas indicate the silver paste deposition on the sample (shown in green). The black lines indicate gold wires embedded in the silver paste.

that no longitudinal contribution enters the transverse voltage measurements. In case that a large anisotropy of the resistivity exists (e.g., $\rho_c \sim 100$ to 1000 ρ_{ab} for the cuprates), a slight misalignment of the contacts may introduce a substantial admixture of longitudinal (magnetoresistance) and transverse (Hall) contributions. In addition, disorder and defects cause the current to deviate from the ideal straight path, even when the contacts are aligned perfectly.

In order to separate the longitudinal and transverse contributions, measurements with Hall bar geometry involved altering the direction of the external magnetic field. The magnetoresistance usually depends on the magnitude, but not the direction of the external field, whereas the Hall voltage depends on both. An efficient method to separate the two contributions is to first determine the longitudinal contribution by canceling the transverse contribution upon performing measurements with the external field in opposite directions. Once longitudinal contribution has been obtained, the transverse contribution can be estimated.

Illustration of the Van der Pauw geometry is shown in Fig. 2.29. This geometry, which can be used for samples with irregular shapes, requires an approximate C_4 rotational symmetry (invariant under a 90 degree rotation) of the sample. The gold wires were embedded in the silver paste which completely covered the four corners. Denoting the current (voltage) in the ab-plane by I_{ij} (V_{ml}), where i, j, m, and l are contact

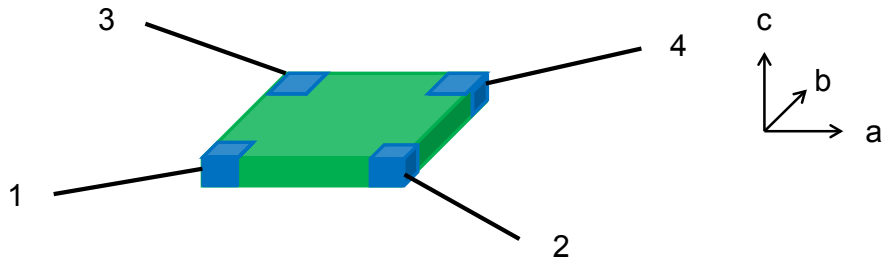

Figure 2.29: Illustrations of Van der Pauw contact geometry for *ab*-plane measurements. Blue areas indicate the silver paste deposition on the sample (shown in green). The black lines indicate gold wires embedded in the silver paste.

number, a ratio between voltage and current can be written as

$$R_{\mathrm{ij,ml}} = V_{\mathrm{ij}}/I_{\mathrm{ml}}, \tag{2.74}$$

The resistance can be expressed as

$$R_{\mathrm{vertical}} = (R_{13,24} + R_{31,42} + R_{24,13} + R_{42,31})/4, \tag{2.75}$$

$$R_{\mathrm{horizontal}} = (R_{12,34} + R_{34,12} + R_{21,43} + R_{43,21})/4. \tag{2.76}$$

In an external magnetic field B, the Hall constant can also be measured with the Van der Pauw geometry. Denoting the ratio in Eq. 2.74 for magnetic field parallel (antiparallel) to crystalline c-axis as $R^{+}_{ab,cd}$ ($R^{-}_{ab,cd}$), in case of a constant current, the Hall constant is

$$R_H = (R^{+}_{14,23} - R^{-}_{14,23} + R^{+}_{23,14} - R^{-}_{23,14} + R^{+}_{41,32} - R^{-}_{41,32} + R^{+}_{32,41} - R^{-}_{32,41})/8B. \tag{2.77}$$

An in-house Quantum Design Inc., physical property measurement system (PPMS, with maximal magnetic field 9 Tesla) and high-field resistive magnets at the National High Magnetic Field Laboratory (NHMFL, with magnetic field up to 34.5 Tesla) were used for the charge transport experiments. Samples were attached to rotational platforms (pucks) in both cases. In order to avoid accidental current flow between the samples and the platform surface, electrically isolating but thermal conducting sapphire plates were inserted between the two. The sample holders for the high-field measurement were similar to that used with the PPMS systems. Stycast glue was used to glue samples to the holder in order to avoid sample levitation at low temperatures.

Lock-in amplifiers were used to extract signals and suppress the measurement noise, and they are critical for the *ab*-plane measurements, for which the electrical resistivity is on the order of 1 to 100 $\mu\Omega$cm. Orthogonality of sinusoidal functions was the key principle used to suppress the measurement noise. The input signal ($V_{\rm in}$, a combination of intrinsic signal and environmental noises) was first multiplied with a sinusoidal reference function [$\sin(\omega t + \phi)$] generated by an oscillator, and then integrated over a period of time (Δt, typically on the order of 1 to 1000 ms):

$$V_{\rm out}(t) = \int_{t}^{t+\Delta t} \sin(\omega t + \phi) V_{\rm in}(t) dt \tag{2.78}$$

In the limit of large Δt, any signal that has frequency other than $\omega/2\pi$ is suppressed. Only when the frequency of reference function equals that of the intrinsic signal, the output is an approximate dc signal. Modern lock-in amplifiers have two detectors (one in-phase detector and one out-of-phase detector). The out-of-phase detector has a reference function with additional $\pi/2$ phase compared to that of the in-phase detector. The voltage of the two detectors ($V_{\rm out}^{\rm in-phase}$ and $V_{\rm out}^{\rm out-of-phase}$) can be expressed as

$$V_{\rm out}^{\rm in-phase}(t) \sim V_{\rm in}\cos(\Delta\phi) \tag{2.79}$$

$$V_{\rm out}^{\rm out-of-phase}(t) \sim V_{\rm in}\cos(\Delta\phi + \pi/2) \sim V_{\rm in}\sin(\Delta\phi), \tag{2.80}$$

where $V_{\rm in}$ is the amplitude of the intrinsic signal and the $\Delta\phi$ is the phase difference between the reference function and the intrinsic signal. The relation between output voltage and phase is

$$V_{\rm out}(t) = \sqrt{[V_{\rm out}^{\rm in-phase}(t)]^2 + [V_{\rm out}^{\rm out-of-phase}(t)]^2}, \tag{2.81}$$

$$\tan(\Delta\phi) = V_{\rm out}^{\rm out-of-phase}(t)/V_{\rm out}^{\rm in-phase}(t). \tag{2.82}$$

Chapter 3

Revised phase diagram of the electron-doped cuprates

This Chapter focuses on the multi-parameter (chemical substitution, oxygen reduction condition, doping and temperature) phase diagram of NCCO constructed using neutron scattering, μSR and SQUID magnetization results. It will be explain how observables such as the Néel temperature, staggered magnetization, instantaneous spin-spin correlation length, magnetic and superconducting volume fractions, spin fluctuation time scales, and μSR relaxation rates were obtained. In addition, this Chapter describe the observation of a clear connection between the normal-state properties and the evolution of the Fermi surface.

3.1 Overview

The "global" phase diagram of the cuprates is very complex: it features multiple competing or coexisting ordering tendencies as a function of chemical substitution, oxygen content, electron/hole doping, temperature, etc., that are often found to be compound specific. Although the emergence of unconventional superconductivity from an antiferromagnetic insulator has been intensively studied for more than three decades, it has

remained unclear if antiferromagnetic correlations drive the supercondcutivity [27]. Superconductivity on the verge of antiferromagnetic order has been observed in correlated-electron systems other than the cuprates [52], including iron-based [46–48, 149], heavy-fermion [51, 150], and organic [50] superconductors.

The parent compounds of the electron-doped cuprate materials have been argued to be either charge-transfer insulators (insulating behavior due to electron correlations) or the Slater insulators (insulating behavior due to antiferromagnetic correlations) [42, 61, 70–72]. These parent compounds have the tetragonal prime (T') structure (see Chapter 1), in which copper and oxygen atoms form a square planar structure. In as-grown samples, without any oxygen manipulation, it was observed that a few percent of oxygen atoms reside at the nominally vacant apical sites (above or below the copper atoms) [42]. These apical oxygens largely modify the planar copper-oxygen environment resulting in a local pyramid T^* or octahedral T structure, and thus change the crystal field splitting. Moreover, they introduce a random disorder potential in the as-grown system.

In order to achieve superconductivity, chemical substitution (nominally Ce^{4+} for Nd^{3+} in the case of $Nd_{2-x}Ce_xCuO_{4+\delta}$) and/or oxygen reduction are required, which changes the electron filling (chemical potential), the local structure, and disorder potential. Without the oxygen reduction process, the T' materials remain non-superconducting up to the chemical solubility limit (typically $x \approx 0.2$). Only after the oxygen reduction, superconductivity emerges at low temperatures.

Substitutional doping at small Ce concentrations was intensively studied and suggested to effectively dilute the magnetic moment on the copper sites [56, 151, 152]. The instantaneous spin-spin correlation length of the substituted materials was found to follow that of the random diluted antiferromagnet [139]. For NCCO samples subjected to the standard oxygen reduction procedure (Chapter 2), neutron scattering measurements indicated that the antiferromagnetic phase has considerable overlap with the superconducting phase [139]. Our group's more recent work [55], in contrast, demonstrated that genuine long-range antiferromagnetic order does not extend nearly as far (it extends to $x \approx 0.12$ in NCCO). This is still much further than in the case of the hole-doped cuprates, antiferromagnetic order in $La_{2-x}Sr_xCuO_4$ vanishes at $p \approx 0.02$ [140]. Naively, when the CuO_2 planes are doped with electrons, the electrons prefer to enter Cu $3d_{x^2-y^2}$

orbitals, leading to a non-magnetic $3d^{10}$ configuration, whereas doped holes prefer to enter planar oxygen sites and rapidly frustrate the antiferromagnetic order (see Fig. 1.4).

The effects of oxygen reduction were initially much less studied. Although a weakening and/or suppression of the antiferromagnetism was universally observed, the exact reason for this has remained still unclear. The oxygen reduction conditions can be broadly categorized into three classes: (1) as-grown, namely no oxygen reduction; (2) the standard reduction condition described in Chapter 2; and (3) the special reduction condition, which is harsher (either in a high temperature or lower oxygen partial pressure) than the standard reduction and uses powders or polycrystals to protect the sample [119]. In this latter case, it was found that the superconductivity doping range is extended to lower Ce concentration ($x \approx 0.04$) [153], indicating the possibility that superconductivity might in principle be achievable without substitutional Ce doping. For thin-film samples subjected to a reduction treatment similar to (3), superconductivity was indeed observed in parent compounds, such as $Nd_2CuO_{4+\delta}$ [154] and $Pr_2CuO_{4+\delta}$ [63, 119], and it was suggested that no long-range antiferromagetic order exists in these samples [119, 155]. How exactly the reduction enables the emergence of superconductivity remains an open question. It is a distinct possibility that the superconducting films with $x = 0$ are effectively doped as a results of oxygen non-stoichiometry [119].

Because both chemical substitution and oxygen reduction modify the chemical potential and change the disorder potential landscape, it is difficult to separate the effects of the two. Resolving this issue in the case of the electron-doped cuprates would constitute significant advance in understanding of these correlated-electron systems.

3.2 Magnetic properties

This Section mainly presents the magnetic properties of NCCO obtained via neutron scattering and μSR techniques. Neutron scattering probes magnetic correlations at (approximately) the picosecond timescale via the magnetic dipole interaction, averaged over the whole sample (Chapter 2). μSR is a highly sensitive local probe of magnetism even in random or dilute spin systems at (approximately) the microsecond timescale, and it probes local magnetism via the spin precession and relaxation of muons implanted in a sample (Chapter 2). Utilizing these two techniques, the magnetic properties of NCCO

subjected to standard oxygen reduction (and in a few cases, also as-grown samples) were obtained at various lengthscales and timescales as a function of Ce concentration and temperature.

3.2.1 Néel temperature

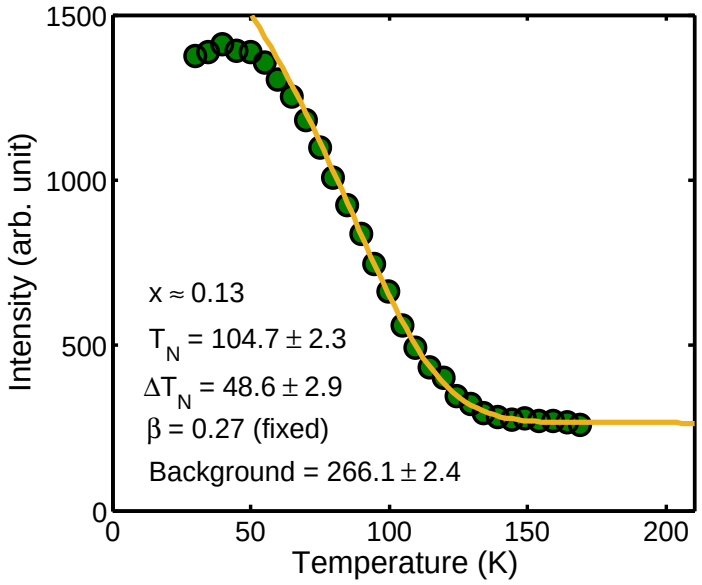

Figure 3.1: Demonstration of the determination of the Néel temperature from the neutron diffraction intensity at (0.5 0.5 1) for a reduced NCCO sample with $x \approx 0.13$. Fit (orange solid line) of the intensity (green dots) to Eq. 3.2 was used to obtain the $T_{\rm N}$. A Gaussian distribution of Néel temperature (width $\Delta T_{\rm N}$) was assumed.

The Néel temperature ($T_{\rm N}$) is the temperature below which an antiferromagnetically correlated spin system orders. It is the analogue of the Curie temperature for ferromagnets. The quantum treatment of antiferromagnetism differs from the classical procedure developed by Louis Néel [157] (the quantum ground state is a superposition of eigen-wave-functions). Experimentally, the measured value of $T_{\rm N}$ is the temperature at which spin fluctuations become slower than the timescale of the probe. In this Section, $T_{\rm N}$ was obtained via both neutron scattering and μSR.

Neutron diffraction intensities (scans of the sample angle, i.e., θ-scans, obtained at

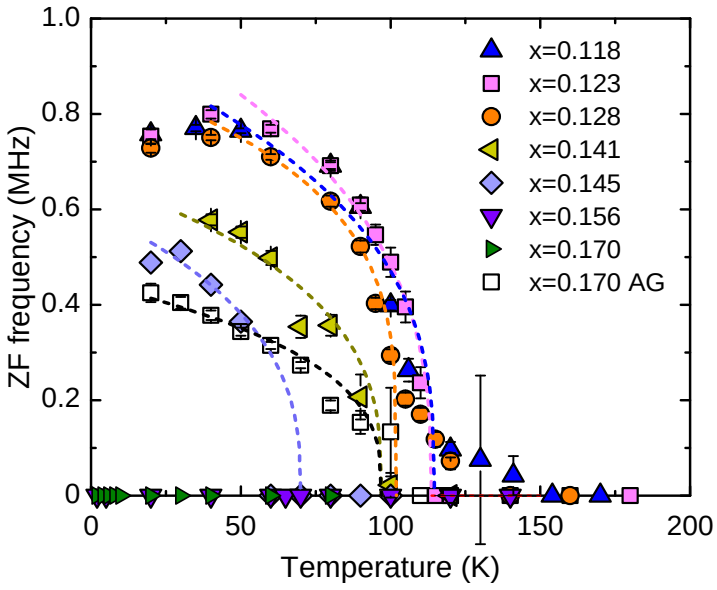

Figure 3.2: Determination of the Néel temperature from ZF μSR for many oxygen-reduced samples and one as-grown (AG) $x = 0.170$ sample. The ZF muon precession frequency ω (symbols) was fit (lines) to a rounded power-law function.

discrete temperatures) at antiferromagnetic Bragg peak positions (which do not coincide with the structural nuclear Bragg peak positions), were used to obtain T_N. T_N was estimated as the temperature at which neutron intensity levels off, taking into account the previously established sample inhomogeneity, which manifests itself in a macroscopic distribution of the transition temperatures [40, 44]. The neutron intensity measures the square of the order parameter (i.e., the staggered magnetization of the antiferromagnetic order, see 2.43). The staggered magnetization (M_{st}) and neutron intensity are

$$M_{st} \propto (T_N - T)^{\beta}, \tag{3.1}$$

$$I \propto M_{total}^2, \tag{3.2}$$

where β is the order parameter critical exponent. Prior measurements of Nd_2CuO_4 yielded a value of $\beta \approx 0.27$ [40, 44]. For a system with macroscopic inhomogeneity, a distribution of T_N should be considered [40, 44]. A Gaussian distribution of T_N was

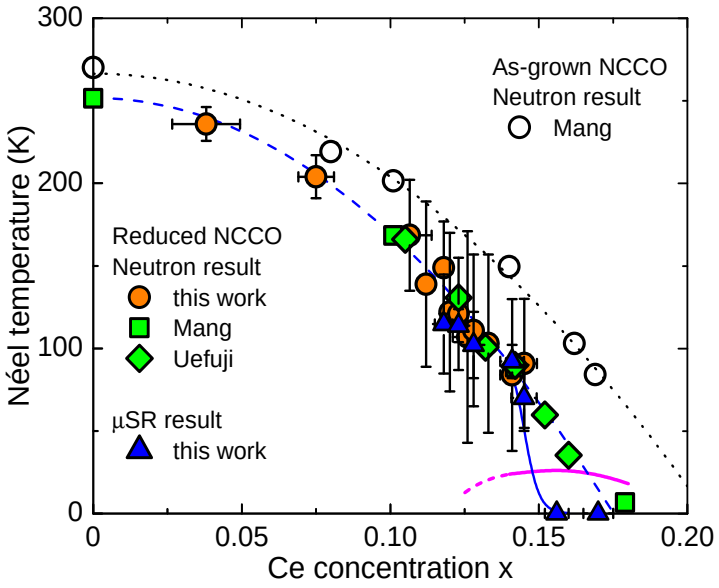

Figure 3.3: Summary of the doping dependence of $T_{\rm N}$ for as-grown and reduced NCCO. Magenta solid and dotted lines indicate the superconducting transition temperature (T_c). Black dotted (neutron data for as-grown NCCO), blue dashed (neutron data for reduced NCCO) and blue solid lines (μSR data for reduced NCCO) are guides to the eyes. With a shift of $\Delta x = -0.03$, $T_{\rm N}$ of as-grown NCCO collapses to that of reduced samples. Neutron data also taken from Mang *et al.* [139] and Uefuji *et al.* [156].

assumed. The data for the Ce-doped samples are not of sufficiently high quality to allow for a reliable determination of β. Because the Néel transition is very broad in temperature for samples with high Ce concentrations, β was fixed to 0.27 in order to extract $T_{\rm N}$. The intensity in Fig. 3.1 obtained at the (0.5 0.5 1) reflection for $x \approx 0.13$ NCCO was fit to Eq. 3.2 convolved with a Gaussian distribution of $T_{\rm N}$.

The Néel temperature was also obtained from the ZF muon precession frequency ω. This frequency is a probe of the strength of the internal magnetic field at the muon stoppage site, and hence of the magnitude of local magnetic moment. For each sample, it was measured at a number of temperatures and fit to the critical function (Eq. 3.1) convolved with a Gaussian distribution of $T_{\rm N}$. Representative μSR data and fits are shown in Fig. 3.2. The high-temperature tails (for $x = 0.118$ and 0.128) were ignored in the fits, but the temperature ranges where the tails exist were added into the error

estimation.

The doping dependence of T_N for NCCO is summarized in Fig. 3.3. The data are for NCCO subjected to standard reduction conditions and without oxygen reduction (as-grown) [55, 139, 156]. The doping dependence of T_N for as-grown samples with Ce concentration $x + \Delta x$ overlaps with that for reduced samples with Ce concentration x, where $\Delta x = -0.03$ [44, 139]. T_N obtained from the ZF muon procession frequency coincides with the neutron diffraction results at $x < 0.145$, but becomes negligible at higher Ce concentrations. This indicates that the magnetic order at $x > 0.145$ appears to be static on the timescale of neutron scattering (approximate 10^{-12} s), but is in fact dynamic on the timescale of μSR (approximate 10^{-6} s). In other words, genuine long-range antiferromagnetic order in NCCO subjected to the standard oxygen reduction does not extend beyond $x = 0.145$, consistent with the behavior of the instantaneous correlation length [55].

3.2.2 Staggered magnetization

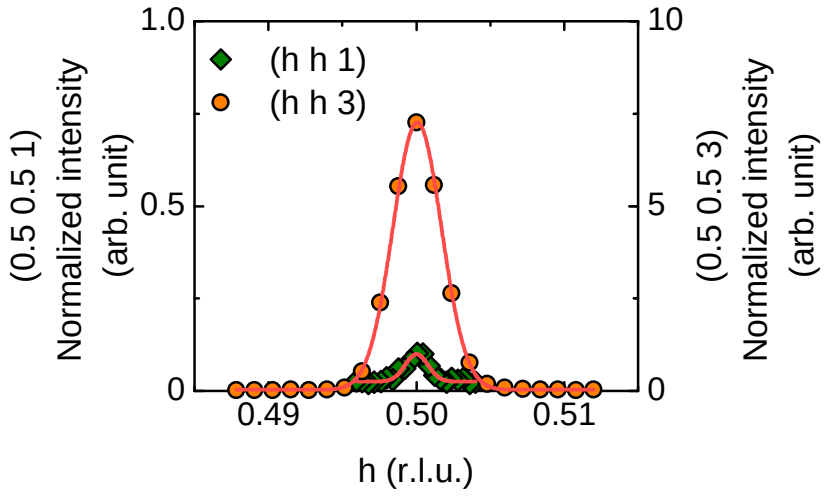

Figure 3.4: Quasi-elastic magnetic Bragg scattering for NCCO with $x = 0.118$ at $T = 6$ K. The neutron scattering data were fit to Gaussian functions (red solid lines). The difference in the full-width at half-maximum is due to a difference in the instrument resolution at the two reflections.

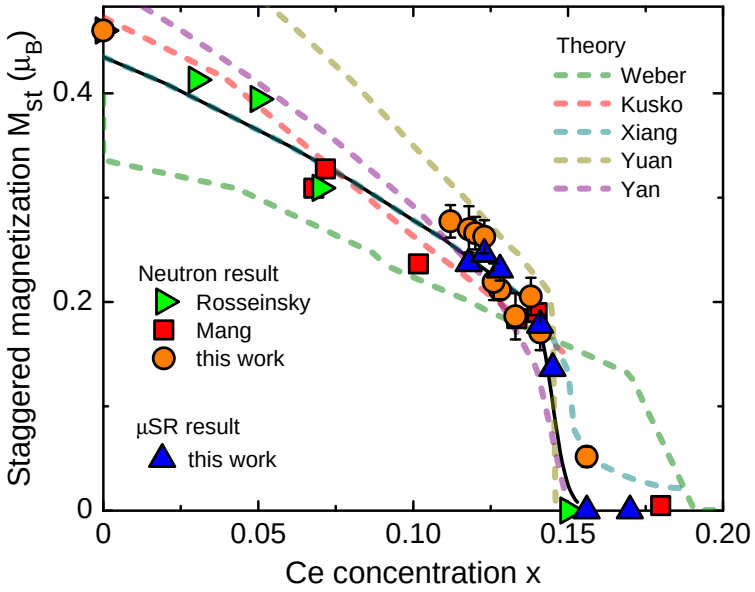

Figure 3.5: Doping dependence of staggered magnetization and local magnetic moment of NCCO. The former was normalized to the values obtained for the parent compound $Nd_2CuO_{4+\delta}$. The ZF muon precession frequency ω at $T = 40$ K, which is below T_N in all samples found to exhibit Néel order, but still much higher than the ordering temperature of the Nd^{3+} moments, was normalized to the neutron data at $x \approx 0.12$. Black solid line is a guide to the eye. Dashed lines show theoretical predictions as a function of Ce concentration [71, 72, 158–161]. Neutron data also taken from Mang *et al.* [139] and Rosseinsky *et al.* [162].

The staggered magnetization, the order parameter of an antiferromagnet, can be expressed as an expectation value per antiferromagnetic unit cell (in units in which the Bohr magneton $\mu_B \equiv 1$)

$$M_{\rm st} = \sum_i (-1)^i s_i = 2 s_i, \tag{3.3}$$

where i indexes the spin sites, and s_i indicates the spin on the $i^{\rm th}$ site. As noted, the neutron intensity at an antiferromagnetic Bragg position is proportional to the square of the staggered magnetization, whereas the ZF muon precession frequency probes the magnitude of the local magnetic field (which approximately proportional to the staggered magnetization, considering a magnetic field produced by a magnetic dipole moment).

Because the electron-doped cuprate materials contain magnetic rare earth elements

such as Nd^{3+}, magnetization at low temperatures includes contributions from both Cu and rare earth elements (which typically order below $T = 30$ K). In order to disentangle the two contributions, neutron diffraction intensities were measured at two Bragg peak positions, (0.5 0.5 1) and (0.5 0.5 3). The total neutron intensity is given by [163, 164]

$$I(0.5\ 0.5\ 1) \propto |S_{\mathrm{Cu}} f_{\mathrm{Cu}} - 1.2 S_{\mathrm{Nd}} f_{\mathrm{Cu}}|^2, \tag{3.4}$$

$$I(0.5\ 0.5\ 3) \propto |S_{\mathrm{Cu}} f_{\mathrm{Cu}} + 1.9 S_{\mathrm{Nd}} f_{\mathrm{Cu}}|^2, \tag{3.5}$$

where S_{Cu} and S_{Nd} denote the Cu and Nd structure factors, respectively, and f_{Cu} and f_{Nd} denote Cu and Nd form factors, respectively.

As shown in Fig. 3.4, the neutron intensities at the two Bragg positions differ from each other. The Cu magnetic moment can be obtained by decomposing the total diffraction intensities. Because the contributions from the Cu and Nd moments have different temperature dependences, a compensation temperature T_{comp}, at which $I(0.5\ 0.5\ 1) \approx 0$ can be defined. In practice, due to the inevitable background, T_{comp} was defined as the temperature at which $I(0.5\ 0.5\ 1)$ reaches its minimum value [44]. At $T = T_{\mathrm{comp}}$, $I(0.5\ 0.5\ 3) \propto S_{\mathrm{Cu}}^2 f_{\mathrm{Cu}}^2$. $T_{\mathrm{comp}} \approx 6$ K was found for NCCO, regardless of Ce concentration.

The normalized staggered magnetization and local magnetic moment as a function of Ce concentration are summarized in Fig. 3.5. In order to avoid contamination from Nd ordered moments, the ZF muon precession frequency at $T = 40$ K was used to extract the local Cu magnetic moment. The μSR data were normalized to the neutron data at $x \approx 0.12$, and they overlap with the neutron data up to about $x = 0.145$ (both quantities decrease mildly as the Ce concentration increases). A sudden drop of both quantities was observed at $x \approx 0.145$, above which a small difference was observed in the doping dependence.

Figure 3.5 also includes the results of theoretical calculations. All of these calculations have some difficulty in capturing the doping dependence of the magnetization over the whole doping range. The work of Kusko *et al.* [158], which is based on the one-band Hubbard model (t-U model), does not explain the assumed doping dependence of the onsite interaction U. The work of Yuan *et al.* [159] is based the t-J model, with J being too small to account for the band gap at small Ce concentration. Yan *et al.*

[160] extend the fluctuation-exchange approach to the Hubbard model and consider the disorder effect of dopants. The mean-field calculation by Xiang *et al.* [161] based on the *t*-*U*-*J* model exaggerates the magnetization at high Ce concentrations. The work by Weber *et al.* [72], which assumes the parent compound to be a Slater insulator, does not explain the sudden drop of magnetization at $x \approx 0.145$. The sudden drop of magnetization may be understood upon considering the underlying first-order phase transition found in this Thesis work.

3.2.3 Instantaneous spin-spin correlation length

The instantaneous spin-spin correlation length ξ is the characteristic length scale over which unpaired electron spins (giving rise to the Cu magnetic moment in the case of the cuprates) are correlated at an instant in time. This observable was obtained with the energy-integrating (two-axis) neutron scattering technique, for which the energy integration (at fixed two-dimensional momentum transfer $q_{2\mathrm{D}}$) was achieved by allowing the final neutron energy to vary [165] (see Chapter 2).

Due to the quasi-two-dimensional nature of the cuprates, $S(Q,\omega)$ is effectively independent of L ($\vec{Q} = (H\ K\ L)$ r.l.u.) and can be written in the terms of the two-dimensional reduced wave vector $\vec{q}_{2\mathrm{D}}$ as $S(q_{2\mathrm{D}},\omega)$. Because of the isotropic nature of the two-dimensional spin correlations, the dynamic structure factor only depends on the magnitude $q_{2\mathrm{D}} \equiv |\vec{q}_{2\mathrm{D}}|$. Upon integration over energy, this becomes instantaneous structure factor $S(q_{2\mathrm{D}})$. $S(q_{2\mathrm{D}})$ for a two-dimensional quantum Heisenberg antiferromagnet is given as [166]

$$S(q_{2\mathrm{D}}) = S(0) f(q_{2\mathrm{D}}\xi), \tag{3.6}$$

$$f(q_{2\mathrm{D}}\xi) = \frac{1 + 0.5 B_f \ln(1 + x^2)}{1 + x^2}, \tag{3.7}$$

where B_f is a constant. Because the signal to noise ratio of the neutron scattering measurement does not allow a lineshape analysis, and the proper functional form for the electron-doped system is unknown, $S(q_{2\mathrm{D}})$ was instead fit to a Lorentzian ($B_f = 0$) convolved with instrument resolution (see Chapter 2).

Representative two-axis data for NCCO with $x = 0.118$ are shown in Fig. 3.6. At 160 K ($T_{\mathrm{N}} \approx 150$ K), the antiferromagnetic correlation length is so large that the full-width

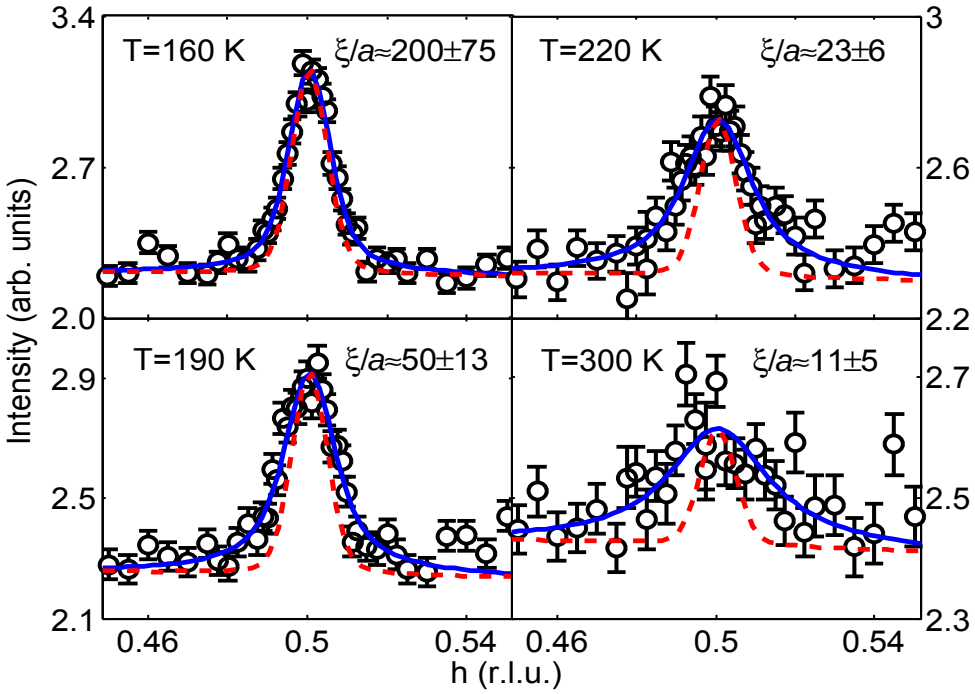

Figure 3.6: Representative two-axis neutron scattering data for $x = 0.118$ NCCO from which the instantaneous structure factor $S(q_{2D})$ and correlation length ξ are extracted. Raw data (scans along $\vec{q}_{2D} = (h\ h)$), fits, and instrument resolution are indicated as black circles, blue solid lines, and red dashed lines, respectively. The instantaneous correlation length ξ is found to increase from about 10 to 200 lattice constants between room temperature and 160 K ($T_N \approx 150$ K). Neutron initial energy $E_i = 14.7$ meV. The collimations were $48'$-$40'$-sample-$20'$. Measurements taken near $L = 0.5$.

at half-maximum of the peak centered at $q_{2D} = (0.5\ 0.5)$ approaches the instrument resolution, and thus the uncertainty of ξ is large. At high temperatures, q_{2D} broadens and the uncertainty due to the non-zero instrument resolution are lower, whereas the uncertainty due to the smaller signal-to-noise ratio is larger than at lower temperatures. In both cases, the estimation of the antiferromagnetic correlation length sensitively depends on determination of the background intensity, and thus it was crucial to obtain sufficient counting statistics.

The temperature dependence of ξ for NCCO at various Ce concentrations is summarized in Fig. 3.7. The correlation length for the x = 0.118 sample has an exponential

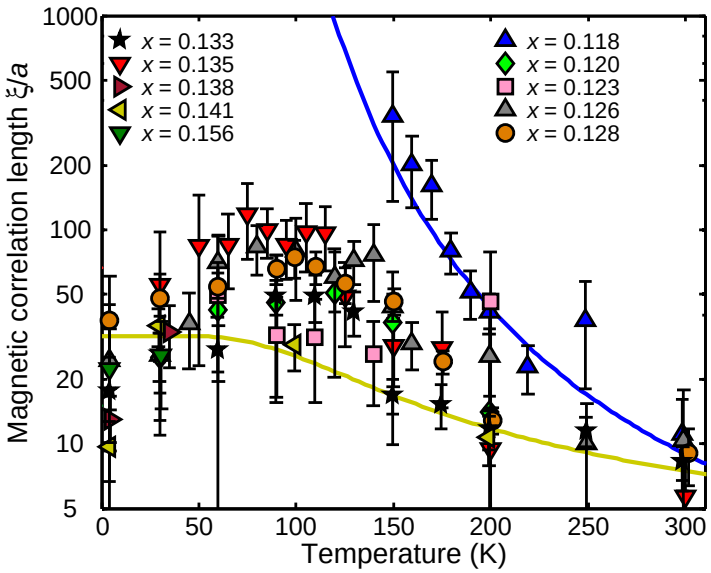

Figure 3.7: Instantaneous spin-spin correlation length for NCCO samples with various Ce concentrations. Magenta and yellow lines show fit to Eq. 3.8 and Eq. 3.10, respectively. This figure includes results for $x = 0.118$, 0.123, 0.126, 0.133, 0.141, and 0.156 from [40].

temperature dependence. The large extrapolated correlation length ($\xi/a \approx 400$) at the sample's Néel temperature ($T_N \approx 150$ K) is consistent with long-range order. However, the correlation length for $x \approx 0.141$ (and higher Ce concentrations) behaves qualitatively differently. It does not diverge and remains finite down to the lowest measured temperatures, despite the fact that quasi-elastic neutron scattering data would seem to suggest Néel order below $T_N \approx 90$ K (see Fig. 3.3). For samples with intermediate Ce concentrations, ξ reaches its maximum value at approximately T_N.

It is interesting to consider the neutron data for NCCO in the context of the quantum nonlinear σ model (QNLσM) [167–169]. The QNLσM is the simplest continuum model which correctly captures the long-wavelength physics contained in classical Heisenberg lattice models [40]. In order to derive the QNLσM model, a lattice Heisenberg model in the $S \to \infty$ limit was used [170]. It is difficult to determine the model parameters theoretically for systems with small S, i.e., where quantum fluctuations need to be considered. The QNLσM features three regimes as a result of a quantum phase transition:

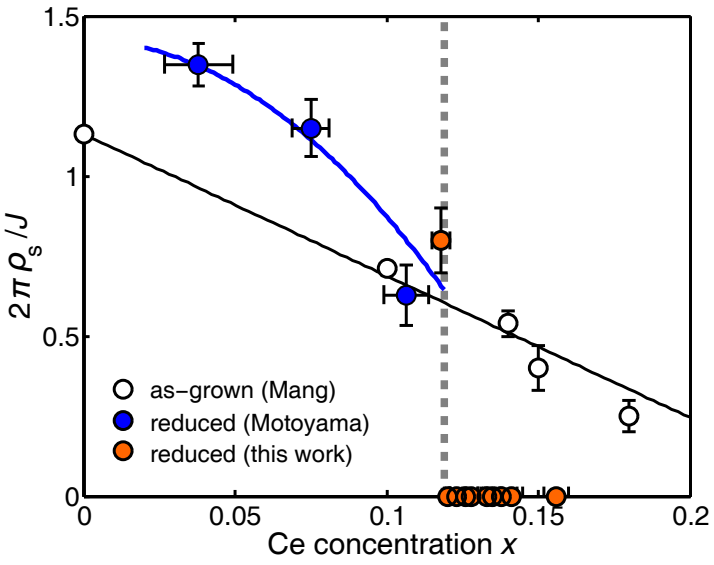

Figure 3.8: Spin stiffness, plotted as $2\pi\rho_s/J$ for as-grown (open circles) [139] and oxygen reduced (orange filled circles) [40, 55] NCCO. The value $J = 125\,\text{meV}$ is the antiferromagnetic superexchange energy estimated for the parent compound Nd_2CuO_4 [44]. The dotted line denotes a linear fit to the as-grown data, whereas the solid blue line is a guide to the eye for the reduced samples. The vertical dashed line indicates $x = 0.12$. Figure adapted and modified from [40].

(1) the renormalized classical regime, where long-range order exists at $T = 0$ K; (2) the quantum critical regime; (3) the quantum disordered regime, where no long-range order exists at $T = 0$ K. At zero temperature, the three regimes are separated by a quantum critical point [167–169]. In the renormalized classical regime, as $T \to 0$, the instantaneous spin-spin correlation length is given as [40, 55]

$$\xi(T) = C_\xi a e^{2\pi\rho_s/k_B T}, \tag{3.8}$$

where a is the lattice constant. C_ξ is a constant and ρ_s is the spin stiffness, which denotes the energy cost of applying a twist of the spins, at $T = 0$. In the quantum critical regime, the spin-spin correlations falls off as an inverse power of temperature ($\xi(T) \sim T^{-1}$). With parameters C_ξ and ρ_s determined from the data phenomenologically, Eq. 3.8 describes correlation length for NCCO samples at Ce concentrations below $x = 0.12$

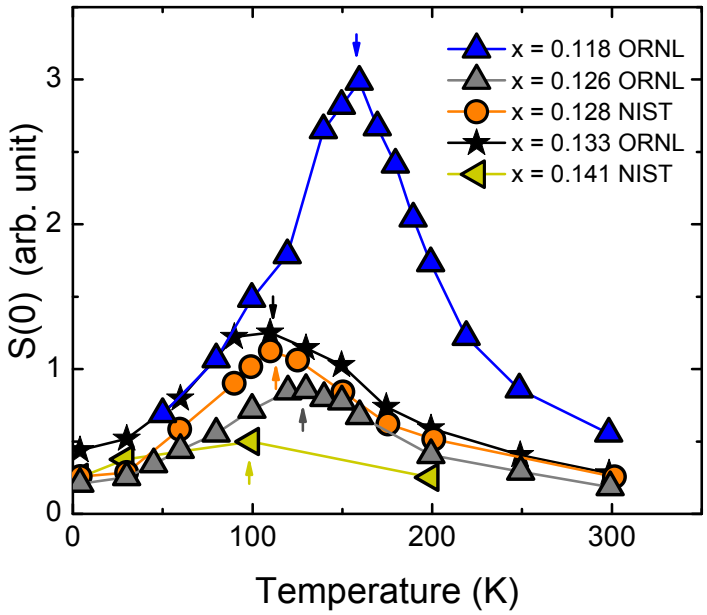

Figure 3.9: Representative data for the instantaneous structure factor amplitude $S(0)$ for NCCO. The temperature at which the amplitude reaches its maximum corresponds to T_N as measured by quasi-elastic neutron scattering (arrows). NIST: National Institute of Standard technology. ORNL: Oak Ridge National Laboratory. This figure includes data from [40].

very well.

Hasenfratz and Niedermayer [171] calculated the prefactor C_ξ and obtained the first order correction in temperature of the correlation length in the renormalized classical regime as

$$\xi(T) = \frac{e}{8}\frac{\hbar c_{\rm s}}{2\pi\rho_{\rm s}}\left[1 - \frac{T}{4\pi\rho_{\rm s}}\right] e^{2\pi\rho_{\rm s}/k_{\rm B}T}, \tag{3.9}$$

where c_s is the spin-wave velocity. In this Thesis work, because $T \ll 4\pi\rho_{\rm s}$, Eq. 3.8 was used to estimate the magnetic correlation length for NCCO samples at low and intermediate Ce concentrations.

Figure 3.8 shows the doping dependence of the spin stiffness and emphasizes the discontinuous nature of the correlation length at $x \approx 0.12$ for NCCO samples subjected to standard reduction condition. For $x > 0.12$, where genuine long-range order no longer exists, the spin stiffness is zero. For $x < 0.12$, ρ_s decreases gradually with increasing Ce

concentration and remains a large fraction of J. It is not clear why the spin stiffness at lower Ce concentrations for the oxygen-reduced samples seems to be larger than that of the as-grown system.

Because the instantaneous structure factor $S(q_{2D})$ with $q_{2D} = 0$ was measured at $L \approx 0.5$, away from the magnetic Bragg position (0.5 0.5 0), the temperature dependence of the amplitude $S(0)$ contains useful information (see Eq. 2.51): for $T > T_N$, $S(0)$ increases upon cooling, due to the increase of antiferromagnetic correlations; for $T < T_N$, $S(0)$ decreases upon cooling, due to a shift of magnetic scattering from the two-dimensional scattering rod to the Bragg positions. The temperature dependence of $S(0)$ was obtained by simply fitting to Gaussian functions. Representative data for $S(0)$ are shown in Fig. 3.9. The temperature at which $S(0)$ reaches its maximum corresponds to T_N as measured by quasi-elastic neutron scattering. $S(0)$ was normalized by the sample mass and across the neutron spectrometers in [40] using $x = 0.133$ data at $T = 30$ K. However, further analysis shows that $S(0)$ for $x = 0.133$ at $T = 30$ K is accidentally much smaller than for other samples at lower and higher Ce concentrations measured at National Institute of Standard Technology (NIST). This issue caused an over-estimation of instantaneous structural factor amplitude for samples measured at NIST in [40]. In Fig. 3.9, $S(0)$ is shown without normalization.

After our group published $\xi(x, T)$ results for reduced NCCO samples with $x = 0.038$, 0.075, 0.106, 0.134, 0.145, 0.154, 0.166, 0.181 [55], we found that a surface-polishing treatment can further improve the samples chemical homogeneity. Our measurements performed at intermediate doping concentrations ($x = 0.134$, 0.145, 0.154) were largely limited to temperatures comparable to or higher than the apparent Néel temperatures (Fig. 3 of [55]). Samples with $x < 0.12$ were measured down to $T = 8$ K. These results left open the possibility of a quantum critical point around $x = 0.134$ (Fig. 1.7). The newer results analyzed in this Thesis work were obtained for samples with improved chemical homogeneity and they extend to temperatures much lower than the apparent Néel temperature. The new results show that the correlation length remains finite at temperatures below the apparent Néel temperature for samples at intermediate Ce concentrations ($x = 0.128$ and $x = 0.133$ as in Fig. 3.7).

The exponentially diverging correlation length for the $x = 0.118$ sample is indicative of a two-dimensional antiferromagnetic system with long-range order in the ground

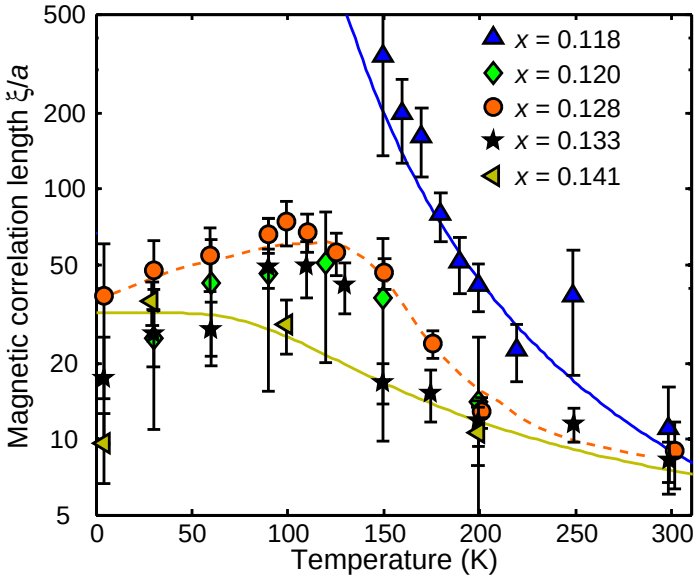

Figure 3.10: Instantaneous spin-spin correlation length (data are the same as in Fig. 3.7) and simulation. The data for NCCO with $x = 0.118$ and $x = 0.141$ were fit to Eq. 3.8 and Eq. 3.10, respectively. The data for $x = 0.128$ were simulated with Eq. 3.11.

state (renormalized classical regime of the QNLσM (Eq. 3.8), whereas ξ for the $x = 0.141$ sample is qualitatively different, consistent with quantum disordered behavior. A heuristic form to describe a correlation length that has a finite value at $T = 0$ K (e.g., the $x = 0.141$ data in Fig. 3.10) was proposed in [111, 140, 172]:

$$\frac{1}{\xi(T)} = \frac{1}{\xi_0} + \frac{1}{\xi_T(T)}\,, \tag{3.10}$$

where $\xi_0 = \xi(T = 0)$, and ξ_T denotes the high temperature dependence, as in Eq. 3.8 or Eq. 3.9. Alternatively, $\xi_T(T)$ could be a simple power-law dependence.

The temperature dependence of the spin-spin correlation length for samples with intermediate doping concentrations can not be described with Eq. 3.8 and Eq. 3.10, nor is it consistent with simple power-law behavior that would be expected in the case of a second-order quantum phase transition. Instead, the behavior of $\xi(x, T)$ is indicative of phase separation. In particular, the correlation length might be limited by non-magnetic regions surrounding magnetic regions. Assuming such microscopic phase separation,

simulations of the correlation length for samples with $0.12 < x < 0.14$ were performed. Because neutron scattering measurements constitute an average over the whole sample, in principle two variables are crucial: (1) the volume fractions of the two types of regions and (2) the size distribution of the regions. Since we have no information regarding the latter, our simple model ignores the possible size distribution.

For a sample with magnetic and non-magnetic regions, we estimate the neutron intensity as

$$I_{\rm total} = V_M I_{\rm mag} + (1 - V_M) I_{\rm non} \,, \tag{3.11}$$

where V_M and $1-V_M$ are the volume fractions of the magnetic and non-magnetic regions, respectively. $I_{\rm mag}$ ($I_{\rm non}$) denotes the intensity due to magnetic (non-magnetic) regions, and we simple use $S(q_{\rm 2D})$ for samples with $x = 0.118$ ($x = 0.141$). The momentum dependence of $I_{\rm total}$ (proportional to $S(q_{\rm 2D})_{\rm total}$) was analyzed with Eq. 2.51 to arrive at a simple estimation of $\xi(x,T)$ and $S(0)_{\rm total}$ for $0.12 < x < 0.14$, as shown in Fig. 3.11.

If the sizes of magnetic and non-magnetic regions are much larger than the correlation length of the sample with $x = 0.118$, $\xi_{\rm total}$ could be directly estimated from the momentum width of $I_{\rm total}$. However, in this case, we found that the resultant volume fractions are very different from our experimental observations [40] (see Fig. 3.12). If the magnetic regions are smaller than the correlation length for the sample with $x = 0.118$, the measured correlation length for samples with phase separation will be affected by the size of the magnetic regions: (1) the measured correlation length is limited to be smaller than the size of the magnetic regions, or (2) the measured correlation length is reduced compared to that in the sample with $x = 0.118$, even though it can be larger than the size of the magnetic regions. In both cases, Eq. 3.11 needs to be modified. In order to obtain reasonable volume fractions consistent with experiments (Fig. 3.12), the correlation length of magnetic regions had to be set to about 150 lattice constants. Physically, the need to set this upper limit is related to the limitation or reduction of correlation length due to phase separation. It is the characteristic length scale of the magnetic regions that sets $\xi_{\rm total}$.

The temperature dependence of correlation length at low temperature, below the temperature at which $\xi_{\rm total}$ takes its maximum value, was found to be mainly determined by the size of non-magnetic regions. Setting the upper limit of the correlation length for magnetic regions to be 150 lattice constant (below $T_{\rm N}$) and the size of non-magnetic

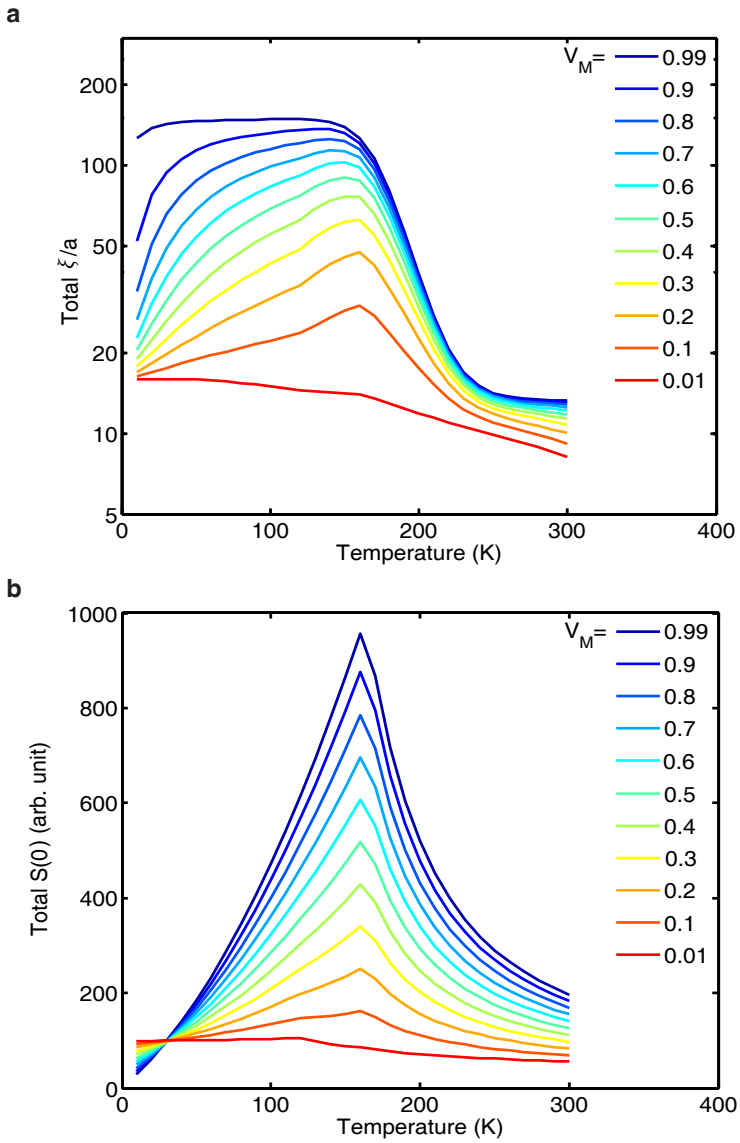

Figure 3.11: Simulation of (a) the correlation length ξ_{total} and (b) the $S(0)_{\text{total}}$ for samples with indicated magnetic volume fraction V_M. The correlation length of magnetic (non-magnetic) regions was set to 150 (15) lattice constants at temperatures below the apparent Néel temperature (see Fig. 3.3).

regions to be 15 lattice constants (consistent with the experimental results for $x = 0.141$), the correlation length (Fig. 3.7 and Fig. 3.10) and volume fractions (Fig. 3.12) for samples with intermediate doping concentrations ($0.12 < x < 0.14$) can be reproduced (Fig. 3.11).

3.2.4 Magnetic and superconducting volume fractions

Magnetic and superconducting volume fractions as function of Ce concentration were studied using μSR of bulk samples and SQUID magnetization of powder samples. The μSR time spectra for NCCO samples at intermediate doping contain contributions from magnetic and non-magnetic regions and can be decomposed into two components (Chapter 2). The magnetic volume fraction can be calculated based on the ratio of the two components

$$V_{\mathrm{M}} = A_{\mathrm{mag}}/(A_{\mathrm{mag}} + A_{\mathrm{non}}), \tag{3.12}$$

where A_{mag} and A_{non} are the prefactors of the magnetic and non-magnetic contributions, respectively.

As shown in Fig. 3.12, a considerable decrease in V_{M} occurs at $x \approx 0.145$, which coincides with a drop in the staggered magnetization, indicative of microscopic phase separation. The superconducting volume fraction V_{SC} was measured by SQUID magnetization. Because of the inevitable chemical inhomogeneity of crystalline samples (Chapter 2), it is possible for a sample to have superconducting regions only near its surface and to be non-superconducting in its interior. These surface superconducting regions would expel magnetic flux (Meissner-Ochsenfeld effect) and result in a diamagnetic signal which resembles that of a bulk superconducting phase. In order to avoid this problem, the NCCO samples were ground into powder before the SQUID magnetization measurements. As shown in Fig. 3.13, although diamagnetic signal was observed in samples with $x = 0.133$, 0.141, and 0.145, the superconducting volume fractions are well below 1. A comparison between V_{M} and V_{SC} is made in Fig. 3.14. The observed anti-correlation between the two volume fractions suggests that the static antiferromagnetic order competes with superconductivity (also see [173, 174]), indicating a possible first-order phase transition.

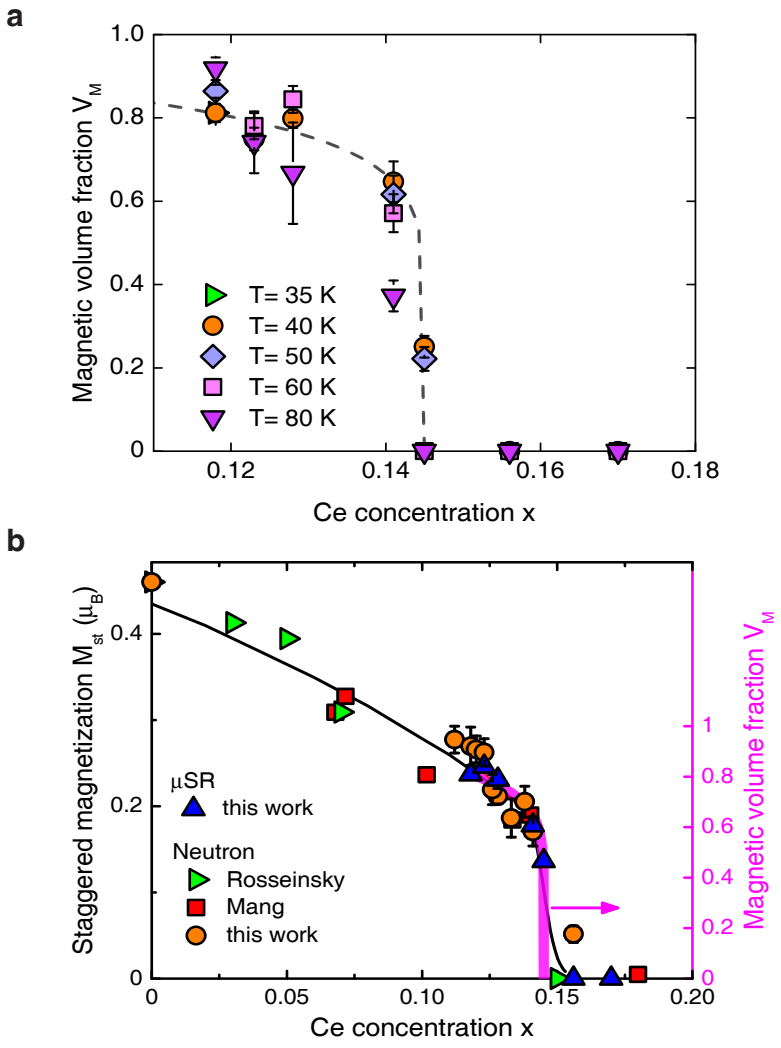

Figure 3.12: (a) Volume fraction (V_{M}) of the antiferromagnetic ordered phase at various temperatures and Ce concentrations obtained from μSR. V_{M} is approximately independent of temperature at $T \ll T_{\mathrm{N}}$. At very low temperatures ($T < 30$ K), V_{M} can not be readily extracted due to the magnetic order that develops on the Nd^{3+} ions. The dashed line is a guide to the eye for V_{M} at $T = 40$ K. (b) Magnetic volume fraction (purple line corresponds to the dashed line in panel a) and staggered magnetization (same data as in Fig. 3.5) as function of Ce concentration. The two quantities track each other.

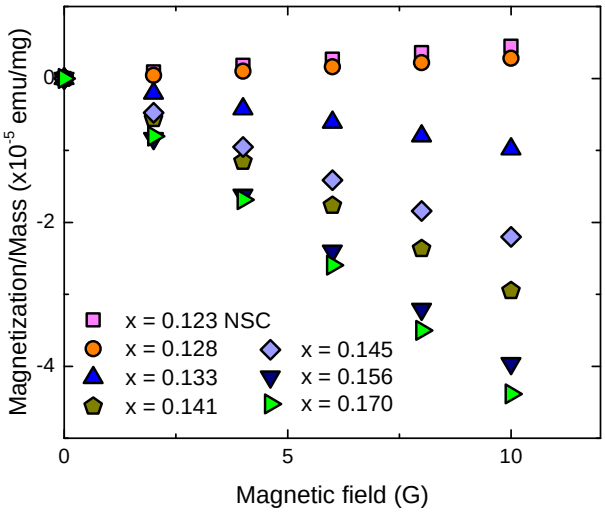

Figure 3.13: SQUID magnetometry results for NCCO powder samples at $T = 2$ K. The samples were obtained by grinding up small pieces of crystal cut from large crystals measured by neutron, μSR, or charge transport techniques. For the sample with $x = 0.123$ (nonsuperconducting: NSC) and $x = 0.128$, the magnetization is positive, indicating zero or negligible superconducting volume fractions. The results at $x = 0.156$ and 0.170 are nearly identical, indicating that $V_{\rm SC} \approx 1$ at $x \approx 0.170$.

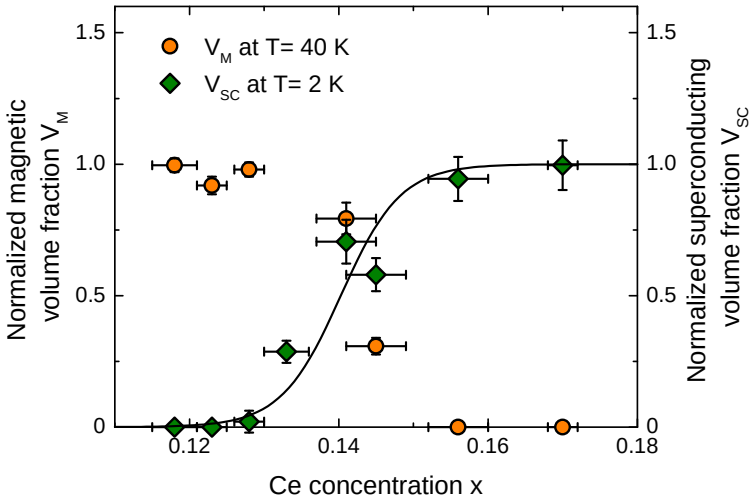

Figure 3.14: Comparison between magnetic ($V_{\rm M}$) and superconducting ($V_{\rm SC}$) volume fractions. The $V_{\rm M}$ data at $T = 40$ K are reproduced from Fig. 3.12. $V_{\rm SC}$ was estimated based on magnetization data at $T = 2$ K, as shown in Fig. 3.13. Values of $V_{\rm SC} = 0$ for non-superconducting samples and $V_{\rm SC} = 1$ for $x = 0.170$ were assumed.

3.2.5 μSR relaxation rates

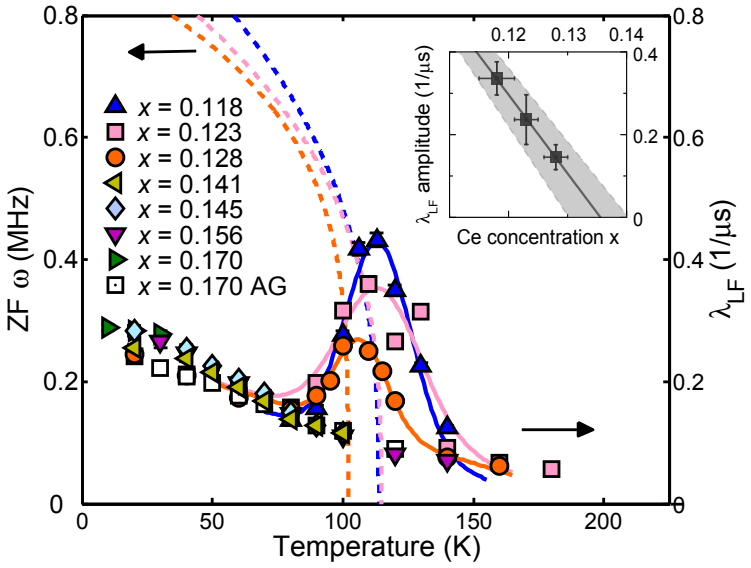

Figure 3.15: Spin-lattice relaxation rate λ_{LF} (symbols) and the ZF muon precession frequency ω (dashed lines; doping levels and colors correspond to those of symbols, reproduced from Fig. 3.2). For $x < 0.13$, the temperature at which the spin-lattice relaxation rate reaches its maximum value coincides with the temperature at which the ZF muon precession frequency goes to zero. This signifies a thermal second-order phase transition. The amplitude of the peak (solid lines are fits to Gaussian functions) in the spin-lattice relaxation rate extrapolates to zero at $x = 0.135 \pm 0.05$ (inset).

Spin-lattice relaxation refers to the evolution of the longitudinal projection of spin magnetization towards its thermodynamic equilibrium value (spin depolarization). This process involves an energy transfer from spins to their surroundings (lattice), but does not require a decoupling of the spins (changes in the spin-spin correlation). On the other hand, spin-spin relaxation denotes the process by which the transverse projection of spin magnetization reaches its thermodynamic equilibrium value and does not explicitly involve any energy transfer. The ZF muon relaxation λ_1 of the magnetic contribution measures the magnetic-field distribution in the sample.

The spin-lattice relaxation can be probed by the longitudinal field (LF) μSR relaxation rate λ_{LF}. With the initial muon spin along the direction of a large external field,

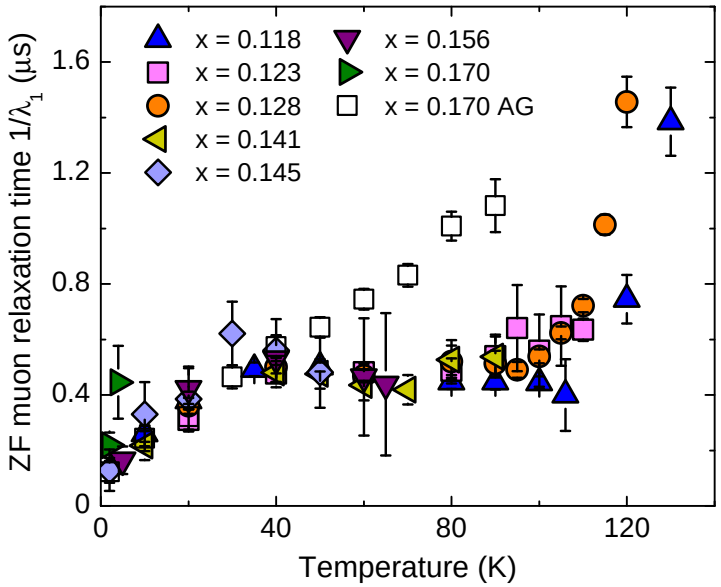

Figure 3.16: ZF muon relaxation time $1/\lambda_1$. The data for samples subjected to standard reduction collapse to a single curve, with a constant universal value of about 0.4 μs between 40 K and T_N.

the intrinsic magnetic field in a material serves as a small perturbation. For NCCO, λ_{LF} is summarized and compared to the zero field (ZF) μSR procession frequency in Fig. 3.15. The temperatures at which the λ_{LF} reaches its maximum value corresponds to a slow-down of the spin fluctuations to the timescale of the probe (about 10^{-6}). The temperatures at which the ZF μSR frequency goes to zero indicates the magnetic ordering temperature. The observed coincidence between the two temperatures signifies a thermal second-order phase transition. As shown in Fig. 3.15, the two temperatures coincide for reduced samples with $x \leqslant 0.128$. No visible feature was observed in λ_{LF} for reduced samples with $x > 0.128$ and for the $x = 0.170$ as-grown sample.

The temperature and doping dependences of the ZF muon relaxation time $(1/\lambda_1)$ is summarized in Fig. 3.16. For reduced samples, $1/\lambda_1$ is weakly doping independent, and we observed data collapse between 40 K and T_N to a universal value of about 0.4 μs. The deviation below $T = 40$ K can be attributed to the formation of Nd^{3+} correlations. For the as-grown (AG) sample with $x = 0.170$, $1/\lambda_1$ behaves very differently and is in rather

good agreement with previous data on an as-grown NCCO sample with $x = 0.155$ [152]. At low temperatures, $1/\lambda_1$ becomes much smaller than the μSR timescale, and thus may be less accurate. The difference between as-grown and reduced samples suggests that the oxygen reduction process induces a substantial change in the magnetic field distribution.

3.2.6 Spin fluctuation timescales

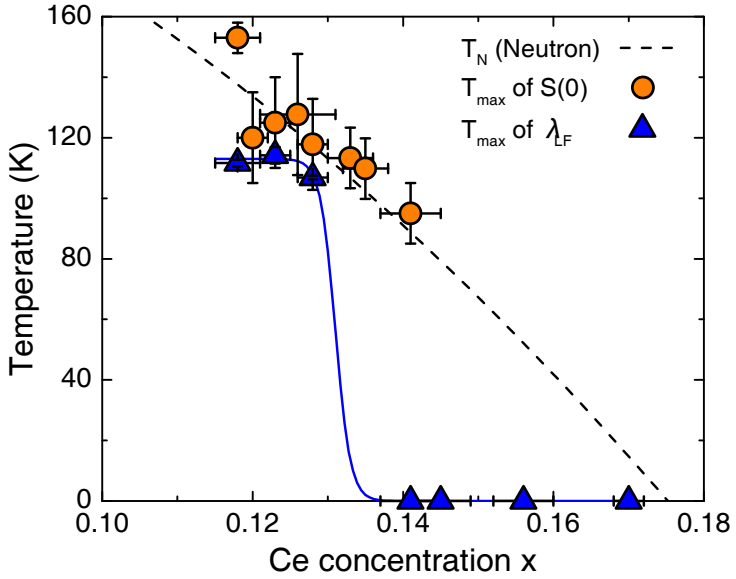

Figure 3.17: Characteristic temperatures for the spin-lattice relaxation rate (Fig. 3.15) and the instantaneous structure factor (Fig. 3.9). The temperatures at which the latter reaches its maximum value coincide with $T_{\rm N}$ (dotted line) measured by quasi-elastic neutron scattering [55]. Blue solid line is a guide to the eye. The area between the dashed and blue lines correspond to an approximate change in the characteristic spin fluctuation timescale between 10^{-12} s and 10^{-6} s.

Figure 3.17 shows the characteristic temperatures for the spin-lattice relaxation rate and the instantaneous structure factor amplitude. While the peak amplitude of $\lambda_{\rm LF}$ approaches zero just below $x = 0.14$ (Fig. 3.15), the temperature dependence of $S(0)$ continues to exhibit a local maximum at higher Ce concentrations. The temperatures at which $\lambda_{\rm LF}$ and $S(0)$ reach their maxima ($T_{\rm max}$) indicate where spin fluctuations slow

down to the μSR timescale (about 10^{-6} s) and the neutron scattering timescale (about 10^{-12} s), respectively. $T_{\max}$ of $S(0)$ closely traces $T_{\rm N}$ measured by nominally elastic neutron scattering experiments [139]. These de facto quasi-elastic neutron scattering measurements were limited by the energy resolution (about 1 meV) of the triple-axis instruments, and may include low-energy spin fluctuations. The area enclosed by the μSR and neutron scattering results for $0.145 < x < 0.175$ corresponds to a change in the spin fluctuation timescale between 10^{-12} s and 10^{-6} s, approximately. A similar change in the spin fluctuations timescale was observed for another electron-doped cuprate material, $La_{2-x}Ce_xCuO_{4+\delta}$ (LCCO), based on transport and μSR experiments [175, 176].

3.2.7 Revised phase diagram of NCCO

The temperature-doping phase diagram was established based on the magnetic properties described in the previous Sections. The instantaneous spin-spin correlation length of NCCO with standard oxygen reduction condition is shown as a smoothed contour plot in Fig. 3.18. This figure also includes previously published results [55]. Long-range antiferromagnetic order (LR-AF) terminates at $x \approx 0.12$. For $0.12 < x < 0.14$, ξ reaches its maximum value at an intermediate temperature that approximately matches the apparent Néel temperature (see Figs. 3.3, 3.7, 3.10) and remains finite at lower temperatures. For $x > 0.14$, ξ monotonically approaches a finite value upon cooling, as reported in [55] (with a possible subtle decrease below T_c). A zoomed-in version of the phase diagram (Fig. 3.19) was constructed based on the data for the magnetic and superconducting volume fractions and the staggered magnetization. Dramatic changes were observed in all three quantities at $x \approx 0.145$.

The magnetic phase diagram of reduced NCCO as a function of temperature and Ce concentration can be categorized into three regimes: (1) The LR-AF regime below approximately $x = 0.12$, where a well-defined, thermal second-order phase transition to an antiferromagnetically ordered state is observed and ξ diverges with an exponential temperature dependence. In this regime, coincidence between maximum μSR spin-lattice relaxation rate and the non-zero ZF muon precession frequency is observed at $T_{\rm N}$, and neutron scattering and μSR experiments give the same transition temperature. The staggered magnetization and magnetic volume fraction are large. This genuine

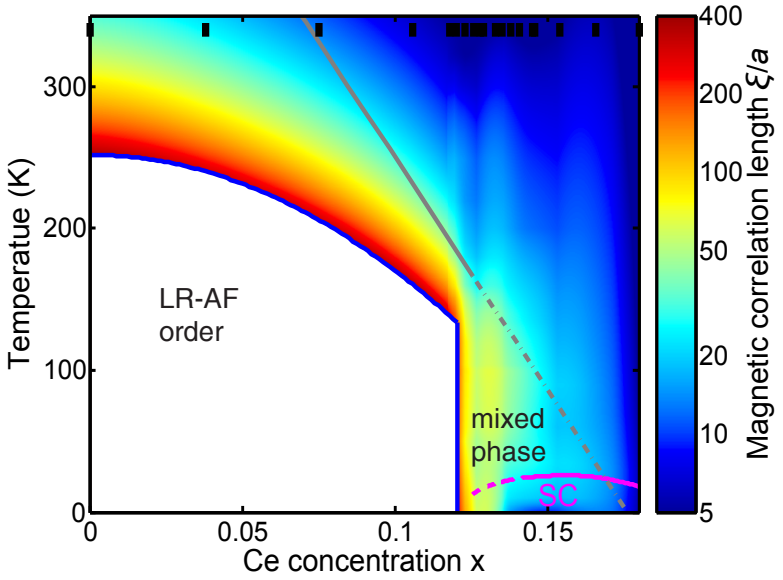

Figure 3.18: Contour plot of the instantaneous magnetic correlation length as a function of temperature and Ce concentration for NCCO subjected to standard oxygen reduction. The color scale is the result of an interpolation of data obtained at discrete Ce concentrations and temperatures. The Ce concentrations of the measured samples are indicated by black bars on top. The Néel phase with long-range antiferromagnetic order (LR-AF), the mixed phase, the superconducting phase (SC) and the pseudogap temperature (T*, grey solid and dashed lines) [53, 54] are indicated. The dashed and solid magenta lines for T_c indicate superconducting volume fractions below and above 50%, respectively (see Fig. 3.14). The Néel temperature determined from neutron scattering and μSR experiments corresponds to an extrapolated two-dimensional antiferromagnetic correlation length of about $\xi/a = 400$.

LR-AF order does not coexist with superconductivity. (2) The nonmagnetic regime at approximately $x > 0.14$, where bulk superconductivity is observed at low temperatures. In this regime, ξ is small and levels off below about 30 lattice constants. The staggered magnetization and magnetic volume fraction are essentially zero. No visible peak in the spin-lattice relaxation rate is observed, although an apparent Néel transition is seen in quasi-elastic neutron scattering measurements. The spin fluctuation timescale therefore lies between the neutron scattering and μSR probing timescales. (3) The mixed-phase regime at approximately $0.12 < x < 0.14$. In this regime, ξ remains finite at low temperature, and the peak in the spin-lattice relaxation rate gradually disappears. The

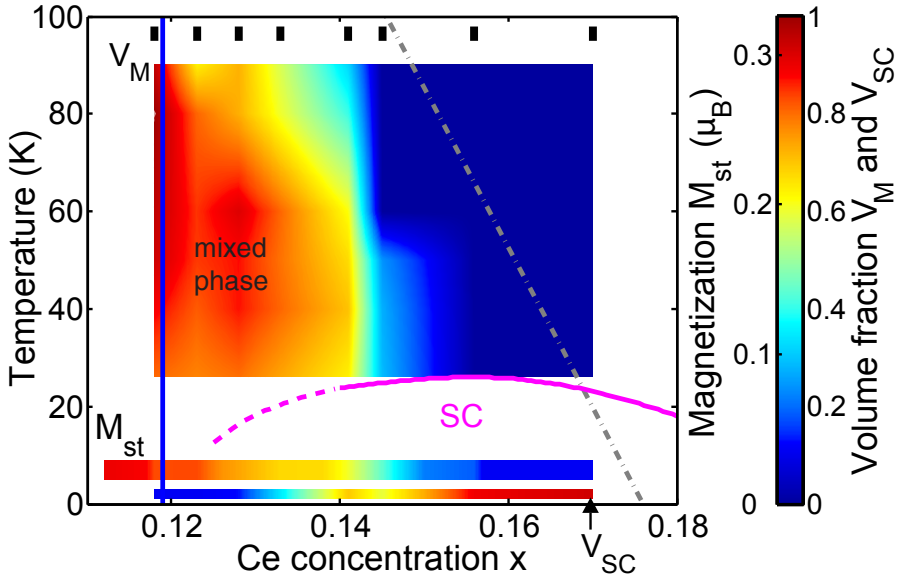

Figure 3.19: Contour plot of magnetic volume fraction, superconducting volume fraction, and staggered magnetization for NCCO subjected to standard oxygen reduction. The color scales are the results of an interpolation of data obtained at discrete Ce concentrations and temperatures. The Ce concentrations of the measured samples are indicated by black bars on top. The mixed-phase, superconducting (SC) phase and pseudogap temperature (T^*, gray dashed line) [53, 95, 177] are indicated. Blue vertical line indicates the boundary between the LR-AF order and the mixed phase. For $x < 0.14$, T_c is shown by a dashed rather than a solid magenta line, since $V_{\rm SC} < 50\%$. This figure is constructed from the staggered magnetization data in Fig. 3.5, magnetic volume fraction data in Fig. 3.12, and superconducting volume fraction data in Fig. 3.14.

staggered magnetization and magnetic volume fraction have small non-zero values. This regime can not be simply classified as a spin-glass state, because no evidence of frozen spins was observed by SQUID measurements down to 4 K.

Figure 3.20 shows the temperature-doping phase diagram for as-grown NCCO. No abrupt changes in ξ, $M_{\rm st}$ and $V_{\rm M}$ are observed below the Ce solubility limit ($x \approx 0.20$) [40, 139]. Because no data for ξ exist below $T_{\rm N}$ and the data for V_M are limited, strictly speaking it is not evident if the mixed-phase regime is absent in as-grown NCCO below the solubility limit. However, ξ is on the order of 50 lattice constant for the sample with $x = 0.18$ at $T \approx T_{\rm N} + 50$ K [139], and both M_{st} (about 0.1 μ_B) and $V_{\rm M}$ (about

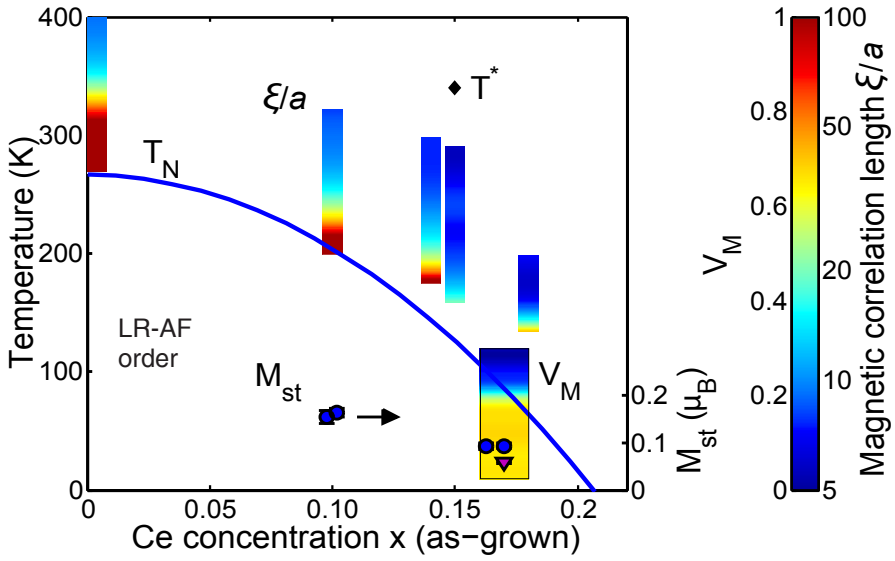

Figure 3.20: Magnetic correlation length, magnetic volume fraction, and staggered magnetization for as-grown NCCO. The color scale is the result of an interpolation of data obtained at discrete Ce concentrations and temperatures. The long-range antiferromagnetic phase (LR-AF) and pseudogap temperature (T*, gray diamond) [53, 95, 177] are indicated. Blue solid curve indicates $T_{\rm N}$ [139]. This figure is constructed with neutron data (x = 0, 0.10, 0.14, 0.15, 0. 166, 0.18) from [40, 139] and μSR data (x = 0.170) from this Thesis work.

0.6) are non-zero for the sample with $x = 0.170$. No discontinuity in the spin stiffness appears in as-grown samples up to the highest measured Ce concentration (see Fig. 3.8). Nevertheless, it is possible that there exists a mixed-phase regime , but that the minority phase is non-superconducting.

3.3 Discussion: multi-parameter phase diagram

Based on the properties described in the previous sections (Néel temperature ($T_{\rm N}$), instantaneous spin-spin correlation length (ξ), the staggered magnetization ($M_{\rm st}$), magnetic ($V_{\rm M}$) and superconducting ($V_{\rm SC}$) volume fractions, a schematic phase diagram for NCCO subjected to standard reduction is shown in Fig. 3.21. Our work indicates that the LR-AF order evolves to the bulk superconducting phase via a mixed phase.

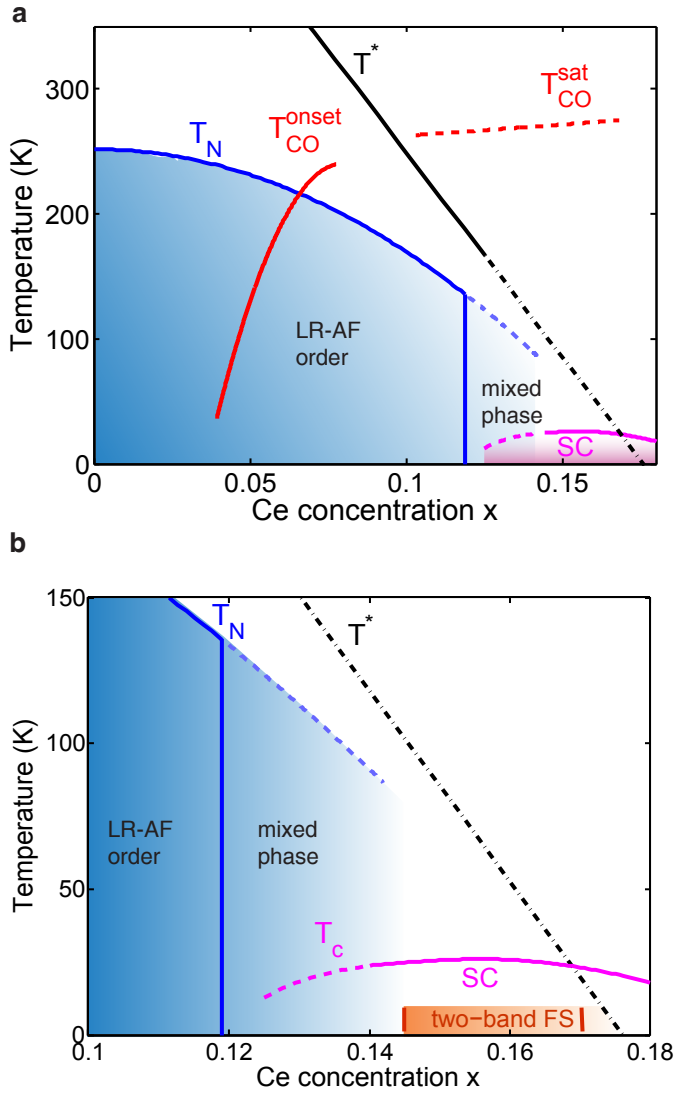

Figure 3.21: (a) Schematic phase diagram of NCCO subjected to standard oxygen reduction. (b) Zoomed-in version of (a). The phase with genuine antiferromagnetic long-range order (LR-AF), the mixed phase, the superconducting transition temperature (T_c), pseudogap temperature (T*) [53, 95], the characteristic temperatures of charge order ($T_{\rm CO}^{\rm onset}$ and $T_{\rm CO}^{\rm sat}$, red solid and dashed curves) [178, 179], and the doping range for which there exists evidence of a two-band Fermi surface are indicated.

This evolution resembles that of other doped antiferromagnets, such as the iron-based superconductors (La(O, F)FeAs, Sm(O, F)FeAs, Ce(O, F)FeAs, and (Ba, K)Fe_2As_2), the heavy-fermion superconductors ($CeRhIn_5$), as well as other doped Mott insulators ($ReNiO_3$, where RE indicates a rare-earth element, and V_2O_3) [52, 180]. At low and moderate Ce concentrations, the magnetic properties of NCCO are similar to those of the parent compound, and the instantaneous correlation length can be effectively described by a site-dilution model [139, 181]. Upon increasing the Ce concentration, ξ abruptly becomes short-ranged at $x \approx 0.12$, which is much smaller than the two-dimensional site percolation threshold ($x = 0.41$ [182]). The short-range spin correlations coexist with superconductivity [55, 183]. Weber, Haule, and Kotliar [71, 72] suggested that the parent compounds of the electron-doped cuprate may actually be Slater insulators and not Mott insulators, in which the charge localization is caused by AF correlations. How to understand the first-order transition to the metallic state in the Slater insulator picture is not entirely clear currently [71, 72]. In contrast, Lee and Kivelson [61, 184] argued that for antiferromagnetic Mott insulators, in which the antiferromagnetic order is a consequence of strong electron-electron correlations, the first-order phase transition from the Mott state to the metallic phase may occur with micro-phase separation. Vojta and colleagues [185, 186] and Sachdev [187, 188] argued that the coexistence of chemically disordered regions and magnetic clusters may cause a smeared quantum phase transition. Magnetic clusters may be locally ordered while the bulk system is in the disordered phase, and each cluster may order independently. Senthil and colleagues [189] proposed a "deconfined quantum critical point," which is associated with fractionalization of the order parameter only at the critical point, for the continuous quantum phase transition between antiferromagnetism and valence bond solids.

The rather abrupt change in the magnetic and superconducting volume fractions at $x \approx 0.145$ is closely related to the evolution of the Fermi-surface topology (see Chapter 4). Neutron and μSR measurements imply that for NCCO with $x > 0.145$ subjected to standard oxygen reduction, the magnetic volume fraction and local moment are essentially zero. The appearance of hole pockets at $x \approx 0.145$ [190] may thus be related to the appearance of dynamic antiferromagnetic correlations, and not to long-range antiferromagnetic order [190]. The presence of the two-band (electron and hole pockets) Fermi surface observed in the phase with dynamic, short-range spin correlations

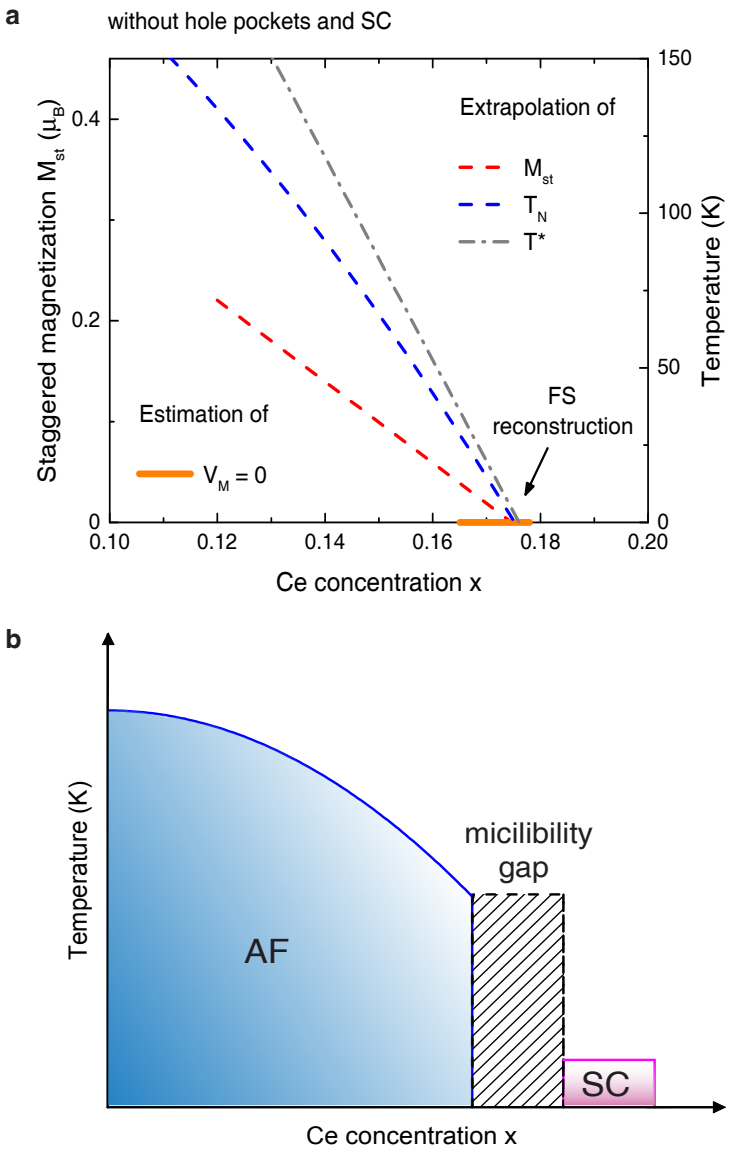

Figure 3.22: Illustrations of (a) an hypothetical phase diagram without hole Fermi pockets and (b) the actual underlying first-order phase transition that in the experimental systems is compromised by disorder effects. The staggered magnetization, Néel temperature, pseudogap temperature and magnetic volume fraction shown in (a) are extrapolated from those at low Ce concentrations ($x < 0.12$).

is not fully understood theoretically [191, 192]. Based on band structure calculations, small hole Fermi pockets appear when the antiferromagnetic backscattering amplitude becomes relatively small compared to the band parameters [193, 194] (see chapter 4). These holes, like those in hole-doped cuprate materials, mighty predominately reside at oxygen sites and rapidly frustrate the magnetic order.

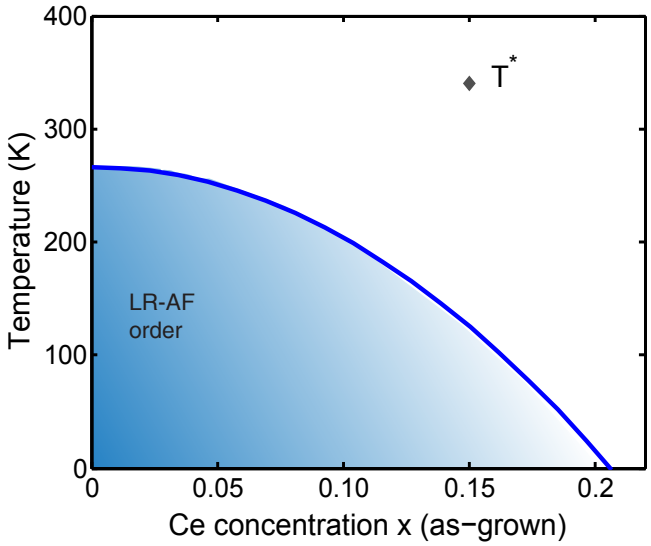

Figure 3.23: Schematic phase diagram for as-grown NCCO, for which no trace of superconductivity has been reported. The static long-range antiferromagnetic order (LR-AF) and pseudogap temperature (T*, grey diamond) [53, 95] are indicated.

Figure 3.22 illustrates a hypothetical magnetic phase diagram based on extrapolation of experimental results at low Ce concentration, which assumes that no small hole Fermi pockets appear upon doping. The magnetic volume fraction, Néel temperature, staggered magnetization and pseudogap temperature all extrapolate to zero around $x = 0.176$, where a Lifshitz transition (from reconstructed to unreconstructed Fermi surface) was seen [195]. In the presence of the hole Fermi pockets, the staggered magnetization and magnetic volume fraction are dramatically suppressed (Fig. 3.14), but the pseudogap temperature (gap in the optical spectroscopy open at a wave number proportional to T^* [95]) and the apparent Néel temperature (observed via neutron scattering, but not μSR, Fig. 3.12) remain unchanged. Note that the emergence of bulk

superconductivity is accompanied by the appearance of the small hole Fermi pockets (Chapter 4). Experimentally, the small hole pockets appear before the Lifshitz transition occurs. Figure 3.22 also illustrates the underlying simplified phase diagram, showing a first-order phase transition between antiferromagnetism and superconductivity. The miscibility gap corresponds to the observed mixed-phase regime, which in the actual experimental systems is related to the disorder effects.

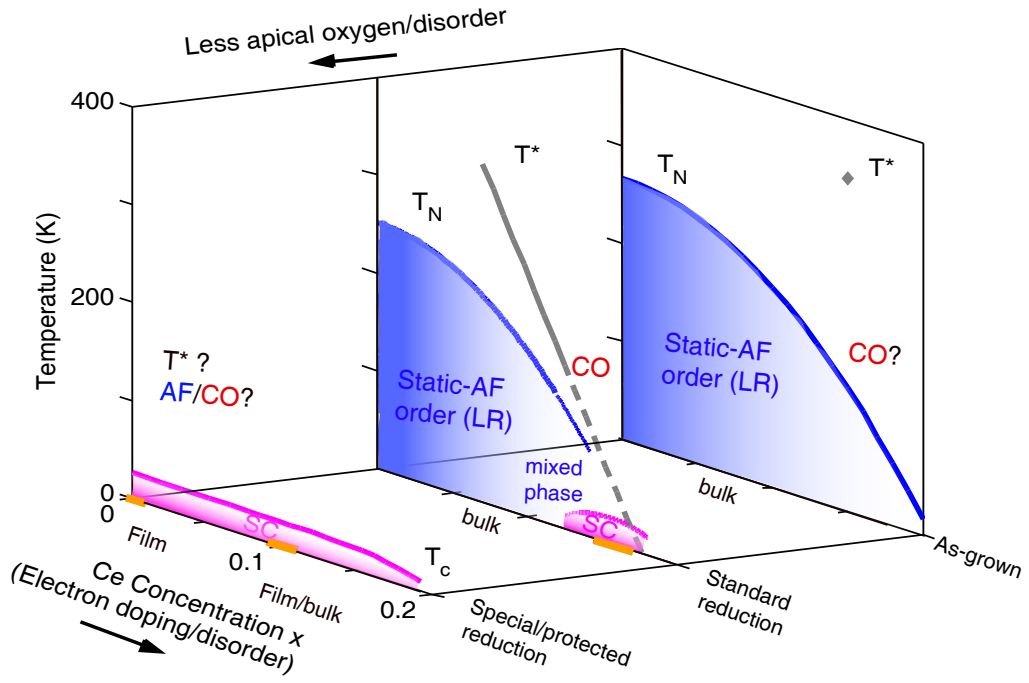

Figure 3.24: Multi-parameter phase diagram of NCCO. The antiferromagnetic and superconducting phases are indicated by shaded blue and magenta areas, respectively. The orange bars on Ce concentration-axes indicate where small hole pockets have been observed (Chapter 4). Charge order (CO) has so far only been reported for NCCO subjected to standard reduction. The pseudogap temperature (T^*), and Néel temperatures (T_N) are indicated.

Results for the magnetic correlation length and staggered magnetization for as-grown NCCO were reported in [139]. The psuedogap temperature was estimated for $x = 0.15$ NCCO [177]. No traces of superconductivity, of hole carriers, and of abrupt transitions

have been observed below the Ce solubility limit ($x \approx 0.20$). The schematic phase diagram of as-grown NCCO is shown in Fig. 3.23.

A new method to successfully manipulate oxygen conditions for thin-film samples (down to $x = 0$) [119] and bulk samples (at moderate doping) [196] has been reported. This method uses a special two-stage reduction process and provides a third slice of the overall phase diagram. Combing existing data for special-reduced, standard-reduced and as-grown materials (e.g., [55, 119, 139, 152–154, 196, 197]), a multi-parameter phase diagram is constructed in Fig. 3.24.

It is challenging but crucial to determine the exact effects of oxygen reduction. Oxygen reduction can be more effective than Ce substitution in suppressing antiferromagnetic order and inducing superconductivity. Because both Ce substitution and oxygen reduction can modify electron density [139], temperature-Ce substitution phase diagram often gives controversial results. A recent study of electron-doped cuprate $P_{1-x}LaCe_xCuO_{4-\delta}$, which estimated the electron density from ARPES, reported a temperature-electron density phase diagram in which the LR-AF phase does not appear to coexist with true superconducting phase [198]. The rather harsh oxygen reduction treatment was reported to: (1) cause a small shift in electron concentration ($\Delta x = 0.03$ for standard reduction) [139], (2) remove nominally absent oxygen (about 2 percent) from apical sites [119], and therefore to decrease disorder potential experienced by the charge carriers in the CuO_2 planes, (3) induce a small fraction (about 1 to 2 percent) of secondary $(Nd,Ce)_2O_3$ decomposition phase that forms epitaxially with $(Nd,Ce)_2CuO_4$, parallel to the CuO_2 planes [114], (4) "heal" a small amount (1 to 2 percent) copper deficiency that might exist in as-grown samples [120]. The emergence of superconductivity coincides with the appearance of fast spin fluctuations and of hole carriers (Chapter 4). Modifications of local structure as a result of the reduction might reshape the CuO_2 plaquettes at the nanoscale and result in a redistribution of electrons between planar and out-of-plane atomic orbitals, and thereby induce the hole carriers into the plane [199].

The revised phase diagram offers guidance to theoretical studies. For example, previous theoretical work on the electron-doped cuprates based on the single-band Hubbard model usually treated the electron concentration as the only tuning parameter and ignored hole carriers and local inhomogeneity [42]. These distinct effects of oxygen

reduction and chemical substitution require independent theoretical descriptions that are currently absent. A disorder-smeared first-order phase transition is most suitable in describing the transition between static long-range antiferromagnetic order and bulk superconducting phase in the electron-doped cuprate materials. Similar disorder-smeared first-order phase transitions have been found to exist in other strongly correlated electronic systems [52, 200] and are associated with interesting phenomena such as colossal magnetoresistance in the manganites [200].

Chapter 4

Hole-related superconductivity in the electron-doped cuprates

This Chapter describes the normal-state magnetoresistivity and two characteristics of the superconducting state, the superfluid density and the upper critical field. Clear connections are observed among the magnetoresistivity, the magnetism (Chapter 3), and the Fermi surface topology. The magnetoresistivity is understood and simulated based on Boltzmann theory and the Fermi surface topology. The characteristics of the normal state (magnetoresistivity, quantum oscillations, and Hall coefficient) and those of the superconducting state (superfluid density and upper critical field) consistently indicate two-band (electron and hole) features and clearly point to hole-related superconductivity in the nominally electron-doped cuprates. The well-known scaling between the superconducting transition temperature and the superfluid density of underdoped hole-doped cuprates is found to hold for the hole superfluid density for the electron-doped cuprates as well.

4.1 Overview

The phase diagram of NCCO discussed in Chapter 3 is closely related to the Fermi surface. Angle-resolved photoemission spectroscopy (ARPES) [205–207] and quantum oscillation experiments [155, 190, 195, 201, 204] have revealed three distinct Fermi surface topologies: (1) deep in the long-range ordered antiferromagnetic (LR-AF) phase

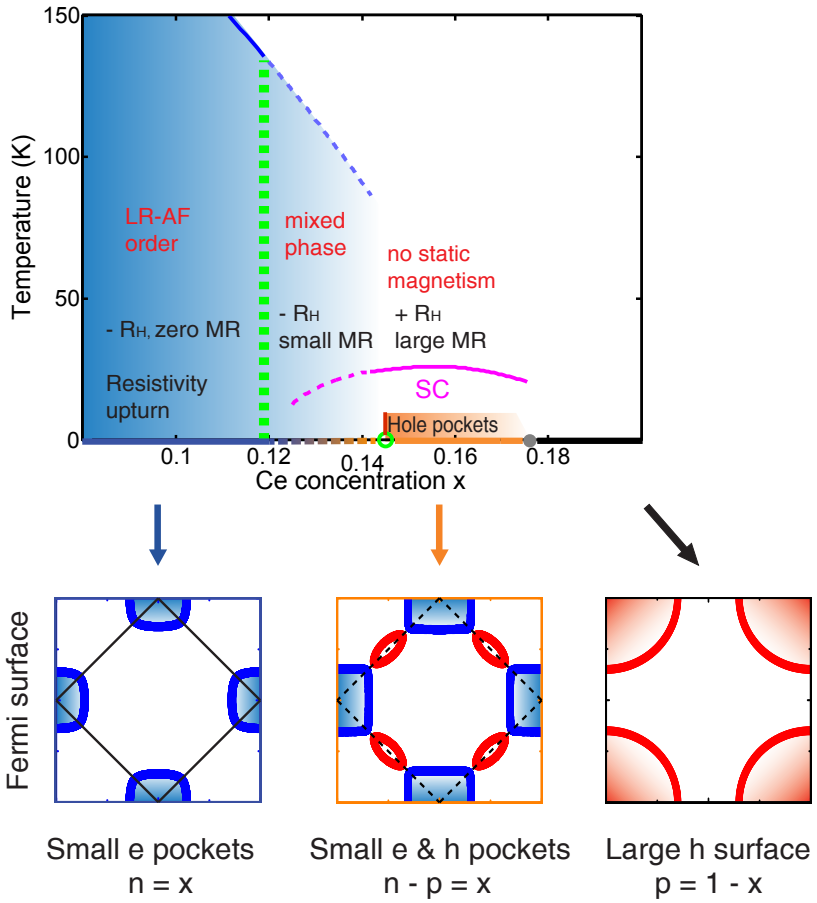

Figure 4.1: Top: Evolution of the Fermi surface of NCCO subjected to standard oxygen reduction. The long-range antiferromagnetic (LR-AF) phase is shown in blue. The superconducting transition temperature (SC) is plotted as a magenta line. The green vertical dashed line and green open circle denote the beginning and end of the mixed phase region with volume fraction $V_{\mathrm{AF}} + V_{\mathrm{SC}} = 1$. The gray circle indicates the Lifshitz transition, estimated based on the extrapolation of the pseudogap temperature at lower Ce concentration [95] and on quantum oscillation measurements [195, 201]. Bottom: Corresponding Fermi surfaces: (1) single-band Fermi surface with electron (e) pockets in the LR-AF phase; (2) two-band Fermi surface at doping levels where bulk superconductivity exists; and (3) large hole (h) Fermi surface at high Ce concentrations. As described in the text, the magnetic properties were determined using neutron scattering and μSR data (Chapter 3), and the Fermi surfaces were obtained based on published transport [95, 190, 202, 203], quantum oscillation [190, 195, 201, 204], and ARPES [205–207] measurements. - (+) R_H denotes negative (positive) Hall constant. MR denotes magnetoresistivity.

that exists only small electron pockets (around (π, 0) and equivalent); (2) for bulk superconducting samples, both small electron and hole (around ($\pi/2$, $\pi/2$) and equivalent) pockets are observed in high magnetic fields; and (3) at very high Ce concentrations, a large hole Fermi surface is expected to be recovered.

In samples subjected to standard oxygen reduction, the three Fermi surface topologies evolve as the function of doping (Chapter 3). As shown in Fig. 4.1, the LR-AF phase and the Fermi surface with electron-pocket exists at $x < 0.12$, the mixed phase exist at $0.12 \leq x < 0.145$, and the bulk superconducting phase and the two-band Fermi surface exist at $0.145 \leq x < 0.175$. The large hole Fermi surface was estimated to exist in NCCO above $x \approx 0.175$ [53, 95], and it has been indeed observed via photomession in other electron-doped cuprates [196]. In addition to the ARPES and quantum oscillation measurements, transport properties also reveal the evolution of the Fermi surface with Ce concentration: the Hall coefficient shows a sign change from negative to positive at intermediate doping [190, 202]; the Seebeck coefficient has a positive contribution for bulk superconducting samples [203]; and the effective carrier number observed in optical conductivity exhibits a jump in its doping dependence [95]. Features of the two-band contribution near the superconducting phase have been observed in other electron-doped cuprates as well, namely in $Pr_{2-x}Ce_xCuO_{4+\delta}$ and $(Pr, La)_{2-x}Ce_xCuO_{4+\delta}$ [64, 77, 208–210]. Moreover, the two-band Fermi surface was observed for Ce-free superconducting samples subjected to the special oxygen reduction treatment[155]. In contrast, for as-grown NCCO, neutron scattering [139], μSR and ARPES [207] results point to a single-band Fermi surface (electron pockets) below the Ce solubility limit.

Lifshitz and colleagues [146–148] showed that the magnetoresistivity is negligible for a single-band system with circular Fermi surface, but that this quantity can be substantial for a two-band Fermi surface. Prior work observed a coincidence between the emergence of superconductivity and the existence of a hole contribution in the normal-state transport properties, and it was proposed that the superconducting ground state may be related to the appearance of hole carries in the electron-doped cuprates [210]. However, there exists no comprehensive direct evidence to support this argument. This Chapter combines normal-state magnetoresistivity, upper critical field and superfluid density data for NCCO and shows strong evidence for hole-related, if not hole-driven superconductivity in the electron-doped cuprates.

4.2 Magnetoresistivity

4.2.1 Two analysis methods

Magnetoresistivity measurements have been intensively employed in the investigation of the Fermi surface of materials. As discussed in Chapter 2, the magnetoresistivity probes the shift of the Fermi surface (alternatively, the deviation of quasiparticles from their original path) in the presence of an external magnetic field. In the weak-magnetic-field limit ($\omega_c\tau < 1$, where ω_c is the cyclotron frequency and τ is the relaxation time), for a two-band Fermi surface with parabolic band dispersions, the magnetic field dependence of the magnetoresistivity is [146–148]

$$\Delta\rho/\rho(H=0) = b_2 H^2, \tag{4.1}$$

where $\Delta\rho = \rho - \rho(H=0)$ and H is the magnetic field. In high magnetic fields ($\omega_c\tau > 1$), deviations from the H^2 field dependence appear.

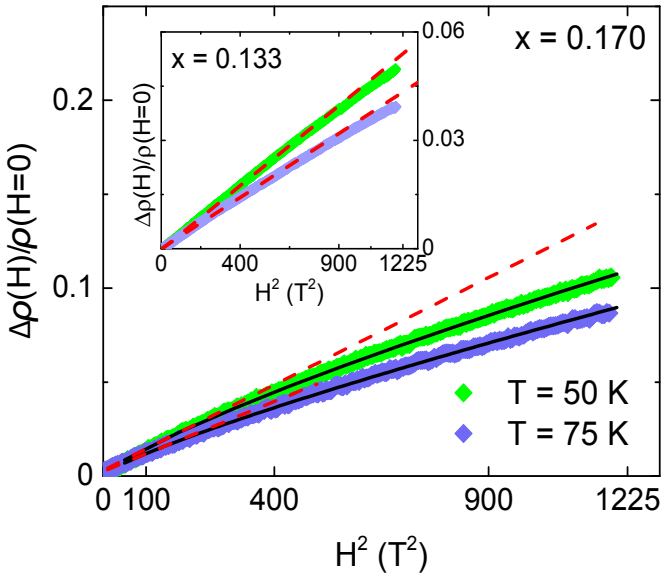

Figure 4.2: Demonstration of two methods used to analyze the magnetoresistivity, for NCCO with x=0.170 and x=0.133 (insert). Method 1: red dashed lines, method 2: black solid curves.

Two distinct methods were used to analyze the field dependence of our NCCO magnetoresistivity data. Because the magnetoresistivity exhibits a quadratic field dependence in low fields and deviates from this behavior at $H > H_{\rm dev}$, where $H_{\rm dev}$ denotes the field at which the deviation occurs, the low-field data were fit to Eq. 4.1 (method 1). The coefficient b_2 measures magnitude of the magnetoresistivity and can be readily extracted from fits of data obtained with $\mu_0 H < 9$ T. The deviation at $H > H_{\rm dev}$, which indicates a saturation effect due to the presence of small closed Fermi surfaces, was observed to be largest for samples with optimal Ce concentration ($x \approx 0.15$), i.e., for which T_c is highest.

The field $H_{\rm dev}$ is estimated as in the fellowing:

$$1 = \omega_c \tau = e H_{\rm dev} \tau / m^*, \tag{4.2}$$

where e is the electron charge, and m^* is the effective mass. For the electron-doped cuprate at small Ce concentrations (electron Fermi pockets only), it was found that $m^*/e\tau = 0.014 \pm 0.001\ T^2$ for NCCO with $x \approx 0.10$, where T is temperature [211], and thus $H_{\rm dev} = 35 \pm 2.5$ at $T = 50$ K. The measured value $H_{\rm dev} \approx 30$ T at the same Ce concentration is comparable to this estimate. The measured $H_{\rm dev} \approx 15$ T for bulk-superconducting samples (two-band Fermi surface) is consistent with the high magnetic field of about 45 T at which quantum oscillations are first seen (the observation of quantum oscillation requires quantized Landau levels to pass the Fermi surface, and thus requires $\mu_0 H \gg H_{\rm dev}$) [195, 201, 204].

The magnitude of the deviation ($D_{\rm MR}$) from the quantitative low-field behavior was defined as the percentage difference between the extrapolated $b_2 H^2 \rho(H = 0)$ behavior and the high-field magnetoresistivity at $H = 34.5$ T:

$$D_{\rm MR} = (\rho_{H^2} - \Delta\rho)/\rho_{H^2}, \tag{4.3}$$

where $\rho_{H^2} = b_2 H^2 \rho(H = 0)$ (recall that $b_2 H^2 \rho(H = 0) = \Delta\rho$ at low magnetic field). Because the doping and temperature dependences of $D_{\rm MR}$ are independent of H, we chose $H = 34.5$ T, the highest field used in our experiment.

The second method (method 2) was to fit the magnetoresistivity to a power-law behavior over the entire measured field range:

$$\Delta\rho/\rho(H = 0) \propto b_n H^n. \tag{4.4}$$

The coefficient b_n is a measure of the magnitude of the magnetoresistivity, whereas $2 - n$ characterizes the magnitude of the high-field deviation. These two methods are compared in Fig. 4.2 and lead to same conclusions as presented in the following Sections.

4.2.2 Electronic phase diagram

In order to better understand the overall phase diagram of the electron-doped cuprates, it is instructive to summarize and compare magnetic and electronic properties of the archetypal compound NCCO subjected to standard reduction. A comparison between the magnetic properties (Chapter 3) and the Fermi surface as a function of Ce concentration is shown in Fig. 4.1. The Ce concentrations for which LR-AF and bulk superconductivity are seen correspond to the distinctly different Fermi-surface topologies with small electron pockets and with small electron and hole pockets, respectively.

Figure 4.3 shows contour plots of the magnetoresistivity (b_2) and the high-field deviation ($D_{\rm MR}$) as a function of Ce concentration and temperature (current along the crystalline a axis and field along the crystalline c axis). These contour plots can be directly compared to the contour plot of the supercondcuting and (static) magnetic volume fractions in Fig. 4.4 (reproduced from Fig. 3.19 with inverted color map) and to Fig. 4.1. Considerable increases in b_2 and $D_{\rm MR}$ are observed at $x \approx 0.145$, coincident with sudden changes in the staggered magnetization ($M_{\rm st}$) and volume fractions $V_{\rm SC}$ and $V_{\rm M}$. The non-magnetic volume fraction in Fig. 4.4 is defined as $V_{\rm NM} \equiv 1 - V_{\rm M}$. Other transport properties in which similar sudden changes are seen at the same doping concentration include the Hall coefficient [190], the Seebeck coefficient [203], and the optical conductivity [95]. This doping level ($x \approx 0.145$) is also the smallest Ce concentration at which a two-band Fermi surface is seen [190].

In the mixed phase ($0.12 < x < 0.145$), photoemission measurements indicate possible traces of hole states [205], whereas transport measurements in high magnetic fields show no evidence of quantum oscillations due to small hole pockets [190]. The magnetic and non-magnetic regions in this spatially inhomogeneous phase must be similar to the material in the LR-AF and the bulk superconducting phase, respectively. For samples in the mixed phase, the measured magnetoresistivity contributions are averaged over the whole sample. The contributions to the magnetoresistivity are negligible (see Fig 4.3). The volume fractions of the magnetic and superconducting regions were

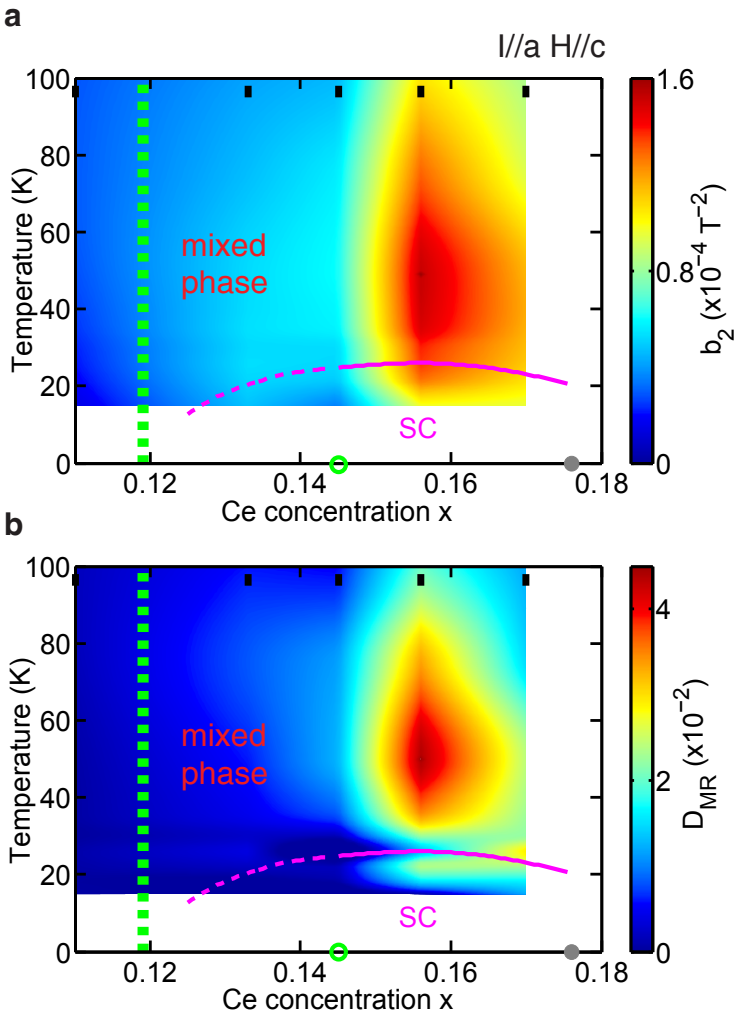

Figure 4.3: Contour plots of magnetoresistivity and high-field deviation (I//a, H//c geometry). (a) b_2 and (b) D_{MR} for NCCO subjected to standard reduction. The Ce concentrations of measured samples are indicated by black bars at the top. The green vertical dashed line denotes the boundary between the LR-AF and the mixed phases. The green open circle on the horizontal axis indicate the Ce concentration above which quantum oscillation revealed small hole pockets [190] and above which bulk superconductivity ($V_{\mathrm{SC}} > 0.5$, T_c indicated by magenta line) is seen. The gray dot on the horizontal axis marks the estimated Lifshitz transition to a state with large hole Fermi surface [53, 95].

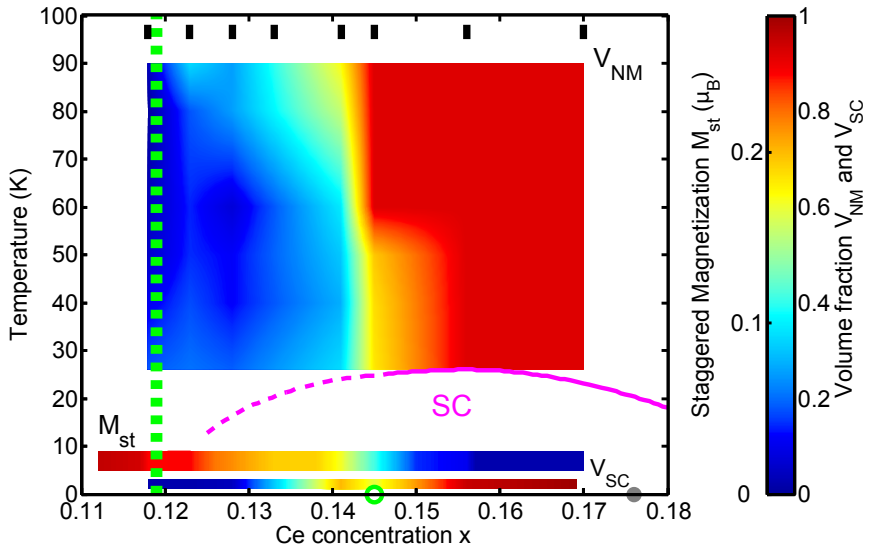

Figure 4.4: Contour plot of the volume fractions $V_{\rm SC}$ and $V_{\rm NM} \equiv 1 - V_{\rm M}$, and of the staggered magnetization for NCCO subjected to standard reduction. The Ce concentrations of measured samples are indicated by black bars at the top. The green vertical dashed line denotes the boundary between the LR-AF and mixed phases. The green open circle on the horizontal axis indicates the Ce concentration above which quantum oscillation have revealed small hole pockets [190] and above which bulk superconductivity ($V_{\rm SC} > 0.5$, T_c indicated by magenta line) is seen. The gray dot on the horizontal axis marks the estimated Lifshitz transition to a state with a large hole Fermi surface [53, 95]. Figure reproduced from Fig. 3.19 with inverted color map.

measured with μSR and powder magnetization, respectively (Chapter 3). The doping dependences of the magnetoresistivity coefficient b_2 and the superconducting volume fraction are compared in Fig. 4.5a: b_2 closely tracks $V_{\rm SC}$ as a function of Ce concentration. An approximate factor of four increase in b_2 is observed at Ce concentrations where bulk superconductivity emerges [202, 209, 212, 213]. In Fig. 4.5b, we estimate the non-magnetic volume fraction $V_{\rm NM}$ from a linear extrapolation of b_2 between $x = 0.11$ ($V_{\rm NM}$ set to zero) and $x = 0.156$ ($V_{\rm NM}$ set to one). The results agrees very well with $V_{\rm SC}$. These data can be simply understood by postulating an underlying first-order phase transition between LR-AF and bulk superconducting phases. We note that well bellow $x = 0.12$, the magnetoresistivity can be negative[214, 215], as also seen in our

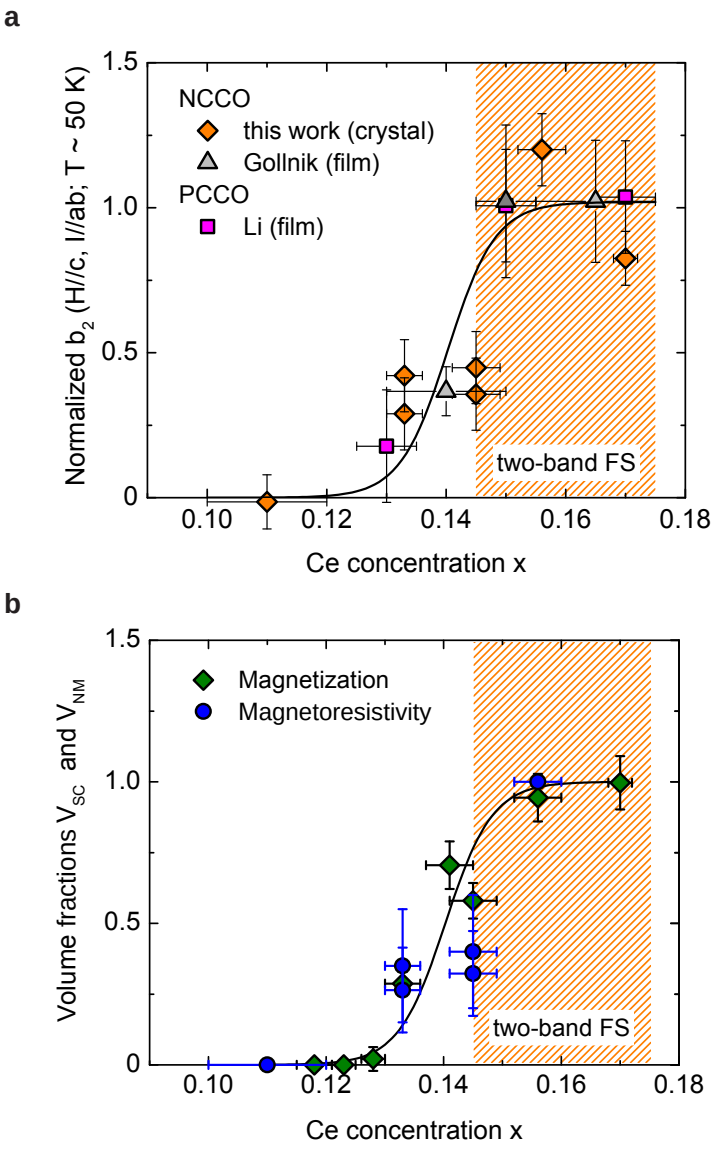

Figure 4.5: Comparison of the doping dependence of the magnetoresistivity coefficient b_2 and the superconducting volume fraction $V_{\rm SC}$. (a) Estimation of b_2 for NCCO [212] and PCCO [209] at $T \approx 50$ K, normalized to 1 in the Ce concentration range where the two-band Fermi surface (two-band FS, orange shaded area) and bulk superconductivity are seen; b_2 closely tracks the superconducting volume fraction (black solid line; see Fig. 3.14). (b) Superconducting volume fraction based on magnetization measurements and estimated non-magnetic volume fraction $V_{\rm NM}$ based on linear interpolation of b_2 (MR). The latter is obtained by setting $V_{\rm NM}$ to 0 for $x = 0.11$ and to 1 for $x = 0.156$ NCCO. The black line is the same as in (a).

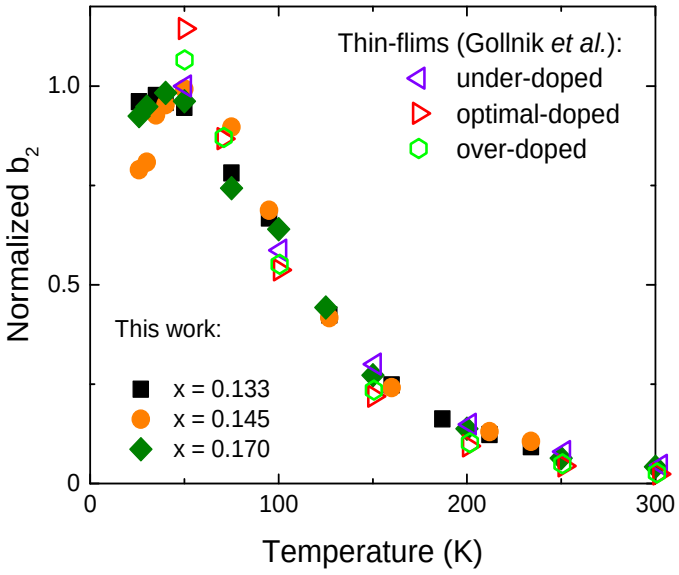

Figure 4.6: Temperature dependence of the magnetoresistivity coefficient b_2 (normalized at $T \approx 70$ K) for three of our NCCO crystals compared with prior thin-films measurements [212]. All six samples are superconducting. No obvious difference is observed for $T > 70$ K.

measurements (data not shown).

In principle, the non-zero magnetoresistivity in the mixed phase may also contain a second contribution, i.e., due to the change in the Fermi surface curvature as a function of doping. As the Ce concentration increases, both ARPES measurements and band calculations revealed that the electron pockets become square-like (in contrast to circle-like at small x) [193, 205]. The square-like electron pockets give rise to an enhance of magnetoresistivity.

It was argued that the Fermi surface may evolve as a function of temperature [53]. The temperature dependence of b_2 (normalized at $T \approx 70$ K) for NCCO with various Ce concentrations is plotted in Fig. 4.6. The value of b_2 collapse to a single curve at $T > 70$ K, suggesting an identical temperature dependence regardless of Ce concentration. The maximum value of b_2 at $T \approx 50$ K for some of the samples was previously argued to be the result of a difference in the scattering rates for electron and hole carriers (anisotropic scattering rate) [213] rather than being caused by a change in the Fermi surface at $T \approx 50$ K. The magnetoresistivity was also measured in other geometries

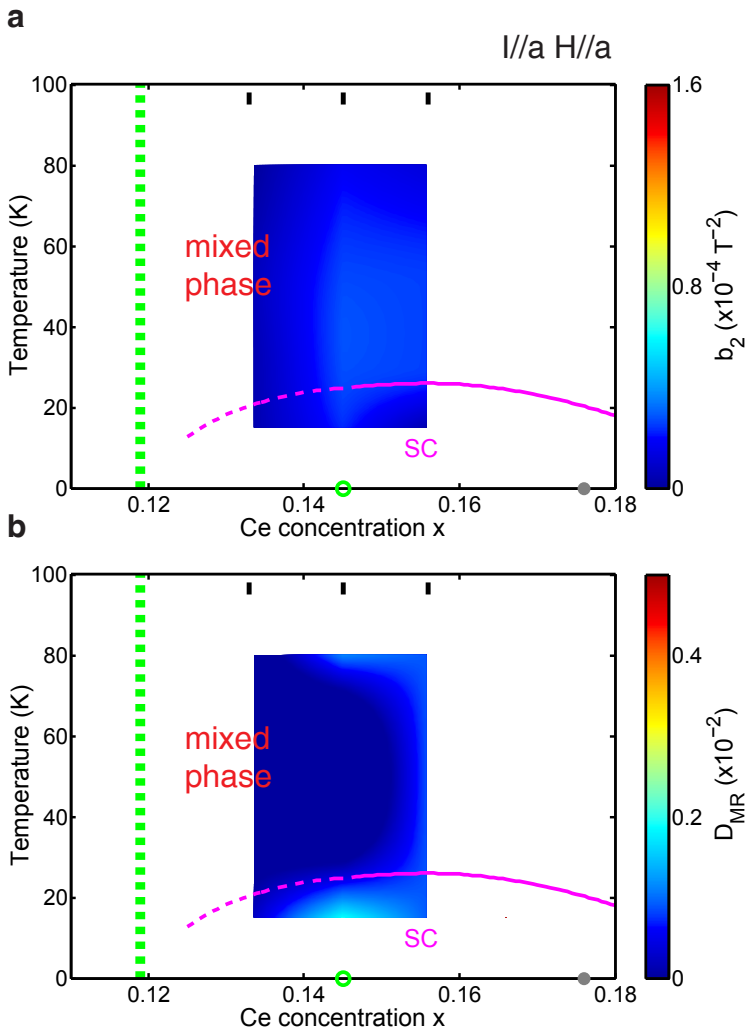

Figure 4.7: Contour plots of magnetoresistivity and high-field deviation (I//a, H//a geometry). (a) b_2 and (b) D_{MR} for NCCO subjected to standard reduction. The Ce concentrations of measured samples are indicated by black bars at the top. The green vertical dashed line denotes the boundary between the LR-AF and the mixed phases. The green open circle on the horizontal axis indicates the Ce concentration above which quantum oscillation have revealed small hole pockets [190] and above which bulk superconductivity ($V_{\mathrm{SC}} > 0.5$, T_c indicated by magenta line) is seen. The gray circle on the horizontal axis marks the estimated Lifshitz transition to a state with large hole Fermi surface [53, 95]. The magnetoresistivity does not exhibit any discernible feature on the studied doing range.

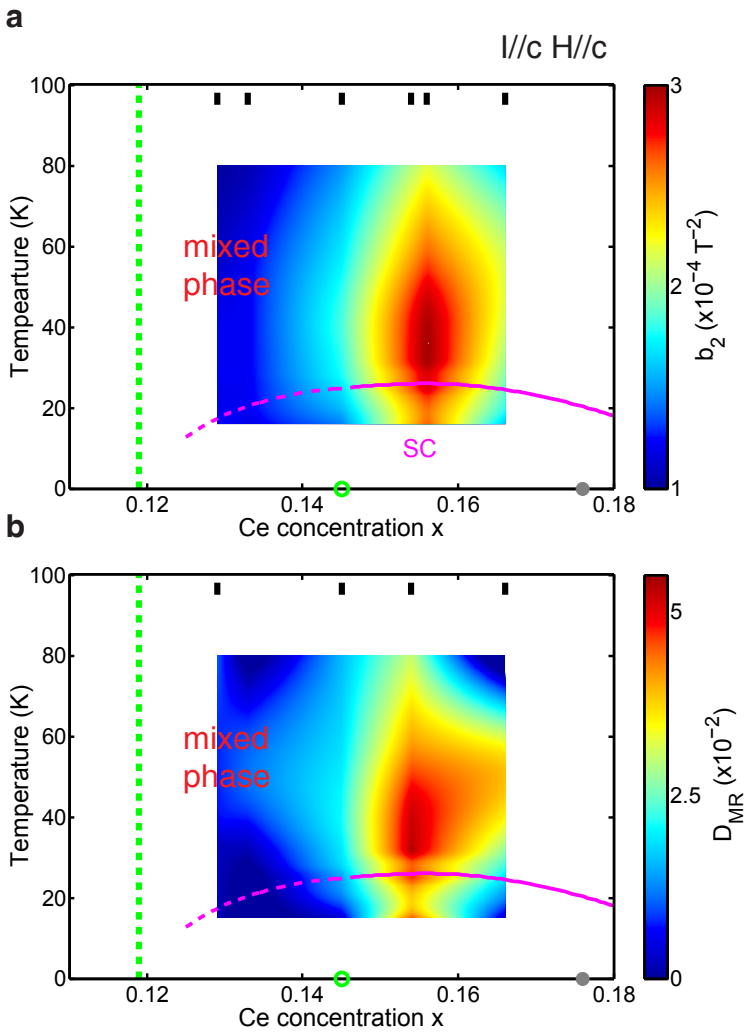

Figure 4.8: Contour plots of magnetoresistivity and high-field deviation (I//c, H//c geometry). (a) b_2 and (b) D_{MR} for NCCO subjected to standard reduction. The Ce concentrations of the measured samples are indicated by black bars at the top. The green vertical dashed line denotes the boundary between the LR-AF and the mixed phases. The green open circle on the horizontal axis indicates the Ce concentration above which quantum oscillation have revealed small hole pockets [190] and above which bulk superconductivity ($V_{\mathrm{SC}} > 0.5$, T_c indicated by magenta line) is seen. The gray circle on the horizontal axis marks the estimated Lifshitz transition to a state with large hole Fermi surface [53, 95].

(I//a, H//a; I//c, H//c; and I//c, H//ab). Considerable increases in the coefficients b_2 and $D_{\rm MR}$ at $x \approx 0.145$ were also observed in measurements in I//c, H//c geometry (Fig. 4.8), but not in I//a, H//a (Fig. 4.7) and I//c, H//ab (not shown) geometries. In addition, no apparent high-field deviation of the magnetoresistivity was seen in I//a, H//a (Fig. 4.7) and I//c, H//ab (not shown) geometries at $\mu_0 H < 35$ T. In I//a, H//a geometry, b_2 is much smaller than in I//a, H//c geometry. As discussed in Chapter 2, magnetoresistivity in I//a, H//a geometry probes non-orbital contributions that are irrelevant to the evolution of the quasi-two-dimensional Fermi surface. On the other hand, the observed magnetoresistivity in I//c, H//c geometry is difficult to understand. One possible explanation is that the electrical current in this geometry has both *ab*-plane and *c*-axis contributions.

4.2.3 Theoretical estimation

The considerable increase in magnetoresistivity at $x \approx 0.145$ can be understood based on Boltzmann theory and the underlying Fermi surface. As discussed in the previous Sections, three distinct Fermi surface topologies (small electron pockets only, both small electron and hole pockets, and a large hole Fermi surface) exist in the electron-doped cuprates. In this Section, the first two Fermi surface topologies are reproduced with the band structure given by the local density approximation [193, 194]. Note that the exact Ce concentration at which the two-band Fermi surface appears depends on the oxygen reduction conditions.

The band dispersion relation, considering existence of an antiferromagnetic gap, can be expressed as [193, 194]

$$E_k^{\pm} = \frac{1}{2}\left[\varepsilon_k + \varepsilon_{k+(\pi,\pi)} \pm \sqrt{(\varepsilon_k - \varepsilon_{k+(\pi,\pi)})^2 + 4\Delta^2}\right], \tag{4.5}$$

where Δ is the coherent antiferromagnetic back-scattering amplitude (i.e., the antiferromagnetic gap amplitude at $\vec{k}$ =(1/2, 1/2)), and ε_k and $\varepsilon_{k+(\pi,\pi)}$ are the original band dispersion and the band dispersion shifted by the antiferromagnetic propagation vector, respectively. The dispersion ε_k can be written as:

$$\begin{aligned}\varepsilon_k = &-2t_1[\cos(2\pi k_x) + \cos(2\pi k_y)] + 4t_2\cos(2\pi k_x)\cos(2\pi k_x) \\ &-2t_3[\cos(4\pi k_x) + \cos(4\pi k_y)] + \mu,\end{aligned} \tag{4.6}$$

where t_1, t_2 and t_3 are band hopping parameters, and μ is the chemical potential. The values of hopping parameters for the electron-doped cuprates used in previous work are $t_1 = 0.38$ eV, $t_2 = 0.32t_1$ and $t_3 = 0.16t_1$ [194]. The band parameters used in this Section slightly differ from those values in order to reproduce the experimental results (hole carriers appear at $x \approx 0.145$). For simplicity, μ, the material specific doping dependence which is not fully understood, was set to zero. This simplification does not qualitatively change the correspondence between Fermi surface topology and Ce concentration, because of the adjustment made for the band hopping parameters, and thus it is reliable in simulating the magnetoresistivity at a qualitative level.

A representative band structure simulated with $\Delta = 0.1$, $t_1 = 0.38$ eV, $t_2 = 0.3t_1$, and $t_3 = 0.18t_1$ is shown in Fig. 4.9. The Fermi energy crosses both the E_k^- and E_k^+ bands, resulting in both hole and electron pockets. In order to estimate the doping dependence of the magnetoresistivity, Fermi surfaces with different Δ values were obtained. For each Δ value, the Ce concentration ($x = n_e - n_h$), electron density (n_e), and hole density (n_h)) were estimated via numerical area-integration of the Fermi surface.

The calculated doping dependence of the Fermi surface is shown in Fig. 4.10. The hole carriers appear at $x \approx 0.145$. The magnetoresistivity was then estimated based on the Fermi surface with three methods: (1) two-band theory [216], (2) Boltzmann theory with an anisotropic scattering rate [212, 217], and (3) spectral function approach [218]). A considerable increase in magnetoresistivity at $x \approx 0.145$ was revealed by all three methods.

(1) **Two-band model**. Assuming two types (electron and hole) of carriers with respective carrier densities (n_e and n_h), mobilities (μ_e and μ_h), effective masses (m_e^* and m_h^*), and relaxation times (τ_e and τ_h), Blatt [216] calculated the magnetoresistivity:

$$\Delta\rho/\rho(H=0) = n_e n_h \mu_e \mu_h (\mu_e - \mu_h)^2 H^2 / (n_e\mu_e + n_h\mu_h)^2, \tag{4.7}$$

where $\mu_e = \tau_e/m_e^*$ and $\mu_h = \tau_h/m_h^*$. Our recent transport study revealed $\tau_e/m_e^* \propto T^{-2}$ and $\tau_h/m_h^* \propto T^{-2}$ ([211, 219], also see Chapter 5). Denoting $\tau_e/m_e^* = \alpha\tau_h/m_h^*$, where $\alpha \neq 1$ is a positive number, Eq. 4.7 shows $\Delta\rho/\rho(H=0) = 0$ at $x < 0.145$ ($n_e \neq 0$, $n_h = 0$) and $\Delta\rho/\rho(H=0) \neq 0$ at $x > 0.145$ ($n_e \neq 0$, $n_h \neq 0$). Values of n_e and n_h were estimated based on numerical area-integration of the Fermi surface (Fig. 4.10). The qualitative doping dependence of $\Delta\rho/\rho(H=0)$ does not depend on the exact value of

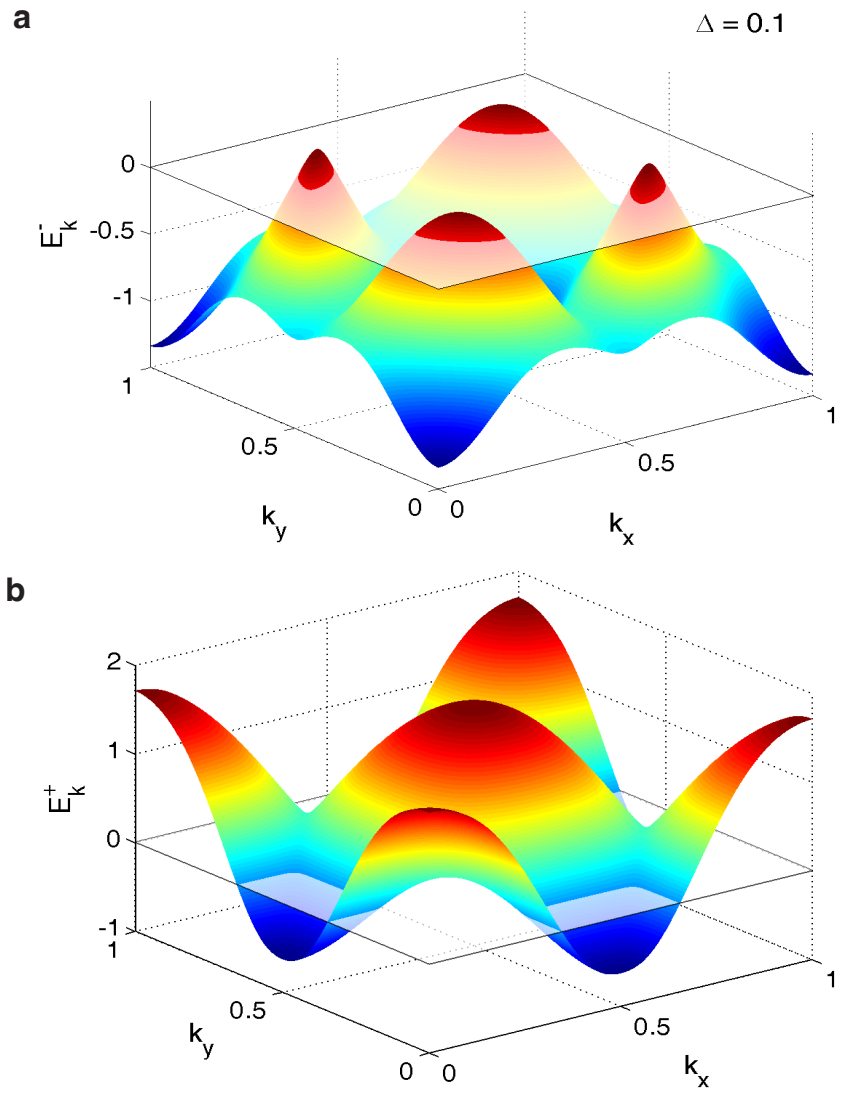

Figure 4.9: Representative band dispersions for (a) E_k^- and (b) E_k^+ bands given by Eq. 4.5 and Eq. 4.6 [193, 194]. The band parameters used were $t_1 = 0.38$ eV, $t_2 = 0.3t_1$, $t_3 = 0.18t_1$, and $\Delta = 0.1$ eV. The Fermi level is indicated as $E_k^{\pm} = 0$.

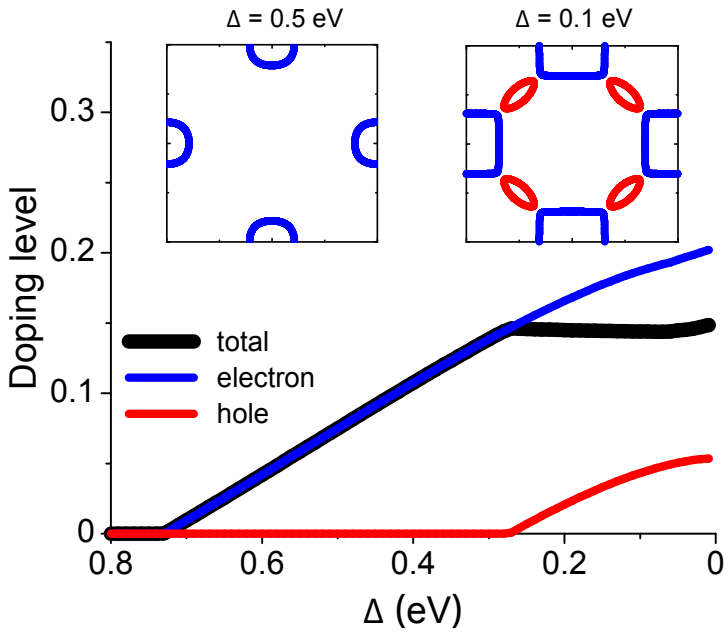

Figure 4.10: Doping dependence of the Fermi surface (inserts), as captured by varying the antiferromagnetic gap amplitude. The estimated density of total (black), electron (blue) and hole (red) carriers are shown as solid lines. Inserts show representative Fermi surfaces for $\Delta = 0.5$ eV and $\Delta = 0.1$ eV. The blue curves denote electron Fermi surfaces ($E_k^+ = 0$), and the red curves denote hole Fermi surfaces ($E_k^- = 0$). The hole carriers appear at $x \approx 0.145$ for the chosen band parameters.

α.

(2) **Boltzmann theory with an anisotropic scattering rate**. Calculations based on Boltzmann theory, on a two-dimensional, fourfold symmetric, but otherwise arbitrary Fermi surface, found that the magnetoresistivity depends on the details of the Fermi surface curvature (the scattering rate is anisotropic in momentum (k) space) [212, 217]:

$$\Delta\rho/\rho(H=0) = (|e|\mu_0 H/\hbar)^2[\langle(dl/ds)^2\rangle_\Sigma + \langle(ld\theta/ds)\rangle_\Sigma^2 - \langle(ld\theta/ds)^2\rangle_\Sigma], \qquad (4.8)$$

where l, s and θ are the local (k space) mean-free path, segment length along the Fermi surface, and angle between the carrier velocity and the electrical field, respectively. The notation $\langle ... \rangle_\Sigma$ denotes $\int \Sigma(s)...ds$, where $\Sigma(s)$ is the conductivity weight of s and $d\theta/ds$ is the local Fermi surface curvature. In order to calculate $\Delta\rho/\rho(H=0)$, $\int \Sigma(s)...ds$

was converted to a numerical summation. The number of points for the summation was chosen such that a moderate variation in the number did not affect the final result. According to [212], the first term in Eq. 4.8 is

$$\langle (dl(k)/ds)^2 \rangle_\Sigma = \int (\tau(k) dv(k)/ds)^2 \sigma(k) ds / \int \sigma(k) ds, \tag{4.9}$$

where $\tau(k)$, $v(k)$ and $\sigma(k)$ are the local (k space) scattering relaxation time, local Fermi velocity, and local conductivity, respectively. Note that s is a function of momentum k. $v(k) = dE_k^-/dk$ denotes the velocity of the hole carriers and $v(k) = dE_k^+/dk$ denotes the velocity of the electron carriers. The local conductivity is given by $\sigma(k) = e^2 l(k)/(4\pi^2\hbar) = e^2\tau v(k)/(4\pi^2\hbar)$. The second and third terms in Eq. 4.8 are given by [212]:

$$\langle (ld\theta/ds) \rangle_\Sigma^2 = \left(\oint \tau(k) v(k) \sigma(k) d\theta / \int \sigma(k) ds \right)^2 \tag{4.10}$$

$$\langle (ld\theta/ds)^2 \rangle_\Sigma = \left(\oint \tau(k) v(k) \sigma(k) d\theta \right)^2 / \int \sigma(k) ds \tag{4.11}$$

The derivation $d\theta/ds$ was chosen to be positive for electron and negative for hole carriers.

(3) **Spectral function approach**. The spectral function was calculated following [218], such that

$$A_k^\pm = \frac{1}{\pi} \frac{W_k^\pm \Gamma^\pm}{(\omega - E_k^\pm)^2 - (\Gamma^\pm)^2}, \tag{4.12}$$

where $W_k^\pm$ denote the weight functions

$$W_k^\pm = \frac{1}{2} \left[\frac{\varepsilon_k + \varepsilon_{k+(\pi,\pi)}}{\sqrt{(\varepsilon_k - \varepsilon_{k+(\pi,\pi)})^2 + 4\Delta^2}} \right], \tag{4.13}$$

and $\Gamma^\pm$ denote the anisotropic scattering rates

$$\Gamma^\pm = \Gamma_0 + C \sqrt{(\frac{\varepsilon_k^\pm}{dk_x})^2 + (\frac{\varepsilon_k^\pm}{dk_y})^2}, \tag{4.14}$$

where Γ_0 is the isotropic component of scattering rate, and C is a constant. The conductivities were calculated as [218]

$$\sigma_{xx,yy}^\pm \propto \int d\omega \sum_k \left[\frac{\partial E_k^\pm}{\partial k_{x,y}} \right]^2 [A_k^\pm(\omega)]^2, \tag{4.15}$$

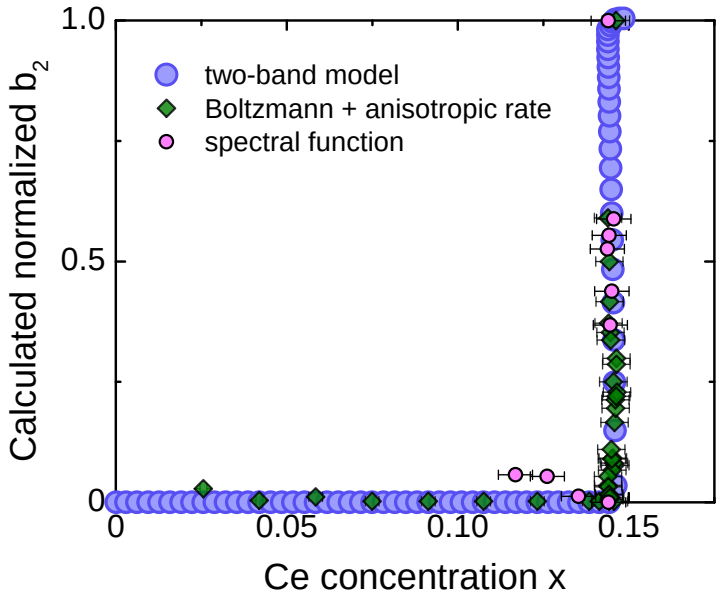

Figure 4.11: Estimated magnetoresistivity as a function of Ce concentration using three methods. In all cases, b_2 was calculated up to $x = 0.15$.

where σ^+_{xx} and σ^+_{yy} (σ^-_{xx} and σ^-_{yy}) denote conductivity tensor elements for electrons (holes), and

$$\sigma^{\pm}_{xy,yx} = \propto \int d\omega \sum_k \left[\frac{\partial E^{\pm}_k}{\partial k_{x,y}} \frac{\partial^2 E^{\pm}_k}{\partial k^2_{y,x}} - \frac{\partial E^{\pm}_k}{\partial k_{y,x}} \frac{\partial^2 E^{\pm}_k}{\partial k^2_{x,y}} \right] [A^{\pm}_k(\omega)]^3, \tag{4.16}$$

where σ^+_{xy} and σ^+_{yx} (σ^-_{xy} and σ^-_{yx}) denote conductivity tensor elements for electrons (holes). The magnetoresistivity is given as

$$\Delta\rho/\rho(H=0) = \mu_0^2 H^2 \sigma^+_{xx}\sigma^-_{xx}(\sigma^+_{xy} - \sigma^-_{xy})^2/(\sigma^+_{xx} + \sigma^-_{xx})^2. \tag{4.17}$$

Note that Eq. 4.17 suggests that $\Delta\rho/\rho(H=0) = 0$ if $\sigma^-_{xx} = 0$ (i.e., $n_h = 0$), similar to Eq. 4.7.

The estimated magnetoresistivity is summarized in Fig. 4.11. A considerable increase in b_2 at $x \approx 0.145$ is revealed by all three methods, which strongly suggests that the increase in magnetoresistivity is due to the appearance of hole pockets with doping.

4.2.4 Magnetoresistivity and the emergence of superconductivity

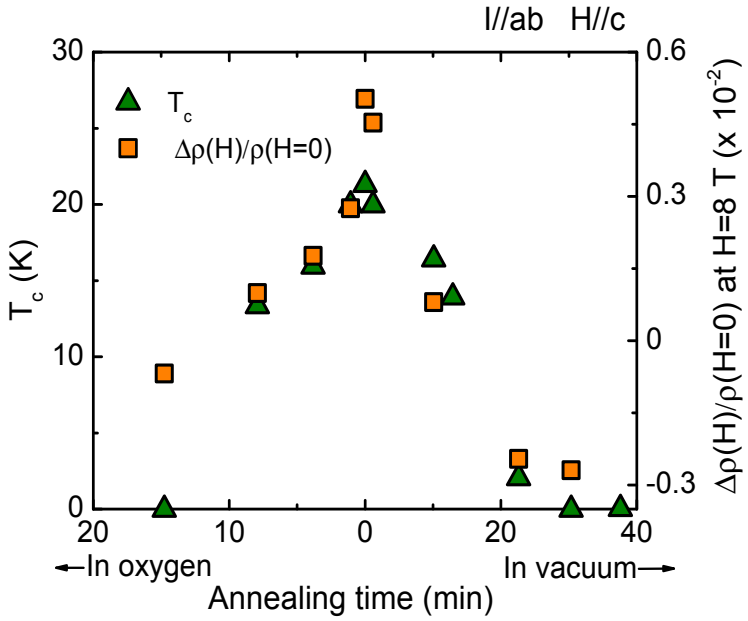

Figure 4.12: Comparison between magnetoresistivity (in I//ab, H//c geometry) and T_c as a function of oxygen reduction condition (annealing time) for NCCO with $x = 0.15$. The normalized magnetoresistivity and T_c collapse onto each other. This figure is reproduced from [202].

Hole carriers were previously proposed to be related to the emergence of superconductivity in the electron-doped cuprate materials based on charge transport measurements [210]. As discussed in the previous Section, magnetoresistivity probes the Fermi surface, and the presence of hole carriers results in a considerable increase in magnetoresistivity. In this Section, the normal-state magnetoresistivity is compared to the superconducting transition temperature (T_c) as a function of Ce concetration, oxygen reduction condition, and Ni impurity amount.

A previous study of $x = 0.15$ NCCO subjected to various oxygen reduction conditions found a strong correlation between the normal-state magnetoresistivity and the superconducting transition temperature [202]. As shown in Fig. 4.12, the magnitude of the magnetoresistivity closely tracks T_c as a function of annealing time. Consistent

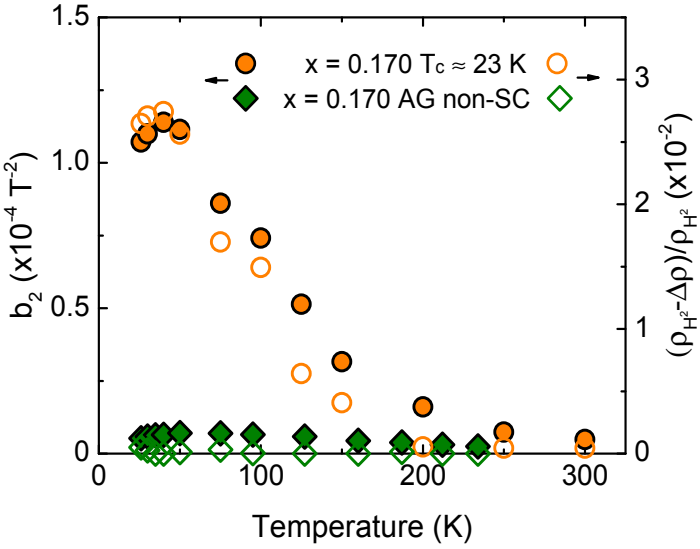

Figure 4.13: Magnetoresistivity (b_2) and high-field deviation for standard-reduced and as-grown, non-superconducting (non-SC) NCCO with $x = 0.170$.

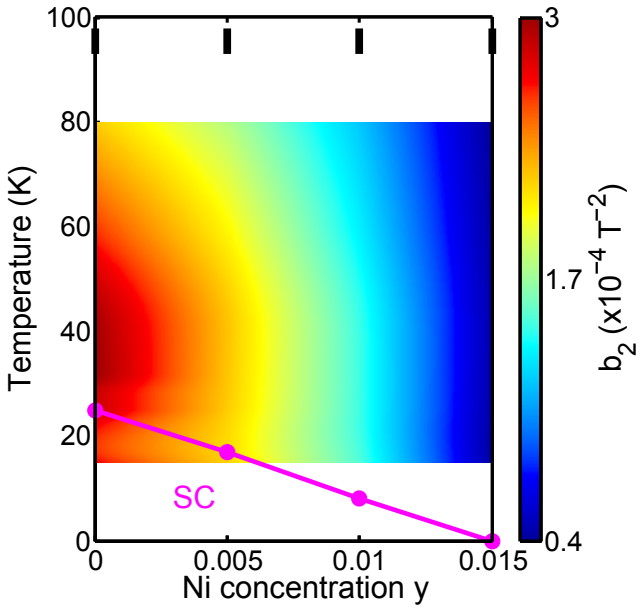

Figure 4.14: Contour plot of magnetoresistivity (b_2) for $x \approx 0.15$ NCCO as a function of temperature and Ni impurity concentration (I//c, H//c geometry). The discrete Ni substitution levels ($y = 0$, 0.005, 0.010, 0.015) that were used to construct this figure are indicated as black bars at the top. The superconducting transition temperatures are shown as magenta dots and line.

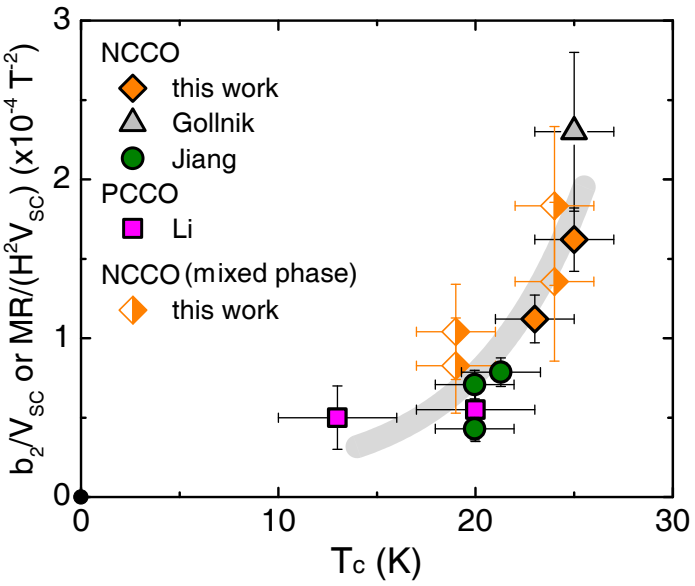

Figure 4.15: Comparison between magnetoresistivity and T_c for NCCO and PCCO [202, 212, 220]. The full symbols indicate samples near optimal Ce concentration with estimated superconducting volume fraction close to unity (Fig. 3.14). Half symbols indicate NCCO samples in the mixed phase ($0.12 < x < 0.145$), and the b_2 for these samples were corrected based on the superconducting (non-magnetic) volume fraction.

with this $x = 0.15$ NCCO result, the coefficient b_2 in our superconducting $x = 0.170$ NCCO (standard oxygen reduction) is an order of magnitude larger than for as-grown, non-superconducting, NCCO with the same Ce concentration (Fig. 4.13). The former corresponds to the two-band Fermi surface part of the phase diagram, whereas the latter corresponds to the situation with electron pockets only. Because oxygen reduction also changes the carrier density and moreover weakens the antiferromagnetic order, and thus enhances the magnetoresistivity, the correlation between the normal-state magnetoresistivity and superconducting transition temperature (Fig. 4.12 [202]) is difficult to understand.

In an attempt to exclude this complication, further magnetoresistivity measurements were performed on NCCO with nickel substitution, $Nd_{2-x}Ce_xCu_{1-y}Ni_yO_{4+\delta}$, with $x \approx 0.15$ and $y = 0$, 0.005, 0.010 and 0.015 subjected to standard reduction. Replacing copper by nickel, T_c of the electron-doped cuprates was found to be strongly

suppressed [221, 222], but no appreciable difference was observed in the antiferromagnetic instantaneous spin-spin correlation length [139]. The suppression of T_c by nickel impurities was proposed to be caused by the Abrikosov-Gorkov pair-breaking mechanism [223]. Remarkably, the correlation between the magnetoresistivity and T_c persists in nickel substituted NCCO samples (Fig. 4.14), implying that this relation is robust and not directly related to the antiferromagnetism.

We find a quantitative correlation between magnetoresistivity and T_c for a large number of thin-films and crystals, as summarized in Fig. 4.15. The magnetoresistivity was either estimated from b_2 or from $[\Delta\rho/\rho(H=0)]/H^2$ [202, 209, 212]. In the mixed phase, b_2 was corrected as $b_2/V_{\rm SC}$ in order to take into account the phase separation.

4.3 Characteristics of two-band superconductivity

4.3.1 Two-band resistive upper critical field

The resistive upper critical field H_{c2}, the magnetic field at which bulk superconductivity is fully suppressed and the normal-state resistivity is recovered, was extracted from magnetoresistivity data at $T < T_c$, such as in the example shown in Fig. 4.16. As shown in Fig. 4.17, the normalized resistive upper critical field $H_{c2}/H_{c2}(T=0)$ for NCCO with various Ce and Ni concentrations, subjected to standard reduction, exhibits a remarkable universal temperature dependence. This universal temperature dependence does not follow that of a single-band BCS superconductor. In contrast, a two-band model, a fit of which is shown in Fig. 4.17, describes the temperature dependence of $H_{c2}/H_{c2}(T=0)$ very well. This two-band model does not explicitly consider the d-wave symmetry of the superconducting order parameter of NCCO [42]. Following [227] and [228], H_{c2} is described by parametric equations:

$$\ln(\frac{T_c}{T}) = \frac{1}{2}[U(s)+U(\eta s)] + \frac{\lambda_0}{w}] - \{\frac{1}{4}[U(s)-U(\eta s) - \frac{\lambda_-}{w}]^2 + \frac{\lambda_{eh}\lambda_{he}}{w^2}\}^{1/2}, \quad (4.18)$$

$$H_{c2} = 2\phi_0 T s/D_e, \quad (4.19)$$

$$\eta = D_h/D_e, \quad (4.20)$$

$$U(s) = \Psi(s+1/2) - \Psi(1/2), \quad (4.21)$$

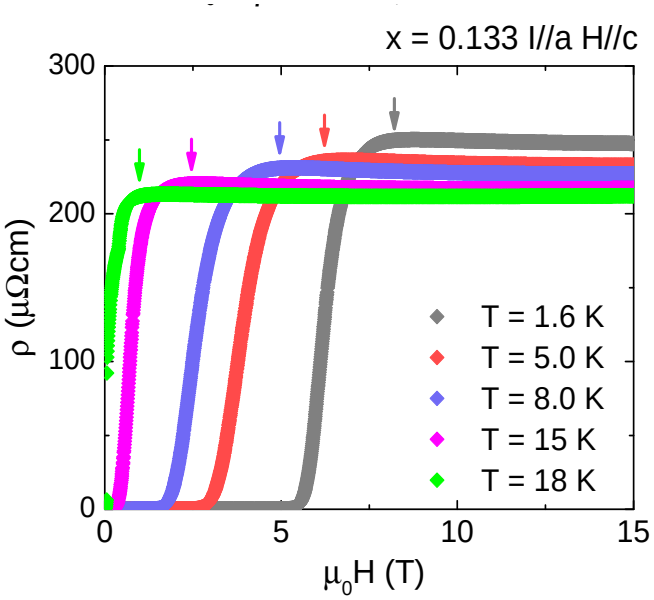

Figure 4.16: Resistive upper critical field H_{c2} extracted from magnetoresistivity for the $x = 0.133$ NCCO sample. The arrows indicate the approximate magnetic field at which superconductivity is fully suppressed and the normal-state resistivity is recovered.

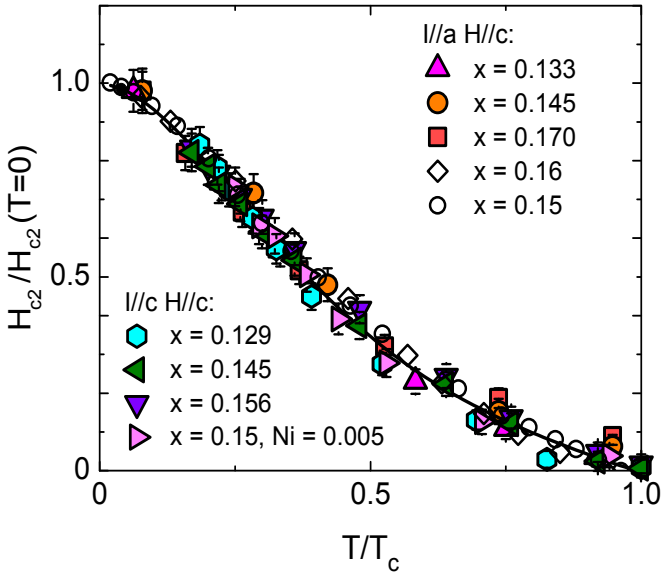

Figure 4.17: Temperature dependence of the reduced resistive upper critical field for NCCO with various Ce concentrations and Ni substitution levels, subjected to standard oxygen reduction. The solid curve is a fit to the two-band model described in the text. The data for $x = 0.16$ (open diamond) and $x = 0.15$ (open circle) are taken from [224] and [225], respectively.

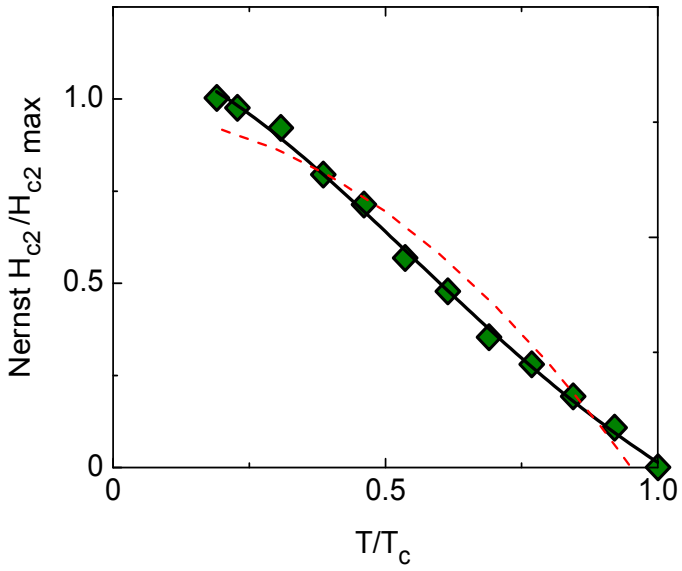

Figure 4.18: Temperature dependence of the Nernst upper critical field, normalized by its maximum value. The solid curve is a fit to the two-band model. The red dashed line is the best fit to a single-band BCS model. Data taken from [226].

where $\lambda_- = \lambda_{ee} - \lambda_{hh}$, $\lambda_0 = \sqrt{\lambda_-^2 + 4\lambda_{eh}\lambda_{he}}$, and $w = \lambda_{ee}\lambda_{hh} - \lambda_{eh}\lambda_{he}$. λ_{ee} (electron-electron), λ_{hh} (hole-hole), λ_{eh} (electron-hole) and λ_{he} (hole-electron) are matrix elements of the BCS coupling constants. D_e and D_h denote the electron and hole diffusivities, respectively, whereas $\phi_0 = h/2e$ denotes the magnetic flux quantum, where h is the Planck constant. $\Psi(x)$ is the digamma function. For simplicity, T_c and ϕ_0 were set to 1 in our analysis. In the fit shown in Fig. 4.17, $D_e = 0.885 \pm 0.139$, $D_h = 0.051 \pm 0.003$, $\lambda_{ee} = 0.250 \pm 0.019$, $\lambda_{hh} = 0.650 \pm 0.036$, and $\lambda_{eh} = \lambda_{he} = 0$.

The resistive upper critical field was argued to correspond to the "ridge" field (H^*), at which the Nernst signal reaches its maximum, and to be lower than the "real" upper critical field [226]. The Nernst effect is a thermoelectric effect in which an electric field is induced when a metallic sample is subjected to a magnetic field and a temperature gradient. Note the difference in the definition of the resistive upper critical field in [226] and in this Section. In order to resolve this ambiguity, the prior data for the Nernst upper critical field were also analyzed. As shown in Fig. 4.18, the single-band BCS model (red dashed line) can not describe these data even at a qualitative level, whereas

the two-band model (black solid line) again describes the data very well. From a fit to the Nernst upper critical field, we found $D_e \approx 0.761 \pm 0.475$, $D_h \approx 0.102 \pm 0.014$, $\lambda_{ee} = 0.151 \pm 0.020$, $\lambda_{hh} = 0.857 \pm 0.095$, and $\lambda_{eh} = \lambda_{he} = 0$, consistent with our analysis for the resistive H_{c2} in Fig. 4.17. The fit parameters for both the resistive and the Nernst upper critical fields suggests a stronger superconducting pairing interaction among hole carriers than among electron carriers ($\lambda_{hh} > \lambda_{ee}$).

4.3.2 Two-band superfluid density

Transverse-field μSR measurements were performed to extract the superfluid density for NCCO with x=0.170. The μSR time spectra were fit to

$$A(t) = Ae^{-\sigma^2 t^2/2}\cos(\omega t + \phi), \tag{4.22}$$

where A, σ, ω and ϕ denote the initial asymmetry, Gaussian relaxation rate, precession frequency and phase, respectively (see Chapter 2). The quantity σ^2 is a measure of the distribution of the internal magnetic field due to the presence of vortices, and it contains two components [142, 145, 229]:

$$\sigma^2 = \sigma_{\rm SC}^2 + \sigma_{\rm NM}^2. \tag{4.23}$$

$\sigma_{\rm NM}$ denotes the nuclear moment contribution, which can be determined from data for $T > T_c$. $\sigma_{\rm SC}$ denotes the superfluid density ρ_s with $\sigma_{\rm SC} \propto \rho_s \equiv n_s/m^*$, where n_s is the carrier density and m^* is the carrier effective mass [142, 145].

The temperature dependence of ρ_s (normalized to its low-temperature value) is plotted in Fig. 4.19. Previous studies suggested that, for the electron-doped cuprates, both an electron contribution (with nodeless superconducting gap) and a hole contribution (superconducting gap with nodes [76, 86]) are required to explain the temperature dependence of the superfluid density [82]. In order to disentangle the electron ($\rho_{\rm s,e}$) and hole ($\rho_{\rm s,h}$) contributions, we used the same method as [82] to analyze our NCCO data. The total superfluid density was decomposed into electron and hole contributions according to

$$\rho_{\rm s,total} = \rho_{\rm s,e} + \rho_{\rm s,h}, \tag{4.24}$$

$$\rho_{\rm s,e}(T) = \rho_{\rm s,e}(0)[1 - ae^{-\Delta/T}], \tag{4.25}$$

$$\rho_{\rm s,h}(T) = \rho_{\rm s,h}(0)(1 - T^2/T_h^2), \tag{4.26}$$

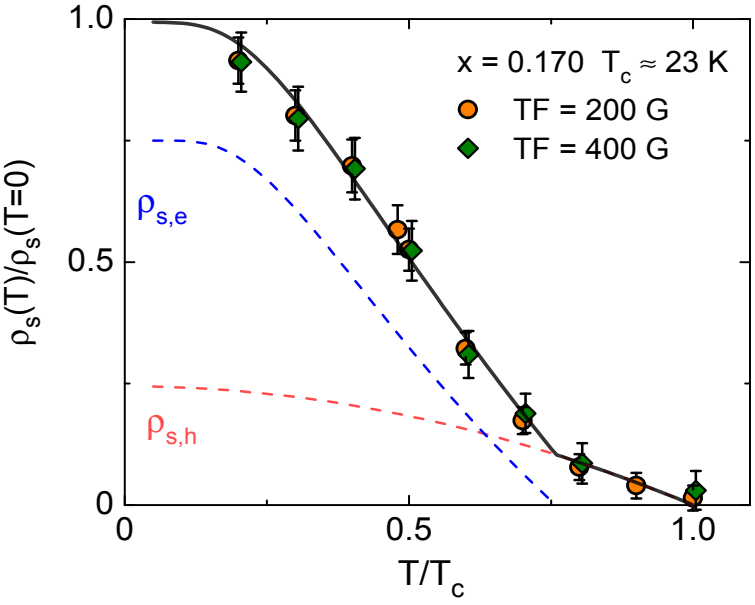

Figure 4.19: Temperature dependence of the reduced superfluid density. The solid curve is a fit to the two-band model as described in the text. Blue and red dashed curves indicate electron and hole contributions, respectively.

where $\rho_{\mathrm{s,e}}(0)$ and $\rho_{\mathrm{s,h}}(0)$ are the zero-temperature superfluid densities, and a is a constant such that $\rho_{\mathrm{s,e}}(T_e) = 0$, where T_e is the superconducting transition temperature of the electrons. Δ is an assumed, simplified isotropic superconducting gap for the electrons obtained from the fit. T_h is the superconducting transition temperature of the hole carriers.

The hole-carrier fraction of the superfluid density, $\rho_{\mathrm{s,h}}(0)/[\rho_{\mathrm{s,h}}(0) + \rho_{\mathrm{s,e}}(0)]$, for NCCO with $x = 0.170$ was estimated to be approximately 25% (Fig. 4.19). Quantum oscillation measurements indicate that, for NCCO with $x \approx 0.15$, electron and hole densities are roughly 0.18 and 0.03, respectively [204]. Incorporating estimated electron and hole effective masses ($m^*_{\mathrm{h}} \approx 0.9m$, $m^*_{\mathrm{e}} \approx 2m$, where m is the electron free mass [204, 211]), the calculation based on normal-state carrier densities gives $\rho_{\mathrm{s,h}}(0)/[\rho_{\mathrm{s,h}}(0) + \rho_{\mathrm{s,e}}(0)] \approx 27\%$, consistent with our decomposition of the superfluid density for $x \approx 0.170$ (see Fig. 4.19).

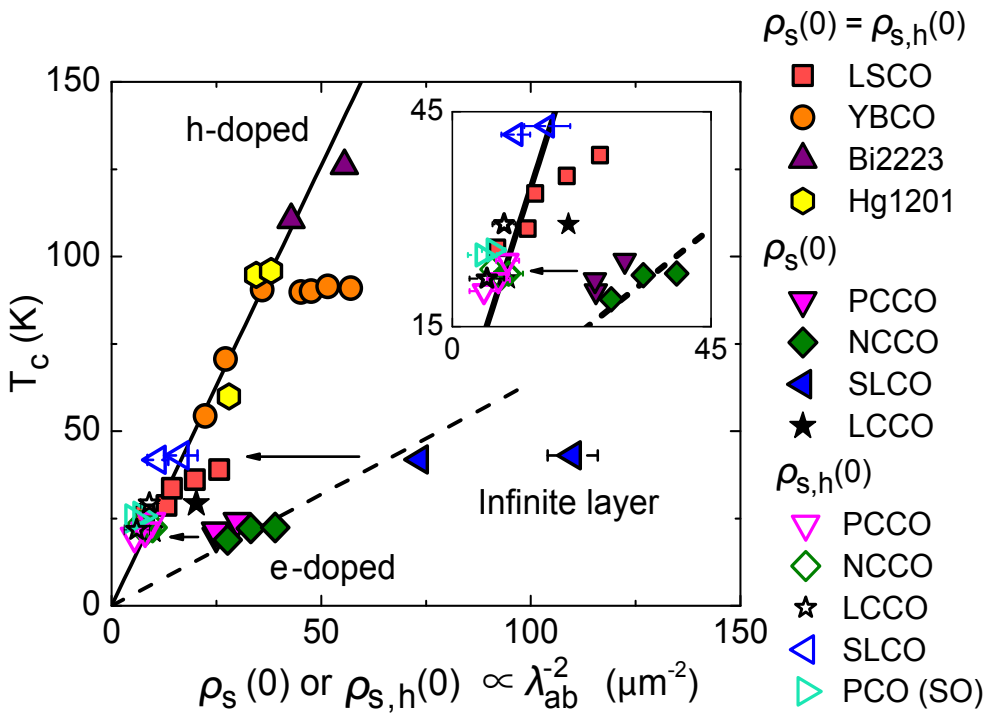

Figure 4.20: Scaling between the hole superfluid density and T_c. Dashed line indicates approximate behavior of $\rho_{s,total}(0)$ for the electron-doped cuprates. Solid line indicates $\rho_{s,h}(0)$ for both the electron- and hole-doped cuprates. Insert shows a zoom of the data at low temperatures. Data from [230] (hole-doepd cuprates LSCO, YBCO, Bi2223), [231] (hole-doped cuprate Hg1201), [232] (electron-doped and infinite layer cuprates PCCO, NCCO, SLCO), [229] (infinite-layer cuprate SLCO), [233] (electron-doped cuprate LCCO), [155] (electron-doped cuprate PCO subjected to special oxygen reduction (SO)). LSCO: $La_{2-x}Sr_xCuO_4$, YBCO: $YBa_xCu_3O_y$, Bi2223: $Bi_2Sr_2Ca_2Cu_3O_x$, Hg1201: $HgBa_2CuO_{4+\delta}$, NCCO: $Nd_{2-x}Ce_xCuO_{4+\delta}$, PCCO: $Pr_{2-x}Ce_xCuO_{4+\delta}$, PCO: $Pr_2CuO_{4+\delta}$, LCCO: $La_{2-x}Ce_xCuO_{4+\delta}$, SLCO: $Sr_{1-x}La_xCuO_2$.

In addition, we note that $\rho_{s,h}(0)/[\rho_{s,h}(0)+\rho_{s,e}(0)]$ for PCCO [82] and for the "infinite-layer" electron-doped cuprate $Sr_{1-x}La_xCuO_2$ (SLCO) [229] was reported to be approximately 20% and 15%, respectively. Uemura and colleagues previously performed μSR measurements of the superfluid density and observed universal scaling between $\rho_s(0)$ and T_c for the hole-doped cuprates below optimal doping [145]. In subsequent work, they observed evidence for a distinct scaling between $\rho_{s,total}(0)$ and T_c for the electron-doped cuprates [230]. Intriguingly, as shown in Fig. 4.20, upon comparing $\rho_{s,hole}(0)$ and T_c, we find a single universal scaling for both electron- and hole-doped cuprates was observed.

For thin-film samples subjected to special reduction [119], a two-band Fermi surface was observed by quantum oscillation measurements [155]. The hole fraction of the superfluid density can be estimated from the quantum oscillation frequency and the effective masses. The frequency $F = 310$ T, corresponding to small hole Fermi pockets, was found for specially-reduced $PrCuO_4$ thin-films with $T_c \approx 26$ K [155]. The normal-state hole density was estimated by comparing the oscillation frequency to that for NCCO ($F = 290$ T for $x \approx 0.15$ NCCO with $T_c \approx 25$ K [204]). Assuming that all the normal-state hole carriers contribute to the superfluid density, we find that the PCO thin films obey the universal scaling as well (Fig. 4.20), which points to a single superconducting ground state, regardless of oxygen reduction conditions.

4.4 Discussion: holes in the electron-doped cuprates

Many prior works provided insights and initial evidence for hole-related superconductivity in the electron-doped cuprates. The existence of hole carriers at intermediate Ce doping concentrations was shown in transport properties such as the Hall coefficient [64, 190, 202, 208, 210], Nernst effect [234], Seebeck coefficient [203] and optical conductivity [53, 95]. In addition, ARPES [205–207] revealed the existence of hole carriers, and quantum oscillation measurements [190, 195, 201, 204] found small hole Fermi pockets in high magnetic field.

The coincidence between the appearance of hole carriers (e.g., hole contribution in transport properties) and the emergence of superconductivity was reported as a function of Ce concentration (e.g., [210]) and oxygen reduction [202]. For example, an increase

in the magnetoresistivity was observed to correlate with the superconducting transition temperature and with a sign change (from negative to positive) in the Hall constant [202]. In addition, features of the hole contribution were reported in the characteristics of superconducting state. For example, Raman scattering experiments revealed that coherent normal-state hole quasiparticles contribute to superfluid density [77, 235]. The superfluid density obtained from measurements of the penetration depth indicates both electron and hole contributions [82, 236]. Moreover, as noted, the resistive upper critical field can also be understood based on electron and hole contributions [225].

However, these measurement have been limited to specific measurements on specific materials. For example, the studies of resistive upper critical field [225] and magnetoresistivity [202] were limited to NCCO at a single Ce concentration ($x = 0.15$). No unified understanding exists for the relationship among the appearance of hole carriers, changes in the normal-state electronic/magnetic properties, and the emergence of superconductivity at quantitative level. How the Fermi surface connects to the underlying phase transition between the LR-AF and bulk superconducting phases was unknown.

In this Thesis work, we first mapped out the underlying first-order phase transition between the LR-AF and bulk superconducting phases based on neutron scattering and μSR measurements (Chapter 3). Combining the magnetic phase diagram with information for the Fermi surface provided by quantum oscillation measurements [190, 195, 201, 204], we found a close connection between Fermi surface topology and the magnetic phase, i.e, a Fermi surface with small electron pockets in the LR-AF phase and a two-band Fermi surface for bulk superconducting samples. Our magnetoresistivity measurements revealed an electronic phase diagram very similar to the magnetic phase diagram. The magnetoresistivity is understood by the evolution of the Fermi surface based on Boltzmann theory. Intriguingly, we observed that the magnetoresistivity closely tracks properties related to the superconductivity, i.e., the superconducting transition temperature and the superconducting volume fraction.

Our measurements for characteristics of the superconducting state were further analyzed following the prior work. The resistive upper critical field was measured by fully suppressing superconductivity with an external magnetic field, and analyzed following the two-band (electron and hole) model in [225, 227, 228]. We found a universal temperature dependence of the resistive upper critical field, which can not be described by

a single-band BCS model, regardless of Ce and Ni concentrations. This universal temperature dependence indicates a pairing interaction among hole carriers that is larger than those among electrons. The temperature dependence of the superfluid density was measured by transverse-field μSR and analyzed following the two-band (electron and hole) model in [82]. Our analysis gives a ratio between electron and hole superfluid densities consistent with normal-state carrier densities and with the ratio previously reported in [82, 233].

Uemura and colleagues previously reported a universal scaling between the superfluid density and superconducting transition temperature for the hole-doped cuprates below optimal doping [145]. Subsequently, they observed distinct scaling ratios for the total superfluid density and T_c for electron-doped cuprates [230]. Remarkably, upon decomposing the electron and hole contributions, we found a single universal scaling between hole superfluid density and T_c for both electron- and hole-doped cuprates, which points to a single mechanism of hole-related superconductivity regardless of nominal dopant type. This scaling is also found to hold for the electron-doped cuprates subjected to special oxygen reduction conditions [119, 155].

Having gained these new insights, we revisit the old question how to understand the emergence of superconductivity in the electron-doped cuprates. The static long-range antiferromagnetism does no co-exist with the bulk superconductivity in the electron-doped cuprates, and this may be understood by the appearance of hole carriers. As in the case of hole-doped cuprates, the hole carriers may prefer to reside on oxygen sites, and thus will rapidly frustrate the antiferromagnetic order. The resultant fast spin fluctuations might provide the paring glue [27, 66, 67]. Our results show that the normal-state charge transport of the electron-doped cuprates is rather conventional. The temperature dependences of the upper critical field and the superfluid density, and the universal scaling between the hole contribution of the superfluid density and T_c suggest that the hole carriers might drive the emergence of the superconductivity in the electron-doped cuprates. It is possible that the hole carriers form Copper pairs first, and once the hole pairs condense, the electrons start to contribute to the superfluid density. The relatively low hole density (at least below the Lifshitz transition) might be the reason why T_c of the electron-doped cuprates is much lower than that of the hole-doped cuprates.

Chapter 5

Normal-state charge transport properties

This Chapter describes charge transport properties observed in the normal-state of the electron- and hole-doped cuprates. Both the *ab*-plane and *c*-axis dc resistivity exhibit a sample-specific resistivity upturn at low temperatures in addition to a T^2 contribution. Universal scaling behavior is observed between resistivity coefficients, which suggests a single mechanism that governs the resistivity upturn in both electron- and hole-doped cuprates. The T^2 contribution is revealed to be depended on the doping level, but not on the specific cuprate compound or nominal dopant type. Upon separating the two contributions, $m^*/\tau \sim C_2T^2$, is observed for the underdoped electron-doped materials, even deep in the antiferromagnetic phase, which resembles the behavior of a Fermi liquid. Remarkably, the value of C_2 is found to be approximately independent of material, dopant type and doping level. In particular, the value of C_2 is nearly the same as in the very overdoped hole-doped cuprates, where Fermi-liquid behavior has been firmly established. This observation suggests that the observed $m^*/\tau \sim C_2T^2$ behavior is universally due to conventional Fermi-liquid Umklapp scattering. The *ab*-plane transport results discussed in this Chapter were published in [211].

5.1 Overview

The generic phase diagram of the electron- and hole-doped cuprate is shown in Fig. 1.5. One of the biggest scientific puzzles presented by the cuprates is the nature of the normal state from which superconductivity emerges upon cooling [237]. The normal-state exhibits many "exotic" physical properties which, despite three decades of remarkably intensive research efforts, are not well understood (e.g, the pseudogap phenomenon below optimal doping and T-linear resistivity near optimal doping). The charge-transport properties studied in this Chapter are the dc electrical resistivity, Hall constant, and quasiparticle scattering rate. In conventional materials, Landau-Fermi quasiparticles approximately behave like electrons, yet with normalized (effective) mass due to the electrons' interactions with their environment. Because charge transport properties correspond to a weighted integration over states near the Fermi surface (see e.g., the calculation of magnetoresistivity in Chapter 4), they typically exhibit complex temperature, magnetic field, pressure, etc., dependences. The development of a satisfactory understanding of these dependences of the charge-transport properties in the cuprates has been remarkably challenging. For example, the quasiparticle concept seems to break down in certain regions of the phase diagram (e.g., [238]). For the hole-doped cuprates, the quasiparticle life time measured by photoemission spectroscopy in the "strange metal" regime (in the normal-state near optimal doping) is extremely short, which has been interpreted to imply that quasiparticles are not well-defined on the timescale of the scattering process [60]. In addition, the Mott-Ioffe-Regel limit, in which the mean-free path of the quasiparticles is comparable to the lattice constant, is seemingly violated in this regime [239, 240].

For the hole-doped cuprates, it was demonstrated that the metallic state in the highly over-doped regime (LSCO with $p \approx 0.3$ per planar Cu atom, i.e., outside the strange metal regime) is a Fermi liquid [241, 242]. The Wiedemann-Franz law is obeyed (the ratio between the electronic contribution to the thermal conductivity and the electrical conductivity is proportioned to temperature for a Fermi-liquid system), which suggests that charge and heat are carried by the same quasiparticles [241, 242]. The Umklapp scattering process (electron-electron scattering that involves lattice vibrations)

in a Landau-Fermi liquid system leads to a resistivity that exhibits quadratic temperature dependence. This temperature dependence was found in the over-doped regime of LSCO [241]. Moreover, the large Fermi surface determined via photoemission spectroscopy measurements [60, 243] agrees with that determined from quantum oscillation measurements [244] and with theoretical expectations for a simple band metal [243].

Upon lowering the doping level, superconductivity emerges and the the normal-state behavior quickly becomes very complex (strange metal, pseudogap). For example, the planar resistivity continuously evolves from the quadratic Fermi-liquid behavior toward an extended linear temperature dependence and, as noted, becomes so large that it has been argued to be incompatible with the notion of quasiparticles (violating the Mott-Ioffe-Regel limit) [240]. The approximate $\rho \propto T$ behavior holds from very high temperatures down to the doping-dependent pseudogap temperature T^*. The transport behavior in the pseudogap regime ($T < T^*$) has been thought to be ill-defined [240]. In addition, below a compound-specific doping level, the low-temperature resistivity develops weak insulator-like behavior characterized by a logarithmic upturn [245–248]. At very low electron concentrations, the low-temperature resistivity diverges sharply, and the undoped materials are commonly thought of as the Mott insulators.

In attempts to explain the complex normal-state transport near and below the optimal doping, many non-Fermi liquid theories have been proposed. In the following, I present some of these ideas.

Marginal Fermi-liquid theory

Motivated by experimental observations for the hole-doped cuprates, Varma and colleagues [249–252] proposed the marginal Fermi-liquid theory for the normal-state transport in the strange metal regime. The theory assumed that the single-particle scattering rate consists of two components: (1) a temperature-independent, elastic anisotropic scattering rate ($1/\tau_{i,k}$) due to small-angle scattering by impurities, and (2) an isotropic, inelastic scattering rate ($1/\tau_M$) that is proportional to temperature. The total scattering rate was expressed as [249–252]

$$1/\tau = 1/\tau_M + 1/\tau_{i,k} \approx A_1 T + 1/\tau_{i,0} \cos^2(2\theta), \tag{5.1}$$

where $1/\tau_{i,0}$ is a constant, and θ describes the location on the Fermi surface in k space.

With suitable parameters, this scattering rate gives [251, 252]

$$\rho \propto 1/\tau \sim T, \tag{5.2}$$

$$\cot(\theta_H) \sim T^2. \tag{5.3}$$

Note that the marginal Fermi-liquid theory suggests distinct temperature dependences for the resistivity and the cotangent of the Hall angle, consistent with transport experiments in the strange metal regime [240].

Two-scattering-rate picture

Anderson [240, 253] proposed a two-scattering-rate picture based on the exotic idea of charge-spin separation. The quasiparticle was proposed to be composed of two components: (1) the excitation of the spin component, namely the spinon, and (2) the excitation of the charge component, namely the holon. The scattering among holons was assumed to dominate the normal-state resistivity, and its scattering rate $1/\tau_h$ was proposed to be proportional to temperature. On the other hand, the cotangent of the Hall angle was proposed to be dominated by scattering among spinons, with a scattering rate $1/\tau_s$ proportional to the square of temperature. The temperature dependences of the normal-state resistivity and the cotangent of the Hall angle were thus written as [240, 253]

$$\rho \propto 1/\tau_h \propto T, \tag{5.4}$$

$$\cot(\theta_H) \propto (\tau_s)^{-1} \propto T^2. \tag{5.5}$$

Note that this two-scattering-rate picture only tackles the normal-state transport in the strange metal regime.

Anisotropic scattering rate picture

Hussey [254] proposed the existence of a doping-dependent anisotropic scattering rate $(1/\tau)$. The model can be regarded as a generalization of Varma's idea [249–252], and it also assumes two components for the scattering rate: (1) a temperature-independent, anisotropic, elastic scattering rate $(1/\tau_0)$, and (2) a temperature-dependent, anisotropic

inelastic scattering rate ($1/\tau_T$) [254]:

$$1/\tau_0 = G_0[1 + \chi \cos^2(2\theta)], \tag{5.6}$$

$$1/\tau_T = G_1 \cos^2(2\theta)T + G_2T^2, \tag{5.7}$$

$$1/\tau = 1/\tau_0 + 1/\tau_T, \tag{5.8}$$

where G_0, G_1, G_2 and χ are material-specific constants. The angle θ describes the position of Fermi surface in k space. Furthermore, Hussey introduced a parallel-resistor model to include the Mott-Ioffe-Regel limit [254]:

$$\rho \propto 1/\tau, \tag{5.9}$$

$$1/\rho_{\text{eff}} = 1/\rho + 1/\rho_{\max}. \tag{5.10}$$

It is argued that this model can give a quadratic temperature dependence of the cotangent of the Hall angle.

Recent dc transport [255, 256] and optical conductivity [257] measurements for the hole-doped cuprates revealed a remarkably simple nature of the carriers in the pseudogap regime of the hole-doped cuprates. Surprisingly, even in close proximity of the undoped insulating state, the charge carriers exhibit a scattering rate that resembles that of a Fermi liquid: below the characteristic temperature T^{**} ($T^{**} < T^*$), the dc resistivity per CuO_2 sheet was shown to exhibit a universal, quadratic temperature dependence and to be inversely proportional to the nominal hole concentration p [255]. In this part of the phase diagram, the Hall coefficient is approximately independent of temperature, takes on a value that corresponds to the nominal hole concentration p [258], and the large resistivity values can therefore be attributed to the low carrier concentration [255] and to an additional non-universal contribution related to disorder [248, 256]. Contrary to longstanding belief, it was furthermore shown that Kohler's rule for the magnetoresistvity (Kohler's rule can be described as $\Delta\rho/\rho(H = 0) \propto f(H\tau)$, i.e., the magnetoresistivity is a function of $H\tau$, where H is the magnetic field and τ is the relaxation time), a characteristic of simple metals, is obeyed, with a Fermi-liquid scattering rate ($1/\tau \propto T^2$) [256]. In addition, optical conductivity measurements revealed the temperature-frequency scaling expected for a Fermi liquid [257].

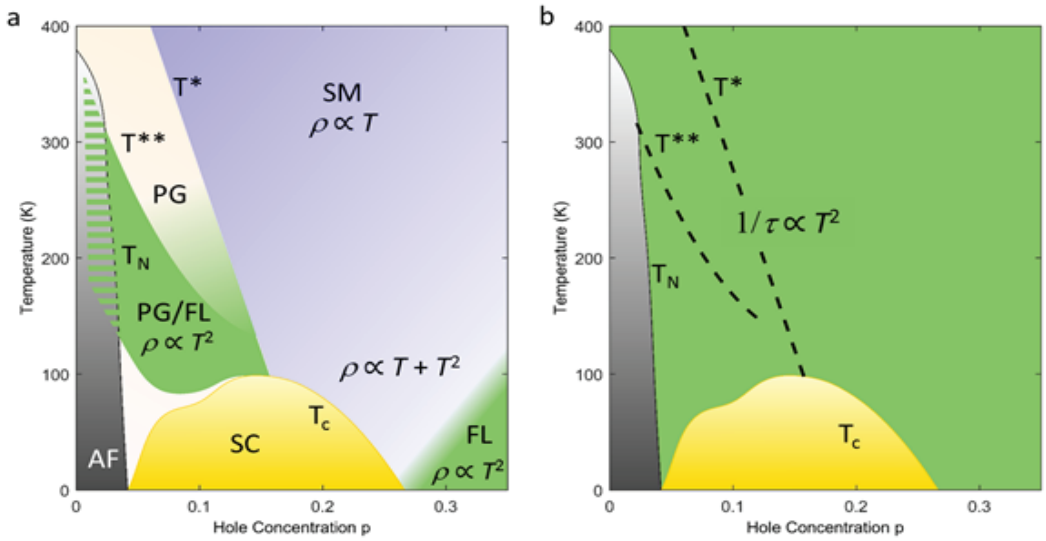

Figure 5.1: Phase diagram for the hole-doped cuprates based on *ab*-plane (a) electrical resistivity and (b) scattering rate [219]. A Fermi-liquid (FL) scattering rate is observed through our the entire phase diagram. SC: superconducting phase. SM: "strange metal" regime. AF: antiferromagnetic phase. PG: pseudogap region. Figure reproduced from [219].

As the transport properties in the hole-doped cuprates resemble those of a Fermi liquid in both the pseudogap and the over-doped metallic regimes, it is intriguing to reinvestigate them in the strange-metal regime, where the notion of quasiparticles has been suspected to break down [240]. In this regard, an important quantity to consider is the cotangent of the Hall angle, which for simple metals is proportional to the transport scattering rate, $\cot(\theta_H) = \rho/(HR_H) \propto m^*/\tau$, where R_H is Hall constant, H the magnetic field, and m^* is effective mass. It has been known for a long time [259] that $\cot(\theta_H) \propto T^2$ at temperatures $T > T^*$, i.e., in the strange-metal region, where $\rho \propto T$. In influential work, this was interpreted as the result of two distinct transport scattering rates [253]. Subsequent experiments for lightly doped $La_{2-x}Sr_xCuO_4$ indicated $\cot(\theta_H) \propto T^2$ in the pseudogap regime [258]. Remarkably, for underdoped $HgBa_2CuO_{4+\delta}$ (Hg1201), a compound that in many respects can be considered a model

cuprate system [256, 260, 261], $\cot(\theta_H) \propto T^2$ was recently found without any noticeable change upon crossing the characteristic temperatures T^* and T^{**}, thus providing a direct link between the strange metal ($T > T^*$) and pseudogap/Fermi-liquid ($T < T^{**}$) regions of the phase diagram [219]. Moreover, upon combining results for various other hole-doped cuprates, it was concluded that the transport scattering rate of the hole-doped cuprates is approximately doping and compound independent, and hence that the (Umklapp) scattering characteristics of the Fermi-liquid at high doping level prevail throughout the entire phase diagram, including the strange-metal regime. Figure 5.1 shows the schematic phase diagrams for the hole-doped cuprates based on the planar resistivity and the cotangent of the Hall angle.

For the electron-doped cuprates, early studies of the planar dc resistivity of optimally-doped NCCO crystals revealed that $\rho \propto T^2$ up to 250 K, and then deviates downward from this resistivity behavior at higher temperatures [262]. Experiments on $Pr_{2-x}Ce_xCuO_{4+\delta}$ (PCCO) thin films reported a scaling of the planar resistivity to a single quadratic temperature dependence from $x = 0.11$ to 0.19 at $T = 100$ to 300 K [210]. Unlike their hole-doped counterparts, $\rho \propto T$ for electron-doped cuprates was only observed relatively recently in a narrow temperature regime above T_c [263], and this was interpreted as a consequence of spin fluctuations. A $\rho \propto T^{1.6}$ power-law behavior was reported for $La_{2-x}Ce_xCuO_{4-\delta}$ (LCCO) from $x = 0.15$ to 0.18 and associated with the Liftshitz transition of the Fermi surface [264]. The cotangent of the Hall angle was found to exhibit a complex temperature dependence [210]. In addition, a large resistivity upturn was observed at low temperatures in the under-doped regime.

5.2 Universal *ab*-plane charge transport properties

5.2.1 Universal scaling of resistivity coefficients

Low-temperature compound-specific upturns have been observed in both the electron- and the hole-doped cuprate superconductors, such as the hole-doped cuprates LSCO, YBCO and $Bi_2Sr_{2-x}La_xCu_2O_{8+\delta}$ (La-Bi2201) and the electron-doped cuprates NCCO, PCCO and $Pr_{1.3-x}La_{0.7}Ce_xCuO_{4-\delta}$ (PLCCO). The magnitude of this upturn appears to be material specific (e.g.[42, 245–248]), and its physical origin has been under debate [42]. Note that this low-temperature resistivity upturn has so far not been observed

in $HgBa_2CuCuO_{4+\delta}$ (Hg1201). Hg1201 is regarded a model compound and believed to feature minimal disorder effects [261].

It was proposed that the resistivity minimum and upturn may be caused by (1) three-dimensional Kondo scattering (which involves interactions between conduction electrons and magnetic impurities) [265, 266], (2) disorder-driven two-dimensional weak localization (localization caused by wave function interference primarily due to self-intersecting scattering paths) [267, 268], (3) a spin scattering process in the antiferromagnetic phase [214], (4) scattering due to magnetic droplets near the antiferromagnetic phase [269, 270], or (5) a logarithmic decrease in the carrier density [271]. Those proposals are unlikely to explain all of the experimental results. For example, the resistivity upturn has been observed in both *ab*-plane and *c*-axis transport experiments (renders two-dimensional weak localization unlikely). It was also observed both within and outside of the antiferromagnetic phase (renders Kondo scattering, spin scattering processes in the antiferromagnetic phase, and scattering due to magnetic droplets near the antiferromagnetic phase unlikely). Evidence for charge localization was found from Hall measurements only at temperatures much lower than the temperature at which the logarithmic resistivity upturn appears, renders the possibility that the resistivity upturn is due to a logarithmic decrease in carrier density unlikely.

In most previous studies, specific temperature ranges were considered based on the predominant temperature dependence of the resistivity, and resistivity data were separately analyzed in each temperature range. For example, in the hole-doped cuprates, the pseudogap temperature (T^*) is the temperature below which the planar resistivity deviates from $\rho \propto T$ [240], and the temperature scale T^{**} was defined as the onset temperature of the $\rho \propto T^2$ behavior [255]. Prior estimates of the scattering rate based on data for the cotangent of the Hall angle ($\cot \theta_H$) were only performed in the temperature and doping ranges where $\cot \theta_H \propto T^2$ [219, 258]. These analyses, which focused on specific temperature ranges and did not address material-specific issues, tend to result in complex behavior of transport properties that hard to understand. For example, as we will see for the electron-doped cuprates, the resistivity upturn can mask a rather conventional underlying intrinsic scattering rate.

It is instructive to recall the systematic study of initially very clean, hole-doped YBCO samples that were subsequently exposed to electron-beam irradiation [248].

Upon increasing the radiation dose, the intrinsic resistivity $\rho_i(T) \propto T^2$ was found to be enhanced by a temperature-independent contribution ρ_0 and a low-temperature upturn, $\Delta\rho(T)$ (Fig. 5.2). The latter appears to originate from local inhomogeneity and/or disorder. In order to capture the distinct contributions, the resistivity was decomposed into three terms [248]:

$$\rho = \rho_0 + \Delta\rho(T) + \rho_i(T). \tag{5.11}$$

Except at very low doping levels and temperatures, $\Delta\rho(T)$ exhibits a logarithmic temperature dependence in YBCO.

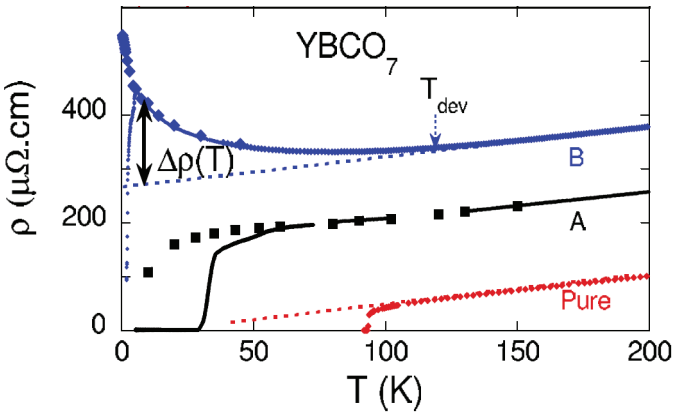

Figure 5.2: Resistivity taken in zero magnetic field (solid lines), its high-temperature extrapolation (dotted lines), and data taken in high magnetic field (symbols) for $YBaCuO_7$. Disorder amount: Pure < A < B. A resistivity upturn is observed for sample B. Figure reproduced from [248].

In this Chapter, the dc resistivity for various electron- and hole-doped cuprate materials is analyzed using a similar method but without fixing any parameters (i.e., the prefactor of $\rho_i(T)$ was not determined from a high-temperature fit). The sample information is listed in Tables A.3 and A.4. We follow the evolution of the three resistivity contributions (Eq. 5.11) as a function of doping concentration for a large number of compounds (electron-doped NCCO [53, 276–279], $La_{2-x}Y_xCuO_{4+\delta}$ (LYCO) [274], PCCO[208, 270, 280, 281], PLCCO [282], and $La_{2-x}Ce_xCuO_{4+\delta}$ (LCCO) [175]; the hole-doped LSCO [245, 272], YBCO [248, 272, 273] and La-Bi2201 [246, 275]). This detailed analysis of new and published result enables us to clearly observe $\rho_i(T) \propto T^2$

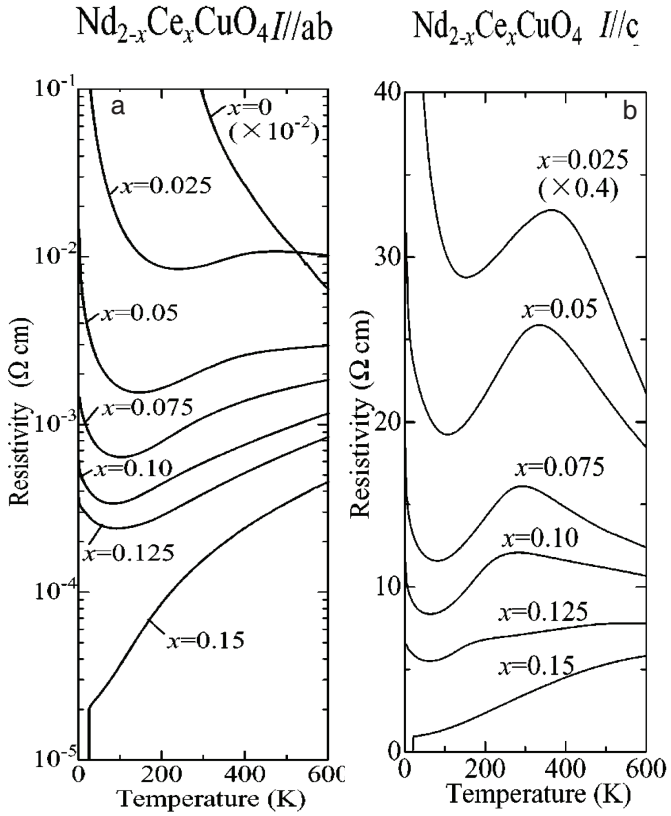

Figure 5.3: Previously reported *ab*-plane and *c*-axis resistivity for NCCO [53]. (a) The *ab*-plane resistivity. (b) The *c*-axis resistivity. Figure reproduced from [53].

and $\Delta\rho(T) \propto -\log(T)$ behavior and to demonstrate its universality across different cuprate compounds.

In order to analyze resistivity data systematically, Eq. 5.11 was rewritten into two identical forms:

$$\rho = \rho_{\rm res} - A_{\log}\log(T/T_{\log}) + A_2T^2, \tag{5.12}$$

$$\rho = A_0 - A_{\log}\log(T/1K) + A_2T^2, \tag{5.13}$$

where $\rho_{\rm res}$ is the residual resistivity at $T = 0$ and $A_0 = \rho_{\rm res} + A_{\log}\log(T_{\log}/1K)$.

Representative *ab*-plane resistivity data for various cuprate materials are shown in

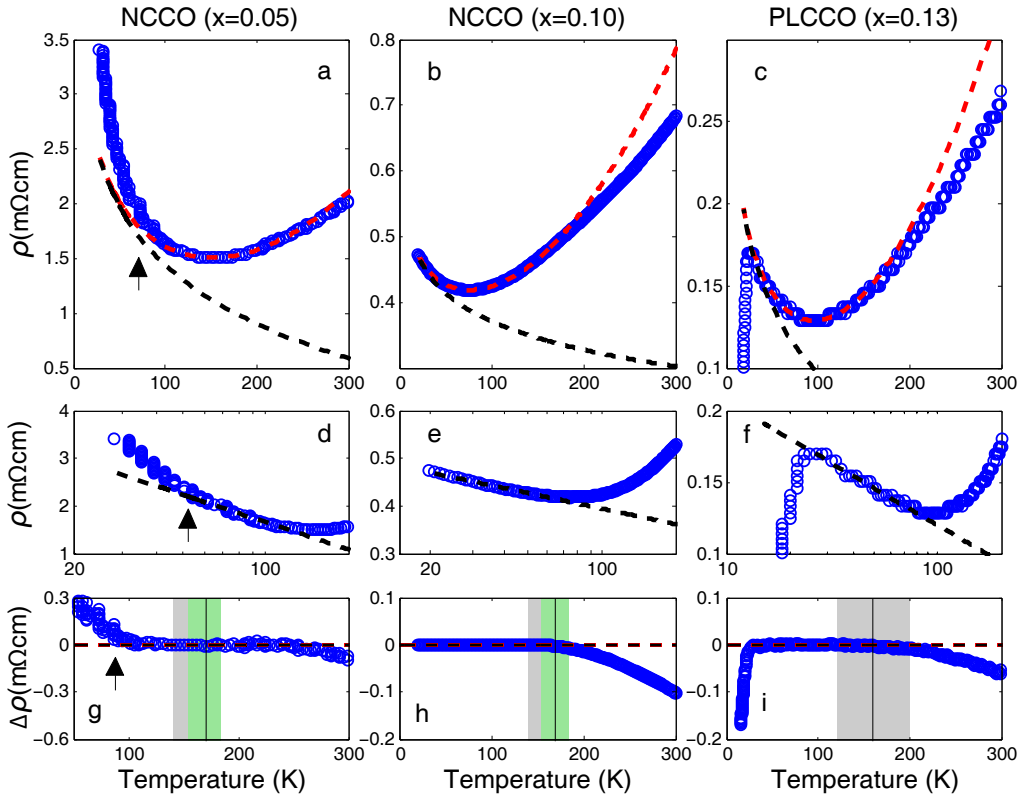

Figure 5.4: Planar resistivity for three electron-doped cuprates. (a, b, c) Raw data (blue circles) are fit to Eq. 5.13 (red dashed curves). The estimated contributions $A_0 - A_{\log} \log(T/1K)$ are shown as black dashed lines. (d, e, f) Semilog plots of the resistivity. The dashed lines indicate the logarithmic contributions. (g, h, i) Differences between raw data and fits. Horizontal black dashed lines indicate zero difference. Black vertical lines indicate the temperatures above which the fits deviate from the data. Grey shaded bands indicate the temperature range in which the underlying quadratic temperature dependence of the planar resistivity breaks down. Arrows indicate the temperature (T_d) below which there is a clear deviation from logarithmic behavior in lightly doped NCCO. The Néel temperature of $x = 0.10$ NCCO obtained via neutron scattering is shown as a green shaded band [55]. The resistivity data for $x = 0.10$ NCCO are cut off at $T \approx 15$ K to avoid nonuniversal traces of filamentary superconductivity present in this particular sample. The $x = 0.05$ NCCO data are taken from [53]. Figure reproduced from [211].

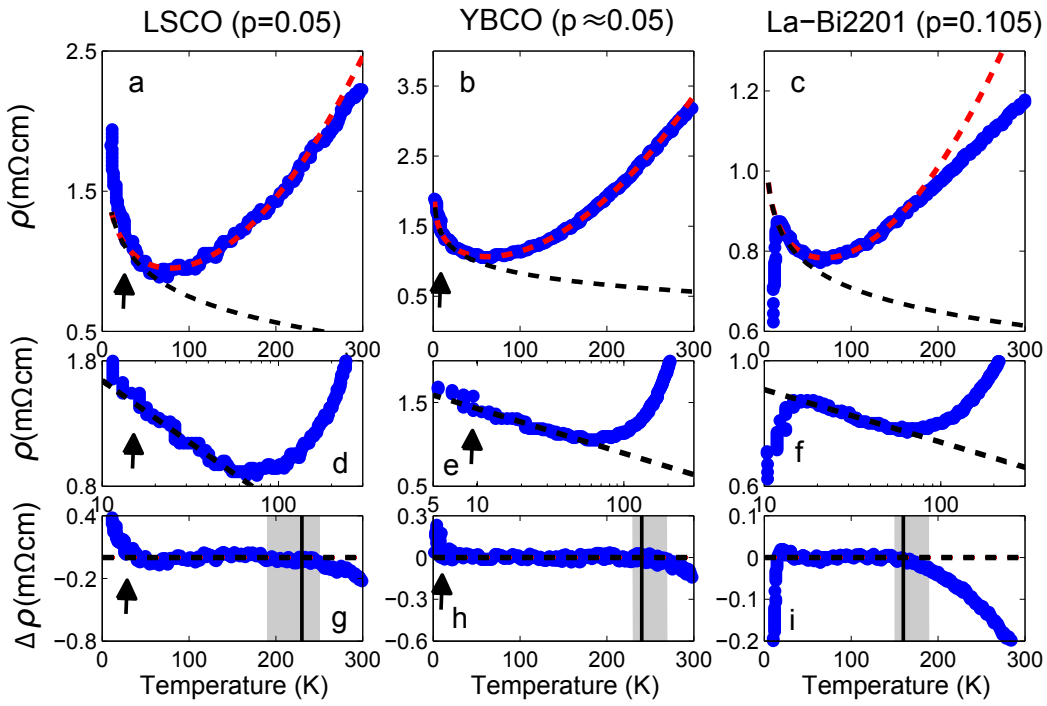

Figure 5.5: Planar resistivity of several hole-doped cuprate materials. (a-c) Raw data (blue circles) and fit to Eq. 5.13 (red dashed curves). The estimated contributions $A_0 - A_{\log}\log(T/1K)$ are shown as black dashed lines. (d-f) Semilog plots of the resistivity. The dashed lines indicate the logarithmic contributions. (g-i) Differences between raw data and fits. Horizontal black dashed lines indicate zero difference. Black vertical lines indicate the temperatures above which the fits deviate from the data. Grey shaded bands indicate the temperature range in which the underlying quadratic temperature dependence of the planar resistivity breaks down [272]. Arrows indicate the temperature (T_d) below which there is a clear deviation from logarithmic behavior in lightly doped LSCO and YBCO. Figure reproduced from [211].

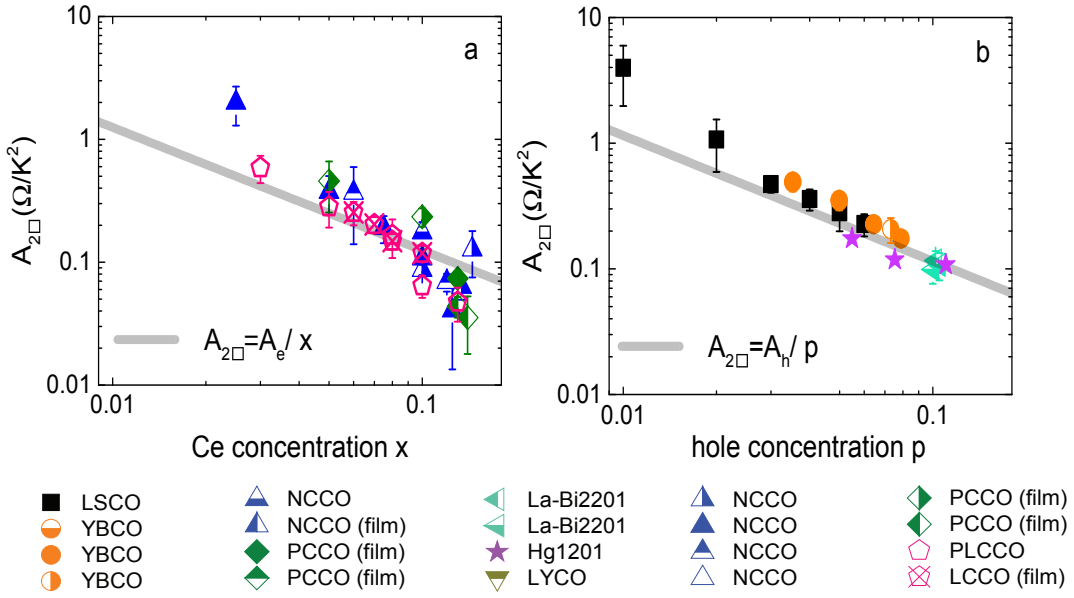

Figure 5.6: Doping dependence of $A_{2\square}$ for (a) the electron- and (b) the hole-doped materials, as obtained from fits to Eq. 5.13. Grey lines are guides to the eye and indicate $1/x$ and $1/p$ dependences, respectively. Error bars are one standard deviation, estimated from fits with various temperature ranges. Data analyzed from [53, 208, 219, 246, 248, 255, 270, 272–282] (see Tables A.3 and A.4). Figure reproduced from [211].

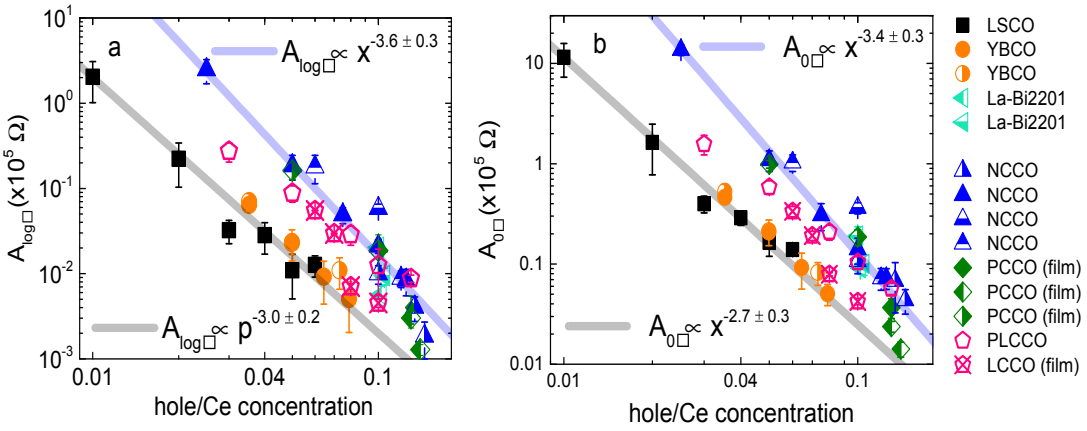

Figure 5.7: Doping dependences of (a) $A_{\log\square}$ and (b) $A_{0\square}$. Estimated power-law index for the electron-doped materials (blue lines) is larger than that for the hole-doped materials (grey lines). Data analyzed from [53, 208, 219, 246, 248, 255, 270, 272–282] (see Tables A.3 and A.4). Figure reproduced from [211].

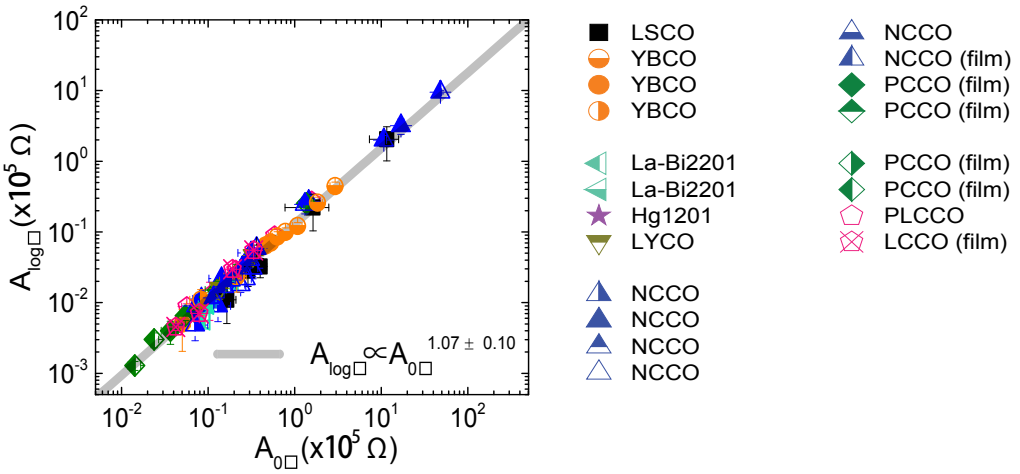

Figure 5.8: Scaling between $A_{\log\square}$ and $A_{0\square}$. Grey line is the result of a power-law fit and shows an approximate linear proportionality. Error bars are one standard deviation estimated from varying the temperature ranges of the fits. Data analyzed from [53, 208, 219, 246, 248, 255, 270, 272–282] (see Tables A.3 and A.4). Figure reproduced from [211].

Fig. 5.4 and Fig. 5.5. The data were fit using Eq. 5.13 with the Levenberg-Marquardt nonlinear least-squares algorithm with A_0, $A_{\log}$ and A_2 as fit parameters [283, 284]. For the hole-doped cuprates, Eq. 5.13 describes the data below T^{**} associated with the onset of a quadratic temperature dependence. For NCCO, Eq. 5.13 describes the data below the Néel temperature. These two characteristic temperatures are associated with significant changes in the Hall constant, R_H, which suggests a delocalization of charge upon heating above these temperatures.

In order to compare the resistivity coefficients between different compounds [255], A_2, A_0 and $A_{\log}$ were converted to the respective sheet resistance coefficients $A_{2\square}$, $A_{0\square}$ and $A_{\log\square}$, which correspond to the resistance of a single copper-oxygen sheet. As shown in Fig. 5.6, $A_{2\square}$ for the electron- and the hole-doped cuprates follows simple $A_{2\square} = A_e/x$ and $A_{2\square} = A_h/p$ behaviors, respectively. Remarkably, the absolute values of $A_{2\square}$ at same nominal doping level for the electron- and the hole-doped materials are very similar (i.e., $A_e \approx A_h$), despite the overall asymmetry of the phase diagram with regard to hole and electron doping. At low doping levels, the low-temperature resistivity upturn can

no longer be well described by the logarithmic contribution (Figs. 5.4 and 5.5). At low doping, the upward deviation of $A_{2\square}$ from a simple power-law dependence (see Fig. 5.6) might indicate a subtle difference between nominal and effective doping concentrations. The full data can be well described by $A_{2\square} = A_e/x_{\text{eff}}$ with $x_{\text{eff}} = x - 0.008$ and $A_{2\square} = A_h/p_{\text{eff}}$ with $p_{\text{eff}} = p - 0.008$. Overall, these simple relationships suggest that, in the under-doped regime, the density of mobile charge carriers is proportional to the density of doped electrons or holes.

The doping dependences of $A_{0\square}$ and $A_{\log\square}$ are shown in Fig. 5.7. At the same nominal doping concentration, the two coefficients are nearly an order of magnitude larger for the electron-doped compounds. Consequently, the resistivity upturn tends to mask the intrinsic resistivity behavior much more strongly than in the hole-doped cuprates. Note that $A_{0\square}$ and $A_{\log\square}$ are smaller for systems in which the rare earth element has a small magnetic moment compared to NCCO, such as PLCCO and LCCO. Similar to $A_{2\square}$, these coefficients exhibit power-law doping dependences: $A_{\log\square} \propto x^{-3.6\pm0.3}$ and $A_{0\square} \propto x^{-3.4\pm0.3}$ (electron doping) and $A_{\log\square} \propto p^{-3.0\pm0.2}$ and $A_{0\square} \propto p^{-2.7\pm0.3}$ (hole doping).

Treating the doping level as an implicit parameter, Fig. 5.8 shows $A_{\log\square}$ versus $A_{0\square}$, which reveals an approximate linear universal scaling that holds over many orders of magnitude. This demonstrates that the logarithmic resistivity upturn, when appears, behaves the same in all cuprates, and it also implies that the dominant contribution to A_0 is not residual elastic impurity scattering (recall that $A_0 = \rho_{\text{res}} + A_{\log}\log(T_{\log}/1K)$). These observations point to a single mechanism that universally governs the appearance of the resistivity upturns in both the electron- and the hole-doped cuprates.

5.2.2 Phase diagram based on charge transport

An intriguing trend is seen for various cuprate materials, upon superimposing $T_{\log}$ and T_d (the temperature T_d below which the logarithmic function no longer describes the resistivity upturn) on the phase diagram. As shown in Fig. 5.9, for both electron-doped (NCCO, PCCO and PLCCO) and hole-doped (LSCO and YBCO) cuprates, T_d extrapolates to zero temperature approximately at the doping level at which superconductivity emerges. Interestingly, $T_{\log}$ seems to track T_d, but non-zero $T_{\log}$ values are still observed for superconducting samples. The resistivity upturn is observed to exist

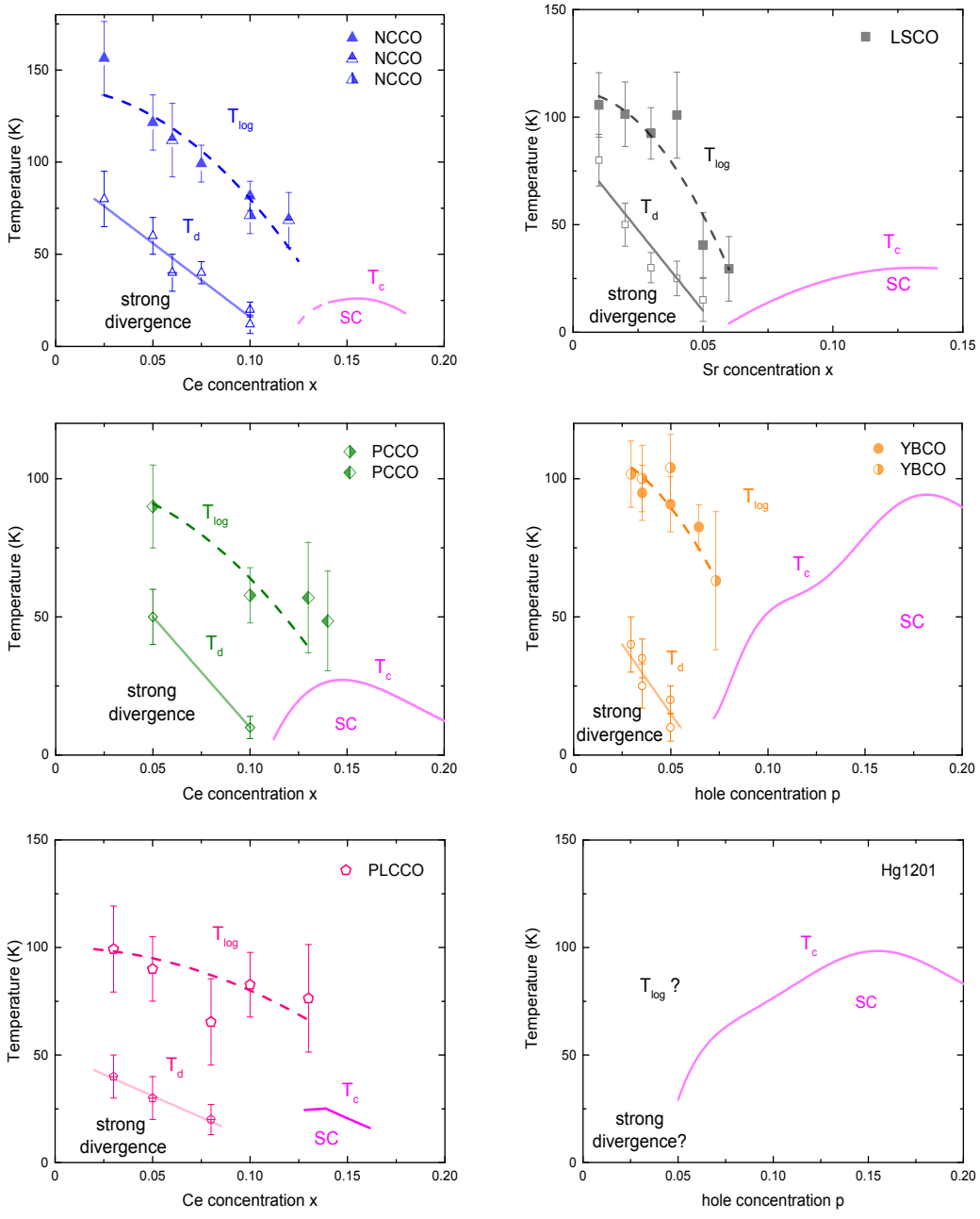

Figure 5.9: Phase diagrams for various cuprate materials showing T_c, $T_{\log}$, and T_d. Intriguingly, T_d roughly extrapolates to zero temperature at the doping concentration where superconductivity emerges.

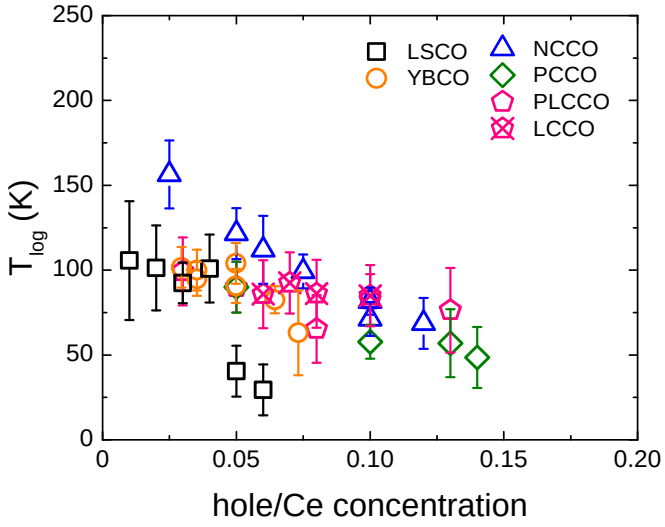

Figure 5.10: Doping dependence of $T_{\log}$ obtained for various cuprate materials. $T_{\log}$ is on the order of 50 - 150 K and exhibits a very similar, monotonic doping dependence for all materials, pointing to a single mechanism that universally governs the appearance of the resistivity upturn in both the electron- and the hole-doped cuprates. Data analyzed from [53, 208, 219, 246, 248, 255, 270, 272–282] (see Tables A.3 and A.4). Figure reproduced from [211].

deep in the antiferromagnetic phase for the electron-doped cuprates and for hole-doped cuprate LSCO ($x = 0.01$). In Hg1201, no resistivity upturn has been observed down to lowest achievable doping level ($p \approx 0.05$ [219, 255]) and $A_{0\square}$ is zero. Therefore, a pivotal open question is whether the non-superconducting phase at low doping is intrinsically an insulator or a metal in this model cuprate. Figure 5.10 compares $T_{\log}$ of various materials as a function of doping concentration. The approximately linear scaling between $A_{\log\square}$ and $A_{0\square}$ (Fig. 5.8) suggests that $T_{\log}$ in Eq. 5.12 does not vary considerably and that $\rho_{res} \approx 0$ in respect to the logarithmic contribution (recall that $A_0 = \rho_{res} + A_{\log} \log(T_{\log}/1K)$). Indeed, $T_{\log}$ is on the order of 50-150 K and exhibits a very similar monotonic doping dependence for all materials in which a low-temperature resistivity upturn is observed.

The free-parameter fit and the fit with A_2 determined at high temperatures (Eq. 5.11, and in [248]) are compared in Fig. 5.11. The free-parameter fit gives an upper bound

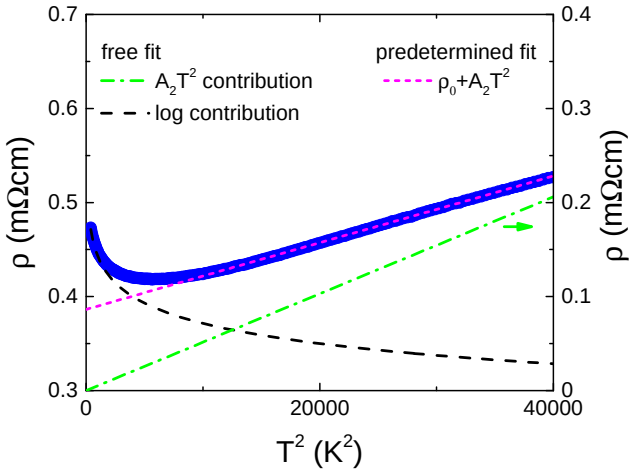

Figure 5.11: Comparison between the two fit methods for $x = 0.10$ NCCO data (blue line). In [248], A_2 was determined from a high-temperature fit (short-dashed magenta line). From the remaining low-temperature contribution, $A_{\log}$ and A_0 were obtained.The free-parameter method, applied in this Thesis work, allows all three parameters in Eq. 5.13 to vary, and the corresponding logarithmic and quadratic contributions are shown by black dashed and green dot-dashed lines, respectively (the magnitude of the quadratic contribution is shown on the right axis). The two methods give upper and lower bound of A_2 (see also Fig. 5.12).

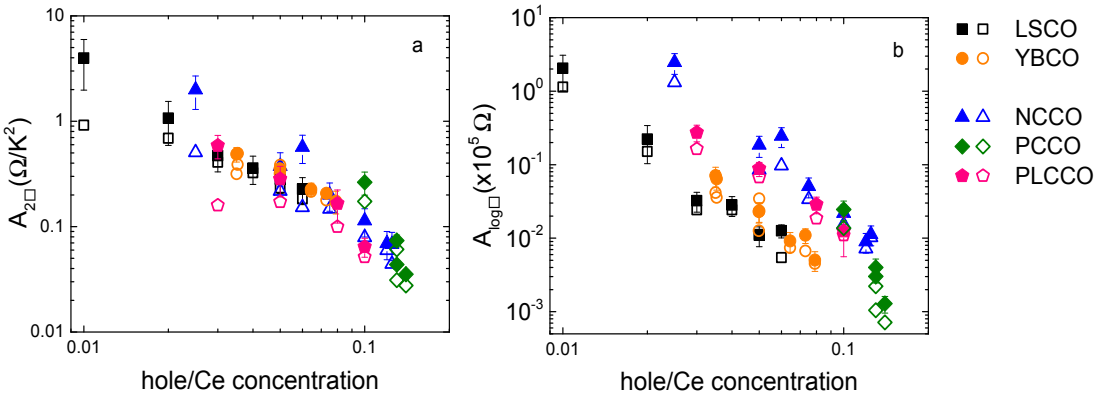

Figure 5.12: Comparison between resistivity coefficients. (a) $A_{2\square}$ and (b) $A_{\log\square}$ obtained by the two methods (see Fig. 5.11). Full and open symbols correspond to the free-fit method and the method with A_2 determined from high temperatures, respectively. The two methods give upper and lower bounds of $A_{2\square}$, and the differences become larger at lower doping levels. $A_{2\square}$ exhibits approximately the same magnitude and doping dependence for the hole- and the electron-doped materials, whereas $A_{\log}$ is significantly larger for the the electron-doped cuprates.

of A_2 and the fit with A_2 determined at high temperatures give a lower bound of A_2. $A_{2\square}$ and $A_{\log\square}$ obtained by the two methods are summarized in Fig. 5.12.

5.2.3 Universal scattering rates

Motivated by the recent finding of a universal scattering rate throughout the phase diagram of the hole-doped cuprates [219], this Section focuses on the scattering rate of the electron-doped cuprates. The scattering rate τ was obtained from the cotangent of the Hall angle, $\cot(\theta_H) = \rho/(HR_H) \propto m^*/\tau$, where ρ denotes the planar resistivity ($\rho = m^*/ne^2\tau$ in the Drude model for conventional systems), R_H denotes the Hall constant ($R_H = 1/ne$ for conventional systems with a single type of charge carrier), H denotes magnetic field, m^* denotes the effective mass, n denotes charge carrier density, and e denotes electron charge. For the hole-doped cuprates LSCO, Hg1201 and Tl2201, $\cot(\theta_H) = C_0 + C_2T^2$ was observed to hold with a universal $C_2 = 0.0175(20)$ and with a compound-, doping-, disorder-dependent C_0. The effective mass m^* was argued to not depend much on compound or doping level for the hole-doped cuprates [219].

A few distinct procedures can be used to obtain $\cot(\theta_H)$ from the measured planar resistivity and Hall constant: (1) directly use $\cot(\theta_H) = \rho/(HR_H)$, where $\rho = \rho_0 + \Delta\rho(T) + \rho_i(T)$, and then fit $\cot(\theta_H)$ in the temperature range where $\cot(\theta_H) \propto T^2$; (2) use $\cot(\theta_H) = \rho_i/(HR_H)$; (3) calculate $\cot(\theta_H) = \rho/(HR_H)$, then fit $\cot(\theta_H)$ to $\cot(\theta_H) = \cot(\theta_H)_i + \cot(\theta_H)_{\log}$. $\cot(\theta_H)_i$ is the intrinsic cotangent of the Hall angle and $\cot(\theta_H)_{\log}$ corresponds to a logarithmic upturn in cotangent of the Hall angle.

Procedure (1) was used in previous studies that analyzed results for LSCO and Hg1201 [219, 258]. Similar to the method to determine A_2 based on a high-temperature fit (Section 5.2), this may lead to inaccurate results at low doping concentrations, where the resistivity upturn can be considerable. Procedures (2) and (3) are used in this Thesis work, and they are found to give very similar results (only results obtained using procedures (1) and (2) are shown in Fig. 5.16).

Procedure (2) is illustrated in Fig. 5.13 and Fig. 5.14. Once the non-universal resistivity upturn is subtracted from the total resistivity, $\cot(\theta_H)$ can be calculated as:

$$\cot(\theta_H) = \rho_i/(HR_H) = C_2T^2, \tag{5.14}$$

where $\rho_i = \rho - [A_0 - A_{\log}\log(T/1K)]$.

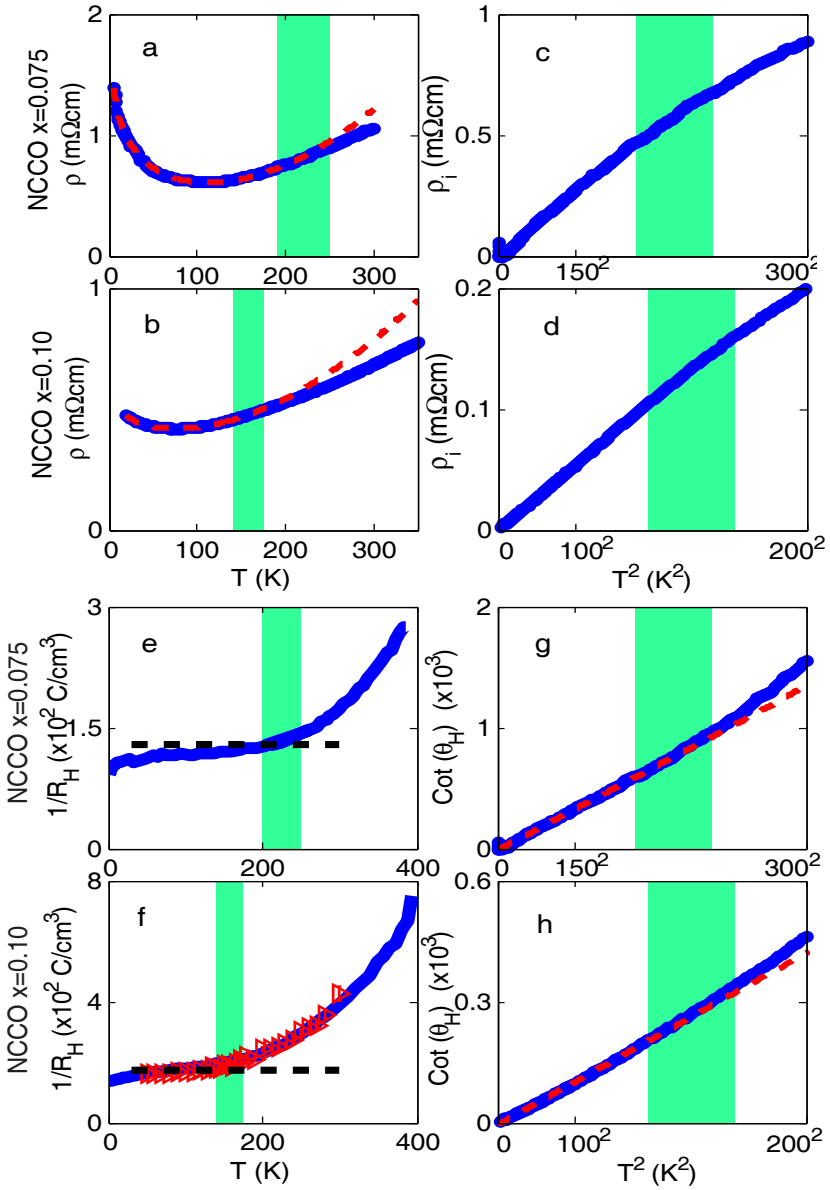

Figure 5.13: Cotangent of the Hall angle for NCCO with $x = 0.075$ and 0.10. Resistivity data and fit for NCCO with (a) $x = 0.075$ (data from [53]) and (b) $x = 0.10$ (our data as in Fig. 5.4). (c, d) Resistivity after subtraction of the logarithmic contribution estimated from the fits in (a, b). (e, f) $1/R_H$ adapted from [95]; $1/R_H$ data obtained for our NCCO ($x = 0.10$) sample (red triangles) agree with the prior work [95]. Black horizontal dashed lines indicate estimations of $1/R_H$ based on Ce concentration x. (g, h) Cotangent of the Hall angle. Red dashed lines indicate $\cot(\theta_H) \propto C_2T^2$. Green bands indicate the uncertainty in the Néel temperatures [55]. Figure reproduced from [211].

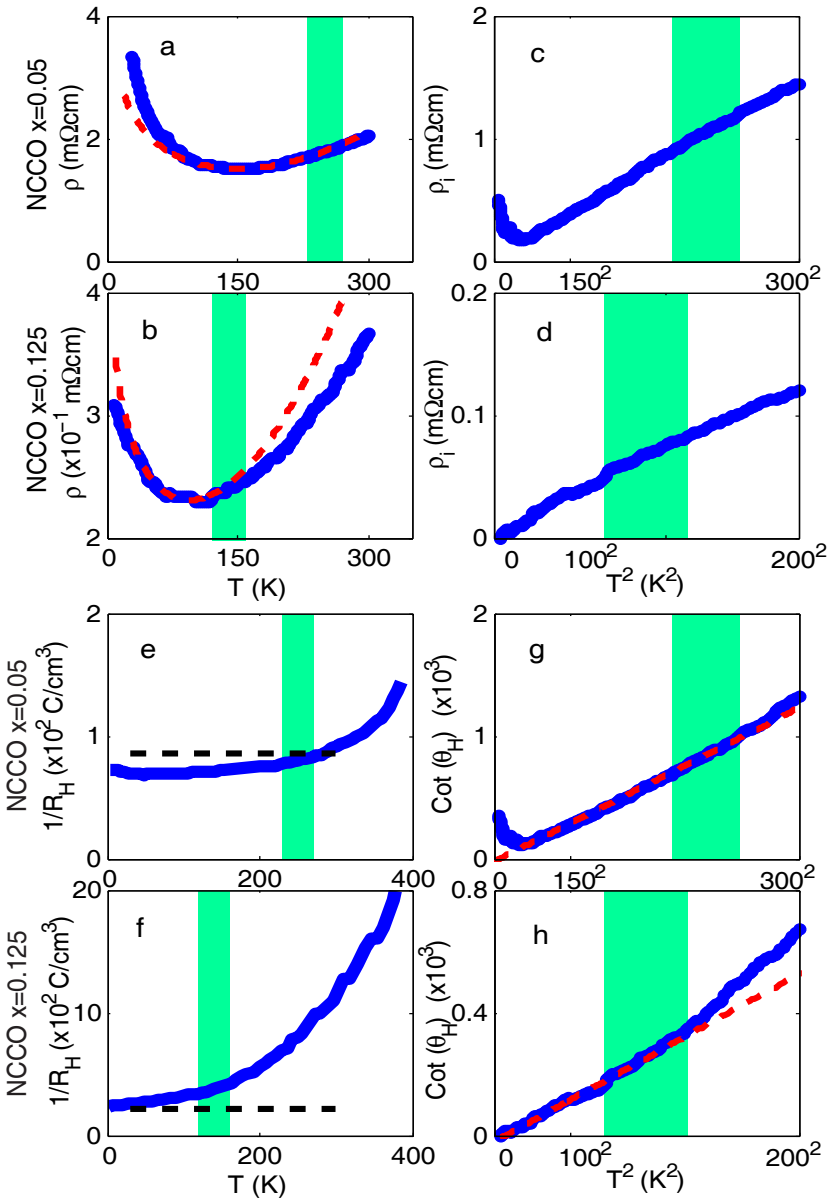

Figure 5.14: Cotangent of the Hall angle for NCCO with $x = 0.05$ and 0.125. Resistivity data and fit for NCCO with (a) $x = 0.05$ and (b) $x = 0.125$ (data from [53]). (c, d) Resistivity after subtraction of the logarithmic contribution from the fits in (a, b). (e, f) $1/R_H$ adapted from [95]. Black horizontal dashed lines indicate estimations of $1/R_H$ bsed on the Ce concentration x. (g, h) Cotangent of the Hall angle. Red dashed lines indicate $\cot(\theta_H) \propto C_2T^2$. Green bands indicate the uncertainty in the Néel temperatures [55]. Figure reproduced from [211].

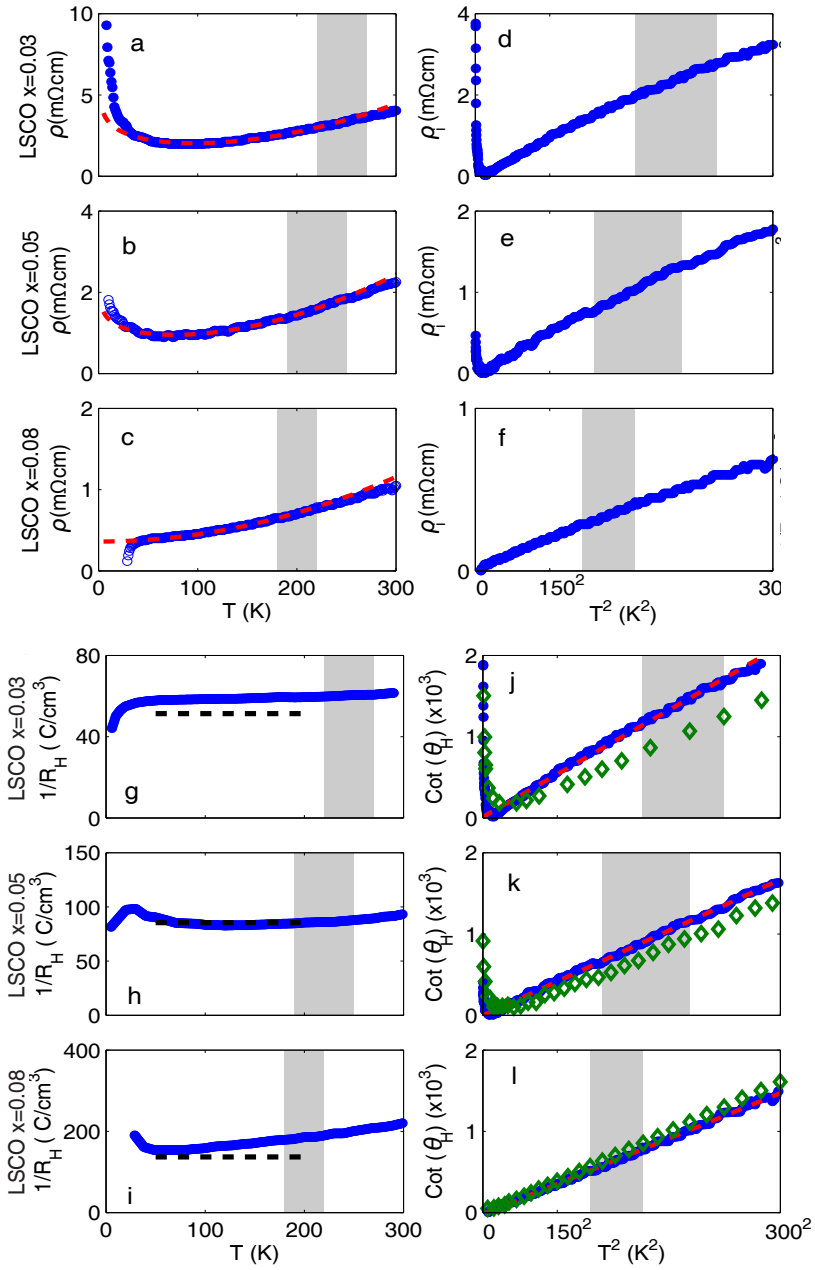

Figure 5.15: Cotangent of the Hall angle for LSCO with $x = 0.03$, 0.05 and 0.08. Resistivity data ([272, 285]) and fits for (a) $x = 0.03$, (b) $x = 0.05$ and (c) $x = 0.08$. (d-f) Resistivity after subtraction of the logarithmic contribution from the fits in (a, b, c). (g-i) $1/R_H$ adapted from [95]. Black horizontal dashed lines indicate estimations of $1/R_H$ based on the Sr concentration x. (j-l) Cotangent of the Hall angle. Red dashed lines indicate $\cot(\theta_H) \propto C_2T^2$. Green diamonds denote results in [272] or obtained with the same method in [272]. Grey bands indicate T^{**} [255]. Figure reproduced from [211].

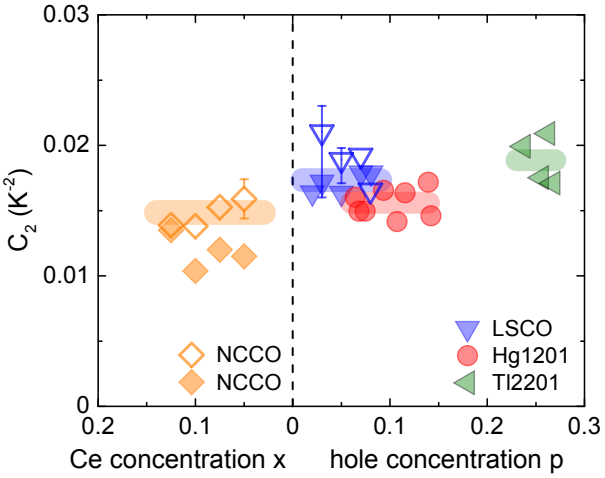

Figure 5.16: Coefficient C_2 for various cuprate materials. LSCO, Hg1201 and Tl2201 results are adapted from [219]. Open symbols were obtained using procedure (2), as described in the text. Solid symbols are reproduced from [219] (procedure (1)).

As seen from Fig. 5.13 and Fig. 5.14, the temperature dependences of the resistivity and of the inverse Hall constant (which in simple metals is proportional to the density of charge carriers) suddenly change at T_N. Using $\cot(\theta_H) = \rho/(HR_H)$, a quadratic temperature dependence of scattering rate is clearly revealed below T_N. Above the Néel temperature, $\cot(\theta_H)$ deviates from the simple quadratic temperature dependence. This coincidence suggests that, at the Néel temperature, where the long-range antiferromagnetic order breaks down due to thermal fluctuations, some of localized charges become mobile [219].

As shown in Fig. 5.15, $\cot(\theta_H)$ for LSCO ($x = 0.03$, 0.05 and 0.08) was obtained by procedure (1) (reproduced from [272]) and procedure (2) (this Thesis work). For samples with $x = 0.03$ (j) and 0.08 (l), the green diamonds denote results obtained with procedure (1) ($x = 0.03$ and 0.08 data adapted from [272, 285]. The $x = 0.05$ data were not shown in [272, 285]. For LSCO with $x = 0.05$ and 0.08, the results obtained with the two procedures agrees rather well. For $x = 0.03$ LSCO, procedure (1) gives a lower bound of $\cot(\theta_H)$, because the low-temperature upturn is ignored, whereas procedure (2) gives a upper bound of $\cot(\theta_H)$, because the low-temperature upturn was forced to

be described by a logarithmic temperature dependence (this description becomes less accurate at low doping/temperature).

Figure 5.16 summarizes the results of the coefficient C_2. The intrinsic metallic transport scattering rate of the cuprates exhibits an underlying quadratic temperature dependence and, moreover, the coefficient C_2 is nearly universal. The relatively small difference in the value of C_2 between the electron- and the hole-doped cuprates can be tentatively attributed to a difference in the effective mass. Unfortunately, no reliable measurement of m^* exists for the electron-doped cuprates in the relevant doping range, but band calculations indicate a smaller value than for of the hole-doped compounds [71, 72, 219]. The effective mass obtained from quantum oscillation measurements at higher Ce concentration ($m^* \approx 2.3$ for $x \approx 0.17$), which is 50% to 70% of that for the hole-doped cuprates, and might account for the small difference seen in C_2 in Fig. 5.16 [204].

In principle, there exist several distinct ways to understand the universal scattering rate and the resistivity upturn. The first is via Matthiessen's rule, which assumes that different scattering rates for different scattering processes simply add up ($1/\tau_{\text{total}} = 1/\tau_1 + 1/\tau_2 + ..$). A second possibility is that the dc resistivity describes a serial-resistor network, which would imply the existence of distinct metallic and non-metallic regions. A recent study revealed that Kohler's rule holds for compounds that exhibit negligible residual resistivity ($\rho_{\text{res}} \approx 0$) and Fermi-liquid behavior ($(\rho - \rho_{H=0})/\rho_{H=0} \propto H^2/\rho_{H=0}^2$, where $\rho_{H=0}$ is the zero-field resistivity) [256]. This scaling involves the orbital contribution of the magnetoresistivity and the temperature dependence of the resistivity. Kohler's rule follows directly from the Boltzmann transport equation and implies the existence of a single scattering rate. For LSCO, which exhibits a large resistivity upturn (large values of $A_{\log}$ and A_0), it was found that Kohler's rule is obeyed only if $\rho_{H=0}$ is replaced by $\rho_{H=0} - A_0$, indicating that the resistivity upturn does not contribute to the magnetoresistivity. This surprising result is incompatible with Matthiessen's rule for a homogeneous system. However, it is compatible with a serial-resistor network in which only the metalic regions contribute to the magnetoresistivity, whereas the non-metallic regions characterized by the logarithmic behavior have a negligible influence. Such upturns naturally appear at sufficiently large temperatures in systems with strongly coupled metallic grains separated by an insulating matrix [286].

5.3 Universal c-axis charge transport properties

For the hole-doped cuprates, a universal exponential insulating behavior of the c-axis resistivity was observed (in $Bi_2Sr_2CaCu_2O_{8+\delta}$, $Bi_2Sr_2Ca_2Cu_3O_{10+\delta}$ and $YBa_2Cu_3O_{7-\delta}$) [289], whereas no such universality has been established yet for the electron-doped cuprates. Previous c-axis optical conductivity studies of the electron-doped cuprates observed a depletion of low-energy optical spectral weight that coincides with a change in c-axis resistivity, indicative of the formation of the pseudogap [53]. The low-frequency c-axis optical spectra were attributed to a conventional Drude response. Quantum oscillation (Shubnikov-de Haas) measurements of the c-axis resistivity revealed small hole Fermi pockets [190, 195, 201, 204]. Theoretically, electrons (near (π, 0) and equivalent in k space) were argued to dominate the c-axis transport [193].

This Chapter reports systematic c-axis dc resistivity measurements of NCCO and compares the obtained data to previously published results. Remarkably, the c-axis resistivity of NCCO, PLCCO and SCCO, although several orders of magnitude larger than the ab-plane resistivity, is described by Eq. 5.13 in the antiferromagnetic phase. Above T_N, a deviation from this behavior appears that is most prominent at lower doping. Just as for the ab-plane resistivity, this deviation can be associated with delocalization of electrons due to the breakdown of the antiferromagnetic order.

Representative c-axis resistivity data for NCCO are shown in Fig. 5.17. The data were fit by Eq. 5.13 using Levenberg-Marquardt nonlinear least-squares algorithm with A_0, A_{log} and A_2 as fit parameters [283, 284]. The resistivity upturn appears at much higher temperatures than for the ab-plane measurements. Similar to the ab-plane resistivity, the upturn at low doping and low temperature can no longer be described by a logarithmic contribution.

As shown in Fig. 5.18, $A_{2,c}$ for the electron-doped cuprates follows a simple $A_{2,c} \propto 1/x_{\rm eff}$ behavior, with $x_{\rm eff}$ between $x - 0.01$ and $x + 0.015$. The c-axis $A_{2,c}$, unlike A_2 obtained from ab-plane measurements, levels off at the boundary between the LR-AF phase and the mixed phase. The doping dependence of $A_{0,c}$ and $A_{\log,c}$ are $A_{\log,c} \propto x^{-2.8\pm0.2}$ and $A_{0,c} \propto x^{-2.4\pm0.2}$.

Treating the doping level as an implicit parameter, comparisons among $A_{2,c}$, $A_{\log,c}$ and $A_{0,c}$ are shown in Fig. 5.19. An approximately linear scaling over many orders

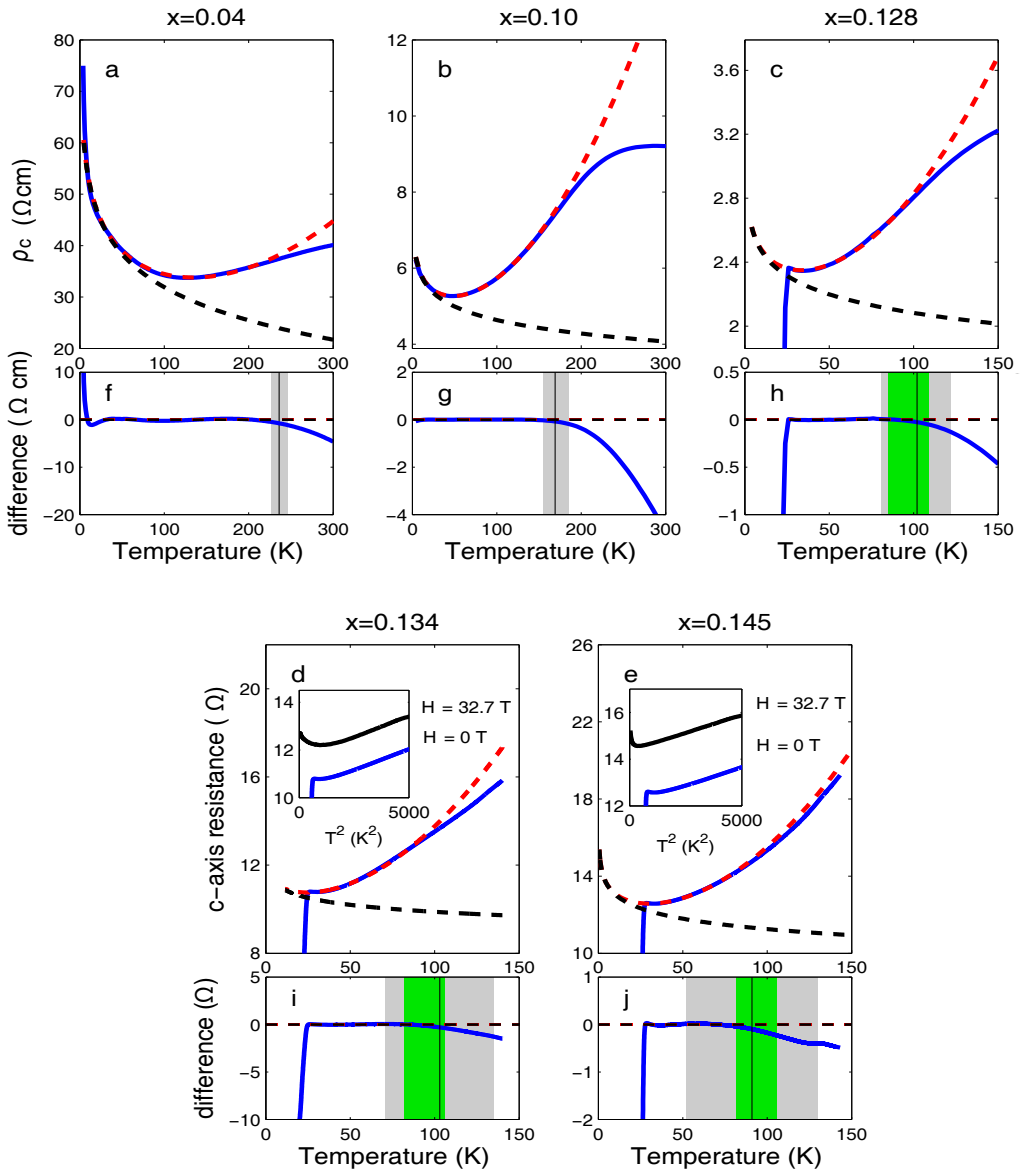

Figure 5.17: Temperature dependence of c-axis resistivity for NCCO at five doping levels. (a-c) Raw resistivity data (blue solid curves) and fits (red dashed curves) to Eq. 5.13. $A_0 - A_{\log}\log(T/1K)$ is shown as black dashed lines. (d, e) c-axis resistance data (blue solid curves) and fits (red dashed curves) to Eq. 5.13. Blue (black) curves are resistance at zero (H = 32.7 T, H//c) magnetic field. (f-j) Difference between raw data and fits (blue solid curves). Black vertical lines denote Néel temperature estimated ($T_{\rm N}$) [55]. Grey shaded areas correspond to a Gaussian distribution of $T_{\rm N}$ due to chemical inhomogeneity [40]. Green shaded areas indicate from deviation of the difference between data and fits. See Tables A.5 for sample information.

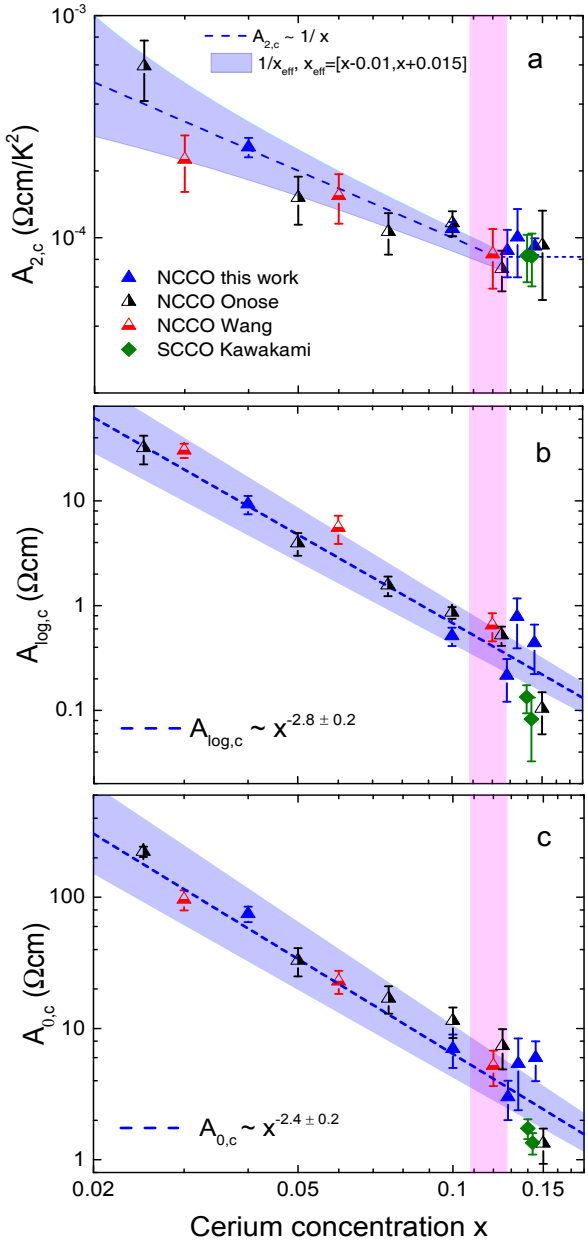

Figure 5.18: Doping dependences of the coefficients $A_{2,c}$, $A_{\log,c}$ and $A_{0,c}$ from fits of ρ_c to Eq. 5.13. The vertical magenta shaded band indicates the boundary between the LR-AF phase and the mixed phase. (a) Doping dependence of $A_{2,c}$. The dashed line and shaded area show $A_{2,c} \propto 1/x_{\text{eff}}$, where x_{eff} is estimated to lie between $x - 0.01$ and $x + 0.015$. $A_{2,c}$ appears to level off in the mixed phase. (b) and (c) show the doping dependences of $A_{\log,c}$ and $A_{0,c}$, respectively. Blue dashed lines indicate fits to power-law dependences, and the shaded bands indicate the uncertainty (± 0.2) in the exponent obtained from the fits. Data analyzed from [53, 276, 287, 288] (see Tables A.5).

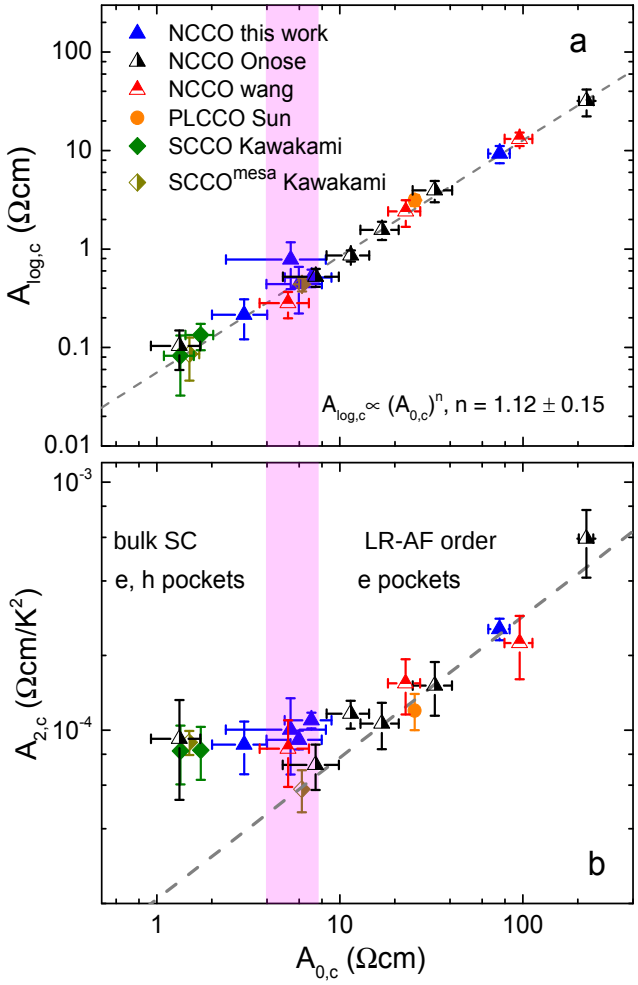

Figure 5.19: Scaling among $A_{2,c}$, $A_{\log,c}$ and $A_{0,c}$. (a) Scaling between $A_{\log,c}$ and $A_{0,c}$. (b) Scaling between $A_{2,c}$ and $A_{0,c}$. Dashed line in (a) and (b) indicate a power-law dependence and guide to the eye, respectively. Magenta shaded bands indicate the approximate boundary between the LR-AF phase and the mixed phase region. Across this boundary, the Fermi surface evolves from having electron (e) pockets only (LR-AF phase) to the both electron and hole (h) pockets (bulk superconducting (SC) phase). $A_{2,c}$ appears to level off in the mixed phase. Data analyzed from [53, 276, 282, 287, 288] (see Tables A.5).

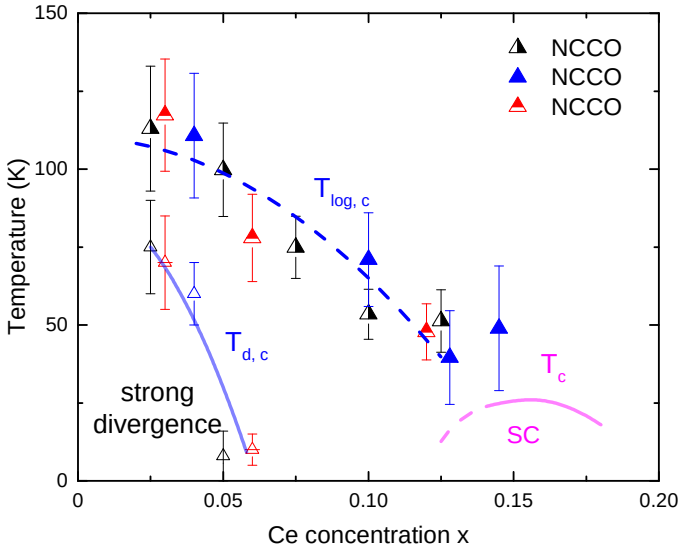

Figure 5.20: $T_{\log,c}$ and strong divergence regime from c-axis resistivity superimposed on phase diagram of NCCO. Data adapted from [53, 276, 277] (see Tables A.5).

of magnitude is observed between $A_{\log,c}$ and $A_{0,c}$. This implies that, for the c-axis transport, the dominant contribution to $A_{0,c}$ is not related to elastic impurity scattering (recall that $A_{0,c} = \rho_{res,c} + A_{\log,c}\log(T_{\log,c}/1K)$). There also exists approximately linear scaling between $A_{2,c}$ and $A_{0,c}$, but this scaling breaks down in the vicinity of the phase boundary between the LR-AF phase and the mixed phase region.

Similar to Fig. 5.9, Fig. 5.20 compares $T_{\log,c}$, $T_{d,c}$ and T_c. In contrast to the observation for the ab-plane transport, the strong divergence regime does not extrapolate to zero temperature at the doping concentration where superconductivity emerges. Both $T_{\log}$ and $T_{\log,c}$ are on the order of 50-150 K and exhibit a very similar monotonic doping dependence.

5.4 Discussion

Universal T^2 scattering rate

Figure 5.16 implies a nearly universal T^2 transport scattering rate in the electron- and the hole-doped cuprate materials, given that the effective mass is thought to depend

only weakly on material, doping concentration, and dopant type. Since this universal behavior includes the Fermi liquid at high hole-doping concentrations, it appears to be the consequence of the Umklapp scattering process which involves electron-electron scattering [219]. Remarkably, this scattering rate was also observed in the strange metal regime (Fig. 5.1), where the notion of Fermi-liquid quasiparticles was questioned [61].

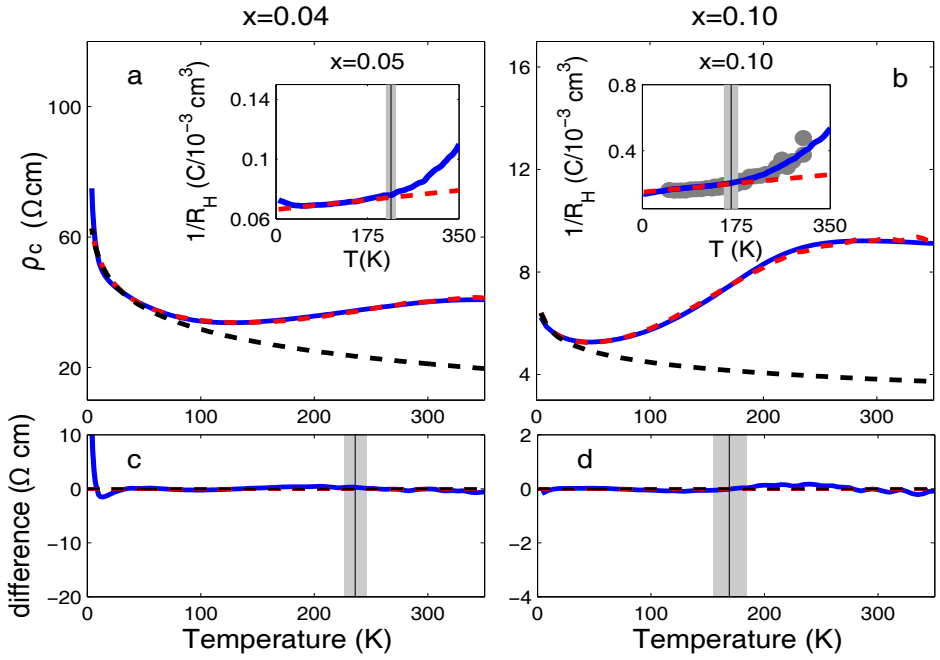

Figure 5.21: Analysis of c-axis resistivity based on Eq. 5.15. (a, b) Our c-axis resistivity data (blue solid curves) and fit (red dashed curves) to Eq. 5.15. The contributions $A_0 - A_{\log} \log(T/1K)$ are shown as black dashed lines. Insets of (a, b) are inverse of ab-plane Hall constant (grey circles: this Thesis work. Blue curves: [95]). Red dashed lines are guides to eye for the low-temperature dependence. The analysis of the $x = 0.04$ data uses R_H for the $x = 0.05$ NCCO [95]. (c, d) Difference between data and fits (blue solid curves). Black vertical lines show $T_{\rm N}$. Grey shaded areas correspond to a Gaussian distribution of $T_{\rm N}$ due to chemical inhomogeneity [40].

As discussed in [219], the universal scattering rate found throughout the hole-doped part of the phase diagram suggests a single scattering mechanism. When interpreted in the simplest manner, this implies that the pseudogap phenomenon signifies the gradual

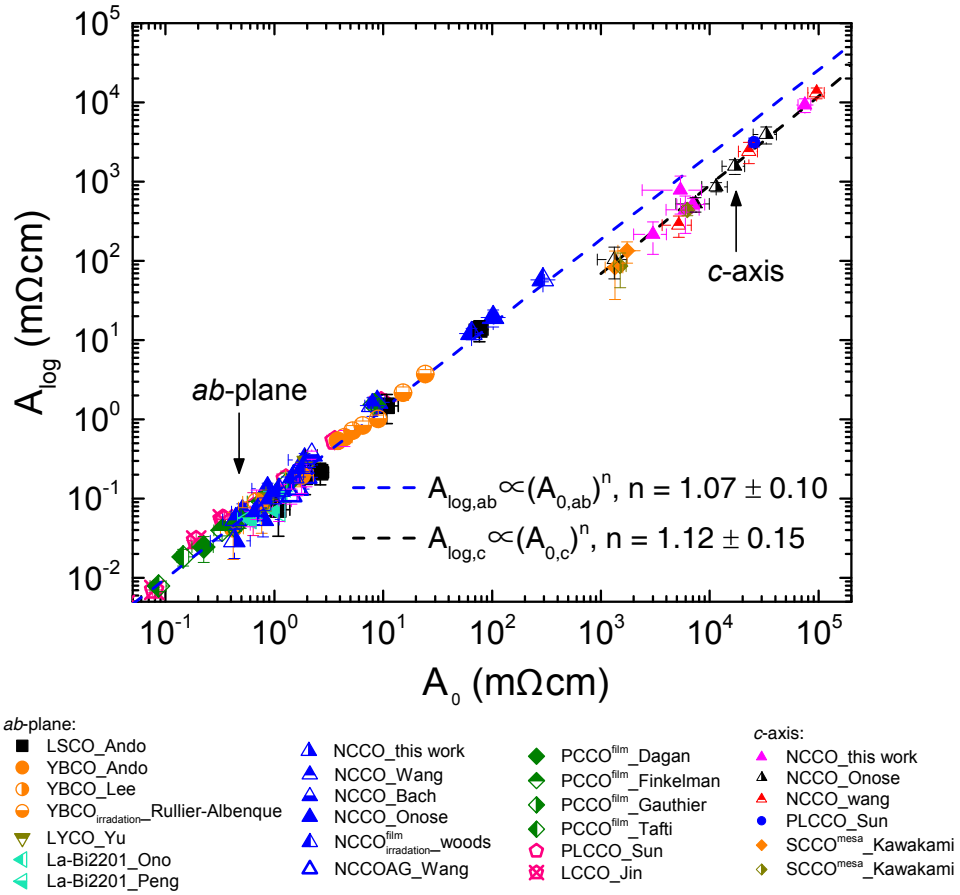

Figure 5.22: Scaling between coefficients $A_{\log}$ and A_0 obtained from Eq. 5.13 for both *ab*-plane and *c*-axis resistivity. Dashed lines are results of power-law fits that give exponents of $n = 1$, within one standard deviation. Data analyzed from [53, 175, 208, 219, 246, 248, 255, 270, 272–274, 274–282] (see Tables A.3, A.4 and A.5).

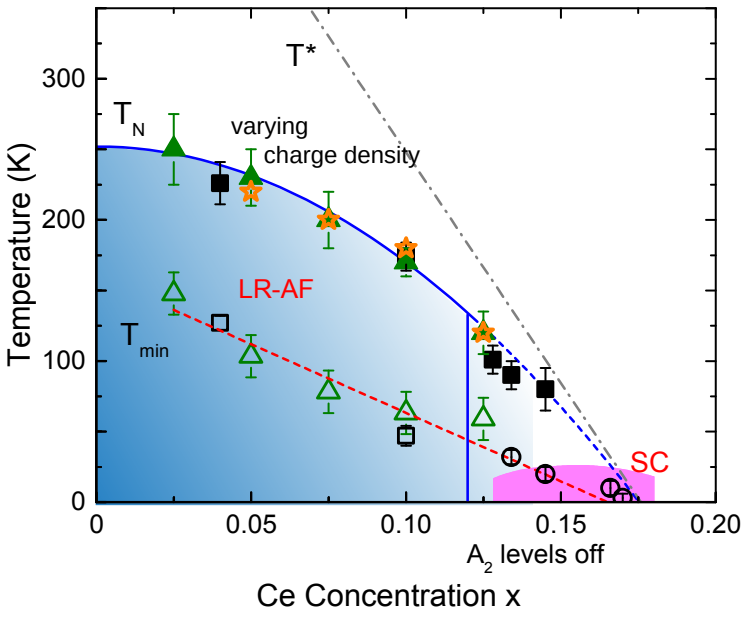

Figure 5.23: Connection between transport properties and the magnetic phase diagram for NCCO subjected to standard oxygen reduction. The pseudogap temperature [53] and the LR-AF phase boundary [55] are presented as gray dot-dashed and blue solid lines, respectively. The blue dashed line denotes the apparent $T_{\rm N}$ measured by quasi-elastic neutron scattering (Chapter 3). The magenta region indicates the superconducting phase. Full black squares (our data) and green triangles (data analyzed from [53]) show temperatures above which c-axis resistivity deviates from Eq. 5.13 (coincide with the apparent $T_{\rm N}$). Orange stars denote temperatures above which $1/R_H$ begins to increase dramatically. Black empty squares (our data) and green empty triangles (data analyzed from [53]) are temperatures where the ρ_c reaches its minimum in non-superconducting NCCO. Black empty circles (our data) are temperatures where the ρ_c reaches its minimum in NCCO once superconductivity is suppressed by high magnetic fields.

localization upon cooling of one hole per planar CuO_2 unit, and that the T-linear resistive behavior in the strange metal regime is the result of a T^2 scattering rate combined with an approximate T-linear dependence of the carrier density. The mechanism that give rise to this temperature dependence is not fully clear. In effect, band theory appears to give an appropriate description of the cuprates at high temperature and high doping levels [42, 219]. Mott localization of one electron/hole per planar CuO_2 unit appears take place in a percolative manner [219].

Connection between the *ab*-plane and *c*-axis transport

As discussed in Section 5.2, the magnitude of the resistivity upturn is related to the amount of disorder. As indicated by the magnetoresistivity measurements, Matthiessen's rule can not explain the resistivity results. Instead, the data are compatible with a serial-resistor network of metallic and non-metallic regions, in which non-metallic regions are characterized by the logarithmic behavior and have a negligible influence on the magnetoresistivity. The existence of the logarithmic resistivity upturn suggests that the metallic regions are embedded in a non-metallic matrix, as otherwise current flow would bypass the non-metallic regions.

The *ab*-plane and *c*-axis resistivity of the electron-doped cuprates are very similar to each other (both show the logarithmic upturn and the T^2 metallic behavior). However, this similarity is not observed in the hole-doped cuprates, for which insulating behavior was seen along the *c*-axis [289]. This suggests that electron and hole carriers behave differently in *ab*-plane versus *c*-axis transport. One possible explanation is that electrons and holes are both mobile in the *ab*-plane, but that only electrons can easily hop between CuO_2 layers. This scenario is consistent with theoretical work which suggests that the *c*-axis transport in the electron-doped cuprates is dominated by electrons (near $(\pi, 0)$ and equivalent in k space) [193].

Assuming that the charge carrier density is given by the inverse of the Hall constant, we can model the *ab*-plane and *c*-axis resistivity with a temperature-dependent carrier density. Remarkably, as shown in Fig. 5.21, the *c*-axis resistivity can be described up to the highest measured temperature using

$$\rho_c = A_0 - A_{\log} \log(T/1K) + (A_2 R_H/R_0)T^2, \tag{5.15}$$

which is a modified form of Eq. 5.15. R_H is the Hall constant and R_0 is the R_H at low temperature.

Figure 5.22 summaries scaling between $A_{\log}$ and A_0 for both ab-plane and c-axis resistivity. The difference between the scaling behavior is rooted in the difference between $A_{0,ab}$ and $A_{0,c}$. It is possible that $A_{0,c}$ includes an additional contribution (e.g., inter-plane hopping) that does not exist in the ab-plane transport. Nevertheless, the overall similarity in the scaling behavior points to the same underlying origin of the resistivity upturn in the electron and hole-doped cuprates. Magnetotransport measurements of NCCO show that the c-axis magnetoresistivity mimics the ab-plane magnetoresistivity (Chapter 4), indicative of a potentially dominant ab-plane contribution to the c-axis transport properties.

Connecting transport with the phase diagram

The phase diagram for NCCO was discussed in Chapters 3 and 4. The magnetic and electronic properties were found to be closely related to the Fermi surface. As shown in Fig. 5.23, the temperature above which ρ_c deviates from Eq. 5.13 (shown as green shaded areas in Fig. 5.4 and Fig. 5.17) and the temperature at which an increase is seen in the Hall constant coincide with $T_{\rm N}$. This behavior is possibly associated with a delocalization of charge carriers and concomitant changes in the Fermi surface due to the breakdown of the antiferromagnetic order.

References

[1] The rise of quantum materials. *Nature Materials* **12**, 105 (2016).

[2] Dalton, J. On the Absorption of Gases by Water and Other Liquids. *Memoirs of the Literary and Philosophical Society of Manchester* **1**, 271 (1803).

[3] Jaeger, G. The Ehrenfest Classification of Phase Transitions: Introduction and Evolution. *Archive for History of Exact Sciences* **53**, 51 (1998).

[4] Planck, M. Ueber das Gesetz der Energieverteilung im Normalspectrum. *Annalen der Physik* **309**, 553 (1901).

[5] Einstein, A. Concerning an Heuristic Point of View Toward the Emission and Transformation of Light. *Annalen der Physik* **17**, 132 (1905).

[6] Bohr, N. On the Constitution of Atoms and Molecules, Part I. *Philosophical Magazine* **26**, 1 (1913).

[7] de Broglie, L.-V. *On the Theory of Quanta.* Ph.D. thesis, University of Paris (1924).

[8] Heisenberg, W. Quantum-theoretical re-interpretation of kinematic and mechanical relations. *Zeitschrift für Physik* **33**, 879 (1925).

[9] Schrödinger, E. An Undulatory Theory of the Mechanics of Atoms and Molecules. *Physical Review* **28**, 1049 (1926).

[10] Pauli, W. On the Connexion between the Completion of Electron Groups in an Atom with the Complex Structure of Spectra. *Zeitschrift für Physik* **31**, 765 (1925).

[11] Dirac, P. A. M. The Quantum Theory of the Electron. *Proceedings of the Royal Society A: Mathematical, Physical and Engineering Sciences* **117**, 610 (1928).

[12] Dirac, P. A. M. A Theory of Electrons and Protons. *Proceedings of the Royal Society A: Mathematical, Physical and Engineering Sciences* **126**, 360 (1930).

[13] Gerlach, W. & Stern, O. Der experimentelle Nachweis der Richtungsquantelung im Magnetfeld. *Zeitschrift für Physik* **9**, 349 (1922).

[14] Gerlach, W. & Stern, O. Das magnetische Moment des Silberatoms. *Zeitschrift für Physik* **9**, 353 (1922).

[15] Zeeman, P. The Effect of Magnetisation on the Nature of Light Emitted by a Substance. *Nature* **55**, 347 (1897).

[16] Fischer, C. F. General Hartree-Fock program. *Computer Physics Communications* **43**, 355 (1987).

[17] Bohm, D. & Pines, D. A Collective Description of Electron Interactions. I. Magnetic Interactions. *Physical Review* **82**, 625 (1951).

[18] Sherrill, C. D. & Schaefer III., H. F. The Configuration Interaction Method: Advances in Highly Correlated Approaches. In *Advances in Quantum Chemistry*, vol. 34, 143 (Academic Press, 1999).

[19] Kohn, W. & Sham, L. J. Self-Consistent Equations Including Exchange and Correlation Effects. *Physical Review* **140**, A1133–A1138 (1965).

[20] Caffarel, M. & Claverie, P. Development of a pure diffusion quantum Monte Carlo method using a full generalized FeynmanKac formula. I. Formalism. *The Journal of Chemical Physics* **88**, 1088 (1988).

[21] Onnes, K. The resistance of pure mercury at helium temperatures. *Commun Phys Lab Univ Leiden* **12**, 120 (1911).

[22] Meissner, W. & Ochsenfeld, R. Ein neuer Effekt bei Eintritt der Supraleitfähigkeit. *Naturwissenschaften* **21**, 787 (1933).

[23] London, F. & London, H. The electromagnetic equations of the supraconductor. *Proceedings of the Royal Society A: Mathematical, Physical and Engineering Sciences* **149**, 71 (1935).

[24] Bardeen, J., Cooper, L. N. & Schrieffer, J. R. Microscopic Theory of Superconductivity. *Physical Review* **106**, 162–164 (1957).

[25] Tinkham, M. *Introduction to Superconductivity* (McGraw-Hill, New York, 1996), 2nd edn.

[26] Ginzburg, V. L. & Landau, L. D. On the theory of superconductivity. *Zhurnal Eksperimental'noi i Teoreticheskoi Fiziki* **20**, 1064 (1950).

[27] Scalapino, D. J. A common thread: The pairing interaction for unconventional superconductors. *Reviews of Modern Physics* **84**, 1383–1417 (2012).

[28] Mackenzie, A. P. & Maeno, Y. p-wave superconductivity. *Physica B : Condensed Matter* **280**, 148 (2000).

[29] Superconductor Cables. http://www.amsc.com/gridtec/superconductor_cable_systems.html.

[30] SCMaglev. https://en.wikipedia.org/wiki/SCMaglev.

[31] Magnetic resonance imaging. https://en.wikipedia.org/wiki/Magnetic_resonance_imaging.

[32] 32 Tesla All-Superconducting Magnet. https://nationalmaglab.org/magnet–development/magnet–science–technology/magnet–projects/32–tesla–scm.

[33] Clarke, J. SQUIDs. *Scientific American.* **271**, 36 (1994).

[34] Superconductivity. https://en.wikipedia.org/wiki/Superconductivity.

[35] Bednorz, J. G. & Müller, K. A. Possible high T_c superconductivity in the Ba-La-Cu-O system. *Zeitschriftfuer Physik B Condensed Matter* **64**, 189–193 (1986).

[36] Schilling, A., Cantoni, M., Guo, J. D. & Ott, H. R. Superconductivity above 130 K in the Hg-Ba-Ca-Cu-O system. *Nature* **363**, 56 (1993).

[37] Mott, N. F. & Peierls, R. Discussion of the paper by de boer and verwey. *Proceedings of the Physical Society* **49**, 72 (1937).

[38] Mott, N. F. Metal-insulator transition. *Reviews of Modern Physics* **40**, 677 (1968).

[39] Axe, J. D. & Crawford, M. K. Structural instabilities in lanthanum cuprate superconductors. *Journal of Low Temperature Physics* **95**, 271 (1994).

[40] Motoyama, E. M. *Neutron scattering studies of the electron-doped high-temperature superconductor neodymium cerium copper oxide.* Ph.D. thesis, Stanford University (2009).

[41] Crystal field theory. https://en.wikipedia.org/wiki/Crystal_field_theory.

[42] Armitage, N. P., Fournier, P. & Greene, R. L. Progress and perspectives on electron-doped cuprates. *Reviews of Modern Physics* **82**, 2421 (2010).

[43] Rybicki, D., Jurkutat, M., Reichardt, S., Kapusta, C. & Haase, J. Perspective on the phase diagram of cuprate high-temperature superconductors. *Nature Communications* **7**, 11413 (2016).

[44] Mang, P. K. *Magnetic, phonon, and structural scattering studies of the electron-doped high-temperature superconductor neodymium cerium copper oxide.* Ph.D. thesis, Stanford University (2004).

[45] Taguchi, M. *et al.* Evidence for Suppressed Screening on the Surface of High Temperature $La_{2-x}Sr_xCuO_4$ and $Nd_{2-x}Ce_xCuO_4$ Superconductors. *Physical Review Letters* **95**, 177002 (2005).

[46] Luetkens, H. *et al.* The electronic phase diagram of the $LaO_{1-x}F_xFeAs$ superconductor. *Nature Materials* **8**, 305 (2009).

[47] Drew, A. J. *et al.* Coexistence of static magnetism and superconductivity in $SmFeAsO_{1-x}F_x$ as revealed by muon spin rotation. *Nature Materials* **8**, 310 (2009).

[48] Zhao, J. *et al.* Structural and magnetic phase diagram of $CeFeAsO_{1-x}F_x$ and its relation to high-temperature superconductivity. *Nature Materials* **7**, 953 (2008).

[49] Chen, H. *et al.* Coexistence of the spin-density wave and superconductivity in $Ba_{1x}K_xFe_2As_2$. *Europhysics Letters* **85**, 17006 (2009).

[50] Kagawa, F., Miyagawa, K. & Kanoda, K. Unconventional critical behaviour in a quasi-two-dimensional organic conductor. *Nature* **436**, 534 (2005).

[51] Park, T. *et al.* Hidden magnetism and quantum criticality in the heavy fermion superconductor $CeRhIn_5$. *Nature* **440**, 65 (2006).

[52] Uemura, Y. J. Superconductivity: Commonalities in phase and mode. *Nature Materials* **8**, 253 (2009).

[53] Onose, Y., Taguchi, Y., Ishizaka, K. & Tokura, Y. Charge dynamics in underdoped $Nd_{2-x}Ce_xCuO_4$: Pseudogap and related phenomena. *Physical Review B* **69**, 024504 (2004).

[54] Zimmers, A. *et al.* Infrared properties of electron-doped cuprates: Tracking normal-state gaps and quantum critical behavior in $Pr_{2-x}Ce_xCuO_4$. *Europhysics Letters* **70**, 225 (2005).

[55] Motoyama, E. M. *et al.* Spin correlations in the electron-doped high-transition-temperature superconductor $Nd_{2-x}Ce_xCuO_{4+\delta}$. *Nature* **455**, 186 (2007).

[56] Matsuda, M. *et al.* Magnetic order, spin correlations, and superconductivity in single crystal $Nd_{1.85}Ce_{0.15}CuO_{4+\delta}$. *Physical Review B* **45**, 12548 (1992).

[57] Kastner, M. A., Birgeneau, R. J., Shirane, G. & Endoh, Y. Magnetic, transport, and optical properties of monolayer copper oxides. *Reviews of Modern Physics* **70**, 897 (1998).

[58] Anderson, P. W. Antiferromagnetism. Theory of Superexchange Interaction. *Physical Review* **79**, 350 (1950).

[59] Dagotto, E. Correlated electrons in high-temperature superconductors. *Reviews of Modern Physics* **66**, 763 (1994).

[60] Damascelli, A., Hussain, Z. & Shen, Z.-X. Angle-resolved photoemission studies of the cuprate superconductors. *Reviews of Modern Physics* **75**, 473 (2003).

[61] Lee, P. A., Nagaosa, N. & Wen, X.-G. Doping a Mott insulator: Physics of high-temperature superconductivity. *Reviews of Modern Physics* **78**, 17 (2006).

[62] Fournier, P. T′ and infinite-layer electron-doped cuprates. *Physica C: Superconductivity and its Applications* **514**, 314 (2015).

[63] Naito, M., Krockenberger, Y., Ikeda, A. & Yamamoto, H. Reassessment of the electronic state, magnetism, and superconductivity in high-Tc cuprates with the Nd_2CuO_4 structure. *Physica C: Superconductivity and its Applications* **523**, 28 (2016).

[64] Zhang, X. *et al.* Transport anomalies and quantum criticality in electron-doped cuprate superconductors. *Physica C: Superconductivity and its Applications* **525**, 18 (2016).

[65] Anderson, P. W. Last Words on the Cuprates. *arXiv* **1612**, 03919.

[66] Chubukov, A. Pairing mechanism in fe-based superconductors. *Annual Review of Condensed Matter Physics* **3**, 57 (2012).

[67] Moriya, T. & Ueda, K. Antiferromagnetic spin fluctuation and superconductivity. *Reports on Progress in Physics* **66**, 1299 (2003).

[68] Laughlin, R. B. Fermi-Liquid Computation of the Phase Diagram of High-Tc Cuprate Superconductors with an Orbital Antiferromagnetic Pseudogap. *Physical Review Letters* **112**, 017004 (2014).

[69] Laughlin, R. B. Hartree-Fock computation of the high-T_c cuprate phase diagram. *Physical Review B* **89**, 035134 (2014).

[70] Tremblaya, A.-M. S., Kyung, B. & Sénéchal, D. Pseudogap and high-temperature superconductivity from weak to strong coupling. Towards a quantitative theory. *Low Temperature Physics* **32**, 424 (2006).

[71] Weber, C., Haule, K. & Kotliar, G. Strength of correlations in electron- and hole-doped cuprates. *Nature Physics* **6**, 574 (2010).

[72] Weber, C., Haule, K. & Kotliar, G. Apical oxygens and correlation strength in electron- and hole-doped copper oxides. *Physical Review B* **82**, 125107 (2010).

[73] Towards a complete theory of high T_c. *Nature Physics* **2**, 138 (2006).

[74] Tsuei, C. C. & Kirtley, J. R. Pairing symmetry in cuprate superconductors. *Reviews of Modern Physics* **72**, 969 (2000).

[75] Gough, C. E. *et al.* Flux quantization in a high-T_c superconductor. *Nature* **326**, 855 (1987).

[76] Blumberg, G. *et al.* Nonmonotonic $d_{x^2-y^2}$ Superconducting Order Parameter in $Nd_{2-x}Ce_xCuO_{4+\delta}$. *Physical Review Letters* **88**, 107002 (2002).

[77] Qazilbash, M. M. *et al.* Evolution of superconductivity in electron-doped cuprates: Magneto-Raman spectroscopy. *Physical Review B* **72**, 214510 (2005).

[78] Emery, V. J. & Kivelson, S. A. Importance of phase fluctuations in superconductors with small superfluid density. *Nature* **374**, 434 (1995).

[79] Cooper, J. R. Power-law dependence of the *ab*-plane penetration depth in $Nd_{1.85}Ce_{0.15}CuO_{4-y}$. *Physical Review B* **54**, R3753 (1996).

[80] Kokales, J. D. *et al.* Microwave Electrodynamics of Electron-Doped Cuprate Superconductors. *Physical Review Letters* **85**, 3696 (2000).

[81] Prozorov, R., Giannetta, R. W., Fournier, P. & Greene, R. L. Evidence for nodal quasiparticles in electron-doped cuprates from penetration depth measurements. *Physical Review Letters* **85**, 3700 (2000).

[82] Luo, H. G. & Xiang, T. Superfluid Response in Electron-Doped Cuprate Superconductors. *Physical Review Letters* **94**, 027001 (2005).

[83] Armitage, N. P. *et al.* Anomalous electronic structure and pseudogap effects in $Nd_{1.85}Ce_{0.15}CuO_4$. *Physical Review Letters* **87**, 147003 (2001).

[84] Sato, T., Kamiyama, T., Takahashi, T., Kurahashi, K. & Yamada, K. Observation of $d_{x^2-y^2}$-Like Superconducting Gap in an Electron-Doped High-Temperature Superconductor. *Science* **291**, 1517 (2001).

[85] Matsui, H. *et al.* Angle-resolved photoemission spectroscopy of the antiferromagnetic superconductor $Nd_{1.87}Ce_{0.13}CuO_4$: Anisotropic spin-correlation gap, pseudogap, and the induced quasiparticle mass enhancement. *Physical Review Letters* **94**, 047005 (2005).

[86] Matsui, H. *et al.* Direct observation of a nonmonotonic $d_{x^2-y^2}$-wave superconducting gap in the electron-doped high-T_c superconductor $Pr_{0.89}LaCe_{0.11}CuO_4$. *Physical Review Letters* **95**, 017003 (2005).

[87] Shan, L. *et al.* Distinct pairing symmetries in $Nd_{1.85}Ce_{0.15}CuO_{4-y}$ and $La_{1.89}Ce_{0.11}CuO_4$ single crystals: Evidence from comparative tunneling measurements. *Physical Review B* **72**, 144506 (2005).

[88] Niestemski, F. C. *et al.* A distinct bosonic mode in an electron-doped high-transition-temperature superconductor. *Nature* **450**, 1058 (2007).

[89] Volovik, G. E. Superconductivity with lines of GAP nodes: density of states in the vortex. *Journal of Experimental and Theoretical Physics* **58**, 469 (1993).

[90] Balci, H., Smolyaninova, V. N., Fournier, P., Biswas, A. & Greene, R. L. Magnetic-field dependence of electronic specific heat in $Pr_{1.85}Ce_{0.15}CuO_4$. *Physical Review B* **66**, 174510 (2002).

[91] Balci, H. & Greene, R. L. Anomalous Change in the Field Dependence of the Electronic Specific Heat of an Electron-Doped Cuprate Superconductor. *Physical Review Letters* **93**, 067001 (2004).

[92] Yu, W., Liang, B. & Greene, R. L. Magnetic-field dependence of the low-temperature specific heat of the electron-doped superconductor $Pr_{1.85}Ce_{0.15}CuO_4$. *Physical Review B* **72**, 212512 (2005).

[93] Tsuei, C. C. & Kirtley, J. R. Phase-Sensitive Evidence for d-Wave Pairing Symmetry in Electron-Doped Cuprate Superconductors. *Physical Review Letters* **85**, 182 (2000).

[94] Darminto, D. A. *et al.* Phase-sensitive order parameter symmetry test experiments utilizing $Nd_{2-x}Ce_xCuO_{4-y}$/Nb zigzag junctions. *Physical Review Letters* **94**, 167001 (2005).

[95] Onose, Y., Taguchi, Y., Ishizaka, K. & Tokura, Y. Doping dependence of pseudogap and related charge dynamics in $Nd_{2-x}Ce_xCuO_4$. *Physical Review Letters* **87**, 217001 (2001).

[96] Kyung, B., Hankevych, V., Dar, A.-M. & Tremblay, A.-M. S. Pseudogap and Spin Fluctuations in the Normal State of the Electron-Doped Cuprates. *Physical Review Letters* **93**, 147004 (2004).

[97] Fauqué, B. *et al.* Magnetic Order in the Pseudogap Phase of High-T_c Superconductors. *Physical Review Letters* **96**, 197001 (2006).

[98] Mook, H. A., Sidis, Y., Fauqu, B., Baldent, V. & Bourges, P. Observation of magnetic order in a superconducting $YBa_2Cu_3O_{6.6}$ single crystal using polarized neutron scattering. *Physical Review B* **78**, 020506 (2008).

[99] Li, Y. *et al.* Unusual magnetic order in the pseudogap region of the superconductor $HgBa_2CuO_{4+\delta}$. *Nature* **455**, 372 (2008).

[100] Dirac, P. A. M. The Quantum Theory of the Emission and Absorption of Radiation. *Proceedings of the Royal Society A: Mathematical, Physical and Engineering Sciences* **114**, 243 (1927).

[101] A. A. Abrikosov, I. E. D., L. P. Gorkov. *Methods of Quantum Field Theory in Statistical Physics* (Prentice Hall Press, 1963).

[102] Bogoliubov, N. On the theory of superfluidity. *Journal of Physics (USSR)* **11**, 23 (1947).

[103] Anderson, P. W. The Resonating Valence Bond State in La_2CuO_4 and Superconductivity. *Science* **235**, 1196 (1987).

[104] Casey, P. A. & Anderson, P. W. Hidden Fermi Liquid: Self-Consistent Theory for the Normal State of High-T_c Superconductors. *Physical Review Letters* **106**, 097002 (2011).

[105] Dhanaraj, G., Byrappa, K., Prasad, V. & Dudley, M. (eds.) *Handbook of crystal growth* (Springer Verlag Berlin, 2010).

[106] Nishinga, T. & Rudolph, P. (eds.) *Handbook of Crystal Growth (Second Edition).* Handbook of Crystal Growth (Elsevier, 2015).

[107] Moll, P. J. W. *et al.* Transport evidence for Fermi-arc-mediated chirality transfer in the Dirac semimetal Cd_3As_2. *Nature* **535**, 266 (2016).

[108] Gomes, K. K., Mar, W., Ko, W., Guinea, F. & Manoharan, H. C. Designer dirac fermions and topological phases in molecular graphene. *Nature* **483**, 306 (2012).

[109] Tanaka, I., Komai, N. & Kojima, H. Phase equilibrium in the Nd-Ce-Cu-O system. *Physica C: Superconductivity* **190**, 112 (1991).

[110] Tokura, Y., Takagi, H. & Uchida, S. A superconducting copper oxide compound with electrons as the charge carriers. *Nature* **337**, 345 (1989).

[111] Vajk, O. *Quantum impurities in a two-dimensional heisenberg antiferromagnet.* Ph.D. thesis, Stanford University (2003).

[112] Gamayunov, K., Tanaka, I. & Kojima, H. TSFZ growth of $Nd_{2-x}Ce_xCuO_4$ single crystals at low oxygen pressure. *Physica C* **235**, 557 (1994).

[113] Richard, P. *et al.* Competition between antiferromagnetism and superconductivity in the electron-doped cuprates triggered by oxygen reduction. *Physical Review Letters* **99**, 157002 (2007).

[114] Mang, P. K. *et al.* Phase decomposition and chemical inhomogeneity in $Nd_{2-x}Ce_xCuO_{4+\delta}$. *Physical Review B* **70**, 094507 (2004).

[115] Higgins, J. S., Dagan, Y., Barr, M. C., Weaver, B. D. & Greene, R. L. Role of oxygen in the electron-doped superconducting cuprates. *Physical Review B* **73**, 104510 (2006).

[116] Radaelli, P. G., Jorgensen, J. D., Schultz, A. J., Peng, J. L. & Greene, R. L. Evidence of apical oxygen in $Nd_{2-x}CuO_y$ determined by single-crystal neutron diffraction. *Physics Review B* **49**, 15322 (1994).

[117] Richard, P. *et al.* Role of oxygen nonstoichiometry and the reduction process on the local structure of $Nd_{2-x}Ce_xCuO_{4\pm\delta}$. *Physical Review B* **70**, 064513 (2004).

[118] Schultz, A. J., Jorgensen, J. D., Peng, J. L. & Greene, R. L. Single-crystal neutron-diffraction structures of reduced and oxygenated $Nd_{2-x}Ce_xCuO_y$. *Physical Review B* **53**, 5157 (1996).

[119] Krockenberger, Y. *et al.* Emerging superconductivity hidden beneath charge-transfer insulators. *Scientific Reports* **3**, 2235 (2013).

[120] Kang, H. J. *et al.* Microscopic annealing process and its impact on superconductivity in T′-structure electron-doped copper oxides. *Nature Materials* **6**, 224 (2007).

[121] Mang, P. K., Larochelle, S. & Greven, M. Spurious magnetism in high-T_c superconductor. *Nature* **426**, 139 (2003).

[122] Billinge, S. J. L. *et al.* Local structural change close to tc in $Nd_{2-x}Ce_xCuO_{4-y}$. *Physica C: Superconductivity* **179**, 279 (1991).

[123] Takagi, H., Uchida, S. & Tokura, Y. Superconductivity produced by electron doping in CuO_2-layered compounds. *Physical Review Letters* **62**, 1197 (1989).

[124] Kim, J. S. & Gaskell, D. R. The phase stability diagrams for the systems $Nd_2CuO_{4-\delta}$ and $Nd_{1.85}Ce_{0.15}CuO_{4-\delta}$. *Physica C: Condensed Matter* **209**, 381 (1993).

[125] Friedrich, W., Knipping, P. & von Laue, M. Interferenz-Ercheinungen bei Rontgenstrahlen. *Annalen der Physik* **346**, 971 (1913).

[126] McMullan, D. Scanning electron microscopy 19281965. *Scanning* **17**, 175 (1995).

[127] Goldstein, J. *Scanning Electron Microscopy and X-Ray Microanalysis* (Plenum, 2003).

[128] Chadwick, J. Possible Existence of a Neutron. *Nature* **129**, 312 (1932).

[129] Nakamura, K. & Group, P. D. Review of particle physics. *Journal of Physics G: Nuclear and Particle Physics* **37**, 075021 (2010).

[130] Fermi, E. *Nuclear Physics* (University of Chicago Press, 1950).

[131] Lovesey, S. W. *The Theory of Neutron Scattering from Condensed Matter* (Clarendon Press, 1984).

[132] Furrer, A., Mesot, J. & Strässle, T. *Neutron Scattering in Condensed Matter Physics* (World Scientific, 2009).

[133] G. Shirane, S. M. S. & Tranquada, J. M. *Neutron scattering with a triple-axis spectrometer* (Cambridge University Press, 2002).

[134] Hove, L. V. Correlations in Space and Time and Born Approximation Scattering in Systems of Interacting Particles. *Physical Review B* **95**, 249 (1954).

[135] Kubo, R. The fluctuation-dissipation theorem. *Reports on Progress in Physics* **29**, 255 (1966).

[136] Dresselhaus, M. S. *Solid State Physics Part III: Magnetic Properties of Solids* (Lecture notes, Massachusetts Institute of Technology, 2001).

[137] Marshall, W. & Lowde, R. D. Magnetic correlations and neutron scattering. *Reports on Progress in Physics* **31**, 705 (1968).

[138] Shirane, G., Shapiro, S. M. & Tranquada, J. M. *Neutron scattering with a triple-axis spectrometer* (Cambridge University Press, 2002).

[139] Mang, P. K., Vajk, O. P., Arvanitaki, A., Lynn, J. W. & Greven, M. Spin Correlations and Magnetic Order in Nonsuperconducting $Nd_{2-x}Ce_xCuO_{4+\delta}$. *Physical Review Letters* **93**, 027002 (2004).

[140] Keimer, B. *et al.* Magnetic excitations in pure, lightly doped, and weakly metallic La_2CuO_4. *Physical Review B* **46**, 14034 (1992).

[141] Zheludev, A. 3-axis resolution library for MatLab, Oak Ridge National Laboratory. https://www.ethz.ch/content/dam/ethz/special–interest/phys/solid–state–physics/neutron–scattering–and–magnetism–dam/images/research/manual.pdf.

[142] Uemura, Y. J. *μSR relaxation functions in magnetic materials* (Proc. 51st Scottish Universities Summer School in Physics, St. Andrews., 1988).

[143] Uemura, Y. J. *Strongly Correlated Systems: Experimental Techniques*, vol. 180 of *Springer Series in Solid-State Sciences* (Springer Berlin, 2015).

[144] Sonier, J. E. Muon Spin Rotation/Relaxation/Resonance (μSR). http://musr.ca/intro/musr/muSRBrochure.pdf.

[145] Uemura, Y. J. *et al.* Universal Correlations between T_c and n/m^* (Carrier Density over Effective Mass) in High-T_c Cuprate Superconductors. *Physical Review Letters* **62**, 2317 (1989).

[146] Lifshitz, I. M., Azbel, M. I. & Kaganov, M. I. The theory of galvanomagnetic effects in metals. *Journal of Experimental and Theoretical Physics* **30**, 220 (1957).

[147] Lifshitz, I. M. & Peschanskii, V. G. Galvanomagnetic characteristics of metals with open fermi surfaces.I. *Journal of Experimental and Theoretical Physics* **35**, 1251 (1959).

[148] Lifshitz, I. M. & Peschanskii, V. G. Galvanomagnetic characteristics of metals with open fermi surfaces.II. *Journal of Experimental and Theoretical Physics* **38**, 188 (1960).

[149] Stewart, G. R. Superconductivity in iron compounds. *Reviews of Modern Physics* **83**, 1589 (2011).

[150] Schröder, A. *et al.* Onset of antiferromagnetism in heavy-fermion metals. *Nature* **407**, 351 (2000).

[151] Thurston, T. R. *et al.* Antiferromagnetic spin correlations in $(Nd,Pr)_{2-x}Ce_xCuO_4$. *Physical Review Letters* **65**, 263 (1990).

[152] Luke, G. M. *et al.* Magnetic order and electronic phase diagrams of electron-doped copper oxide materials. *Physical Review B* **42**, 7981 (1990).

[153] Brinkmann, M., Rex, T., Bach, H. & Westerholt, K. Extended Superconducting Concentration Range Observed in $Pr_{2-x}Ce_xCuO_{4+\delta}$. *Physical Review Letters* **74**, 4927 (1995).

[154] Krockenberger, Y., Yamamoto, H., Mitsuhashi, M. & Naito, M. Universal superconducting ground state in $Nd_{1.85}Ce_{0.15}CuO_4$ and Nd_2CuO_4. *Japanese Journal of Applied Physics* **51**, 010106 (2012).

[155] Breznay, N. P. *et al.* Quantum oscillations suggest hidden quantum phase transition in the cuprate superconductor Pr_2CeO_4. *arXiv* **1510**, 04268.

[156] Uefuji, T., Kurahashi, K., Fujita, M., Matsuda, M. & Yamada, K. Electron-doping effect on magnetic order and superconductivity in $Nd_{2-x}Ce_xCuO_4$ single crystals. *Physica C: Superconductivity* **378**, 273 (2002).

[157] Anderson, P. W. An Approximate Quantum Theory of the Antiferromagnetic Ground State. *Physical Review* **86**, 694 (1952).

[158] Kusko, C., Markiewicz, R. S., Lindroos, M. & Bansil, A. Fermi surface evolution and collapse of the mott pseudogap in $Nd_{2-x}Ce_xCuO_4$. *Physical Review B* **66**, 140513 (2002).

[159] Yuan, Q., Chen, Y., Lee, T. K. & Ting, C. S. Fermi surface evolution in the antiferromagnetic state for the electron-doped t-t'-t''-J model. *Physical Review B* **69**, 214523 (2004).

[160] Yan, X.-Z. & Ting, C. S. Fluctuation-Exchange Study of Antiferromagnetism in Disordered Electron-Doped Cuprate Superconductors. *Physical Review Letters* **97**, 067001 (2006).

[161] Xiang, T., Luo, H. G., Lu, D. H., Shen, K. M. & Shen, Z. X. Intrinsic electron and hole bands in electron-doped cuprate superconductors. *Physical Review B* **79**, 014524 (2009).

[162] Rosseinsky, M. J., Prassides, K. & Day, P. Magnetic order and crystal chemistry of neodymium cerium copper oxide, $Nd_{2-x}Ce_xCuO_{4-\delta}$. *Inorganic Chemistry* **30**, 2680 (1991).

[163] Matsuda, M. *et al.* Three-dimensional magnetic structures and rare-earth magnetic ordering in Nd_2CuO_4 and Pr_2CuO_4. *Physical Review B* **42**, 10098 (1990).

[164] Skanthakumar, S., Lynn, J. W., Peng, J. L. & Li, Z. Y. Observation of noncollinear magnetic structure for the Cu spins in Nd_2CuO_4-type systems. *Physical Review B* **47**, 6173 (1993).

[165] Birgeneau, R. J. *et al.* Instantaneous spin correlations in La_2CuO_4. *Physical Review B* **59**, 13788 (1999).

[166] Tyč, S., Halperin, B. I. & Chakravarty, S. Dynamic Properties of a Two-Dimensional Heisenberg Antiferromagnet at Low Temperatures. *Physical Review Letters* **62**, 835 (1989).

[167] Chakravarty, S., Halperin, B. I. & Nelson, D. R. Low-temperature behavior of two-dimensional quantum antiferromagnets. *Physical Review Letters* **60**, 1057 (1988).

[168] Chakravarty, S., Halperin, B. I. & Nelson, D. R. Two-dimensional quantum heisenberg antiferromagnet at low temperatures. *Physical Review B* **39**, 2344 (1989).

[169] Manousakis, E. The spin-$\frac{1}{2}$ Heisenberg antiferromagnet on a square lattice and its application to the cuprous oxides. *Reviews of Modern Physics* **63**, 1 (1991).

[170] Haldane, F. D. M. Nonlinear field theory of large-spin heisenberg antiferromagnets: Semiclassically quantized solitons of the one-dimensional easy-axis Néel state. *Physical Review Letters* **50**, 1153 (1983).

[171] Hasenfratz, F., P.and Niedermayer. The exact correlation length of the antiferromagnetic $d = 2 + 1$ Heisenberg model at low temperatures. *Physics Letters B* **268**, 231 (1991).

[172] Vajk, O. P., Greven, M., Mang, P. K. & Lynn, J. W. Neutron scattering, magnetometry, and quantum Monte Carlo study of the randomly diluted spin-1/2 square-lattice Heisenberg antiferromagnet. *Solid State Communications* **126**, 93 (2003).

[173] Lake, B. *et al.* Spins in the vortices of a high-temperature superconductor. *Science* **291**, 1759 (2001).

[174] Lake, B. *et al.* Antiferromagnetic order induced by an applied magnetic field in a high-temperature superconductor. *Nature* **415**, 299 (2002).

[175] Jin, K., Zhang, X. H., Bach, P. & Greene, R. L. Evidence for antiferromagnetic order in $La_{2-x}Ce_xCuO_4$ from angular magnetoresistance measurements. *Physical Review B* **80**, 012501 (2009).

[176] Saadaoui, H. *et al.* The phase diagram of electron-doped $La_{2-x}Ce_xCuO_{4+\delta}$. *Nature Communications* **6**, 6041 (2015).

[177] Onose, Y. *et al.* Anomalous pseudogap formation in a nonsuperconducting crystal of $Nd_{1.85}Ce_{0.15}CuO_4$: Implication of charge ordering. *Physical Review Letters* **82**, 5120 (1999).

[178] Neto, E. H. d. S. *et al.* Charge ordering in the electron-doped superconductor $Nd_{2-x}Ce_xCuO_{4+\delta}$. *Science* **347**, 282 (2015).

[179] Neto, E. H. d. S. *et al.* Doping-dependent charge order correlations in electron-doped cuprates. *Science Advances* **2**, e1600782 (2016).

[180] Frandsen, B. A. *et al.* Volume-wise destruction of the antiferromagnetic Mott insulating state through quantum tuning. *Nature Communications* **7**, 12519 (2016).

[181] Vajk, O. P., Mang, P. K., Greven, M., Gehring, P. M. & Lynn, J. W. Quantum impurities in the two-dimensional spin one-half Heisenberg antiferromagnet. *Science* **295**, 1691 (2002).

[182] Newman, M. E. J. Efficient Monte Carlo Algorithm and High-Precision Results for Percolation. *Physical Review Letters* **85**, 4104 (2000).

[183] Zhao, J. *et al.* Electron-spin excitation coupling in an electron-doped copper oxide superconductor. *Nature Physics* **7**, 719 (2011).

[184] Lee, D. H. & Kivelson, S. A. Two classes of Mott insulator. *Physical Review B* **67**, 024506 (2003).

[185] Hoyos, J. A. & Vojta, T. Theory of Smeared Quantum Phase Transitions. *Physical Review Letters* **100**, 240601 (2008).

[186] Ubaid-Kassis, S., Vojta, T. & Schroeder, A. Quantum Griffiths Phase in the Weak Itinerant Ferromagnetic Alloy $Ni_{1-x}V_x$. *Physical Review Letters* **104**, 066402 (2010).

[187] Sachdev, S. Quantum Criticality: Competing Ground States in Low Dimensions. *Science* **288**, 475 (2000).

[188] Sachdev, S. *Quantum Phase Transitions* (Cambridge University Press, 2011).

[189] Senthil, T., Vishwanath, A., Balents, L., Sachdev, S. & Fisher, M. P. A. Deconfined quantum critical points. *Science* **303**, 1490 (2004).

[190] Helm, T. *et al.* Correlation between fermi surface transformations and superconductivity in the electron-doped high-T_c superconductor $Nd_{2-x}Ce_xCuO_{4+\delta}$. *Physical Review B* **92**, 094501 (2015).

[191] Sachdev, S., Metlitski, M. A. & Punk, M. Antiferromagnetism in metals: from the cuprate superconductors to the heavy fermion materials. *Journal of Physics: Condensed Matter* **24**, 294205 (2012).

[192] Eun, J., Jia, X. & Chakravarty, S. Quantum oscillations in electron-doped high-temperature superconductors. *Physical Review B* **82**, 094515 (2010).

[193] Andersen, O. K., Liechtenstein, A. I., Jepsen, O. & Paulsen, F. LDA energy bands, low-energy hamiltonians, t, t'', $t_\perp(k)$, and $J_\perp$. *Journal of Physics and Chemistry of Solids* **56**, 1573 (1995).

[194] Lin, J. & Millis, A. J. Theory of low-temperature hall effect in electron-doped cuprates. *Physical Review B* **72**, 214506 (2005).

[195] Helm, T. *et al.* Magnetic breakdown in the electron-doped cuprate superconductor $Nd_{2-x}Ce_xCuO_{4+\delta}$: The reconstructed fermi surface survives in the strongly overdoped regime. *Physical Review Letters* **105**, 247002 (2010).

[196] Horio, M. *et al.* Suppression of the antiferromagnetic pseudogap in the electron-doped high-temperature superconductor by protect annealing. *Nature Communications* **7**, 10567 (2016).

[197] Idemoto, Y., Oyagi, I. & Fueki, K. Determination of thermodynamic data of $Ln_{1.85}Ce_{0.15}CuO_4$ and Ln_2CuO_4 (Ln=Nd,Sm,Eu) by the EMF method. *Physica C: Superconductivity* **195**, 269 (1992).

[198] Song, D. *et al.* Electron Number-Based Phase Diagram of $P_{1-x}LaCe_xCuO_{4-\delta}$ and Possible Absence of Disparity between Electron- and Hole-Doped Cuprate Phase Diagrams. *Physical Review Letters* **118**, 137001 (2017).

[199] Billinge, S. J. L. & Egami, T. Short-range atomic structure of $Nd_{2-x}Ce_xCuO_{4-y}$ determined by real-space refinement of neutron-powder-diffraction data. *Physical Review B* **47**, 14386 (1993).

[200] Dagotto, E. Complexity in Strongly Correlated Electronic Systems. *Science* **309**, 257 (2005).

[201] Helm, T. *et al.* Evolution of the Fermi Surface of the Electron-Doped High-Temperature Superconductor $Nd_{2-x}Ce_xCuO_{4+\delta}$ Revealed by Shubnikov–de Haas Oscillations. *Physical Review Letters* **103**, 157002 (2009).

[202] Jiang, W. *et al.* Anomalous transport properties in superconducting $Nd_{1.85}Ce_{0.15}CuO_{4+\delta}$. *Physical Review Letters* **73**, 1291 (1994).

[203] Xu, X.-Q. *et al.* Thermoelectric power of $Nd_{2-x}Ce_xCuO_{4+\delta}$ crystals. *Physical Review B* **45**, 7356 (1992).

[204] Kartsovnik, M. V. *et al.* Fermi surface of the electron-doped cuprate superconductor $Nd_{2-x}Ce_xCuO_{4+\delta}$ probed by high-field magnetotransport. *New Journal of Physics* **13**, 015001 (2011).

[205] Armitage, N. P. *et al.* Doping Dependence of an n-Type Cuprate Superconductor Investigated by Angle-Resolved Photoemission Spectroscopy. *Physical Review Letters* **88**, 257001 (2002).

[206] Matsui, H. *et al.* Evolution of the pseudogap across the magnet-superconductor phase boundary of $Nd_{2-x}Ce_xCuO_{4+\delta}$. *Physical Review B* **75**, 224514 (2007).

[207] Ikeda, M. *et al.* Effects of chemical pressure on the fermi surface and band dispersion of the electron-doped high-T_c superconductors. *Physical Review B* **80**, 014510 (2009).

[208] Dagan, Y., Qazilbash, M. M., Hill, C. P., Kulkarni, V. N. & Greene, R. L. Evidence for a Quantum Phase Transition in $Pr_{2-x}Ce_xCuO_{4+\delta}$ from Transport Measurements. *Physical Review Letters* **92**, 167001 (2004).

[209] Li, P., Behnia, K. & Greene, R. L. Evidence for a quantum phase transition in electron-doped $Pr_{2-x}Ce_xCuO_{4-\delta}$ from thermopower measurements. *Physical Review B* **75**, 020506 (2007).

[210] Dagan, Y. & Greene, R. L. Hole superconductivity in the electron-doped superconductor $Pr_{2-x}Ce_xCuO_{4-\delta}$. *Physical Review B* **76**, 024506 (2007).

[211] Li, Y., Tabis, W., Yu, G., Barišić, N. & Greven, M. Hidden Fermi-liquid Charge Transport in the Antiferromagnetic Phase of the Electron-Doped Cuprate Superconductors. *Physical Review Letters* **117**, 197001 (2016).

[212] Gollnik, F. & Naito, M. Doping dependence of normal- and superconducting-state transport properties of $Nd_{2-x}Ce_xCuO_{4-y}$ thin films. *Physical Review B* **58**, 11734 (1998).

[213] Lambacher, M. *Crystal growth and normal state transport of electron doped high temperature superconductors.* Ph.D. thesis, Technische Universität München (2008).

[214] Dagan, Y., Qazilbash, M. M. & Greene, R. L. Tunneling into the Normal State of $Pr_{2-x}Ce_xCuO_4$. *Physical Review Letters* **94**, 187003 (2005).

[215] Kotov, V. N., Sushkov, O. P., Silva Neto, M. B., Benfatto, L. & Castro Neto, A. H. Negative hopping magnetoresistance and dimensional crossover in lightly doped cuprate superconductors. *Physical Review B* **76**, 224512 (2007).

[216] Blatt, F. J. *Physics of Electronic Conduction in Solids* (McGraw-Hill, 1968).

[217] Harris, J. M. *et al.* Violation of kohler's rule in the normal-state magnetoresistance of $YBa_2Cu_3O_7$ and $La_{2-x}Sr_xCuO_4$. *Physical Review Letters* **75**, 1391 (1995).

[218] Storey, J. G. Hall effect and Fermi surface reconstruction via electron pockets in the high-T_c cuprates. *Europhysics Letters* **113**, 27003 (2016).

[219] Barišić, N. *et al.* Hidden fermi-liquid behavior throughout the phase diagram of the cuprates. *arXiv* **1507**, 07885.

[220] Li, P., Balakirev, F. F. & Greene, R. L. High-Field Hall Resistivity and Magnetoresistance of Electron-Doped $Pr_{2-x}Ce_xCuO_{4+\delta}$. *Physical Review Letters* **99**, 047003 (2007).

[221] Jayaram, B., Chen, H. & Callaway, J. Magnetism of Fe, Ni, and Zn in $Nd_{1.85}Ce_{0.15}CuO_4$: comparison of experiment and theory. *Physical Review B* **52**, 3742 (1995).

[222] Brinkmann, M., Rex, T., Stief, M., Bach, H. & Westerholt, K. Residual resistivity and oxygen stoichiometry in $Pr_{2-x}Ce_xCuO_{4+\delta}$ single crystals. *Physica C: Superconductivity* **269**, 76 (1996).

[223] Abrikosov, A. & Gorkov, L. Contribution to the theory of superconducting alloys with paramagnetic impurities. *Journal of Experimental and Theoretical Physics* **12**, 1243 (1961).

[224] Hidaka, Y. & Suzuki, M. Growth and anisotropic superconducting properties of $Nd_{2-x}Ce_xCuO_{4-y}$ single crystals. *Nature* **338**, 635 (1989).

[225] Charikova, T. B. *et al.* Upper critical field in electron-doped cuprate superconductor $Nd_{2x}Ce_xCuO_{4+\delta}$: Two-gap model. *Physica C: Superconductivity* **488**, 25 (2013).

[226] Wang, Y. *et al.* Dependence of Upper Critical Field and Pairing Strength on Doping in Cuprates. *Science* **299**, 86 (2003).

[227] Gurevich, A. Enhancement of the upper critical field by nonmagnetic impurities in dirty two-gap superconductors. *Physical Review B* **67**, 184515 (2003).

[228] Hunte, F. *et al.* Two-band superconductivity in $LaFeAsO_{0.89}F_{0.11}$ at very high magnetic fields. *Nature* **453**, 903 (2008).

[229] Khasanov, R. *et al.* Nodeless superconductivity in the infinite-layer electron-doped cuprate superconductor $Sr_{0.9}La_{0.1}CuO_2$. *Physical Review B* **77**, 184512 (2008).

[230] Uemura, Y. J. *et al.* Basic similarities among cuprate, bismuthate, organic, Chevrel-phase, and heavy-fermion superconductors shown by penetration-depth measurements. *Physical Review Letters* **66**, 2665 (1991).

[231] Panagopoulos, C. *et al.* Superfluid response in monolayer high-T_c cuprates. *Physical Review B* **67**, 220502 (2003).

[232] Luetkens, H. *et al.* Field and Temperature Dependence of the Superfluid Density in $LaFeAsO_{1-x}F_x$ Superconductors: A Muon Spin Relaxation Study. *Physical Review Letters* **101**, 097009 (2008).

[233] Skinta, J. A., Kim, M., Lemberger, T. R., Greibe, T. & Naito, M. Evidence for a transition in the pairing symmetry of the electron-doped cuprates $La_{2-x}Ce_xCuO_{4-y}$ and $Pr_{2-x}Ce_xCuO_{4-y}$. *Physical Review Letters* **88**, 207005 (2002).

[234] Li, P. & Greene, R. L. Normal-state Nernst effect in electron-doped $Pr_{2-x}Ce_xCuO_{4-\delta}$: Superconducting fluctuations and two-band transport. *Physical Review B* **76**, 174512 (2007).

[235] Liu, C. S., Luo, H. G., Wu, W. C. & Xiang, T. Two-band model of Raman scattering on electron-doped high-T_c superconductors. *Physical Review B* **73**, 174517 (2006).

[236] Das, T., Markiewicz, R. S. & Bansil, A. Nodeless *d*-wave superconducting pairing due to residual antiferromagnetism in underdoped $Pr_{2-x}Ce_xCuO_{4-\delta}$. *Physical Review Letters* **98**, 197004 (2007).

[237] Keimer, B., Kivelson, S. A., Norman, M. R., Uchida, S. & Zaanen, J. From quantum matter to high-temperature superconductivity in copper oxides. *Nature* **518**, 179 (2015).

[238] Anderson, P. W. *The Theory of Superconductivity in the High-T_c Cuprates* (Princeton University Press, 1997).

[239] Hussey, N. E., Takenaka, K. & Takagi, H. Universality of the Mott–Ioffe–Regel limit in metals. *Philosophical Magazine* **84**, 2847 (2004).

[240] Hussey, N. E. Phenomenology of the normal state in-plane transport properties of high-T_c cuprates. *Journal of Physics: Condensed Matter* **20**, 123201 (2008).

[241] Nakamae, S. *et al.* Electronic ground state of heavily overdoped nonsuperconducting $La_{2-x}Sr_xCuO_4$. *Physical Review B* **68**, 100502 (2003).

[242] Nakamae, S. *et al.* Erratum: Electronic ground state of heavily overdoped nonsuperconducting $La_{2-x}Sr_xCuO_4$. *Physical Review B* **79**, 219904 (2009).

[243] Yoshida, T. *et al.* Electronlike Fermi surface and remnant (π, 0) feature in overdoped $La_{1.78}Sr_{0.22}CuO_4$. *Physical Review B* **63**, 220501 (2001).

[244] Hussey, N. E., Abdel-Jawad, M., Carrington, A., Mackenzie, A. P. & Balicas, L. A coherent three-dimensional fermi surface in a high-transition-temperature superconductor. *Nature* **425**, 814 (2003).

[245] Ando, Y., Boebinger, G. S., Passner, A., Kimura, T. & Kishio, K. Logarithmic Divergence of both In-Plane and Out-of-Plane Normal-State Resistivities of Superconducting $La_{2-x}Sr_xCuO_4$ in the Zero-Temperature Limit. *Physical Review Letters* **75**, 4662 (1995).

[246] Ono, S. *et al.* Metal-to-Insulator Crossover in the Low-Temperature Normal State of $Bi_2Sr_{2-x}La_xCuO_{6+\delta}$. *Physical Review Letters* **85**, 638 (2000).

[247] Doiron-Leyraud, N. *et al.* Onset of a Boson Mode at the Superconducting Critical Point of Underdoped $YBa_2CuO_3O_y$. *Physical Review Letters* **97**, 207001 (2006).

[248] Rullier-Albenque, F., Alloul, H., Balakirev, F. & Proust, C. Disorder, metal-insulator crossover and phase diagram in high-T_c cuprates. *Europhysics Letters* **81**, 37008 (2008).

[249] Varma, C. M. Marginal Fermi-Liquid Theory of the High Tc Materials. In *High-Temperature Superconductivity*, 19 (Springer US, 1991).

[250] Varma, C. M., Littlewood, P. B., Schmitt-Rink, S., Abrahams, E. & Ruckenstein, A. E. Phenomenology of the normal state of Cu-O high-temperature superconductors. *Physical Review Letters* **63**, 1996 (1989).

[251] Abrahams, E. & Varma, C. M. What angle-resolved photoemission experiments tell about the microscopic theory for high-temperature superconductors. *Proceedings of the National Academy of Sciences, USA* **97**, 5714 (2000).

[252] Abrahams, E. & Varma, C. M. Hall effect in the marginal Fermi liquid regime of high-T_c superconductors. *Physical Review B* **68**, 094502 (2003).

[253] Anderson, P. W. Hall effect in the two-dimensional luttinger liquid. *Physical Review Letters* **67**, 2092 (1991).

[254] Hussey, N. E. The normal state scattering rate in high-T_c cuprates. *The European Physical Journal B* **31**, 495 (2003).

[255] Barišić, N. *et al.* Universal sheet resistance and revised phase diagram of the cuprate high-temperature superconductors. *Proceedings of the National Academy of Sciences, USA* **110**, 12235 (2013).

[256] Chan, M. K. *et al.* In-Plane Magnetoresistance Obeys Kohler's Rule in the Pseudogap Phase of Cuprate Superconductors. *Physical Review Letters* **113**, 177005 (2014).

[257] Mirzaei, S. I. *et al.* Spectroscopic evidence for fermi liquid-like energy and temperature dependence of the relaxation rate in the pseudogap phase of the cuprates. *Proceedings of the National Academy of Sciences, USA* **110**, 5774 (2013).

[258] Ando, Y., Kurita, Y., Komiya, S., Ono, S. & Segawa, K. Evolution of the Hall Coefficient and the Peculiar Electronic Structure of the Cuprate Superconductors. *Physical Review Letters* **92**, 197001 (2004).

[259] Chien, T. R., Wang, Z. Z. & Ong, N. P. Effect of zn impurities on the normal-state hall angle in single-crystal $YBa_2Cu_{3-x}Zn_xO_{7-\delta}$. *Physical Review Letters* **67**, 2088 (1991).

[260] Zhao, X. *et al.* Crystal growth and characterization of the model high-temperature superconductor $HgBa_2CuO_{4+\delta}$. *Advanced Materials* **18**, 3243 (2006).

[261] Barišić, N. *et al.* Demonstrating the model nature of the high-temperature superconductor $HgBa_2CuO_{4+\delta}$. *Physical Review B* **78**, 054518 (2008).

[262] Tsuei, C. C., Gupta, A. & Koren, G. Quadratic temperature dependence of the in-plane resistivity in superconducting $Nd_{1.85}CuO_4$: Evidence for fermi-liquid normal state. *Physica C* **161**, 415 (1989).

[263] Jin, K., Butch, N. P., Kirshenbaum, K., Paglione, J. & Greene, R. L. Link between spin fluctuations and electron pairing in copper oxide superconductors. *Nature* **476**, 73 (2011).

[264] Butch, N. P., Jin, K., Kirshenbaum, K., Greene, R. L. & Paglione, J. Quantum critical scaling at the edge of fermi liquid stability in a cuprate superconductor. *Proceedings of the National Academy of Sciences, USA* **109**, 8440 (2012).

[265] Sekitani, T., Naito, M. & Miura, N. Kondo effect in underdoped n-type superconductors. *Physical Review B* **67**, 174503 (2003).

[266] Yu, W., Liang, B. & Greene, R. L. c-axis longitudinal magnetoresistance of the electron-doped superconductor $Pr_{1.85}Ce_{0.15}CuO_4$. *Physical Review B* **74**, 212504 (2006).

[267] Anderson, P. W. Absence of diffusion in certain random lattices. *Physical Review* **109**, 1492 (1958).

[268] Fournier, P. *et al.* Anomalous saturation of the phase coherence length in underdoped $Pr_{2-x}Ce_xCuO_4$ thin films. *Physical Review B* **62**, R11993 (2000).

[269] Chen, W., Andersen, B. M. & Hirschfeld, P. J. Theory of resistivity upturns in metallic cuprates. *Physical Review B* **80**, 134518 (2009).

[270] Finkelman, S. *et al.* Resistivity at low temperatures in electron-doped cuprate superconductors. *Physical Review B* **82**, 094508 (2010).

[271] Laliberté, F. *et al.* Origin of the metal-to-insulator crossover in cuprate superconductors. *arXiv* **1606**, 04491.

[272] Ando, S., Y.and Komiya, Segawa, K., Ono, S. & Kurita, Y. Electronic Phase Diagram of High-T_c Cuprate Superconductors from a Mapping of the In-Plane Resistivity Curvature. *Physical Review Letters* **93**, 267001 (2004).

[273] Lee, Y. S. *et al.* Electrodynamics of the nodal metal state in weakly doped high-T_c cuprates. *Physical Review B* **72**, 054529 (2005).

[274] Yu, W. *et al.* Oxygen-doped Mott-Hubbard cuprate superconductor $La_{1.85}Ce_{0.15}CuO_4$. *Physical Review B* **75**, 020503 (2007).

[275] Peng, Y. *et al.* Disappearance of nodal gap across the insulator-superconductor transition in a copper-oxide superconductor. *Nature Communications* **4**, 2459 (2013).

[276] Wang, C. H. *et al.* Effect of Ce doping and oxygen content on pseudogap and anisotropy in $Nd_{2-x}Ce_xCuO_{4+\delta}$. *Superconductor Science and Technology* **18**, 763 (2005).

[277] Wang, C. H. *et al.* Influence of doping level on the Hall coefficient and on the thermoelectric power in $Nd_{2-x}Ce_xCuO_{4+\delta}$. *Physical Review B* **72**, 132506 (2005).

[278] Bach, P. L., Saha, S. R., Kirshenbaum, K., Paglione, J. & Greene, R. L. High-temperature resistivity in the iron pnictides and the electron-doped cuprates. *Physical Review B* **83**, 212506 (2011).

[279] Woods, S. I. *et al.* Destruction of superconductivity in $Nd_{2-x}Ce_xCuO_{4+\delta}$ thin films by ion irradiation. *Physical Review B* **58**, 8800 (1998).

[280] Gauthier, J. *et al.* Different roles of cerium substitution and oxygen reduction in transport in $Pr_{2-x}Ce_xCuO_4$ thin films. *Physical Review B* **75**, 024424 (2007).

[281] Tafti, F. F. *et al.* Nernst effect in the electron-doped cuprate superconductor $Pr_{2-x}Ce_xCuO_4$: Superconducting fluctuations, upper critical field H_{c2} , and the origin of the T_c dome. *Physical Review B* **90**, 024519 (2014).

[282] Sun, X. F., Kurita, Y., Suzuki, T., Komiya, S. & Ando, Y. Thermal Conductivity of $Pr_{1.3-x}La_{0.7}Ce_xCuO_4$ Single Crystals and Signatures of Stripes in an Electron-Doped Cuprate. *Physical Review Letters* **92**, 047001 (2004).

[283] Levenberg, K. A Method for the Solution of Certain Non-Linear Problems in Least Squares. *Quarterly of Applied Mathematics* **2**, 164 (1944).

[284] Marquardt, D. An Algorithm for Least-Squares Estimation of Nonlinear Parameters. *SIAM Journal on Applied Mathematics* **11**, 431 (1963).

[285] Ando, Y., Lavrov, A. N., Komiya, S., Segawa, K. & Sun, X. F. Mobility of the Doped Holes and the Antiferromagnetic Correlations in Underdoped High-T_c Cuprates. *Physical Review Letters* **87**, 017001 (2001).

[286] Beloborodov, I. S., Lopatin, A. V., Vinokur, V. M. & Efetov, K. B. Granular electronic systems. *Reviews of Modern Physics* **79**, 469 (2007).

[287] Kawakami, T., Shibauchi, T., Terao, Y., Suzuki, M. & Krusin-Elbaum, L. Evidence for Universal Signatures of Zeeman-Splitting-Limited Pseudogaps in Superconducting Electron- and Hole-Doped Cuprates. *Physical Review Letters* **95**, 017001 (2005).

[288] Kawakami, T. & Suzuki, M. Direct observation of intrinsic Josephson junction characteristics in electron-doped $Sm_{2-x}Ce_xCuO_{4+\delta}$. *Physical Review B* **76**, 134503 (2007).

[289] Su, Y. H., Luo, H. G. & Xiang, T. Universal scaling behavior of the c-axis resistivity of high-temperature superconductors. *Physical Review B* **73**, 134510 (2006).

[290] Vishik, I. *Quantum impurities in the electron-doped hightemperature superconductor neodymium cerium copper oxide: crystal growth, characterization, and magnetic neutron scattering.* Undergraduate thesis, Stanford University (2006).

[291] Liang, R., Bonn, D. A. & Hardy, W. N. Evaluation of CuO_2 plane hole doping in $YBa_2CuO_3O_y$ single crystals. *Physical Review B* **73**, 180505 (2006).

Appendix A

Sample information

The characteristics of samples measured by neutron scattering, μSR, and charge transport experiments are summarized in this Appendix. The analyses in Chapters 3, 4, and 5 include previously published data and data taken by previous group members.

A.1 NCCO samples for neutron scattering and μSR

Name	Techniques	Nominal x	Actual x	T_c(K)
M19[1]	Neutron [55]	0.10	0.106(7)	0
M40[1,5]	Neutron [55], μSR	0.15	0.166(10)	23
E1[1]	Neutron [55]	0.04	0.038(11)	0
Yu-12:15:04[1]	Neutron [55]	0.125	0.129(6)	–
E5[1]	Neutron [55]	0.075	–	0
E6[1]	Neutron [55], μSR	0.15	0.154(7)	24
E8[1]	Neutron [55]	0.1325	0.134(6)	–
E9[1,5]	Neutron [55], μSR	0.1375	0.145(4)	19
E13[1]	Neutron [55]	0.17	0.181(4)	–
E15[4,5]	μSR	0.134	0.141(4)	–
E19A[2,5]	Neutron, μSR	0.125	0.133(3)	24
E20[2]	Neutron	0.131	0.138(5)	19
E21[2,3,5]	Neutron, μSR	0.135	0.141(4)	24
E22 (as-grown)[2]	Neutron	0	0	0
E23[2,3,5]	Neutron, μSR	0.146	0.156(4)	25
E24[2,5]	Neutron, μSR	0.121	0.128(2)	20
E26[2,4]	Neutron, μSR	0.105	0.118(3)	0
E28B[2]	Neutron	0.115	0.126(5)	16
E32B[2]	Neutron	0.11	0.120(1)	12
E34A[2,4]	Neutron, μSR	0.114	0.123(2)	0
YM6[3]	Neutron	0.13	0.135(3)	24
YM16[3,5]	Neutron, μSR	0.16	0.170(2)	23
YM16 (as-grown)[5]	μSR	0.16	0.170(2)	0

Table A.1: NCCO samples measured by neutron scattering and μSR techniques (Chapter 3).

The samples listed below the horizontal line were prepared and characterized as described in Chapter 2, and have improved homogenity compared to the older samples listed above the line. [1] Results reported in [55]. [2,3] Neutron experiments led by previous group members (Eugene Motoyama or Patrick Mang) and myself, respectively. [4,5] μSR measurements led by previous group members (Eugene Motoyama or Mun Chan) and myself, respectively. The actual chemical composition and onset T_c were determined via ICP/EDS and SQUID measurements (see Chapter 2). This Thesis work analyzed the newer data and those taken by previous group members. All the unpublished data obtained by Eugene Motoyama are featured in his Thesis [40].

A.2 NCCO samples for high-magnetic-field transport

Name	Nominal x	Actual x	T_c(K)	geometry
M40[1,2]	0.15	0.166(10)	23	3,4
E3[1]	0.04	0.042(6)	0	3,4
Yu-12:15:04[2]	0.125	0.129(6)	–	3
E6[2]	0.15	0.154(7)	24	3
E9[1]	0.1375	0.145(4)	19	1,2,3,4
Ni-0.005 (Ni=0.005)[2]	0.15	–	17	3
Ni-0.010 (Ni=0.010)[2]	0.15	–	8	3
Ni-0.015 (Ni=0.015)[2]	0.15	–	0	3
Z10[1]	0.10	0.11(10)	0	1
E19[1]	0.125	0.133(3)	24	1,2,3,4
E23[1]	0.146	0.156(4)	25	1,2,3,4
YM16[1]	0.16	0.170(2)	23	1
YM16(as-grown)[1]	0.16	0.170(2)	0	1

Table A.2: NCCO samples for high-magnetic-field transport measurements (Chapter 4).

The measurement geometries were: (1) I//a, H//c, (2) I//a, H//a, (3) I//c, H//c, (4) I//c, H//ab. [1,2] High-field transport experiments led by myself and a previous group member, Neven Barišić, respectively. The actual chemical composition and onset T_c were determined via ICP/EDS and SQUID measurements (see Chapter 2). The Ni-doped samples were grown by Inna Visik [290]. This Thesis work analyzed all the data for samples listed in this Table.

A.3 Electron-doped cuprate samples for ab-plane charge transport analysis

Material	Reference	x	Special condition	T_N(K)
NCCO	this Thesis	0.10	–	165
NCCO	this Thesis	0.134*	–	100
NCCO	this Thesis	0.145*	–	80
NCCO	[53]	0.025	–	250
NCCO	[53]	0.05	–	250
NCCO	[53]	0.075	–	230
NCCO	[53]	0.10	–	165
NCCO	[53]	0.125	–	120
NCCO	[278]	0.10	–	165
NCCO	[279]	0.14	Irradiation intensity 2.0	–
NCCO	[279]	0.14	Irradiation intensity 2.5	–
NCCO	[279]	0.14	Irradiation intensity 3.0	–
NCCO	[279]	0.14	Irradiation intensity 4.0	–
NCCO	[279]	0.14	Irradiation intensity 4.5	–
NCCO	[279]	0.14	Irradiation intensity 12.5	–
NCCO	[279]	0.14	Irradiation intensity 18.5	–
NCCO	[277]	0.06	–	240
NCCO	[276]	0.06	–	240
NCCO	[276]	0.12	–	–
NCCO	[276]	0.12	as-grown	170
NCCO	[276]	0.13	as-grown	160
NCCO	[276]	0.14	as-grown	150
NCCO	[276]	0.14	annealed at 500° C	–
NCCO	[276]	0.14	annealed at 600° C	–
NCCO	[276]	0.14	annealed at 700° C	–
NCCO	[276]	0.14	annealed at 800° C	–
LYCO	[274]	0.15	Sample A3	–
LYCO	[274]	0.15	Sample A4	–
PCCO	[208]	0.13	–	–
PCCO	[281]	0.13	–	–
PCCO	[281]	0.14	–	–
PCCO	[280]	0.05	–	–
PCCO	[280]	0.10	–	–
PCCO	[270]	0.12	sample 1	–
PCCO	[270]	0.12	sample 2	–
PCCO	[270]	0.12	sample 3	–

PCCO	[270]	0.12	sample 4	–
PLCCO	[282]	0.03	–	–
PLCCO	[282]	0.05	–	–
PLCCO	[282]	0.08	–	–
PLCCO	[282]	0.10	–	–
PLCCO	[282]	0.13	–	–
LCCO	[175]	0.06	–	–
LCCO	[175]	0.07	–	–
LCCO	[175]	0.08	–	–
LCCO	[175]	0.10	–	–

Table A.3: Electron-doped cuprate samples for which *ab*-plane charge transport is analyzed (Chapter 5).

* The actual chemical composition was determined via ICP/EDS measurements (see Chapter 2). The listed Néel temperatures for NCCO were obtained from neutron scattering experiments (see Chapters 2 and 3). All other Ce concentration x are nominal values. This Thesis work analyzed all the data listed in the Table.

A.4 Hole-doped cuprate samples for ab-plane charge transport analysis

Material	Reference	x or δ	Estimated p	Special condition	T_{N}(K)	T^{**}(K)
LSCO	[272]	x=0.01	0.01	–	245	–
LSCO	[272]	x=0.02	0.02	–	–	–
LSCO	[272]	x=0.03	0.03	–	–	–
LSCO	[272]	x=0.04	0.04	–	–	–
LSCO	[272]	x=0.05	0.05	–	–	–
LSCO	[272]	x=0.06	0.06	–	–	–
YBCO	[272]	δ=0.30	0.035*	–	225	280
YBCO	[272]	δ=0.35	0.05*	–	–	230
YBCO	[272]	δ=0.40	0.065*	–	–	200
YBCO	[272]	δ=0.45	0.079*	–	–	180
YBCO	[273]	δ=0.28	0.03*	–	250	300
YBCO	[273]	δ=0.30	0.035*	–	225	280
YBCO	[273]	δ=0.35	0.05*	–	–	230
YBCO	[273]	δ=0.43	0.073*	–	–	190
YBCO	[248]	δ=0.60	0.123*	Irradiation step 7	–	–
YBCO	[248]	δ=0.60	0.123*	Irradiation step 6	–	–
YBCO	[248]	δ=0.60	0.123*	Irradiation step 5	–	–
YBCO	[248]	δ=0.60	0.123*	Irradiation step 4	–	–
YBCO	[248]	δ=0..60	0.123*	Irradiation step 3	–	–
La-Bi2201	[246]	x=0.84	0.102**	–	–	–
La-Bi2201	[275]	–	0.10	–	–	–
La-Bi2201	[275]	–	0.105	–	–	–

Table A.4: Hole-doped cuprate samples for which ab-plane charge transport is analyzed (Chapter 5).

* Hole concentration of YBCO estimated with the method in [291]. ** Hole concentration of La-Bi2201 estimated using data from [275]. Hole concentration of LSCO is taken to be $p = x$. The listed Néel temperatures for LSCO and YBCO was taken from [272, 273]. T^{**} is a characteristic temperature below which the ab-plane resistivity exhibits a quadratic temperature dependence [255]. This Thesis work analyzed all the data listed in the Table.

A.5 Electron-doped cuprate samples for c-axis charge transport analysis

Material	Reference	x	Special condition	T_N(K)
NCCO	this Thesis	0.042*	–	240
NCCO	this Thesis	0.10	–	165
NCCO	this Thesis	0.128*	–	102
NCCO	this Thesis	0.134*	–	102
NCCO	this Thesis	0.145*	–	85
NCCO	[53]	0.025	–	250
NCCO	[53]	0.05	–	250
NCCO	[53]	0.075	–	230
NCCO	[53]	0.10	–	165
NCCO	[53]	0.125	–	120
NCCO	[53]	0.150	–	–
NCCO	[276]	0.03	–	–
NCCO	[276]	0.06	–	–
NCCO	[276]	0.12	–	–
PLCCO	[282]	0.03	–	–
SCCO	[287]	0.14	–	–
SCCO	[287]	0.143	–	–
SCCO	[288]	–	Mesa	–

Table A.5: Electron-doped cuprate samples for which c-axis charge transport is analyzed (Chapter 5).

* The actual chemical composition and onset T_c were determined via ICP/EDS and SQUID measurements (see Chapter 2). All other Ce concentrations x are nominal values. The listed Néel temperatures for NCCO were obtained from neutron scattering experiments (see Chapters 2 and 3). This Thesis work analyzed all the data listed in the Table.